MAX PLANCK INSTITUTE
OF COLLOIDS
AND INTERFACES

Correlations between osteocyte lacuno-canalicular network and material characteristics in bone adaptation and regeneration

Dissertation

zur Erlangung des akademischen Grades
doctor rerum naturalium (Dr. rer. nat.)
im Fach Physik

eingereicht an der
Mathematisch-Naturwissenschaftlichen Fakultät
der Universität Potsdam

von

M. Sc. Victoria Schemenz

Tag der Disputation: 30. Juni 2022

Promotionsausschuss:

Vorsitzende:	Prof. Dr. Svetlana Santer
1. Gutachter:	Prof. Dr. Dr. hc. Peter Fratzl
2. Gutachterin:	Assoc. Prof. Dr. Bettina Willie
3. Gutachter:	Prof. Dr. Henrik Birkedal
Direkter Betreuer und Mentor:	Dr. Wolfgang Wagermaier

Published online on the

Publication Server of the University of Potsdam:
https://doi.org/10.25932/publishup-55959
https://nbn-resolving.org/urn:nbn:de:kobv:517-opus4-559593

Erklärung zur Selbstständigkeit

Ich versichere, dass ich diese Arbeit selbstständig verfasst habe, keine anderen als die angegebenen Quellen und Hilfsmittel benutzt habe und die wörtlich oder inhaltlich übernommenen Stellen als solche kenntlich gemacht habe.

Potsdam, den 26.01.2022, _____

M. Sc. Victoria Schemenz

"All that I am, or hope to be, I owe to my angel mother"
Abraham Lincoln

Abstract

The complex hierarchical structure of bone undergoes a lifelong remodeling process, where it adapts to mechanical needs. Hereby, bone resorption by osteoclasts and bone formation by osteoblasts have to be balanced to sustain a healthy and stable organ. Osteocytes orchestrate this interplay by sensing mechanical strains and translating them into biochemical signals. The osteocytes are located in lacunae and are connected to one another and other bone cells through small channels, the canaliculi. Lacunae and canaliculi form a network (LCN) that is able to transport ions and enables cell-to-cell communication. Osteocytes might also contribute to mineral homeostasis by direct interactions with the surrounding matrix. If the LCN is acting as a transport system, this should be reflected in the mineralization pattern. The central hypothesis of this thesis is that osteocytes are actively changing their material environment. Characterization methods of material science are used to achieve the aim of detecting traces of this interaction between osteocytes and the extracellular matrix. First, healthy murine bones were characterized. The properties analyzed were then compared with three murine model systems: 1) a loading model; 2) a healing model; and 3) a disease model, where the Fbn1 gene is dysfunctional causing defects in the formation of the extracellular tissue.

The measurement strategy included routines that make it possible to analyze the organization of the LCN and the material components (i.e., the organic collagen matrix and the mineral particles) in the same bone volumes and compare the spatial distribution of different data sets. The three-dimensional network architecture of the LCN is visualized by confocal laser scanning microscopy after rhodamine staining and is then quantified. The calcium content is determined via quantitative backscattered electron imaging, while small- and wide-angle X-ray scattering are employed to determine the thickness and length of local mineral particles.

First, tibiae cortices of healthy mice were characterized to investigate how changes in LCN architecture can be attributed to interactions of osteocytes with the surrounding bone matrix. The tibial midshaft cross-sections showed two main regions, consisting of a band with unordered LCN surrounded by a region with ordered LCN. The unordered region is a remnant of early bone formation and exhibited short and thin mineral particles. The surrounding, more aligned bone showed ordered and dense LCN as well as thicker and longer mineral particles. The calcium content was unchanged between the two regions.

In the mouse loading model, the left tibia underwent two weeks of mechanical stimulation, which results in increased bone formation and decreased resorption in skeletally mature mice. Here the specific research question addressed was how do bone material characteristics change at the new formed bone due to loading? The new bone formed in response to mechanical stimulation showed similar properties in terms of the mineral particles, like the ordered calcium region but lower calcium content. There was a clear, recognizable border between mature and newly formed bone. Nevertheless, some canaliculi went through this border connecting the LCN of mature and newly formed bone.

Additionally, the question should be answered whether the LCN topology and the bone matrix material properties adapt to loading. Although, mechanically stimulated bones did not show differences in calcium content compared to controls, different correlations were found between the local LCN density and the local calcium content depending on whether

the bone was loaded or not. These results suggest that the LCN may serve as a mineral reservoir.

For the healing model, the femurs of mice underwent an osteotomy (a surgery in which a fracture is created by a cut in the midshaft region) and were allowed to heal for 21 days. Thus, the spatial variations in the LCN topology and mineral properties within different tissue types and their interfaces, namely calcified cartilage, bony callus and cortex, could be simultaneously visualized and compared in this model. All tissue types showed structural differences across multiple length scales. Calcium content increased and became more homogeneous from calcified cartilage to bony callus to lamellar cortical bone. The degree of LCN organization increased as well, while the lacunae became smaller, as did the lacunar density between these different tissue types. In the calcified cartilage, the mineral particles were short and thin. While most of the callus had a woven-like structure, it also served as a scaffold for more lamellar tissue, which showed thinner mineral particles, but a higher degree of alignment in both, mineral particles and the LCN. The cortex showed the highest values for mineral length, thickness and degree of orientation. Although only a few canaliculi connected callus and cortical region, this indicates that communication between osteocytes of both tissues should be possible.

A mouse model for the disease Marfan syndrome, which includes a genetic defect in the fibrillin-1 gene, was investigated. In humans, Marfan syndrome is characterized by a range of clinical symptoms such as long bone overgrowth, loose joints, reduced bone mineral density, compromised bone microarchitecture, and increased fracture rates. Thus, fibrillin-1 seems to play a role in the skeletal homeostasis. Therefore, the present work studied how Marfan syndrome alters LCN architecture and the surrounding bone matrix. The mice with Marfan syndrome showed longer tibiae than their healthy littermates from an age of seven weeks onwards. In contrast, the cortical development appeared retarded, which was observed across all measured characteristics, i. e. lower endocortical bone formation, looser and less organized lacuno-canalicular network, less collagen orientation as well as a trend to thinner and shorter mineral particles.

In each of the three model systems, this study found that changes in the LCN architecture spatially correlated with bone matrix material parameters. While not knowing the exact mechanism, these results provide indications that osteocytes can actively manipulate a mineral reservoir located around the canaliculi to make a quickly accessible contribution to mineral homeostasis. However, this interaction is most likely not one-sided, but could be understood as an interplay between osteocytes and extra-cellular matrix, since the bone matrix contains biochemical signaling molecules that can change osteocyte behavior. Bone (re)modeling can therefore not only be understood as a method for removing defects or adapting to external mechanical stimuli, but also for increasing the efficiency of possible osteocyte-mineral interactions during bone homeostasis. With these findings, it seems reasonable to consider osteocytes as a target for drug development related to bone diseases that cause changes in bone composition and mechanical properties.

Zusammenfassung

Knochen haben eine komplexe hierarchische Struktur, die einen lebenslangen Umbauprozess durchläuft, bei dem der Knochen sich seinen mechanischen Anforderungen anpasst. Um ein gesundes und stabiles Organ zu erhalten müssen Knochenresorption (durch Osteoklasten) und Knochenbildung (durch Osteoblasten) ausgewogen sein. Osteozyten lenken dieses Wechselspiel, indem sie mechanische Belastungen wahrnehmen und sie in biochemische Signale übersetzen. Die Osteozyten sitzen in Lakunen und sind durch Kanälchen untereinander und mit anderen Knochenzellen über ein Netzwerk (LCN) verbunden, das in der Lage ist, Ionen zu transportieren und eine Kommunikation von Zelle zu Zelle zu ermöglichen. Außerdem vermutet man, dass Osteozyten auch durch direkte Wechselwirkungen mit der umgebenden Matrix zur Mineralhomöostase beitragen könnten. Im Mittelpunkt dieser Arbeit steht die Frage, ob Osteozyten ihre materielle Umgebung aktiv verändern können. Um Spuren dieser Wechselwirkung zwischen Osteozyten und der extrazellulären Matrix nachzuweisen, werden materialwissenschaftliche Charakterisierungsmethoden eingesetzt. Zunächst wurden gesunde Mäuseknochen charakterisiert. Die erworbenen Ergebnisse wurden dann mit drei murinen Modellsystemen verglichen: 1) einem Belastungsmodell; 2) ein Heilungsmodell und 3) ein Krankheitsmodell, bei dem das Fbn1-Gen dysfunktional ist und Defekte in der Bildung des extrazellulären Gewebes verursacht werden.

Die Messstrategie umfasste Routinen, die es ermöglichen, die Organisation des LCN und der Materialkomponenten (d.h. die organische Kollagenmatrix und die mineralischen Partikel) in denselben Knochenvolumina zu analysieren und die räumliche Verteilung der verschiedenen Datensätze zu vergleichen. Die dreidimensionale Netzwerkarchitektur des LCN wird durch konfokale Laser-Scanning-Mikroskopie nach Rhodamin-Färbung gemessen und anschließend quantifiziert. Der Kalziumgehalt wird mittels quantitativer Rückstreuelektronenbildgebung bestimmt, während Klein- und Weitwinkel-Röntgenstreuung verwendet werden, um die Dicke und Länge der Mineralpartikel zu bestimmen.

Zunächst wurden Querschnitte der Unterschenkel von gesunden Mäusen charakterisiert, um zu untersuchen, ob Veränderungen in der LCN-Architektur auf Wechselwirkungen von Osteozyten mit der umgebenden Knochenmatrix zurückgeführt werden können. Die Kortizes zeigten zwei Hauptregionen, ein Band mit ungeordneter LCN-Architektur, umgeben von einer Region mit geordneter LCN. Die ungeordnete Region ist ein Überbleibsel der frühen Knochenbildung und wies kurze und dünne Mineralpartikel auf. Der umgebende, stärker ausgerichtete Knochen zeigte ein geordnetes und dichtes LCN, sowie dickere und längere Mineralpartikel. Der Kalziumgehalt blieb bei beiden Regionen unverändert.

Im Mausbelastungsmodell wurde das linke Schienbein zwei Wochen lang mechanisch stimuliert, was zu einer erhöhten Knochenbildung führt. Hier sollte die Forschungsfrage beantwortet werden, wie sich Knochenmaterialeigenschaften an (Re-)Modellierungsstellen aufgrund von Belastung ändern. Der, als Reaktion auf die mechanische Stimulation, gebildete neue Knochen zeigte ähnliche Eigenschaften in Bezug auf die Mineralpartikel, wie die geordnete Kortexregion. Es gab eine klar erkennbare Grenze zwischen reifem und neu gebildetem Knochen. Trotzdem gingen einige Kanälchen durch diese Grenze, die die LCN aus reifem und neu gebildetem Knochen verband.

Für das Heilungsmodell wurden die Oberschenkel von Mäusen einer Osteotomie unterzogen (einer Operation, bei der durch einen Schnitt in der Diaphyse ein Bruch erzeugt wird).

Danach konnte die Fraktur 21 Tage heilen. Dadurch konnten in diesem Modell gleichzeitig verkalkter Knorpel, knöcherner Kallus und Kortex untersucht werden. Dafür wurde die räumliche Verteilung der LCN-Topologie sowie die Mineraleigenschaften der verschiedenen Gewebetypen und ihrer Grenzflächen visualisiert und verglichen. Alle Gewebetypen zeigten strukturelle Unterschiede über mehrere Längenskalen hinweg. Der Kalziumgehalt nahm von kalzifiziertem Knorpel zu knöchernem Kallus zu lamellarem kortikalem Knochen zu und wurde homogener. Der Grad der LCN-Organisation nahm ebenfalls zu, während die Lakunen vom Kallus zum Kortexgewebe kleiner wurden, ebenso wie die Lakunendichte. Im verkalkten Knorpel waren die Mineralpartikel kurz und dünn. Der größte Teil des Kallus wies eine Geflechtsknochenstruktur auf und diente als Gerüst für lamellares Gewebe, das dünnere Mineralpartikel, aber einen höheren Grad an Ausrichtung sowohl in den Mineralpartikeln als auch im LCN aufwies. Der Kortex zeigte die höchsten Werte für Minerallänge, Dicke und Orientierungsgrad. Obwohl nur wenige Kanälchen den Kallus und kortikale Regionen verbinden, weist dies darauf hin, dass eine Kommunikation zwischen Osteozyten beider Gewebe möglich sein sollte.

Es wurde auch ein Mausmodell für das Marfan-Syndrom untersucht, das einen Gendefekt im Fibrillin-1-Gen beinhaltet. Beim Menschen ist das Marfan-Syndrom durch eine Reihe klinischer Symptome gekennzeichnet, wie z. B. übermäßiges Wachstum der Gliedmaßen, überstreckbare Gelenke, verringerte Knochenmineraldichte, beeinträchtigte Knochenmikroarchitektur und erhöhte Frakturraten. Somit scheint Fibrillin-1 eine Rolle in der Skeletthomöostase zu spielen. Deswegen untersuchte die vorliegende Arbeit, ob und wie das Marfan-Syndrom die LCN-Architektur und die umgebende Knochenmatrix verändert. Die Mäuse mit Marfan-Syndrom zeigten bereits ab einem Alter von sieben Wochen längere Schienbeine als ihre gesunden Wurfgeschwister. Im Gegensatz dazu erschien die kortikale Entwicklung verzögert, was über alle gemessenen Merkmale hinweg beobachtet wurde, d.h. niedrigere endokortikale Knochenbildung, lockereres und weniger organisiertes LCN, geringerer Grad an Kollagenorientierung sowie ein Trend zu dünneren und kürzeren Mineralpartikel.

In jedem der drei Modellsysteme fand diese Studie, dass Änderungen in der LCN-Architektur räumlich mit Parametern des Knochenmatrixmaterials korrelierten. Obwohl der genaue Mechanismus nicht bekannt ist, liefern diese Ergebnisse Hinweise darauf, dass Osteozyten ein Mineralreservoir aktiv manipulieren können. Dieses Reservoir befindet sich um die Kanälchen herum und dieser Prozess würde es ermöglichen, einen schnell zugänglichen Beitrag zur Mineralhomöostase zu leisten. Diese Interaktion ist jedoch höchstwahrscheinlich nicht einseitig, sondern könnte als Wechselspiel zwischen Osteozyten und extrazellulärer Matrix verstanden werden, da die Knochenmatrix biochemische Signalmoleküle enthält, die das Verhalten von Osteozyten verändern können. Knochen(re)modellierung kann daher nicht nur als Methode zur Defektbeseitigung oder Anpassung an äußere mechanische Reize verstanden werden, sondern auch zur Effizienzsteigerung möglicher Osteozyten-Mineral-Interaktionen während der Knochenhomöostase. Angesichts dieser Ergebnisse erscheint es sinnvoll, Osteozyten als Ziel für die Arzneimittelentwicklung im Zusammenhang mit Knochenerkrankungen in Betracht zu ziehen, die Veränderungen der Knochenzusammensetzung und deren mechanischen Eigenschaften verursachen.

Acknowledgement

I want to thank all the people who contributed to this thesis, supported me through sometimes harsh times and inspired me over the years. It was a great experience - not only scientific-wise, but also the surrounding. I am thankful for all the interesting people I met, the beautiful places, I have visited, and all I have learned. Thank you for improving my language skills in English, French, a bit Spanish and last, but not least Austrian.

First of all, I like to thank Peter Fratzl for the opportunity to work at the biomaterials department of the Max Planck Institute of Colloids and Interfaces. Thank you so much for building up such a nice working environment, I could not imagine a better place to make a PhD. I really want to thank you for the fruitful discussions and all of your input for the project.

Equally, I want to thank my supervisor and mentor Wolfgang Wagermaier for the opportunity to work on such a great project, for his continuous support as well as for the chances he has given me to go abroad and all the nice discussion (scientific or not). Thank you for allowing me to write this thesis in LaTeX, even if you didn´t like it. Now you can switch back to Word. Last but not least thank you for buying me toilette paper (and other stuff) during my quarantine before Christmas 2020 ;)

I want to express my gratitude to Bettina Willie for providing the samples of this project, discussions about my work, helping my physicists brain through the biological questions, the opportunity to participate in the Marfan project and to stay abroad in her lab at Shriners Hospital in Montreal, Canada. Thank you also for your feedback on the work of this thesis and for taking over the supervision of my thesis.

Special thanks go to Henrik Birkedal, that he agreed to review this work and be part of my examination committee.

Big thanks go to Richard Weinkamer for the interesting discussions - not only about mountains – and all the comments on the drafts. They lead me to much better understanding and nice texts.

I also want to acknowledge Paul Zaslansky, who believed so much in me, that he hired me for a Postdoc position in his lab before I´ve even submitted this thesis. It´s done now. I am ready for the adventure with you!!!

Thank you Sarah and Max for being great co-workers, it was a pleasure to work with you. We have suffered together and shared a sense of achievement. I am grateful to you for cheering me up during dark moments, for making the long hours in the computer lab enjoyable and for video meeting, coffee rounds, walk&talks and all the discussions. I enjoyed it a lot.

Dear Alex, I am sorry for my bad German in comparison to our supervisors and John. But thank you for your introduction in the world of bone research and the fun you brought into my life. Without you, I would not have known, neither that osteocytes fulfill wishes nor how to dance the osteocyte dance.

I want to thank Andreas Roschger for sharing his amazing knowledge with me, especially in qBEI, but also at the CLSM and SHG. I am still wondering whether the cooling of the multi photon laser would be better with Mai Tai or without. I would like to thank you for all your input.

Thanks to all colleagues at the biomaterials department and the workshop at the MPIKG, especially to Birgit Schonert for providing all the help and details in terms of sample preparation. Without this excellent input the experiments would not have been accomplishable. Special thanks to André Gjardy, without whom I would not have known anything about this project, for his introduction into the project and the work at MPI. I want to thank also Daniel Werner for the help with the μCT. I will always remember the birthday of EasyTom. Huge thanks to Toni Tang for being such a productive team in synchrotron experiments and your advices.

Many thanks go also to Bettina Willie's lab for welcoming me and introducing me to new techniques during my research stay in their lab. Especially, I want to thank Elizabeth Zimmermann and Alice Bouchard for their helping hands during the imaging. But I also need to thank the mice, who gave their life for this studies. I know your bones now by heart and think, you have done a good service for research.

I really want to thank the team of the Ludwig Boltzmann Institute for Osteology; especially Ghazal Hedjazi who helped me to understand and work with SHG, Markus Hartmann, Stéphane Bluin, Petra Keplinger, Sonja Lueger and Phaedra Messmer for assistance during sample preparation, data acquisition and evaluation of qBEI. And for the nice welcome in Vienna. Additionally, Nadja Fratzl-Zelman for inviting me to the LBIO retreats, where I learned a lot.

A special thank goes also to Roland Brunner and Fereshteh Falah Chamasemani of the Materials Center Leoben Forschung GmbH for evaluation and understanding the μCT data of the lacunae.

I am also thankful to the ESRF for the opportunity given to perform experiments at their facility and in particular, I want to thank Manfred Burghammer and his team from ID13 at the ESRF for the help and especially the patience when explaining the beamline setup.

In addition, I want to thank the Berlin-Brandenburg School for Regenerative Therapies (BSRT) and in particular Sabine Bartosch, for enriching the experience of the PhD program. It's hard to sum up all the skills and the new things I learned through the different courses and events organized by the BSRT, as well as the many interesting people I was able to meet on the way. Thanks to the DAAD for the opportunity to realize the visit and experiments in Bettina Willie's lab.

Final thanks go to my family and friends. You have been my greatest source of joy and support over the past few years. Thank you all for encouraging me and for being there for me through all the ups and downs. It was nice that we didn't lose sight of each other even when the distance was great and I can tell you that I can contact you more often from now on. Even if it is unfair not to mention most of you, I have to introduce myself to some very special people :

I want to thank Felix Albrecht for listening to all of my complains and his belief in me–even when I didn´t. I want to thank Ines and her family - a baby picture in a while is better than every drug! Linda, thank you for the exchange of thoughts and memes. This thesis would not be the same without the help of my friends Bernhard Riester, Jan Bader and Andreas Wolf. Thank you for reviewing and your feedback.

A huge thanks goes also to Johannes, who stayed with me through the whole process of my dissertation, even through the hard times and with thousands of kilometers between us.

At the end I want to express my love and my gratitude towards my family. Most of the time, you were not sure what I am doing, but I could always count on you.

Thank you all so much!

Contents

1. Introduction and scope of this thesis

Bone has a complex hierarchical structure, which is adapted at every level to perform its mechanical, metabolic and protective functions [Weinkamer and Fratzl, 2011, Reznikov et al., 2014a]. At the nanoscale level, bone is a composite of a collagen matrix, nano-sized mineral particles of carbonated hydroxyapatite ($Ca_{10}(PO_4)_6(OH)_2$) and water [Fratzl et al., 2004, Weiner and Wagner, 1998]. Collagen and minerals form mineralized collagen fibrils – the building block of bone material. They self-assemble to larger structures with different degrees of organization [Giraud-Guille et al., 2008]. This extracellular matrix (ECM) undergoes a continuous remodeling, which is an effective interplay between bone resorption by osteoclasts and bone formation by osteoblasts [Fratzl and Weinkamer, 2007, Raggatt and Partridge, 2010]. During deposition of new bone, some osteoblasts get embedded in the mineral matrix and become osteocytes [Franz-Odendaal et al., 2006]. These cells build not only a cell-to-cell communication system, but also a system of extracellular spaces where also bone tissue can be perfused–the so-called lacuno-canalicular network (LCN). Osteocytes are cells known to orchestrate the bone remodeling by sensing mechanical strains and translating them into biomechanical signals [Bonewald, 2011, Klein-Nulend et al., 2013], but osteocytes might also contribute to mineral homeostasis by direct interactions with the surrounding matrix [Kerschnitzki et al., 2011b, Bonucci, 2009].

The overarching aim of the research project behind this thesis is to test the hypothesis that the osteocyte network acts as a mechanosensing system and as a transport system in (de)mineralization processes. To test this hypothesis, emphasis is placed on the organizational characteristics of the cellular component (i.e. the structure of the LCN) and of the material component (i.e., mineral particles and organic collagen substrates) within the same bone samples and then to analyze the spatial correlations between them. Whereas both, the structure and properties of the ECM as well as those of the LCN are still a subject of intense investigations, this thesis aims to study their relation to each other. Hence, a combination of several techniques has to be used to characterize the osteocyte network organization together with the measurement of bone ultra-structural properties on the submicron level within the same bone volume. This study should offer a way to better understand the influence of cell-cell organization during bone formation and remodeling as well as cell-matrix interactions, i.e. the impact of osteocyte network organization in relation to the bone characteristics such as matrix orientation and mineralization. This may help to clarify the role of osteocytes during homeostasis. Furthermore, these insights could give advice whether these cells should be considered as a target for drug development in the context of bone diseases which cause changes in the bone material and mechanical properties.

To fulfill this purpose, different models are studied in this thesis:

The different structures of healthy, cortical bone, namely lamellar and woven bone [Bach-Gansmo et al., 2015], are compared to each other. These results are compared again with bone regions of new bone formation and resorption after mechanical stimulation with in-vivo loading experiments (chapter 5). Then, the properties of the different tissue types in healing bone are studied as well as their transition zones (chapter 6). Finally, the results of the investigations are matched to diseased bone with defects in the formation of the extracellular tissue matrix, i.e. bones from mice with the Marfan syndrome (MFS) (chapter 7).

To achieve the main objectives, the following approach is applied to all systems:

- quantify bone mineral characteristics and the topology of the LCN in the different bone structures and
- elucidate, if and how the LCN topology and bone matrix parameters are correlated to each other.

Special attention is put onto the bone mineral characteristics and the topology of the LCN at transition zones between different tissue types. It is also investigated whether the architecture of the LCN and matrix properties improve after new bone formation to test if initially formed bone can act as an endogenous scaffold.

Therefore, all models undergo the following characterization steps:

- sample preparation (chapter 4.2),
- structural characterization of the LCN by rhodamine staining and confocal laser scanning microscopy (CLSM) (chapter 4.3) as well as high resolution micro-computed tomography (μCT) measurements on selected samples (chapter 4.3.2),
- characterization of the calcium content with quantitative backscattered electron imaging (qBEI) (chapter 3.3.2),
- 2D mapping of the mineral nanostructure via high resolution small and wide angle X-ray scattering (SAXS/WAXS) (chapter 3.4.3) and
- correlation analysis of the different 3D and 2D maps of the bone samples (chapter 4.6).

The data evaluation in this work goes beyond the usual evaluation of experimental data of such kind. The 2D and 3D images from CLSM, qBEI and SAXS/WAXS are only one part of the searched information. To achieve the specific objectives as formulated above, it is necessary to investigate the combined information from all of these methods and align the images in a common coordinate system. For this purpose, the sample preparation and the experimental procedure that are used in this doctoral thesis have been developed in recent years (especially at the Max Planck Institute of Colloids and Interfaces (MPIKG) and cooperation partners). However, the size and resolution of the measured regions surpass the ones of previous studies. For the first time, all measurements could be carried out on the same sample volume, so that the images can be aligned in a common coordinate system with the help of a developed Python script (see section 4.6). In addition to spatial correlations within the images, this enables cross-correlations between the various parameters to be examined. While earlier work developed the basic methods and fundamentally examined the hypothesis of osteocytic osteolysis, this type of analysis is being applied for the first time to very specific, larger bone studies and linked to clinical studies.

2. Bone structure, remodeling and development

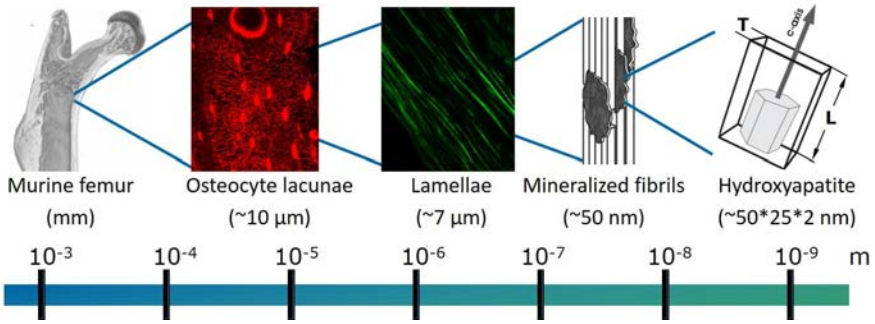

Figure 2.1.: Hierarchical organization of a murine long bone. Long bones show trabecular structure at the joints (metaphysis and epiphysis) and compact cortical in the midshaft region (diaphysis). At the cell level, osteocyte lacunae are connected by canaliculi. The bone matrix consists of collagen lamellas of assembled fiber bundles whereby each fiber is built of mineralized single collagen fibrils. The figure of the mineralized fibrils is taken from [Fratzl and Weinkamer, 2007] with permission of Elsevier.

2.1. Bone as a dynamic biomaterial

Bones form the skeletal system in all vertebrates. For example, the human skeleton consists of around 200 (depending on the age [Neumann and Gest, 2020]) different bones, which differ in shape, size and mechanical properties, depending on their anatomical location and function. But all have in common that they are on the one hand constructed to resist high forces without breaking, but on the other hand are light weight [Fratzl et al., 2004]. Additionally, bone cells act in a well-organized way in order to adjust bone shape due to external stimuli [Duncan and Turner, 1995]. Thus, bone is not only a static material but undergoes continuous remodeling over the whole lifetime [Currey and Shahar, 2013].

2.1.1. Multiscale structure of long bones

To reach maximum resistance to fracture and at the same time be as light as possible, bone is built by using a hierarchical structure ranging from the molecular up to the macroscopic level [Weiner and Wagner, 1998, Fratzl and Weinkamer, 2007], which is illustrated in Figure 2.1.

At the nanoscale, bone is made of 70% inorganic material and 30% organic matrix, of which approximately $90-95\%$ is collagen type I and the rest noncollageneous proteins and lipids [Felsenberg, 2001]. In bone, collagen consists of polypeptide chains with an amino acid sequence consisting of Glycine-X-Y repeats, which are coiled in a left-handed helix. Three of these chains always assemble in a right-handed triple helix forming the collagen type I molecule [Van der Rest and Garrone, 1991]. In collagen, about one third of the X residues is proline, while one third of the Y residues is hydroxyproline. The presence of hydroxyproline is essential to stabilize the triple helix. Typically, the molecules have a length of 300 nm and a diameter of 1.5 nm [Orgel et al., 2011].

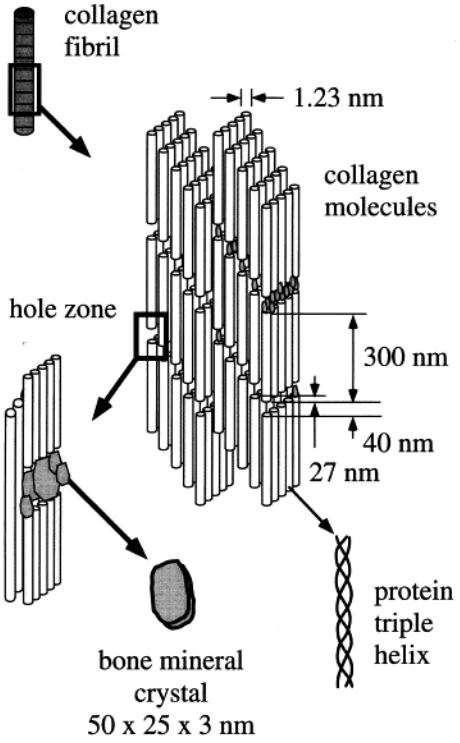

Figure 2.2.: Sketch of mineralized collagen structure. Triple helical collagen type I assembles to fibrils which in turn assemble into fibers including bone mineral crystals. From [Rho et al., 1998] with permission of Elsevier.

Multiple collagen molecules are staggered along the axial direction periodically separated by 67 nm on each end. Together they form so-called collagen fibrils of around 100 nm diameter with overlapping zones of approximately 32 nm and gap zones of 35 nm (see Figure 2.2) [Fratzl, 2008, Orgel et al., 2011]. Hydroxyapatite particles ($Ca_{10}(PO_4)_6(OH)_2$, HAP) deposit in the collagen gap zones and grow into plate like structures which are supposed to be mainly parallel to the longitudinal axis of the collagen fibril. Studies indicate that the size of mineral particles depends on the tissue age [Lange et al., 2011, Hoerth et al., 2014]. While the thickness varies mainly between 1.5 nm and 4 nm, the length has a wider variety from 14 nm to 30 nm [Fratzl, 1994, Lange et al., 2011].

Mineral particles generally contain various impurities or inclusions of other elements that replace either the calcium ions, the phosphate or the hydroxyl groups in the lattice. The most common substitute is carbonate whose amount in hydroxyapatite particles (HAP) is also considered an indicator of tissue age [Akkus et al., 2004]. Aside from crystals contained in fibrils, there is also extrafibrillar mineral, which appears to be more needle like [Reznikov et al., 2018].

Collagen fibrils assemble in arrays on the next level, which are subsequently arranged into bundles. Between these bundles are thin layers of disordered material in which cellular processes are embedded [Reznikov et al., 2014a]. These cellular processes lie in narrow canals, the so-called canaliculi, which connect osteocytes (lying in lacunae) via the lacuno-canalicular network (LCN) (see chapter 2.1.2). In lamellar bone, the bundles consist of unidirectional arrays and fanning arrays arranged in layers, with changing bundle orientation in each layer [Weiner and Wagner, 1998].

Another bone type is circumferential lamellar bone, found, for example, in the cortex

of murine long bones. Osteoblasts lay this circumferential lamellar bone radially on the endosteal and periosteal bone surfaces. The core zone, which lies between the periosteal and endosteal circumferential lamellar bone, comprises older and more disorganized bone tissue [Bach-Gansmo et al., 2013]. In the so-called woven bone, the fibers are loosely packed and poorly oriented. According to former studies, woven bone seems to act as a scaffold for the later formation of more structured bone [Liu et al., 2010, Kerschnitzki et al., 2011a]. Hence woven bone occurs during bone growth (see chapter 2.2.1) or early stages of bone healing (see chapter 2.2.4) with a relatively high deposition rate greater than 4 µm per day [Currey, 2006]. In many vertebrates the remodeling process removes or replaces this woven bone scaffold with lamellar bone [Kerschnitzki et al., 2011a]. But due to the stochastic character of the remodeling process, leftovers from the bone formation procedure may remain in a central band of the cortical bone in rat and mice [Sontag, 1986, Bach-Gansmo et al., 2015] (see also 2.2.1).

At the next higher hierarchical level (left side of Figure 2.1), one distinguishes between spongy trabecular and compact cortical bone [Rho et al., 1998]. In mature long bones, the outer layer consists of dense cortical bone, whose low porosity of $< 10\%$ is mainly caused by blood vessels and cellular spaces [Currey and Shahar, 2013]. In areas of high compressive loading, such as the femoral head or vertebrae, the cortical bone shell is filled with spongy trabecular bone with high porosity ($> 80\%$). There are no blood vessels inside the trabeculae, but between them, i.e. the nutrition is provided by the surrounding bone marrow [Fratzl and Weinkamer, 2007]. On a micrometer scale, the lamellar bone structure is a mix of organized and disordered regions and is quite similar to the lamellar structure in compact bone. A significant proportion of the fibrils are aligned with each of the long axes of connected trabeculae [Reznikov et al., 2015].

2.1.2. Osteocytes and their role in bone mineralization

Bone is a dynamic living tissue that can constantly adapt to changing external biophysical stimuli in its environment in order to improve its functionality [Hart et al., 2017]. Even without external stimuli, dynamic self-repair mechanisms ensure continuous damage repair and thus strengthen the bone material, as it (i) increases the blood supply, (ii) removes dead bones, (iii) removes microcracks and (iv) contributes to the mineral homeostasis of the body [Currey, 2006]. The whole remodeling process is a result of the interaction of bone cells and schematically shown in Figure 2.3. Osteoclasts resorb bone and leave small cavities behind. Those cavities are then filled by osteoblasts with osteoid (non-mineralized bone matrix), which comprises collagen, proteoglycans (PG) and glycosaminoglycans (GAG). As the new osteoid builds up (formation phase, Figure 2.3), the mineralization of the osteoid begins. Some osteoblasts are incorporated into the bone matrix and differentiate into osteocytes [Franz-Odendaal et al., 2006]. The remaining osteoblasts differentiate into lining cells or die as a result of apoptosis. As the mineralization process progresses, the bone surface returns to its original resting state. However, the process of osteoblast incorporation and differentiation into osteocytes occurs not only during bone remodeling, but also during bone formation.

Osteocytes are the most abundant cells in bone (90% to 95% of all bone cells in adult bone [Bonewald, 2011]). They are located within the bone in so-called lacunae and interact with neighboring cells via their dendrites, the canaliculi. Together, the cell-bodies and dendrites form a functional network connecting cells, bone surface, bone marrow and blood vessels: the LCN. In addition, the surface area is 100 times larger than the area that osteoclasts and osteoblasts encounter on the bone surface [Marotti et al., 1995, Buenzli, 2015].

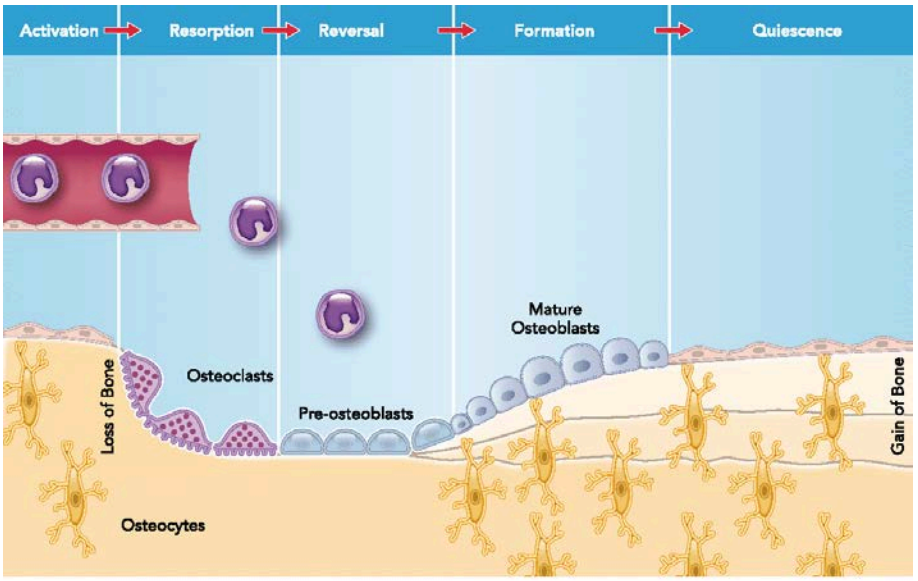

Figure 2.3.: Scheme of the bone remodeling process. The remodeling cycle consists of six consecutive phases: quiescence, activation, resorption, reversal, formation, and termination. During the resorption phase, osteoblasts respond to signals generated by osteocytes. Therefore, the phase is limited in time depending on the level of stimuli responsible for the differentiation and activity of the osteoclasts. It follows the reversal phase characterized by creating a cement line to connect the old and new bones. Osteoprogenitor cells (precursors of osteoblasts) appear along the cavities, proliferate and undergo mitosis. Finally, they differentiate into osteoblasts. The osteoblasts then deposit bone matrix called osteoid in the cavity. Signals for completion of bone remodeling includes terminal osteoblast differentiation. The resting state of the bone surface persists until the next cycle of remodeling begins. Image from [Siddiqui and Partridge, 2016] with permission of The American Physiological Society.

Osteocytes have a variety of functions concerning a lot of bone life processes, but are not yet fully understood. For example, osteocytes control bone remodeling in response to environmental influences such as mechanical stress or hormonal changes by coordinating osteoclasts and osteoblasts [Bonewald, 2011]. It is suggested that programmed cell death (apoptosis) of osteocytes directs neighboring viable osteocytes to synthesize cytokines, which then recruit osteoclasts to remove dead cells and initiate remodeling of the surrounding matrix [Jilka et al., 2012, Verborgt et al., 2000]. Furthermore, osteocytes release sclerostin, which inhibits a process that is responsible for the apoptosis of osteoblasts (WNT / β-catenin signaling pathways) [Winkler et al., 2003]. At the same time, they control also bone loss through the release of receptor activator of nuclear factor $\kappa - B$ ligand (RANKL), which is involved in osteoclastogenisis [O'Brien et al., 2013].

Bones store a large amount of ions, especially calcium and phosphate. In particular, the LCN has very good access to the bone mineral due to its large surface area, which offers the possibility of getting on the calcium and the organism's phosphate metabolism. Osteocytes express fibroblast growth factor 23 (FGF23); a hormone that promotes the excretion of phosphate in the urine and is therefore part of the phosphate regulation mechanism [Feng et al., 2013]. They are also involved in the calcium metabolism [Marenzana et al., 2005]. Various studies have shown that osteocytes have the ability to remove minerals from their perilacunar tissue [Teti and Zallone, 2009, Qing and Bonewald, 2009]. This is called "osteocytic osteolysis" [Bélanger et al., 1967]. It has also been observed that lacunae significantly enlarge during calcium deficiency, such as during breastfeeding where the calcium level in the bone changes [Qing et al., 2012]. Os-

teocytes can also change their direct microenvironment when environmental factors change. Jagodovskii et al. found, for example, a connection between "osteocytic osteolysis" and microgravity by finding "broad osteocyte lacunae that could be associated with perilacunar osteolysis" after sending rats into space for a 22-day space flight [Iagodovskiĭ et al., 1977]. Since the canalicular surface is much larger than the lacunar surface and has direct access to the mineralized bone tissue, it is also possible that the canaliculi participate in the breakdown and replacement of bone minerals, as various studies suggest [Kerschnitzki et al., 2013, Qing and Bonewald, 2009, Qing et al., 2012, Hesse et al., 2015]. However, due to the small dimensions of the canaliculi, the number of studies on this topic is more limited.

Summarizing, the ability of osteocytes to remove and add minerals from the tissue around the lacunae and canaliculi thus has important effects on mineral metabolism, but also on the local mechanical tension field of the lacunae, which influences the osteocyte and its reaction to mechanical loads. It is therefore not surprising that the group at the Max Planck Institute of Colloids and Interfaces (MPIKG) found local bone mineral properties that correlate with the topology of the osteocyte network [Kerschnitzki et al., 2013, Roschger et al., 2019].

2.2. Bone as a living tissue

2.2.1. Bone growth

Longitudinal growth

At the ends of long bones, entrapped between epiphyseal and metaphyseal bone, there is the so-called growth plate. The growth plate can be divided into horizontal zones, which differ in the different stages of differentiation of chondrocytes (see Figure 2.4). At the epiphyseal end of the growth plate is the reserve zone with resting chondrocytes, which are also known as stem cells. These cells are important for the orientation of the underlying chondrocyte columns and thus for unidirectional bone growth [Abad et al., 2002]. When they enter the zone of proliferation, they divide, arrange themselves in a columnar fashion, and synthesize large amounts of extracellular matrix proteins. At some point, proliferating chondrocytes lose their ability to divide. They begin to differentiate, become pre-hypertrophic, and enlarge. Fully differentiated hypertrophic chondrocytes are round in appearance but still produce matrix proteins. At the same time, the intracellular calcium concentration increases and at some point they begin to mineralize the longitudinal septa in the surrounding matrix (zone of temporary calcification) [Sawae et al., 2003]. The chondrocytes in this mineralized zone then eventually die.

Blood vessels invade this area and pave the way for osteoclast precursors [Gerber et al., 1999]. Eighty percent of the longitudinal septum of the growing cartilage is rapidly restored in the metaphyseal region immediately following the invasive vessels [Fazzalari et al., 1997]. The remaining longitudinal septa serve as supports on which osteoblasts deposit bone matrix. This is how the first trabeculae are formed. With increasing distance from the growth plate, the metaphyseal trabeculae in the center of the bone, become thinner and eventually reabsorb completely, at least as long as further length growth is maintained. Therefore, hardly any trabeculae can be found in the diaphysis. That means, the central metaphyseal trabeculae of the long bones are temporary structures during skeletal development that undergo a lifecycle of transformation and destruction [Rauch, 2005]. The trabeculae at the periphery of the metaphysis had a markedly different fate. It is the trabeculae that transmit the load from the growth plate to the cerebral cortex. They become thicker and thicker until they are finally fused and integrated into the metaphyseal cortex [Cadet et al., 2003]. As they grow, many of these peripheral metaphyseal trabeculae eventually end up in the diaphyseal cortex. In summary, it can be said that bone gains additional length when

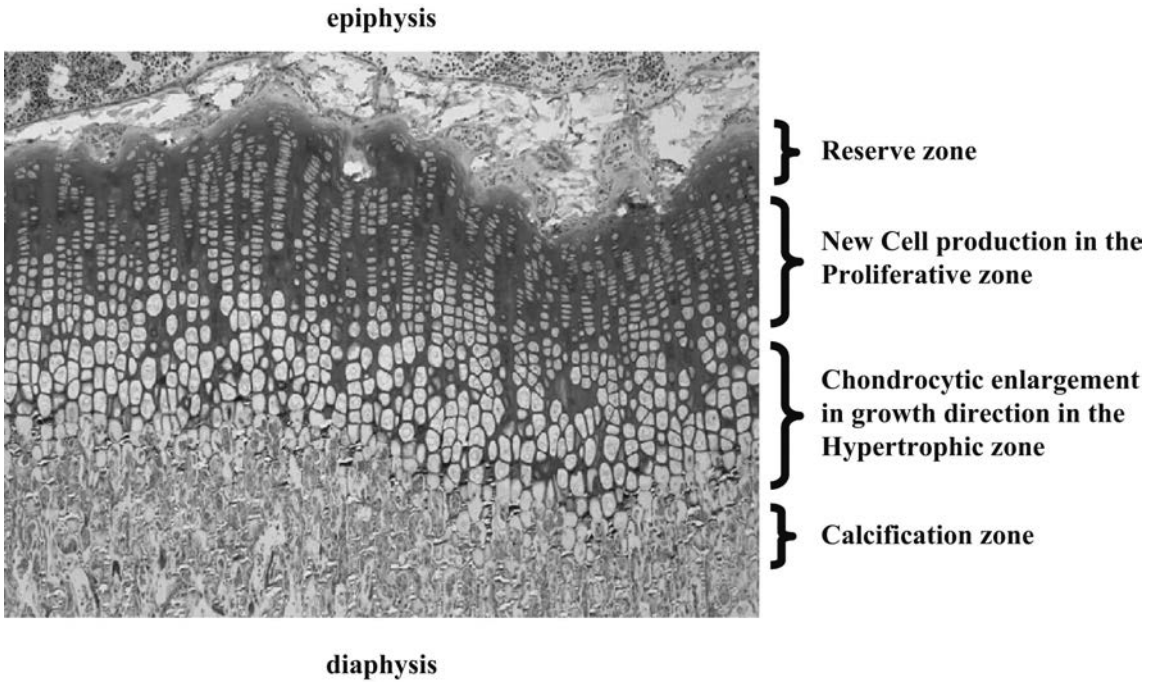

Figure 2.4.: Microscope image of the growth plate. The image is indicating the position of the reserve zone, as well as the proliferative and hypertrophic zones where chondrocytes proliferate and subsequently undergo hypertrophy. The figure is taken from [Villemure and Stokes, 2009] with permission of Elsevier.

new material (both extracellular and intracellular) is squeezed between the reserve of the growth plate and the temporary calcification region. This is the only place where the actual length is added. I.e. events in the growth plate and metaphysis do not add anything to the total length of the bone [Rauch, 2005].

Cortical development

"It is clear that if bones just grew in length without increasing in width, they would become unstable and break at some point."[Rauch, 2005], because the bending strength of an elongated structure like the long bone diaphysis is related to the third power of its diameter. Therefore, bone growth in width is one of the most important determinants of bone strength [Seeman, 2003]. In aging mice, the mechanical properties of the bones are preserved by maintenance of cross-sectional moment of inertia. Similarly to humans, the cortical area shrinks while the periosteal radius increases [Stein et al., 1998]. The cortical structure development is affected by three main processes: consolidation of the trabeculae (i.e., corticalisation), remodeling of the cortical structure from woven to lamellar bone, and periosteal apposition. Additonally, there are also different pattern of bone formation and resorption at the periosteal and endosteal surface (see Figure 2.5 and Figure 2.6):

The young long bones initially consist of loosely connected mineral struts that seem to almost float in the soft tissue [Sharir et al., 2013, Lange et al., 2011]. The cortex is formed by fusing trabeculae, which derive from the growth plate [Enlow, 1962, Cadet et al., 2003]. At the junction between the growth plate and the cortical bone is the groove of Ranvier, which supplies chondrocytes to the developing growth plate and osteoblasts to the growing cortex. As the cortex coagulates, it shows rough, irregular and unorganized woven bone (see Figure 2.5) [Enlow, 1962]. As the entire bone expands, especially in the longitudinal direction, the circumference also increases and the struts restructure.

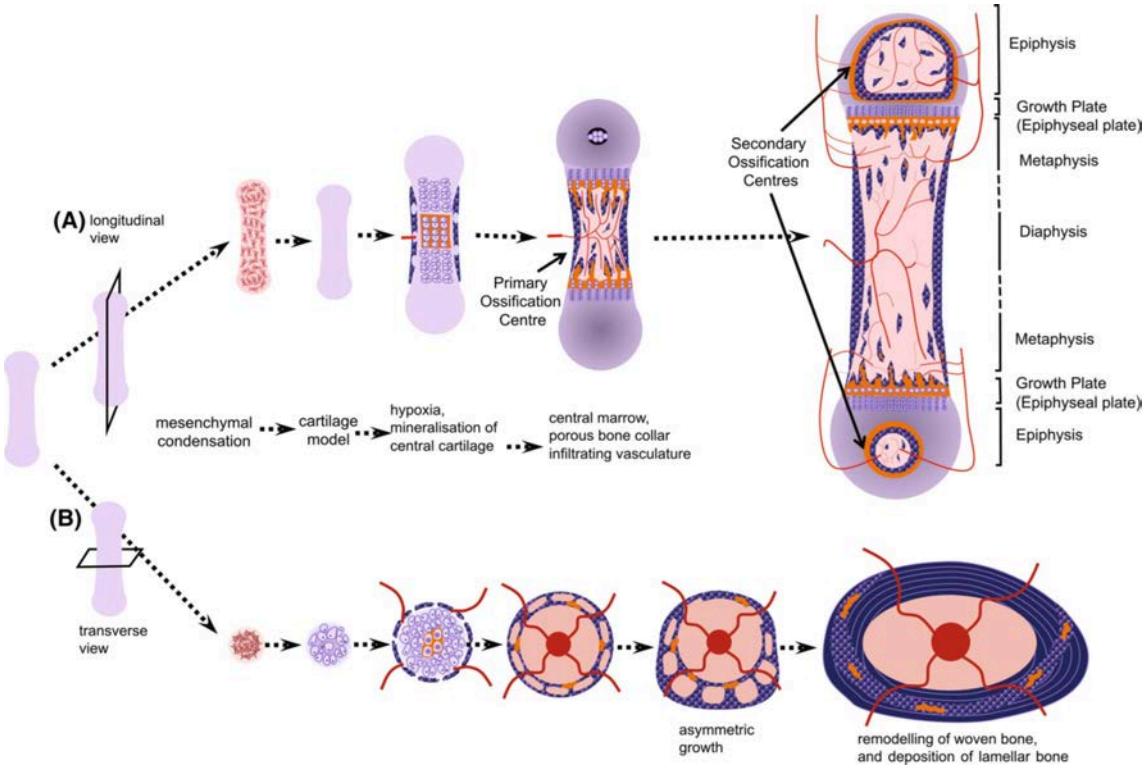

Figure 2.5.: Sketch of bone development. ((A) shows the longitudinal growth, while (B) shows the development of the cross-section. First, mesenchymal stem cells condense and differentiate into a cartilage scaffold. Later chondrocytes become hypertrophic, releasing minerals that accumulate in the cartilage; At the same time, new bone is deposited on the perichondrium by osteoblasts and forms a porous bone collar. This pre-bone structure is gradually remodeled through bone resorption and bone formation. Remnants of cartilage bone and woven bone are gradually replaced with lamellar bone. The figure is taken from [Isojima and Sims, 2021] with permission of Springer.

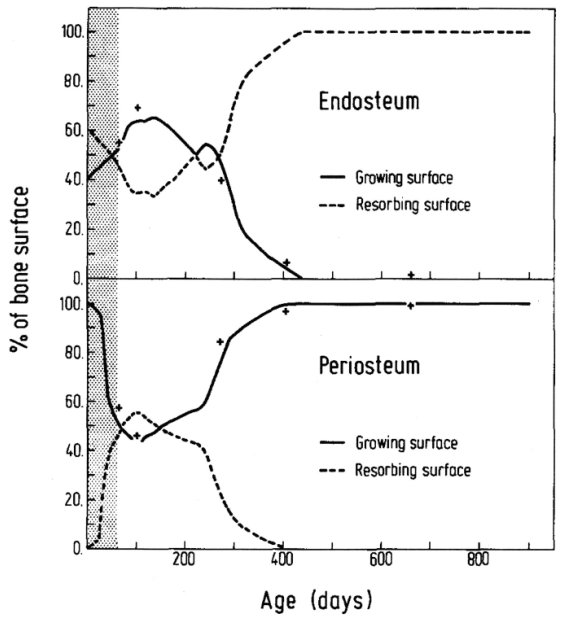

Figure 2.6.: Development of cortical surfaces in a rat femur. The growing and resorption of the endosteal and periosteal surface of a rat femur have been measured as a function of age and are shown with "+" and regression lines, respectively. The dotted area shows only extrapolated from morphological parameters. Reprinted from [Sontag, 1986] page 60 with permission of Elsevier.

In the next step, until an age of around 14 days, the porous cortex is transformed into a dense hollow cylinder with firmer bone material that meets the increasing mechanical requirements induced by crawling and increasing body weight [Bortel et al., 2015]. This bone is gradually replaced by lamellar bone during asymmetrical growth. New lamellar bone is deposited on both the inner (endocortical) and outer (periosteal) surface of the cortex in response to mechanical forces. At the same time, enchondral bone and mineralized cartilage are resorbed by osteoclasts, leaving a central core of bone and cartilage (see Figure 2.5). These leftovers from the bone formation procedure (see [Danielsen et al., 1993, Bach-Gansmo et al., 2013] are present at least until an age of 104 weeks, but it decrease in porosity with advancing age [Ferguson et al., 2003]. This asymmetric process, known as modeling drift, is involved in both, bone enlargement and changes in bone shape during growth [Shipov et al., 2013, Maggiano et al., 2015] and for age-related changes in bone shape [Ferguson et al., 2003]. There may be several control mechanisms for this, including the responses of mechanically sensitive osteocytes, which send specific signals in different directions to induce formation and regeneration [Isojima and Sims, 2021].

This phase is followed by a high increase of bone and marrow volume, bone surface areas and the diameter, while the appositional rate decreases [Sontag, 1986]. The young adult phase defines a transitional state, as the drift of the entire midshaft decreases while the diameter increases, so that the proportion of growing surface area decreases at the endosteum and increases at the periosteum [Sontag, 1986]. The periosteal circumference of the femur continued to increase over 104 weeks. In aged mice, however, a shift in the normal mechanisms that regulate bone shape and position can be observed [Ferguson et al., 2003] The transverse drift becomes less important and, averaged over the entire cortical-enosteal area, there is a continuous net bone loss (see Figure 2.6). In doing so, the middle diaphysis of the femur develops from a concentric elliptical shape at maturity to one that is more amorphous in aged mice. These observations may be due to increased bone resorption with age and in part to slow and discontinuous periosteal formation. This agrees with the

results that in aged mice osteoblast precursors are less able to proliferate and differentiate [Silbermann et al., 1987] and osteoclast precursors increase in number [Perkins et al., 1994]. Furthermore, fluorescent markings showed that in old mice, disorganized bone formation, which indicates remodeling, apparently counteracted endosteal resorption.

2.2.2. Bone adaptation after mechanical stimulation

Julius Wolff reported in 1867 that the organization of trabeculae inside the human femoral neck follows stress trajectories and therefore reflects tension and compression curves [Wolff, 1867]. In particular, he states that the form of bone is determined by its loading circumstances, which is now called Wolff's law. Thus, it has been recognized since a long time that bone is a dynamic tissue that optimizes its structure in size, shape, mechanical and physical properties in response to environmental signals such as stress.

In the 1980s, Harold Frost described in his mechanostat theory, that bone mass and architecture are controlled locally by bone cells that respond to the difference between real mechanical stress and a target stress [Frost, 1987]. He defined a "lazy" or "dead zone" of strain, where no change will happen, as well as the minimum effective strain above and below this equilibrium range that must be exceeded in order to trigger a response. In other words, bone is formed when the actual load exceeds a certain threshold and reabsorbed when the actual load falls below another threshold.

There is broad consensus that osteocytes are involved in mechanosensitivity and mechanotransduction [Tatsumi et al., 2007, Bonewald et al., 2013], as mechanical strain is sensed by cellular processes of osteocytes followed by changes in gene expression such as energy metabolism, gene activation and the production of growth factors and other proteins [Skerry et al., 1989, Dodds et al., 1993]. However, it is still not clear how the osteocyte perceives mechanical stress, but several mechanisms have been suggested. The most common theories are osteocyte apoptosis, direct stress and fluid flow.

Osteocyte aptosis: One hypothesis is, that local stress can produce micro-cracks in the extracellular matrix (ECM) disrupting the canalicular network and cell dendrites. This may lead to osteocyte apoptosis [Verborgt et al., 2000, Dooley et al., 2012], which in turn initiates a remodeling process by recruiting osteoclasts [Jilka et al., 2012].

Direct stress: Another possibility is, that the osteocytes sense the local substrate strain directly. This theory has been under debate, because the loads measured in-vivo on the bone surface (in the range of 0.04 to 0.03 % and rarely more than 0.01 % of the physiological load [Yang et al., 2011] are far lower than the strain threshold at which osteocytes reacted in in-vitro experiments (0.4 Pa to 2 Pa [Klein-Nulend et al., 1995]), but Varga et al. have demonstrated with synchrotron X-ray phase nano-tomography and finite element modeling (FEM), that the global strain may be amplified up to 70 times in the LCN, which would fit to the results of the in-vitro experiments [Varga et al., 2014].

Fluid flow: The mechanical stress induces an extracellular fluid flow [Knothe Tate, 2003, Verbruggen et al., 2014], which leads to shear stresses on the osteocyte's plasma membrane [Weinbaum et al., 1994, You et al., 2001] or dendrite deformations [Wang et al., 2007], which leads to an activation of intracellular signal transmission. The hypothesis that fluid flow is the main mechanosensing mechanism is supported by in-vitro experiments which showed the greater mechanosensitivity of osteocytes to fluid flow compared to osteoblasts and fibroblasts [Owan et al., 1997]. In addition, osteocytes seem to react stronger to shear stresses induced by fluid flow than to other forms of mechanical stress (e.g. stretching of the substrate). A. van Tol has shown, that the fluid flow calculated with the LCN and Kirchoff´s law is a better predictor for bone formation and resorption and than strain calculations of with FEM [Van Tol et al., 2020]. However, this does not seem to explain

the whole process. Presumably, the osteocytes can react to mechanical stimuli by a variety of sensors and signal mechanisms.

2.2.3. Mechanical loading and its effect on bone

For a better understanding of the effects of loading, several animal models have been developed [Main et al., 2020], which can be devided into four main groups:

- non-invasive models using voluntary or non-voluntary exercises,
- intrinsic invasive (osteotomy),
- extrinsic invasive (implantation of pins to apply force) and
- extrinsic non-invasive (external mechanical actuator) models

This work concentrates on a extrinsic invasive model, which allows to control the applied load to the bones. Namely the tibial axial compression model. Here, the load is applied only on one tibia. Hence, the contralateral non-loaded limb serves as an internal control, which reduces number of animals for the study [Sugiyama et al., 2010].

In this model, the knee and foot of the mouse are fixed with plastic or metal fasteners (see Figure 2.7). By collapsing the machine, compressive loads are applied along the length of the tibia. The advantage of this setup is that it utilizes the natural curvature of the tibia proximal to the tibia-fibular junction to induce tensile loads on the anterior-medial surface and compressive loads on the posterior-lateral surface of the diaphysis. While the bone stresses needed to induce bone formation (1200 $\mu\epsilon$ in C57BL/6 mice [Lynch et al., 2010, Sugiyama et al., 2008]) are about two to three times the load that occurs on the tibia mid-shaft during normal gait for the mouse [De Souza et al., 2005, Sugiyama et al., 2012], the stress distribution (shown in Figure 2.8) is fairly physiological and consistent with locomotor stress distributions measured in vivo [De Souza et al., 2005] or modeled via finite element (FE) simulations [Prasad et al., 2010].

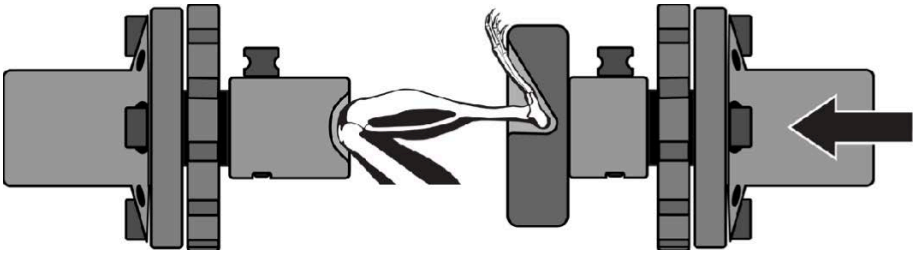

Figure 2.7.: Sketch of the tibial axial compression model. The hindlimb of the mouse is positioned in the loading device, which is used to load the mice tibia. The arrow indicates the direction of loading. The figure is reprinted from [Willie et al., 2020] with permission of Elsevier.

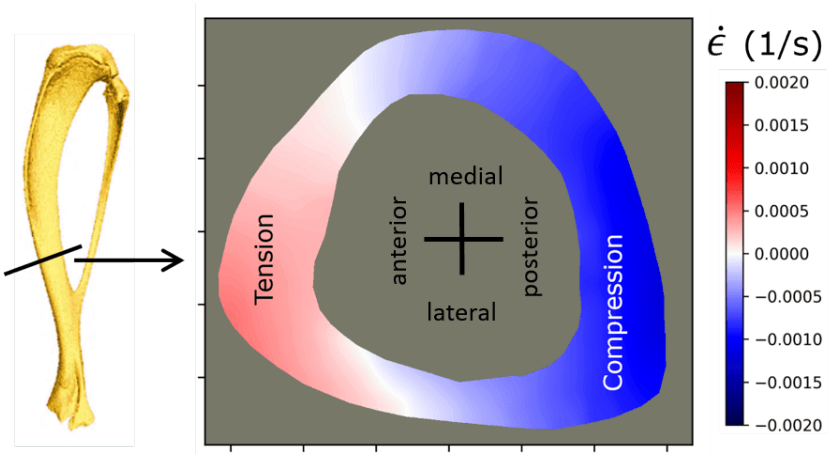

Figure 2.8.: FE model showing tensile strains on anterior-medial and compressive on posterior-lateral side.

It has been shown, that mechanical loading results in increased endocortical and periosteal bone formation and decreased endocortical resorption, with endocortical mechanoresponsiveness being better preserved with age than the periosteal formation response [Birkhold et al., 2016]. The functional adaptation of the bone composition is also site-specific and thus presumably mechanically driven [Buckley et al., 2014]. Studies in space have shown changes in the composition of the organic matrix and/or the bone mineralization in the absence of gravity and thus no load, which leads to a deterioration in the material properties of the bone in rodents [Lafage-Proust et al., 1998]. Exercise studies in humans show that exercise can lead to increased volumetric bone mineral density as well as increased bone mineral content [Hartley et al., 2020, Kesavan et al., 2005]. It is assumed that mechanical stress leads to increased collagen synthesis [Tidswell et al., 2008] and to altered tension properties of the collagen network [Isaksson et al., 2009a, Isaksson et al., 2009b].

Do Aido et al. found no difference in bone composition between newly formed tissue due to mechanical loading and existing tissue. According to them, however, the age of the animal has an influence on the changes in bone composition due to stress [do Aido et al., 2015]. Kohn et. al. have shown that the exercise program they used (daily treadmill) do not result in any morphological adaptation in postpubertal C57BL/6 mice, but in changes in structural and mechanical properties at the tissue level, namely improved mineralization (increased mineral-to-matrix ratio) and an altered mineral composition (decreased carbonate-to-mineral ratio) in pre-existing bone tissue [Kohn et al., 2008]. A possible mechanism to explain these changes could be the perilacunar remodeling by the osteocytes [Qing and Bonewald, 2009]. Bergstrom et. al. reported that mechanically loaded bone showed reduced mineralization and crystallinity, and collagen content in the proximal part of the loaded bone became more heterogeneous [Bergström et al., 2017].

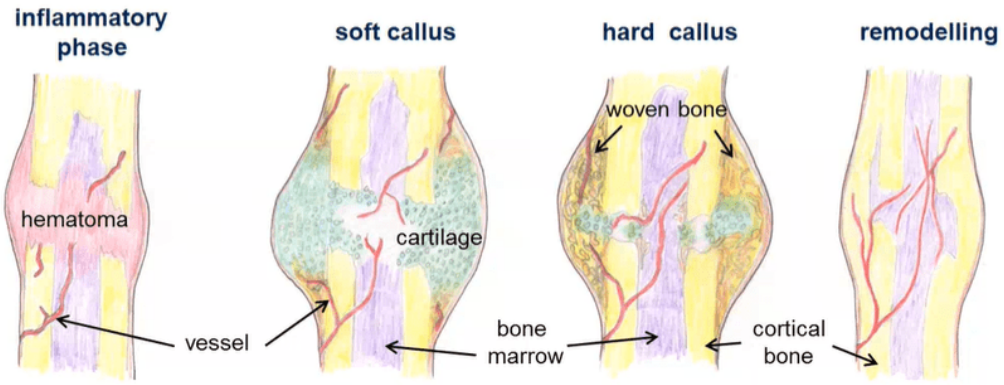

Figure 2.9.: Consecutive phases of bone healing Secondary bone healing starts with inflammatory phase forming a hematoma between the fracture ends. During the reperative phase soft (cartilage) and hard (woven bone) callus are formed. Followed by a replacement of the woven bone by lamellar bone and slow remodeling to the pre-injury shape and mechanical function of the bone. Figure from [Schmidt-Bleek et al., 2014].

2.2.4. Bone healing after fracture

Bone is not only able to adapt to the mechanical needs, but regenerates from a fracture almost scar free to its initial state [Einhorn, 1998]. This regeneration process is very similar to the bone development process and includes bone formation, modeling and remodeling.

Depending on the geometry of the fracture, one distinguishs between primary (direct) healing and secondary (indirect) healing. If the fracture ends have direct contact without a fracture gap but rigid fixation, the bone heals directly via bone remodeling - without callus formation [Marsell and Einhorn, 2012, Einhorn, 1998]. This happens only rarely in comparison to the more usual secondary healing [Sfeir et al., 2005], in which the two ends of the fracture are stabilized under less rigidly fixed conditions. This process is a combination of intramembranous and enchondral ossification.

The phases of secondary healing are illustrated in Figure 2.9. After the fracture, dead material is removed from the affected zone and a hematoma is formed (inflammatory phase). Then the reparative phase takes place, where a callus gets formed for mechanical stabilization of the fracture ends. This callus initially consists of fibrous connective tissue and is replaced by cartilage [Dimitriou et al., 2005], which is then resorbed by osteoclasts. Followed by osteoblasts forming woven bone, to replace the mineralized soft callus by a hard callus [Al-Aql et al., 2008, Marsell and Einhorn, 2012]. At the same time intramembranous ossification starts at the fracture ends forming a hard callus either. This mineralized tissue has a rather disordered structure and its mechanical properties do not reach those of the pre-fractured cortical bone. Nevertheless, this structure serves as a scaffold on which ordered lamellar bone can be formed [Currey, 2006, Shapiro, 2008]. In the final remodeling phase, the braided bone is successively replaced by lamellar bone, which leads to the restoration of the shape and function of the pre-fractured bone structure [Schmidt-Bleek et al., 2014]. The spatio-temporal sequence of tissue formation, replacement and remodeling during secondary healing is similar in most mammals and leads to complex tissue patterns in which different tissues are in contact with each another.

2.3. Skeletal features of Marfan syndrome

Marfan syndrome (MFS) is a multisystem disorder caused by mutations in the fibrillin-1 (Fbn1) gene affecting all connective tissues. Therefore, clinical symptoms are observable in the skeletal, cardiovascular and ocular systems. MFS is a rare disease with a prevalence of approximately 1:5.000 to 1:10.000, while the most accurate number with a full evaluation is coming from Denmark with 6.5:100.000 cases [Groth et al., 2015]. The most serious complications involve the heart and aorta, with an increased risk of mitral valve prolapse and aortic aneurysm [Cook and Ramirez, 2014].

Typical symptoms in the skeleton are for example long bone overgrowth, arachnodactyly (spider fingers), joint hyperextensibility, which leads the typical image of very tall people with long arms and fingers. Additionally, Marfan patients show low bone mass and low bone mineral density (osteopenia) [Carter et al., 2000, Kohlmeier et al., 1995, Moura et al., 2006]. Studies also find a higher risk of peripheral traumatic fracture in children [Kohlmeier et al., 1995] and a higher fracture risk in general [Folkestad et al., 2021].

There are, among others, two established mouse models of MFS: $Fbn^{mgR/mgR}$ and $Fbn1^{C1039G/+}$, which display phenotypic features in the skeleton and the aorta similar to those of patients with classic MFS [Walji et al., 2016]. The $Fbn1^{C1039G/+}$ mice mimic the human heterozygous MFS mutation in Fbn1. The observed characteristics of MFS are skeletal deformaties and deterioration of the aortic wall [Judge et al., 2004]. The $Fbn^{mgR/mgR}$ mice are more severely affected with a life expectancy of only three to four month, due to aortic aneurysms. They develop severe kyphosis, overgrowth of the ribs and of other long bones [Pereira et al., 1999] as well as osteopenia associated with normal osteoblast differentiation [Nistala et al., 2010a].

Studies of these mice find that fibrillins distinct alterations of the growth factors transforming growth factor beta (TGFβ) and bone morphogenetic proteins (BMP) bioavailability without affecting the number of osteoblasts and osteoclasts but influencing their differentiation and activity [Nistala et al., 2010c, Nistala et al., 2010a, Tiedemann et al., 2013]. This implies that Fbn1 may contribute to the regulation of skeletal homeostasis.

Because of the manifolds of symptoms, the treatment of Marfan syndrome has to be interdisciplinary. Thereby, the first aim is avoiding cardiovascular complications. Current therapies are β-blocker medications to reduce blood pressure and cardio thoracic surgery to avoid aortic dilatation. With these therapies patients with Marfan syndrome have almost normal life expectancy [Shores et al., 1994, Groth et al., 2015]. Consistent with the involvement of the TGFb pathway in MFS symptoms, treatment with losartan, an angiotensin II receptor 1 (AT1R) blocker (ARB) that reduces TGFb signaling [Lavoie et al., 2005], produces alterations of the aortic wall structure and relieves root dilation of the aorta in children with severe MFS [Brooke et al., 2008], too. However, some MFS patients do not respond to losartan and this treatment does not show improvement of other pathological symptoms of MFS for example in the skeleton [Nistala et al., 2010a].

3. Physical characterization techniques for bone tissue

3.1. Confocal laser scanning microscopy

One of the easiest ways to investigate small objects and structures is light microscopy. One or more lenses produce an enlarged image of a sample placed in the focal plane. At the same time, the light scattered from objects above or below this plane reduces the contrast. Therefore, the image quality depends on the thickness of the sample. To reduce the dependency on sample thickness and improve image quality, confocal microscopes use an additional lens, collecting the scattered light from the sample. This objective lens is followed by a small pinhole aperture where only light from one focal point in the sample passes through [Minsky, 1987] (see Figure 3.1). Therefore, imaging samples in three dimensions in the millimeter range is done by sequential scanning in x, y and z direction.

Fluorescence imaging

In contrast to conventional microscopes, confocal laser scanning microscopy (CLSM) uses lasers of different wavelengths as light sources which leads to the possibility of fluorescence imaging. Therefore, auto fluorescent materials as well as those that are specially colored with fluorescent molecules (fluorochromes) can be measured in reflection mode. These materials absorb light of a defined wavelength, which leads to an electronic transition into an excited state ($S0 \rightarrow S1(3)$, see Figure 3.2a). After a short delay time of a few picoseconds with transitions down to the lowest vibrational energy level of the excited electronic state ($S1(3) \rightarrow S1(0)$), the molecule relaxes into the ground state ($S1(0) \rightarrow S0$) accompanied by the emission of a fluorescence photon as shown in the Jablonksi diagram in Figure 3.2a. Due to non-emissive transitions between the electronic states the emitted photons have a lower energy in comparison to the incoming photons. Therefore, the energy of the fluorescent radiation is below the excitation energy and accordingly, the wavelength increases, which is shown in Figure 3.2b.

This so-called Stokes shift is used to improve the contrast of confocal images by filtering the incoming light from the emitted light. Additionally, fluorochromes can be used to highlight special features by seperating their signal from the (unspecific) autofluorescence signal. In bone research, common dyes are Tetracycline (for humans) and Calcein or Alizarin (for animals). Furthermore, researchers at the MPIKG have developed a staining method with Rhodamine6G to visualize the LCN [Roschger, 2015, Kerschnitzki, 2012]. Rhodamine6G solution stains non-mineralized tissue as well as osteoid. Due to its small molecular size, Rhodamine6G stains all inner surfaces of the porosities in the mineralized tissue including osteocyte lacunae and canaliculi [Kerschnitzki et al., 2013, Kerschnitzki et al., 2011a] (see also chapter 4.3).

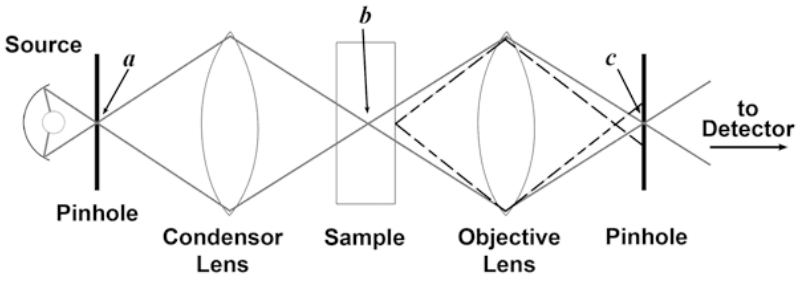

Figure 3.1.: Illustration of the beam path in a confocal laser scanning microscope. The optical path of the confocal beam is shown by a solid line. The light focuses on the entrance pinhole (a). This pinhole provides then a bright and focused light source. The light from this point source is collected by a condenser lens and focuses on point (b) in the sample. The light emitted from the focusing spot in the sample is collected by the objective lens and the second (exit) pinhole (c) filters again only light from the focal point. The beam path of the light scattered from out-of-focus layer is shown as dashed line . Picture from [Price and Jerome, 2018] with permission of Springer Nature.

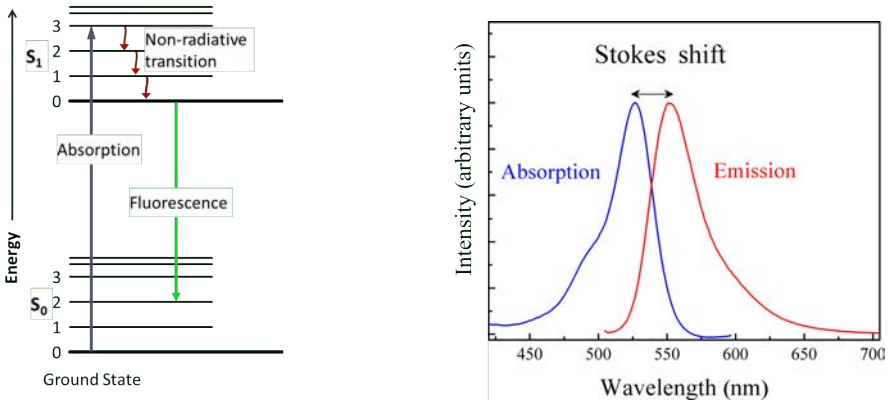

(a) **(b)**

Figure 3.2.: Sketch of the fluorescence process. 3.2a Jablonski diagram: After an electron has absorbed a high-energy photon, the system is excited into an higher electronically state. The system relaxes first in vibration states and finally emits a photon at a longer wavelength compared to the incoming one. 3.2b Normalized absorption and emission spectra of Rhodamine6G. Here, the emitted photon has less energy than the absorbed photon, which is called Stokes shift and makes it easier to filter the emitted light.

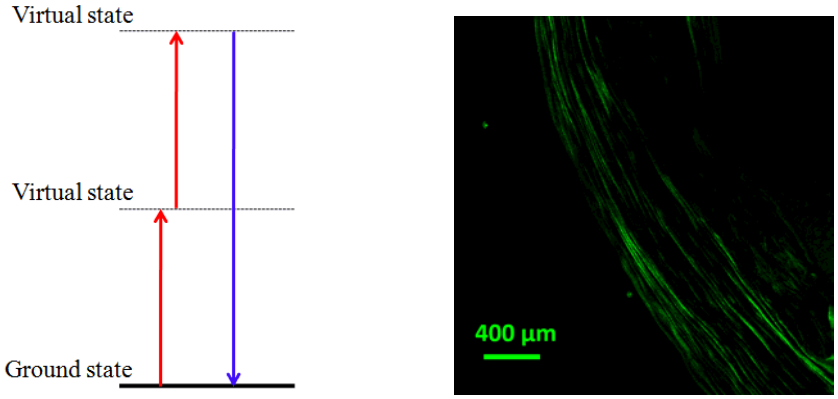

(a) (b)

Figure 3.3.: Illustration of second harmonic imaging. (a) Sketch of the second harmonic generation process at energy levels. (b) Example image of second harmonic generation microscopy measurement of collagen in a murine bone. The contrast of the SHG image is changing from dark to bright when collagen fibrils are orthogonal to the incident light. The scale bar is equal to 200 µm.

3.2. Multiphoton second harmonic generation imaging

When two photons of the same frequency interact with a material, they can generate a new photon with twice the frequency or half the wavelength of each initial photon (see Figure 3.3a). This non-linear process is a special case of harmonic generation and is called second harmonic generation (SHG) [Franken et al., 1961]. Whether a material is able to cause SHG depends on its second-order nonlinear, electronical susceptibility and its symmetry. As an even-order nonlinear optical phenomen, SHG does not occur in media with inversion or centro-symmetry [Gauderon et al., 2001].

Using a short-pulse laser, appropriate filters can easily seperate the excitation from the emitted, frequency-doubled SHG signal. This allows a very high resolution comparable to confocal microscopy without the need of pinholes. Therefore, biological science uses this effect for example to visualize collagen fibers, which are due to their helical structure not centrosymmetrical [Cox et al., 2003]. Here, the intensity of the signal depends on the collagen concentration, degree of order, orientation of the collagen [Freund et al., 1986] if the collagen fibril is parallel to the incident light no second harmonic is generated), the diameter of the fibrils [LaComb et al., 2008] and the amount of cross linking of the collagen [Lutz et al., 2012]. An example can be seen in Figure 3.3b.

3.3. Electron microscopy

3.3.1. Electron interactions

To reach higher resolution for visualization and characterization of materials than by light microscopy, one can use a focused electron beam for scanning electron microscopy (SEM). When the primary electron hits the sample there are different interactions possible (see Figure 3.4) depending on the energy of the electron, the surface structure and material of the sample: emission of secondary electrons by inelastic scattering (Figure 3.4a), elastic scattering (Figure 3.4b) or the emission of electromagnetic radiation (Figure 3.4c and d) [Goldstein et al., 1981].

When the electrons of the incoming beam strike the sample surface, part of their kinetic energy transfers to the electrons of the sample, which can now conquer the surface barrier and emit [Seiler, 1983]. These secondary electrons (SE) have very low energies of $\approx 50\,\mathrm{eV}$.

This leads to a limit of their mean free path in solid matter to a few nanometers of the surface of the sample. This highly localized reaction, leads to information of the sample surface with a pixel size below 1 nm [Goldstein et al., 1981].

Backscattered electrons are beam electrons that are scattered back during elastic collisions with the atom nuclei of the sample. The backscattered electrons have a much higher energy than SE corresponding to a larger mean free path. Therefore backscattered electrons (BSE) emerge from comparably deeper locations within the specimen and the resolution of BSE images is lower than the one of SE images. The number of BSE is related to the atomic number Z of the elements in the measured samples. Therefore, images of the BSE signal provide information about the distribution of different elements in the sample [Skedros et al., 1993].

If the electron beam removes an inner shell electron from the sample material, an electron with a higher energy level fills this hole and emits an electronic-magnetic wave with a specific energy difference. The energy or wavelength of these waves can be measured by energy- or wavelength dispersive X-ray spectroscopy to map the distribution of different elements in the sample [Goldstein et al., 1981].

3.3.2. Quantitative backscattered electron imaging

Due to the high amount in bone, Calcium dominates the BSE signal of bone with its relatively high atomic number (Z = 20). Therefore, backscattered electron imaging is used to measure the local calcium concentration, respectively the degree of mineralization [Boyde and Jones, 1983]. P. Roschger et al. introduced the method of quantitative backscattered electron imaging (qBEI) [Roschger et al., 1998] to calculate the calcium concentration ($wt\%Ca$) based on the measurement of the average Z displayed as certain grey value (GV) with the formula given in Eq. (3.1).

$$wt\%Ca = 0.1733 \cdot GV - 4.332 \tag{3.1}$$

Based on this, qBEI images can be used to obtain the bone mineralization density distribution (BMDD) correlating each calcium concentration with its frequency of appearance in the analyzed image [Roschger et al., 1998]. As result of the constant incorporation of mineral in the bone modeling process (see chapter 2.1.2), qBEI shows the history of the bone, because older (lamellar) tissue appears brighter than newly formed bone [Ruffoni et al., 2007]. Thus, the image can be used for characterize of the BMDD and for comparison between regions, samples and individuals. The BMDD histogram is characterized by the following five parameters [Roschger et al., 1998] :

- Ca_{Peak}: most frequently measured calcium concentration
- Ca_{Mean}: weighted mean of calcium concentration
- Ca_{Width}: full width at half height of the distribution
- Ca_{Low}: percentage of bone area which is less mineralized than the 5% percentile
- Ca_{High}: percentage of bone area which is higher mineralized than the 95% percentile

Since Ca_{Width} becomes smaller the more homogenous the mineralization pattern is, it could be seen as a measurement of the heterogeneity of mineralization, while Ca_{Peak} and Ca_{Mean} carry information on the degree of mineralization.

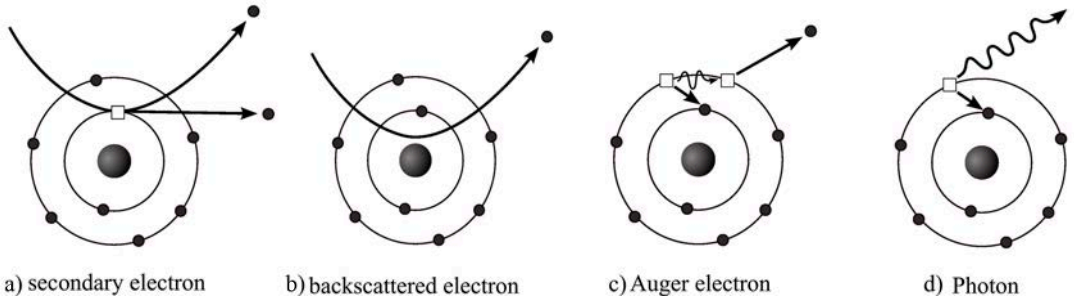

Figure 3.4.: Sketch of electron interactions with material. After a primary electron hits the surface of a material, different mechanisms can occur. b) Some of the primary beam electrons are able to escape the sample surface, after elastic scattering, still carrying energy just below that of the incoming beam. a) The primary electron can cause the ejection of an inner-shell electron. Subsequent decay of this excited state results in the emission of c) Auger electrons or d) characteristic x-rays.

3.4. X-ray characterization techniques

3.4.1. Synchrotron radiation

Accelerated particles emit electro-magnetic waves - the so-called "Bremsstrahlung". This is also true for high-energy particles forced into a circular path, i.e. tangential acceleration. Here, most of the radiation follows the tangential direction. Due to its discovery at a synchrotron accelerator [Elder et al., 1947], this special type of radiation is called synchrotron radiation (SR). First seen as unwanted but unavoidable loss of energy, synchrotron radiation is used as a brilliant light source for research since 1956 [Tomboulian and Hartman, 1956]. At first, people have used those rings originally built for high-energy physics research. Second-generation rings were then built directly as light sources [Balerna and Mobilio, 2015]. But since 1992, there are third-generation rings with straight sections for insertion devices (undulators and wigglers) for higher brilliances and lower electron-beam emittance [Winick, 1998].

The broad spectrum, covering wavelengths from microwaves to hard X-rays, allows scientists to realize various experiments. The high-intensity photon beam leads to rapid experiments while the high brilliance and high stability of the beam allows sub-micron measurements [Winick, 1998, Margaritondo, 2015].

3.4.2. Interaction of X-rays with materials

X-rays are electro-magnetic waves with wavelengths ranging from 10 pm to 10 nm corresponding to energies in the range 124 eV to 124 keV. If X-rays hit matter, they will be absorbed and transformed into other types of energy (heat, fluorescence radiation, ...) or interact with the atoms by elastic or inelastic scattering. Here, the interaction depends on the energy of the X-rays and the elemental composition of the material, but less on its chemical properties, since the X-rays photon energy is much higher than chemical binding energies [Snyder, 1999].

Absorption

The probability of absorption of photons per unit mass is approximately proportional to Z^3/E^3, where Z is the atomic number and E is the energy of the incident photon [Bushberg et al., 2012]. However, there are abrupt changes in interaction probability close to inner shell electron binding energies, i.e. the absorption edges. The high amount of

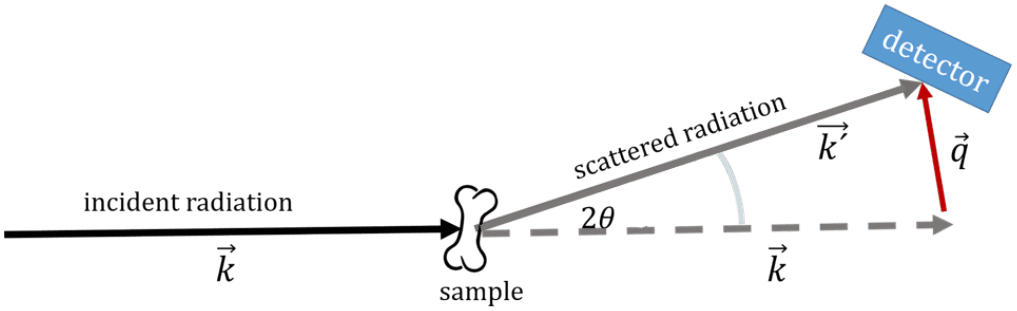

Figure 3.5.: Schematic view of X-ray scattering. The incident beam vector $\vec{k}$ is transmitted through the sample and the scattered vector $\vec{k'}$ hits the detector. The scattering vector is described as $\vec{q}$.

calcium (Z = 20) in bones, together with their high density, leads to high absorption of X-rays and that is why bone can clearly be seen on (medical) radiographs.

When a photon is absorbed, it transfers all of its energy to an electron that is emitted from the atom. In doing so, a photoelectron is generated, which in turn could ionize other atoms along its emission path. An outer electron fills the vacant position and produces either characteristic X-ray or an Auger electron. These effects can be used for element detection by X-ray spectroscopy or Auger electron spectroscopy.

Inelastic scattering

When a photon hits a free or loosely bound electron, this electron can take over part of the photon energy while a photon of the remaining energy is emitted in a different direction from the original, conserving the overall momentum of the system. This reaction was discovered by Compton [Compton, 1923] and is called Compton scattering. Here the scattering has a random manner and the scattered radiation has no phase relationship with the incident radiation. Therefore, one can not observe any interference pattern to get structure information. If anything, the resulting radiation is part of the background.

Elastic scattering

When photons collide with strongly bound electrons, like it is shown in Figure 3.5, the electric field of the incident wave (photon) accelerates the electron, causing it to emit radiation at the same frequency as the incident wave. Thus, every electron emits spherical waves (with the electron in the respective center) producing interference patterns depending on the observation angle 2θ and characteristic to the internal structure of the material, i.e. the orientation and distances of the atoms relative to each other. The resulting scattering pattern is described by the scattering vector $\vec{q}$, which is defined as difference between wave vector of the incident beam ($\vec{k}$) and the wave vector of the scattered beam ($\vec{k'}$) (see Eq. (3.4)).

$$\vec{q} = \vec{k} - \vec{k'} \tag{3.2}$$

$$\left|\vec{k}\right| = \left|\vec{k'}\right| = \frac{2\pi}{\lambda} \tag{3.3}$$

$$|\vec{q}| = 2\left|\vec{k}\right| \cdot \sin\theta = \frac{4\pi}{\lambda} \cdot \sin\theta \tag{3.4}$$

3.4.3. Small and wide angle X-ray scattering

Depending on the scattering angle θ and therefore the origins of the scattering signal, one differentiates between small angle X-ray scattering (SAXS) and wide angle X-ray scattering (WAXS). Thereby, every scattering process is characterized by the reciprocity law, which results in an inverse relationship between particle size and scattering angle [Glatter and Kratky, 1982]. Small distances between scattering centers influence the scattering behavior in the area of large angles (WAXS), while large distances influence the scattering behavior in the area of small angles (SAXS).

If the scattering angle θ is less than $5\,^\circ$, one speaks about SAXS. The SAXS signal arises from the contrast due to two discrete phases of different electron densities with sharp interfaces [Kratky et al., 1951, Porod, 1951]. In bone, these two phases are represented by the mineral particles with high electron density and collagen and all other organic components with low electron density. The scattering intensity distribution $I(q, \psi)$ of the SAXS signal Eq. (3.5) (with azimuthal angle ψ, sample volume V and the instrumental constant K) leads to information on size, orientation and shape of submicron mineral particles.

$$I(\vec{q}) = \frac{K}{V} \left| \int_V \rho(\vec{r}) \cdot e^{i\vec{q}\vec{r}} d^3r \right|^2 \tag{3.5}$$

Periodic structures in the nanometer range within the sample material, such as atoms of a (crystalline) material, which form imaginary planes, the distances between these planes being called d-spacing. These reflections are also called Bragg peaks and appear in two-dimensional photon detectors as circular diffraction patterns (Debye-Scherrer rings) for ideal powders. If the crystalline structures are not perfectly ordered, the intensity of the Bragg peaks decreases while the width of the peaks increases [Olszta et al., 2007]. The peak position is defined by the crystal lattice of the structure. These reflections can only occur at scattering angles at which Bragg's law (Eq. (3.6)) applies .

$$n\lambda = 2d \cdot \sin\theta, \tag{3.6}$$

with an arbitrary integer n, λ the wavelength of the incoming beam, d the distance between the lattice planes in the crystal structure and θ is half the scattering angle, called the Bragg angle.

Particle thickness (T parameter)

According to Porod [Porod, 1951], the scattering intensity in a two-phase system with sharp interfaces decreases with q^{-4} for large q values Eq. (3.8). This can be used to determine the T parameter, which is the mineral particle thickness of HAP platelets in bone, by the decay of the scattering signal [Fratzl et al., 1991, Fratzl, 1994, Rinnerthaler et al., 1999]. Accordingly the T parameter is calculated as Eq. (3.11), where Φ describes the volume fraction and σ describes the total surface area of all particles per unit volume. Comparing this with Eq. (3.13), the T parameter is only a direct measure of the mineral particle thickness, if $\Phi = 0.5$.

$$T = \frac{4}{\pi P} \int_0^\infty q^2 I(q) dq \text{with } I = I_{exp}(q) - B \tag{3.7}$$

$$\lim_{q \to \infty} I(q) = \frac{P}{q^4} + B \text{with Porod constant } P \text{and a background constant } B \tag{3.8}$$

$$\text{with } P \approx 2\pi\sigma \tag{3.9}$$

$$\text{and} \int_0^\infty q^2 I(q) dq \approx 2\pi^2 \cdot \sigma(1-\sigma) \tag{3.10}$$

$$\rightarrow = \frac{4\Phi(1-\Phi)}{\sigma} \tag{3.11}$$

From SAXS, the T parameter can be determined with Eq. (3.12), assuming N mineral particles in a volume V with side length a, b and c with a volume fraction $\Phi = N \cdot abc/V$. As described in chapter 2.2, HAP particles could be assumed to be thin mineral platelets [Fratzl et al., 2004] with the mineral platelet thickness a as shortest dimension, i.e. $a \ll b \leq c$. Therefore the T parameter could be simplified to Eq. (3.13) showing the correlation of the T parameter to the mineral particle thickness.

$$T = 2(1-\Phi)\frac{abc}{ab+bc+ac} \tag{3.12}$$

$$\approx 2(1-\Phi)a \tag{3.13}$$

$$\text{with } \Phi = 0.5 \text{ in bone}$$

$$\rightarrow T \approx a \tag{3.14}$$

Degree of orientation (ρ parameter)

The average orientation of the mineral crystals is related to the shape of the SAXS pattern [Fratzl et al., 1996b]. If all crystals are oriented in one direction, the scattering image shows a thin stripe. If there are crystals oriented also in other directions, their SAXS patterns are rotated correspondingly. This implies that for randomly oriented crystals the SAXS pattern is circular. Therefore, plotting the azimuthal profile of the intensity distribution $I(\psi)$ in radial direction for oriented particles shows two peaks (see Figure 3.6), while less oriented particles flatten the curve. Integrating leads to the so-called ρ parameter, the degree of mineral particle orientation [Rinnerthaler et al., 1999]. A uniform orientation of all particles within the observed sample volume is described by a value of $\rho = 1$. $\rho = 0$ describes a sample volume without predominant, rather random, mineral orientation. Finally, the ρ parameter can be simplified to Eq. (3.15), where the denominator $(B + A_1 + A_2)$ describes the total area under the curve $I(\psi)$ and $A_1 + A_2$ the area under the curve $I(\psi)$ excluding the constant background.

$$\begin{aligned} \rho &= \frac{\text{Mineral}_{aligned}}{\text{Mineral}_{aligned} + \text{Mineral}_{unaligned}} \\ &= \frac{A_1 + A_2}{B + A_1 + A_2} \end{aligned} \tag{3.15}$$

In addition, the ratio of the intensity of the two Gaussian curves and the total scattering intensity can be used to determine the projected degree of orientation (PDO) of structures within the examined sample volume. [Hauge Bünger et al., 2006]

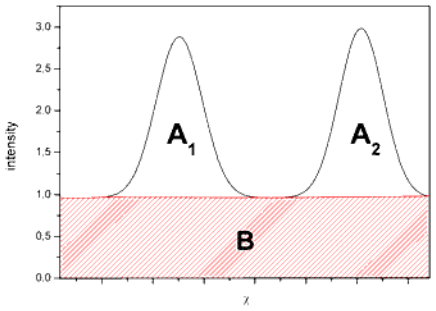

Figure 3.6.: Azimuthal plot $I(\psi)$ of the scattering intensity. The two peaks are 180° separated and fitted with Gaussian functions. A_1 and A_2 correspond to the fraction of aligned mineral particles and B represents the fraction of unaligned mineral particles.

Particle length (L parameter) and d-spacing

WAXS includes diffraction intensities at a scattering angle of 2θ greater than 5°. Thus, it contains information in the sub-nanometer length scale. When X-rays are transmitted through the sample, they are diffracted in predictable patterns based on the internal structure of the sample (Bragg's law). Bone generally gives distinctive X-ray diffraction patterns that contain numerous well-defined wide-angle rings. Analyzing the WAXS signal of bone samples obtains information about the crystallographic planes from the HAP [Finean and Engström, 1953]. Due to the perpendicular angle between sample and incident beam, the assumed structure of the bone material and the hexagonal structure of HAP(see 2.2), the strongest peak in the WAXS signal is the 002-reflection. Information about the d-spacing in c-direction is encoded in the position of the reflection ring [Handschin and Stern, 1995], while the width of the peak depends on the mineral crystal size, i.e. the length (in c-direction).

This crystal length L can be calculated with Scherrer's equation Eq. (3.16), where λ is defined as the incident wavelength, θ as the Bragg angle of the peak, B is the full width at half maximum (FWHM) of the 002-peak and k the so called Scherrer constant [Pabisch et al., 2013]. Here, k is a measure for the crystal shape and has typically values between 0.87 and 1.0 [Scherrer, 1912]. The width of the peak (B) is not only caused by the finite size of the crystals, but also by the perfection of the mineral crystal,the so-called crystallinity [Bonar et al., 1983]. In this respect, the measured particle size could be larger, but with many defects. For the experimental evaluation also the instrumental broadening (B_I) has to taken into account. [Danilchenko et al., 2002]. Therefore, it is needed to measure a reference material where the line broadening is only caused by the instrumental set up and not by the crystal size. However, using a Voigt function the broadining can be neglected for the diffraction line profile of biological apatite [Danilchenko et al., 2002] and is therefore used for the evaluation.

$$L = \frac{k \cdot \lambda}{B \cdot \cos\theta} \tag{3.16}$$

3.4.4. Micro-computed tomography

X-ray computed tomography (CT) is a commonly used technique for non-destructively imaging of objects. The mechanism is based on the transmission of X-ray beams through a sample interacting with its atoms as mentioned above. In bone, the photoelectric effect is the main interaction mechanism and this depends on the atomic number of the object´s materials, i.e. the larger the nuclear number of elements in the region considered, the less radiation passes through. The X-rays passing through the object are captured by a detector resulting in a 2D X-ray projection of the object - projection radiography. Rotating either the X-ray source and detector or the object produces a set of 2D projections. Therefore, all points within the object are imaged from different directions. These information are then used to reconstruct a three-dimensional image.

Since bone and its surrounding soft tissue have a big difference in their atomar composition, X-ray imaging delivers a high absorption contrast between both [Bouxsein et al., 2010]. Additionally, CT can be used for a large range of resolutions, which allows hierarchical imaging from whole bodies down to the tissue level [Stauber and Müller, 2008]. Using SR for micro-computed tomography (μCT), including its monochromatic beam for stronger contrast differences [Nuzzo et al., 2002] and its high brilliance for better resolutions, it is possible to reach resolutions below 1 µm [Schneider et al., 2007]. Thus, even three-dimensional ultrastructural features like osteocyte lacunae can be investigated (see chapter 6).

In contrast to most of the other methods presented here, μCT can be used also with living animals. For example, in-vivo μCT is used to track the development of bone geometry (bone formation and resorption) over weeks by combining it with image registration techniques [Bouxsein et al., 2010, Willie et al., 2013, Webster et al., 2012, Birkhold et al., 2014].

4. Material and Methods

4.1. Animal handling

4.1.1. Femoral osteotomy protocol

For performing an osteotomy, i.e. an operation to fracture the bone, the mice are anesthetized with a 2% isoflurane oxygen mixture. The left femur is shaved on the lateral side and opened with a scalpel. The operateur drills four holes into the femur and mounts an external unilateral fixator in the cranio-lateral direction onto the femur with four Mini-Schanz screws (pins) (0.45 mm, RISystem, Davos, Switzerland). Using a 0.44 mm Gigli wire saw (RISystem AG, Davos, Switzerland), a 0.5 mm osteotomy between the inner screws is created. Postoperative analgesia is provided for three days after operation by administering 25mg Tramadol hydrocholoride (Tramal®, Grünenthal GmbH, Aachen, Germany) per ml in the drinking water. Three weeks after the osteotomy the mice are sacrificed and the femora dissected, the fixator is taken out and the bones are put quickly in 70% ethanol. The animal experiments are completed according to the policies and procedures approved by the local legal research animal welfare representative (Shriners FACC 2016-7821).

4.1.2. In-vivo mechanical loading

Non-invasive loading of bones in living animals allows to study the mechanoresponse of bones. In our project the loading process is done analog to the long experienced protocol of Willie [Willie et al., 2013, Birkhold et al., 2014]:

An in-vivo loading device (Testbench ElectroForce LM1, TA Instruments, New Castle, USA) applies cyclic compressive loading to the left tibiae of about four months old C57BL/6J mice. Meanwhile, the right tibia serves as an internal control. The mouse's left knee is situated into a curved cup while the foot lays on a plate, joined to the loading device, through which a preload of -1 N is applied (see Figure 4.1a). Previous to our study, the controlled dynamic loading experiment has been calibrated experimentally in similar mice (26 weeks old female C57Bl/6), using strain gauges in-vivo on the anterior-medial surface of the tibial midshaft. Based on this calibration, a cyclic load with a peak force of 11 N is applied to the left tibia reaching a peak strain of $+1200\mu\epsilon$ [Willie et al., 2013] with a constant strain rate. The loading cycle is shown in Figure 4.1c. It includes a 0.1 s rest phase with the preload of $-1N$ between two loads and a 5 s rest every four cycles. 216 cycles are applied day by day at 4 Hz to the left tibiae 5 days/week for two weeks. Between the loading sessions, the mice have no restriction on their cage activity, to have normal background loading. During the loading period the mice are anesthetized using isoflurane inhalation (2% in 1 l/min O_2). On μCT scanning days (starting day, day 5, day 10 and day 15, see Figure 4.1b), mice are anesthetized using an anesthetic/analgesic cocktail (60 mg/kg ketamine and 0.3 mg/kg medetomidine). The first in-vivo μCT scan before loading serves also as baseline image to assure, that the studied animals show no handedness and therefore no significant difference in bone density, morphology, and microstructure between later loaded and non-loaded limbs [Main et al., 2020]. These animal experiments are carried out according to the policies and procedures approved by the local legal representative (LAGeSo Berlin, G0168/13) .

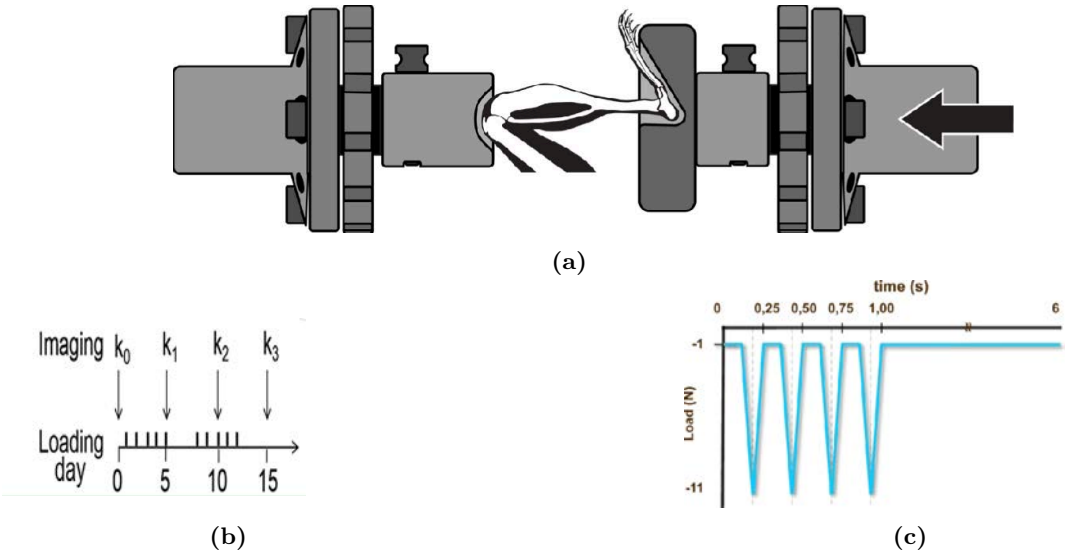

Figure 4.1.: Sketch of the experimental set-up of in-vivo loading to study the mechanoresponse of bone. a) The loading device is used to load the hind limbs of the mice (tibiae) five times per week for two weeks, as indicated in the schedule (b). In vivo μCT scans are taken on imaging days, indicated with k_0 to k_3. The loading cycles consists of 4 peak loads of 11 N with a frequency of 4 Hz followed by rest of 5 s (c). This cycle is repeated 216 times. Figure a and b are adapted from [Willie et al., 2020] with permission from Elsevier.

4.1.3. In-vivo micro-computed tomography and time lapse image registration

To evaluate the bone formation and resorption as response to the in-vivo loading, the mid diaphysis of the tibiae undergoes in-vivo μCT scans with an isotropic voxel size of 10.5 µm covering 5% of the tibia length on day 0 and 15 (VivaCT 40; Scanco). To prevent motion artifacts, the mice are anesthetized via isofluoran and kept in a fixed position using a custom-made mouse bed during the scans (similar to Figure 4.2).

Later, the μCT images of the same bone but different point in time, are aligned in a common coordinate system using a registration algorithm used in several other studies [Birkhold et al., 2014, Razi et al., 2015]. Following this protocol, the imaged voxels in the fused dataset can then be classified as newly formed, resorbed, or quiescent bone to create a time-lapse of the bone (re)modeling process.

4.1.4. Static microCT analysis

Due to the high resolution and 3D representation, μCT measurements are used to study bone morphology. For analysing the very same, the software CT-Analyser® (CTAn) provided by SkyScan is used. A global threshold determined by Otsu's method [Otsu, 1979] seperates the cortical and trabecular bone from background (nonmineralized tissue and water). Following the recommentations of Bouxsein et al. [Bouxsein et al., 2010], the outcome parameters in the cortical region are: total volume (TV), bone volume (BV), bone volume fraction (BV/TV), cortical area (Ct.Ar), total area (Tt.Ar), cortical thickness (Ct.Th) and principal moments of inertia (I_{max}, I_{min}).

4.2. Ex-vivo sample preparation

After sacrificing and dissection of the hind limbs, the bones are fixed in 70 % ethanol. The following preparation steps are done based on the established protocol of the biomaterials department at the MPIKG [Kerschnitzki et al., 2011b] and include:

1. A graded dehydration series with increasing ethanol solutions (80%, 90%, 95%, 100%) and 24h per step to avoid crack formation.

2. Cutting the edges with a diamond saw to improve the following infusions. Therefore, the sample is glued on a PMMA block with dentistry glue. See Figure 4.3a.

3. Storing the sample two days in Rhodamine6G solution (0.02 %wt in 100 % ethanol) stains the LCN and low-mineralized tissue.

4. Replacing the staining solution by methyl methacrylate (MMA) infiltration solution.

5. Putting the bone samples in cylindrical acrylic sample holders filled with fluid MMA, which is then polymerized under high temperature over three days (Figure 4.3b).

6. Trimming the polymethyl methacrylate (PMMA) blocks with a low-speed diamond saw (Buehler IsoMet, Lake Bluff, Illinois) to the region of interest with parallel surfaces and polishing the surface of interest with diamond powder.

7. Confocal laser scanning microscopy

8. Quantitative backscattered electron imaging

9. Cutting slices of 5 µm to 6 µm thickness and mount them on SiN-Windows for high resolution scanning SAXS and WAXS measurements at the synchrotron.

All samples in this work undergo the last three steps. Since this order of measurement methods allows to apply the different methods in the same volumes of interest (see Figure 4.3c), direct comparisons of bone material properties and the architecture of the LCN are possible. All experimental procedures used in this work to characterize certain sample features are explained below.

Figure 4.2.: Photograph of a mgr/mgr mouse in a custom made bed for in-vivo μCT. Here, the mouse is positioned into the bed (white plastic). Especially, the feet are taped to a foot bank, which is then repositioned (and fixed with the red tape) stretching the legs for clear and straight CT images, which makes the segmentation much easier. The tail is taped slightly to the fur for the same reason. The mouse is also attached to a tube infusing isoflurane for anaesthesia during the imaging time.

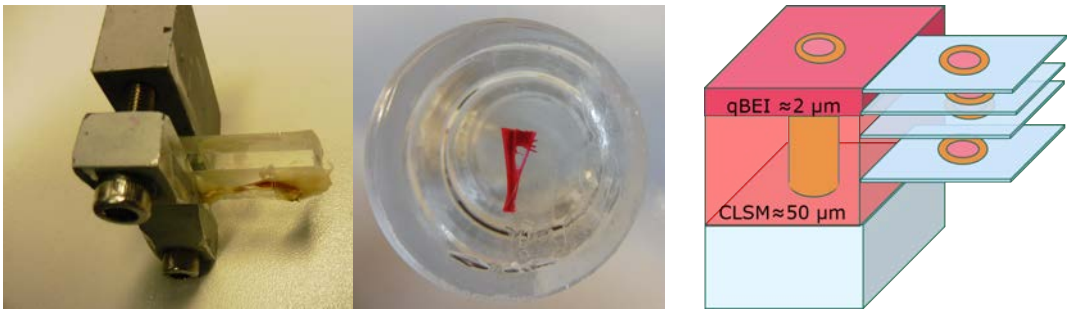

(a) (b) (c)

Figure 4.3.: Sample preparation (a) cutting the edges of dehydrated samples to enable better infusion, (b) staining and hot embedding in PMMA, followed by (c) measuring the bone properties with different methods in comparable volumes.

4.3. Measurements of osteocyte lacuno-canalicular network properties

4.3.1. Visualization and quantification of the lacuno-canalicular network by confocal laser scanning microscopy

Within the last years, the group at the MPIKG improved the procedure to gain information on the LCN architecture by staining all bone surfaces with Rhodamine6G [Kerschnitzki et al., 2013, Kerschnitzki et al., 2011b], imaging the LCN with CLSM and analysing the resulting images [Van Tol et al., 2020, Roschger et al., 2020].

Therefore, a Leica TCS SP8 DLS (Digital LightSheet) confocal laser scanning microscope (Wetzlar, Germany) equipped with a 40x oil-immersion lens with a numerical aperture NA = 1.3 (Leica, HC PL APO CS2 40x/1.30 OIL) is used. The excitation wavelength of the Argon laser is set to 514 nm, while the emission is measured in a range from 550 nm to 650 nm with a pinhole size of 68 µm. An immersion liquid from Leica between lens and cover slide as well as between cover slide and sample limits the differences of the refractive index in the optical pathway and thus aberrations.

The image resolution is set to a pixel size of 0.38 µm and the image size is 1024 x 1024 px. Due to the limiting factors such as opaqueness of the mineralized bone, the image stacks are measured until a penetration depth up to 60 µm with a spatial z-resolution of 0.34 µm. However, this resolution is not fine enough to resolve the morphology of single canaliculi (with diameter around 200 nm to 300 nm [Varga et al., 2014]), but can assess the network topology of full cross-sections of murine tibiae (cross-sectional area around 1200 μm^2) with 16 images in a 4x4 grid and a measurement time of approximately two hours. Due to the use of the immersion liquid, the sample drifts slightly in x and y direction during the measurement time. Therefore, an overlap of 10% does not only simplify the later stitching but also counteracts the drifting. Additionally, extra images were taken above and below the sample, allowing positioning errors in z direction.

As first step of image processing, the measured stacks need to be stitched. For the following analyzis, it is important to connect canaliculi between the overlapping images and avoid their doubling. To facilitate the stitching, BigStitcher in ImageJ provided by [Hörl et al., 2019] is used. These cross-sectional stacks are then evaluated and quantified by the custom-made python software package by Repp (updated and improved by van Tol) called tool for interactive network analysis (TINA) [Repp et al., 2017]. This software includes a standardized adaptive threshold through binarization followed by skeletonization, network analyzis (for example density, knot distribution, orientation, ...) including cell recognition and evaluation (density, shape, orientation,...). Using these results, ImageJ is used to generate maps of the canaliculi density ([Can.Dn.]= $\mu m/\mu m^3$), which is the total length of all canaliculi per unit volume (7.4 x 7.4 x 7.4 μm^3).

4.3.2. Quantification of the lacunar morphology by micro-computed tomography

μCT gives more accurate information on the distribution, shape and orientation of lacunae in bone than CLSM. Due to its high brilliance, which allows the achievement of finer resolutions [Stampanoni et al., 2002] and the use of a monochromatic beam for accurate density representations, synchrotron-based phase contrast μCT enhances the visibility of edges of lacunae and pores again and simplifies the segmentation process. It even makes it possible to image whole murine bones with sub-micron resolution in a short period of time.

In this work, synchrotron-based phase contrast μCT at the beamline ID19 at the ESRF is used for the comparison of lacunae in callus and cortex of the healing femur after osteotomy. Since the results are already published, the following section is based on [Schemenz et al., 2020]. The pixel size of the detector at ID19 is 650 x 650 nm^2 with a field of view of 1.4 x 1.4 mm^2. The best contrast performance for the following analyzes is achieved with a sample-to-detector distance of 25 nm. With a counting time of only 80 ms, each sample can be scanned in 10.5 min, 4200 to 4600 projection images are recorded.

The measured images are analyzed in cooperation with F. Chamasemani and R. Brunner at the Materials Center Leoben Forschung GmbH (MCL), using Python 3.6 for image analysis and Avizo® (version 2019.1) for visualization. Welch's t-test is used to evaluate the effects of the tissue type. Here, the aim is a) to compare the lacunae properties for the cortical region and the bony callus in general, b) understand how these properties behave at the interface between those regions.

For the first evaluation, a volume of interest (VOI) of 1723 x 1560 x 13 μm^3 is divided into 70 cubic subvolumes (65 x 65 x 65 μm^3) within both, the cortical region and the bony callus. Due to the heterogeneous structure of rodent long bones (lamellar bone, woven bone and no regular border to the callus), the selection is done by hand avoiding the bone surface and interface regions, (see Figure 4.4a and Figure C.1). Hereby, the cubes are large enough for sufficient statistics, but at the same time small enough to be able to investigate a spatial heterogeneity of the lacunar density. The segmentation is validated by checking layer by layer, that the selected cubes only contain cortical or bony callus.

The grey values of the cortical and callus regions differ from each other. This is exploited for the second evaluation approach in a second VOI of 739 x 747 x 65 µm and it is set manually points at the interface between the regions, which are then connected to a spline interpolation (see Figure 4.4b). Here, the distance between lacuna and interface is defined as the shortest distance between the center of mass of each special lacuna to the defined interface. The segmented pores off the callus and cortical region are shown in blue in Figure 4.4c.

However, for both approaches, the lacunar analyzing is made according to former studies [Dong et al., 2014, Mader et al., 2013]. As the pixel size equals the layer thickness, the number of voxels in the pore times the vooxel size defines Lacunar volume (Lc.V). For the lacunar density, Lc.N/TV, only those lacunae are considered, whose center of mass lay within the cubic subvolume. The shape of the lacunae is characterized with help of the inertia matrices of each lacuna with reference to its center of mass and their eigenvalues λ_{1-3} with $\lambda_1 < \lambda_2 < \lambda_3$. To differentiate the lacunae morphology, one considers firstly, the lacunar stretch $Lc.St = (\lambda_3 - \lambda_1)/\lambda_3$, where the extrema indicate either a perfect sphere (Lc.St = 0) or an infinitely stretched object (Lc.St.= 1). If $Lc.St \neq 0$, the lacunar oblateness $Lc.Ob = 2\frac{\lambda_2-\lambda_3}{\lambda_1-\lambda_3} - 1$ characterizes whether the the lacuna is more prolate, ($Lc.Ob \approx -1$) or oblate, when λ_2 is closer to λ_3 than to λ_1 ($Lc.Ob \approx 1$) [Mader et al., 2013].

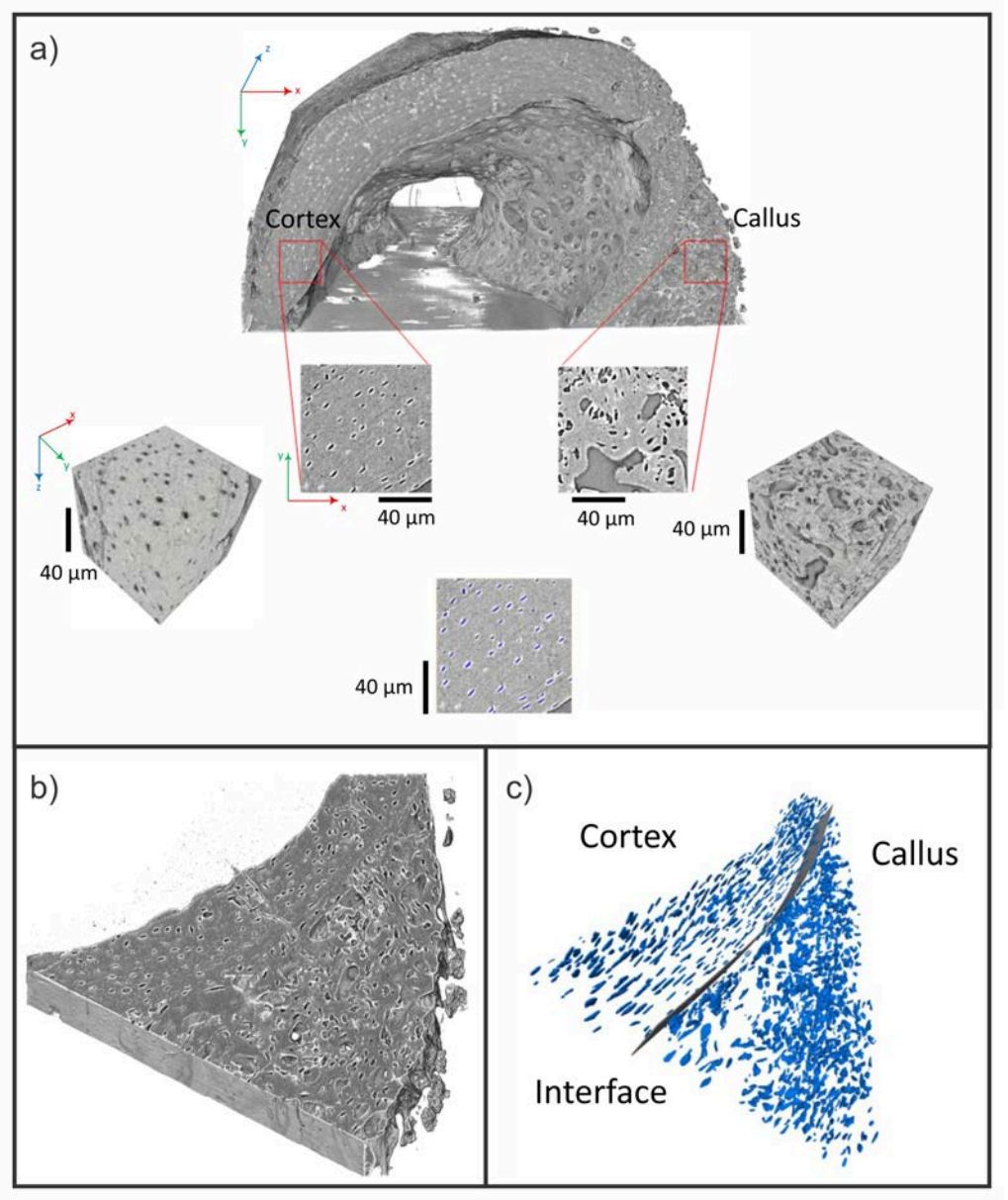

Figure 4.4.: Evaluation of the synchrotron-based micro-computed tomography measurements. 3D reconstruction of a part of the studied bone with callus and cortical bones (a). For example, cubes with a side length of 65 μm are also shown, which are used to determine the lacunar density and reference values for the lacunar parameters in the respective region. In order to analyze the behavior at the transition between the regions, one is manually defined a dividing line between the contrasting bone types, cortical tissue and callus. The VOI for this approach is displayed as a phase contrast image (b) and segmented volume with a defined interface between the bony callus and the cortical tissue (c).

4.4. Measurements of bone matrix properties

4.4.1. Quantification of the Calcium content in bone by quantitative backscattered electron imaging

As already described in 3.3.2, the intensity of backscattered electrons correlates with the degree of mineralization [Roschger et al., 1998]. Therefore, qBEI became a method for quantification of the calcium concentration in bone samples. The measurements for this work were done at the Ludwig Boltzmann Institute for Osteology (LBIO) in Vienna, either with the Zeiss Supr40 field emission cathode scanning electron microscope (FESEM) (chapter 6 and 5.6) or Zeiss DSM962 (chapter 7). Comparisons of the two instruments can be found in [Hartmann et al., 2021] and [Roschger, 2015], concluding that qBEI measurements can only be compared quantitatively, from the same device and the same measurement conditions [Hartmann et al., 2021]. Since the models in this work are quite different, there will be no comparison of these measurements anyway.

However, the measurement procedure is the same for both machines and described precisely in the named studies. Before the qBEI experiments, the sample surfaces are coated with carbon by vacuum evaporation (Ager Scientific, SEM carbon coater, Essex, UK) to achieve a conducting surface and prevent charging by using SEM. At the same time, a high-purity aluminum sample (99.9999%, MAC Consultants UK) is also coated with carbon in order to quantify the influence of carbon deposition on the qBEI measurement.

The backscattered signal of the SEM is calibrated using a high-purity two-element reference sample with aluminum ($Z = 13$) in the center, surrounded by carbon ($Z = 6$). In the calibration routine the brightness and contrast of the detector are adjusted to give a grey level of 25 ± 1 for carbon and 225 ± 1 for aluminum. In the following, 10 mm sample-detector-distance, 130x nominal magnification, 20 kV acceleration voltage and a probe current between 270 pA to 320 pA are used. The pixel size was 0.88 µm in both directions. To calculate the BMDD and mentioned qBEI parameters, the images are segmented to the regions of interest and only grey levels above 25 are considered for further calculations.

4.4.2. Quantification of mineral properties by small and wide angle X-ray scattering

Data acquisition

Shape, size and arrangement of the mineral particles and the mineral density distribution have a great influence on the mechanical properties of bone [Stock et al., 2011, Akkus et al., 2004, Whalen et al., 1988, Roschger et al., 2008]. Assuming bone mineral particles as thin platelets, SAXS provides information about the thickness and alignment of the particles, while WAXS is used to calculate the length L and the inner crystal lattice spacing in c-direction. Furthermore, scanning SAXS/WAXS measurements can provide information in the micrometer range by scanning an area, but obtain also information in the nanometer range by analyzing the patterns at distinct positions in the area.

To determine thickness and orientation of the mineral particles within some defined areas of the bone slices, synchrotron SAXS mapping measurements were carried out at the microfocus beamline (ID13) at the European Synchrotron Radiation Facility (ESRF). The mapping experiments were performed with a nominal beam size of approximately 1.5 x 2 µm and 2 µm step size. All scattering images are averaging the signals from all particles in the pathway of the beam and to avoid contributions from too many particles, it is established to have a sample thickness in the range of the beam diameter. Here, the slices have a thickness of just a few µm. The transversal cross section of murine long bones consists of a relatively thin ring attached to the PMMA. During cutting this set-up produces high forces

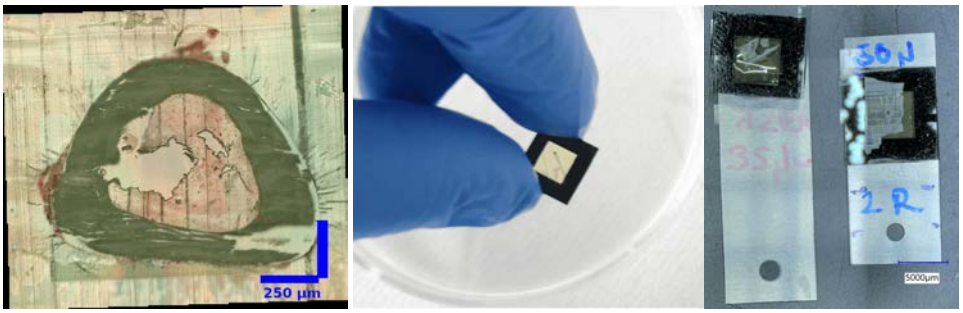

(a) (b) (c)

Figure 4.5.: Mounting procedure of bone samples (a) A cut sample with slices in the PMMA, grey bone cortex and soft tissue in pink. (b) dipping the sample into the gelatine and fishing it with the SiN window. (c) Mounting the SiN windows on aluminium frames. For the synchrotron measurements several of these aluminium frames are then put on an aluminium bar to simplify sample changes during beam times.

to the bone, which is why the samples are relatively likely to be stretched and compressed followed by tearing during the cutting process (exemplarily seen in Figure 4.5a). After cutting, the thin slices are mounted to 1 µm thick nitride windows with 500 µm thick silicon frames (Norcada Inc., Edmonton, Canada) by dipping into gelatine, examplarily shown in Figure 4.5b. Afterwards, they are glued to aluminium frames to mount them later on the sample holder of the beamline (see Figure 4.5c).

Experimental setup at ESRF

The sample holder is mounted with a magnetic mechanism on a xyz translation stage, which can be moved relatively to the incident beam. The scattering patterns themselves are then measured with an Eiger X 4M detector (Dectris AG, Baden Dättwil, Schweiz) with an image size of 2070 x 2167 px and a pixel size of 75 x 75 μm^2. To achieve a q-range covering 0.1 nm^{-1} to 20 nm^{-1}, i.e. regions for SAXS and WAXS analyzes, the detector is positioned approximately 225 mm away from the sample. All measurements are done with a wavelength of 0.95 Å (photon energy of 13 keV). The exposure time per measuring point is optimized for each project, but lays in the range of 0.04 s to 0.1 s. Parallel to scattering measurements, the calcium fluorescence signal is measured with an X-ray fluorescence (XRF) detector approximately 20 mm apart from the sample.

Depending on the individual sample, the number of measuring points varies between 30400 and 500000. To evaluate such high amount of data, the group at MPIKG has developed together with cooperation partners from Deutsche Elektronen-Synchrotron (DESY) and ESRF a software for fast reduction and analysis of large X-ray data sets [Benecke et al., 2014] called Directly Programmable Data Analysis Kit (DPDAK). Hereby, the evaluation can be parallelized on several kernels, which reduces the calculation time to a fractional amount. The evaluation for this work is done with DPDAK v.1.2 and 1.4 using integration and calibration algorithms from the pyFAI package [Kieffer and Wright, 2013]. The calibration of beam center position, detector tilt and exact sample-to-detector distance is done with the help of an Al_2O_3 standard sample.

After calculation and filtering for values within the bone material, the results of SAXS- and WAXS measurements are plotted with Origin as 3D scatter plots with a decent color scale depending on their values but as similar as possible across all projects.

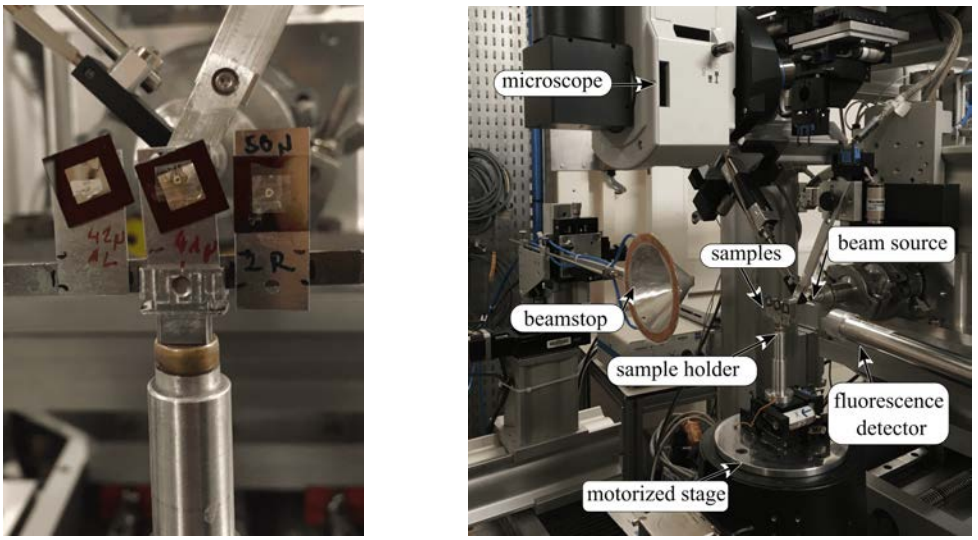

(a) **(b)**

Figure 4.6.: Experimental setup for SAXS measurements at the beamline ID13 at the ESRF. a) The prepared and precharacterized samples are mounted on an aluminium plate, then on a magnetic sample holder. b) This is positioned on a motorized stage and can be moved in x and y direction, perpendicular to the beam path, so that large areas of the sample are scanned. The scattering pattern is recorded by the detector, while the beam stop shields the direct beam. Using the microscope, the exact region of interest is determined.

Evaluation of small angle X-ray scattering measurements

The acquired 2D SAXS patterns are integrated azimuthal and radial, leading to the intensity functions $I(q)$ and $I(\mathcal{X})$ of the scattering length q and azimuthal angle $\mathcal{X}$, respectively.

ρ parameter As described in chapter 3.4.3, the ρ parameter is defined as degree of orientation and is calculated by the intensity profile $I(\mathcal{X})$. The measured intensity ($I_{measured}$) is corrected by subtracting the background intensity (intensity without the sample, but silicon nitride windows, I_{bg}).

T parameter The T parameter is obtained from $I(q)$ using Porod´s law $\lim_{q\to\infty} I(q) = {}^{P}/_{q^4} + B$ with the Porod constant P and the background constant B. Both P and B should be determinable from a fit of the linear region of the so-called Porod plot showing $I \cdot q^4$ versus q^4 (see Figure 4.7c). More precisely, the Porod constant is equal to the intercept of the fitted linear graph of the curve with the y-axis.

As described in chapter 4.4.2, the T parameter can be calculated with

$$T = \frac{4}{\pi P} \int_0^\infty q^2 I(q) dq \text{with } I = I_{exp}(q) - B, \tag{4.1}$$

whereby the integral can be solved by determining the area $\tilde{I}$ under the curve of the Kratky plot (Figure 4.7d), showing $Iq^2(q)$. But due to the beam stop, there are no values for small q. Also values for large q have to be determined by extrapolation. Therefore, the function is divided into three part $\tilde{I}_0, \tilde{I}_1, \tilde{I}_2$ with :

$$\tilde{I} = \tilde{I}_0 + \tilde{I}_1 + \tilde{I}_2 \tag{4.2}$$

$$= \int_0^{q_{min}} q^2 I(q) dq + \int_{q_{min}}^{q_P^{min}} q^2 I(q) dq + \int_{q_P^{min}}^{\infty} q^2 I(q) dq \tag{4.3}$$

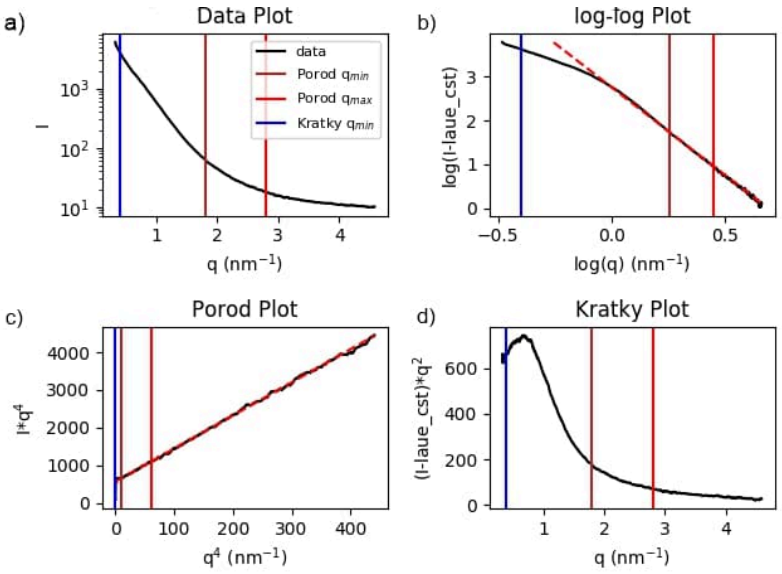

Figure 4.7.: Graphical results of T parameter evaluation by the software DPDAK. Data obtained from radially integrated SAXS patterns in (a) a linear plot, (b) log-log plot, (c) Porod plot and (d) Kratky plot.

Estimating the function I_q to be linear in the area $\tilde{I}_0$, one could consider the area from I(0) to $I_{q_{min}}$ as a triangle with the area

$$\tilde{I}_0 = \int_0^{q_{min}} q^2 I(q) dq \approx I_{q_{min}} \cdot q_{min} \cdot 1/2. \tag{4.4}$$

For $q > q_P^{min}$, $I_{exp}(q) \approx B + P/q^4$, where B is the Laue constant, describing the background of the scattering, caused by anything different than the mineral crystals, and P is again the Porod constant. That means, the slope of the logarithmic plot should be around -4 (see Figure 4.7b). This leads to eq Eq. (4.7).

$$\tilde{I}_2 = \int_{q_P^{min}}^{\infty} q^2 I(q) dq \tag{4.5}$$

$$\approx \int_{q_P^{min}}^{\infty} P/q^4 q^2 dq \tag{4.6}$$

$$= P/q_P^{min} \tag{4.7}$$

Lastly, $\tilde{I}_1 = \int_{q_{min}}^{q_P^{min}} q^2 I(q) dq$ can be calculated directly from the measured data.

According to these assumptions, DPDAK calculates the T parameter for every measured point. The resulting T parameter are filtered within Excel afterwards, so that only those values are coming into account, which match all the presumptions. Thereby, the slope of the linear regression in the log-log plot is expected to be between -4.1 nm to -3.9 nm.

4.5. Evaluation and angle dependence of the L parameter

The crystal length L along the c-axis was determined from the full width at the half maximum of the (002) peak intensity in the WAXS signal using Scherrer´s equation given in Eq. (3.16) with the full width at the half maximum B of the peak in radians (see also chapter 3.4.3).

It was shown, that the crystal orientation correlates with the intensity distribution of the Debye Scherrer rings of the WAXS signal. If the Debye Scherrer rings show an uniform intensity, the crystals are randomly oriented. If a ring shows pronounced increases of intensities in certain directions, the crystals have a preferred orientation [Wenk and Heidelbach, 1999].

First evaluations of the L parameter maps from the whole cortices have shown patches of high L values in irregular occurrences, but disrupting the general pattern in the cortex. This is exemplified in Figure 4.8(a) by grey patches. Comparing these maps with the microscopic images (Figure 4.8(a) and (b) one could observe similarities between the named patches and the topography of the sample slices. In the given example, many of the patches in Figure 4.8(a) seem to correspond to darker regions in Figure 4.8b. The topography function of the Keyence digital microscope VHX-550E produces indeed a wavy structure like it can be seen in Figure 4.8(c) and (e) for the small regions (Figure B.1 and B.2 show the topography for the whole sample). This is probably caused by compression during the cutting process.

Rotating the sample around one axis along a line where the material of the sample is compressed and therefore an increase can be observed, makes it possible to measure how the L parameter changes with the incident angle to the sample. Therefore, additional experiments were done at the μSpot beamline at Berliner Elektronenspeicherring-Gesellschaft für Synchrotronstrahlung m. b. H. (English: Berlin Electron Storage Ring Society for Synchrotron Radiation) (BESSY) belonging to the Helmholtz Zentrum Berlin für Materialien und Energie, Berlin, Germany. The results are presented in Figure 4.8 (d) and (f) and show an angular dependence of the L parameter. As already mentioned in chapter 3.4.3, the best result should be in a perpendicular angle between c-axis of the mineral particle and incident beam [Finean and Engström, 1953].

The sample rotation is an artificial change of angle between incident beam and mineral particles. But increasing and decreasing heights of the sample (waviness in beam direction) like the could been observed in Figure 4.8 introduce changing angles as well. That means, the resulting L parameter depends on the measuring position of the wave, which explains why WAXS maps of bone cross sections like it is described in 3.4.3 show an irregular, "wavy" behavior of the L parameter (shown in Figure 4.8(a).

Lattice constant in c-direction and d-spacing

The position of the 002 peak refers directly to the d-spacing in the corresponding crystallographic direction, i.e. the inter-atomic space in c-direction. Therefore, it can be converted to the c-lattice constant with Eq. (4.11) [Handschin and Stern, 1995].

$$\frac{1}{d_{hkl}^2} = \left(\frac{h^2+k^2+hk}{a^2}\right)\frac{4}{3} + \frac{l^2}{c^2} \tag{4.8}$$

$$d_{hkl}^2 = \frac{1}{\left(\frac{h^2+k^2+hk}{a^2}\right)\frac{4}{3} + \frac{l^2}{c^2}} \tag{4.9}$$

$$d_{002} = \sqrt{\frac{c^2}{l^2}} = \frac{c}{2} \tag{4.10}$$

$$c = d_{002} \cdot 2 \tag{4.11}$$

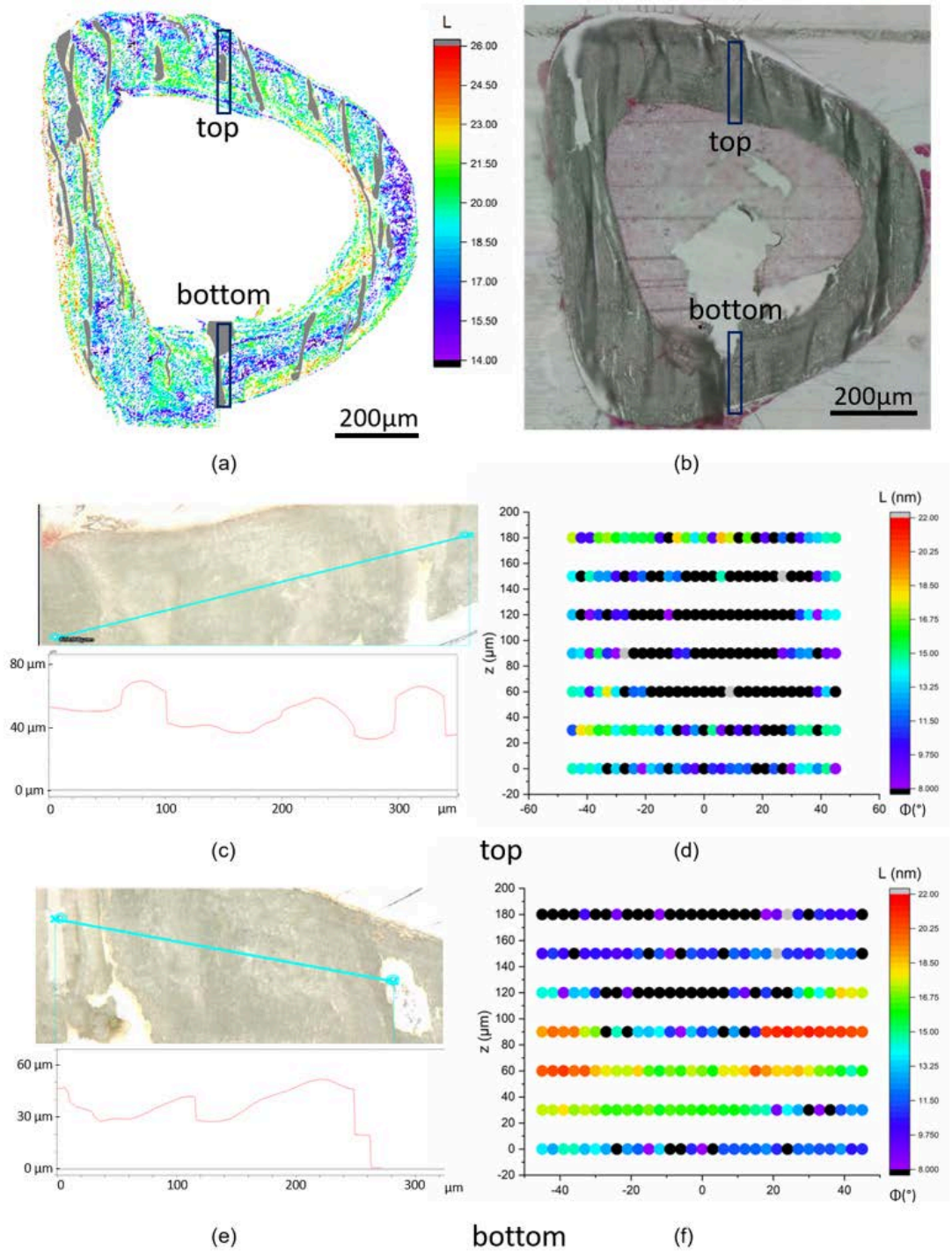

Figure 4.8.: Angle dependence of the L parameter. a) L parameter map of a murine cortex from a non loaded tibia (2R). The grey areas are added manually at regions with very high L values. b) corresponding microscope image of the sample slice mounted on a SiN window. For further analyzes, (c) and (e) show the topographical analyzes of regions at the top of the sample (c) and the bottom (e). Using a Keyence digital microscope, the turquoise line is drawn in the middle of the cortex - hitting the rectangles of (a) and (b) - to analyse the surface roughness which is shown in the corresponding plots with the red line. At the μSpot beamline at BESSY additional WAXS measurements have been done. There, the sample was rotated around a vertical axis, marked with rectangles in (a) and (b). The results are shown in (d) and (f), where the L parameter is plotted as a function of the z position and the angle. The black points are equal to very low L values below 8 nm.

4.6. Development of routines for image registration

Especially in the case of a biological material such as bone with its hierarchical structure, an analysis of this material on different length scales is preferable for receiving information about the local homogeneities and inhomogeneities on the micro- and nanometer level [Rinnerthaler et al., 1999, Gourrier et al., 2007]. Different methods are used to gain this aim, giving information mainly only for one parameter in one hierarchical level. To get a full image, all information have to be measured at the same VOI and superimposed afterwards.

Image registration of the qBEI images and CLSM z-projections makes it possible to visualize the LCN architecture within its mineralized surrounding by using the the standard deviation (STD) projection type of ImageJ v.1.51n [Schneider et al., 2012] for the z-stacks of approximately 2 µm of the LCN (information depth of qBEI measurements [Goldstein et al., 2012]). A fixed threshold with the graphics software Adobe Photoshop (CS5 v.12.0.4) is used to extract the LCN from the z-projections for visualization. As osteocyte lacunae at the block surface are clearly visible in both data sets, these features allowed accurate image registration for qualitative comparisons.

For quantitative comparisons, a python script for manual image registration is used, which is attached in appendix A. This script loads the results of the precedent measurement as 8-bit images or tables and creates (in line 60-77 or 4.6) a table where all values are related to the same coordinates (origin in the middle) with the same resolution (line 4 in the snippet). Which resolution to choose, depends on the data. In general, it seems better to average several points of a map by choosing the minimal resolution. Otherwise, one produces a pseudo-accuracy with values for points, which are not measured. Therefore, all comparisons including the canalicular density will have a resolution of 8 µm and those with SAXS and WAXS measurements comparing to calcium content will have a resolution of 2 µm (step size of the measurements).

```
1  def join_data(imgs):
2      by_type = list(zip(*imgs))
3      scales = np.array(by_type[1])
4      scales /= 8
5      scaled_offsets = [s * np.array(offset) for s, offset in zip(scales,
       by_type[2])]
6      ymin = [int(so[0]) for so in scaled_offsets]
7      ymax = [int(img.shape[0] * s + so[0]) for img, so, s in zip(by_type[0],
        scaled_offsets, scales)]
8      xmin = [int(so[1]) for so, s in zip(scaled_offsets, scales)]
9      xmax = [int(img.shape[1] * s + so[1]) for img, so, s in zip(by_type[0],
        scaled_offsets, scales)]
10     w, h = max(xmax) - min(xmin), max(ymax) - min(ymin)
11     canvas = np.zeros((h, w, len(imgs)), dtype=np.float64)
12     as_np = np.stack(scaled_offsets, axis=0)
13     offset_shift = -np.amin(as_np, axis=0).astype(int)
14     for i, img in enumerate(imgs):
15         scaled_img = cv2.resize(img[0], (xmax[i] - xmin[i], ymax[i] - ymin[
       i]))
16         canvas[ymin[i] + offset_shift[0]:ymax[i] + offset_shift[0], xmin[i]
        + offset_shift[0]:xmax[i] + offset_shift[1],
17         i] = scaled_img
18     return canvas
```

Figure 4.9.: Snippet of the python script for image registration, creating the unified table for all data in one coordinate system.

To use the script, one has to create a folder with the images or tables including their resolution in µm as suffix, i.e. "name_resolution". In the given example 4.9, grey values from qBEI measurements, the calculated network density, a map of the identified cell lacunae after skeletonization with the software TINA as well as the corresponding network are loaded. But also the resulting maps of SAXS and WAXS measurements are included. These data are included by smaller parts (lateral, posterior, medial and anterior) to counteract the general deformation of the thin slices after cutting (4.9 line 3-5). The particular offset coordinates in pixel for each map as well as the rotation angle are added in brackets.

```
1 if __name__ == "__main__":
2     offsets = {  "A4LqBEI_0.88": (0,0, 0) ,"CLSM_1114L-fluor_0.395":
      (430,850,-5),"B4L_network_density_40um_0.36": (480,950, -5) , "cells_0
      .395":(430,850,-5),
3                  "Danterior-T_2.2":(50,300,33), "lateral-T_1.95":(20,150,27)
      ,"medial-T_1.95":(40,220,20), "posterior-T_1.9":(90,115,22),
4                  "Danterior-L_2.2":(50,300,33), "lateral-L_1.95":(20,150,27)
      ,"medial-L_1.95":(40,220,20), "posterior-L_1.9":(90,115,22),
5                  "Danterior-c_2.2":(50,300,33), "lateral-c_1.95":(20,150,27)
      ,"medial-c_1.95":(40,220,20), "posterior-c_1.9":(90,115,22)}
```

Figure 4.10.: Snippet of the python script for image registration with loaded data and their relative offset coordinates.

To create the table, the script has to be executed in the shell with the suffix -d by calling the folder of the saved data and naming the table .

```
1 python example.py foldername -d "tablename.csv"
```

Figure 4.11.: Shell commando to perform the script and creating a table.

Extraction of colormap coordinates with ImageJ
ImageJ (Fiji) is used to select an arbitrary region on the color maps. Hereby, it is important to adjust the image size. Then, one can select any region of interest, for example the cortex with the freehand tool and save the XY Coordinates as text file. Since ImageJ always has the origin in the upper left corner, one may have to recalculate the coordinates in order to filter the data from the parameter table.

4.7. Correlation between calcium content and canalicular density

Due to the small diameter of the canaliculi ($Can.Dm \approx 290\,\text{nm}$ to $440\,\text{nm}$ [Varga et al., 2014]), they can not be resolved in the qBEI images (pixelsize = 881.4 nm). That means, that the qBEI signal $CaCont_{Matrix}$ contains not only the calcium content of the measured region, but also contains the canaliculi without any calcium.

$$Can.Dn = Can.Length/\text{unit volume} \tag{4.12}$$

$$Can.V = \pi \cdot (Can.Dm/2)^2 \cdot Can.Length \tag{4.13}$$

$$CaCont_{Matrix} = CaCont + Cont_{canaliculi} \tag{4.14}$$

$$CaCont = CaCont_{Matrix} - Cont_{canaliculi} \tag{4.15}$$

$$= CaCont_{Matrix} \cdot \left(1 - \pi \cdot \left(\frac{Can.Dm}{2}\right)^2 \cdot Can.Dn\right) \tag{4.16}$$

$$\tag{4.17}$$

That means, there is a linear relation between CaCont and Can.Dn with a y-intercept equal to the $CaCont_{Matrix}$, and the SLOPE equal to

$$\text{SLOPE} = CaCont_{Matrix} \cdot \pi \cdot \left(\frac{Can.Dm}{2}\right)^2. \tag{4.18}$$

Assuming canaliculi with a fixed diameter laying in a homogenous bone matrix, one would expect, that an increase of the canalicular density, i.e. increasing porosity, leads to lower calcium content. However, Roschger et al. [Roschger et al., 2019] have studied the SLOPE of human osteons by plotting the Can.Dn versus calcium content. Most of the evaluated osteons have shown a positive correlation. That is, dense network regions show an accumulation of minerals. They suspect that this accumulation takes place in the immediate vicinity of canaliculi, which form mineral reservoirs that can be used by osteocytes. Significant differences between individuals indicate that the extent of the mineral load on the reservoir zone could be an important parameter for mineral homeostasis.

5. Characterization of osteocyte lacuno-canalicular network and material properties in healthy bone with and without mechanical stimulation

5.1. Objectives

The cortical bone of mice has been the subject of many studies, thereby different bone types in the mouse have been observed: ordered lamellar bone and a more unordered intracortical band including cartilage islands and woven bone [Bach-Gansmo et al., 2013, Shipov et al., 2013]. This chapter characterizes potential spatial correlations of the LCN and the bone material characteristics of both regions (ordered and unordered) to improve the understanding how LCN and bone mineral particles interact.

The left tibiae of the studied mice have experienced in-vivo mechanical loading providing bone formation and resorption (see chapter2.2.3 and 4.1.2). The newly formed bone will be characterized and compared to the older bone regions. Additionally, the structural characteristics of loaded and non-loaded bones will be compared to each other. Are there differences between left, loaded and right, non-loaded bones of the same individual? This special model is expected to provide hints whether the mechanical strain correlates with the architecture of the LCN and the mineral matrix properties.

5.2. Measurement procedure

The left tibiae of six female, skeletal mature (26 weeks) C57BL/6J mice (Jackson Laboratory, Bar Harbor, Maine, USA) underwent in-vivo loading for two weeks (described in 4.1.2). Because of the high resolution (voxelsize = 10.5 µm) in the longitudinal micro-computed tomography (μCT) measurements and to reduce radiation exposure as well as the time the animals are under anesthesia, only part of the tibiae could be imaged with the VivaCT 40 of Scanco. This leads to a certain variability in the animal placement (repositioning error) and therefore differences in the resulting images. The region of interest for time lapse image registration, is cut to 5% of the total tibial length, where all scans of the different time points overlap [Van Tol, 2020]. The samples are cut with a 50 µm thick diamond wire in a precision cutting machine. The whole preparation was done by A. van Tol and a description can be read in his PhD thesis [Van Tol, 2020]. It remains to be noted, that the following experiments are done on cross sections. Due to former observations of our group [Aido et al., 2014], no calcein was injected to avoid possible influences on the bone material properties. The qBEI measurements have been done at the Ludwig Boltzmann Institute for Osteology (LBIO) using the field emission cathode scanning electron microscope (FESEM).

The study started with six mice (numbered as 1, 2, 3, 4, 5 and 6), whose left tibiae (marked with L) have experienced in-vivo loading for two weeks and the right (R) tibiae serve as non-loaded control bones. Not all of the samples could be measured with all methods. Additionally, some problems occured after measurements, which again diminished the number of evaluated samples. Mouse 3 had to be removed from the project because of

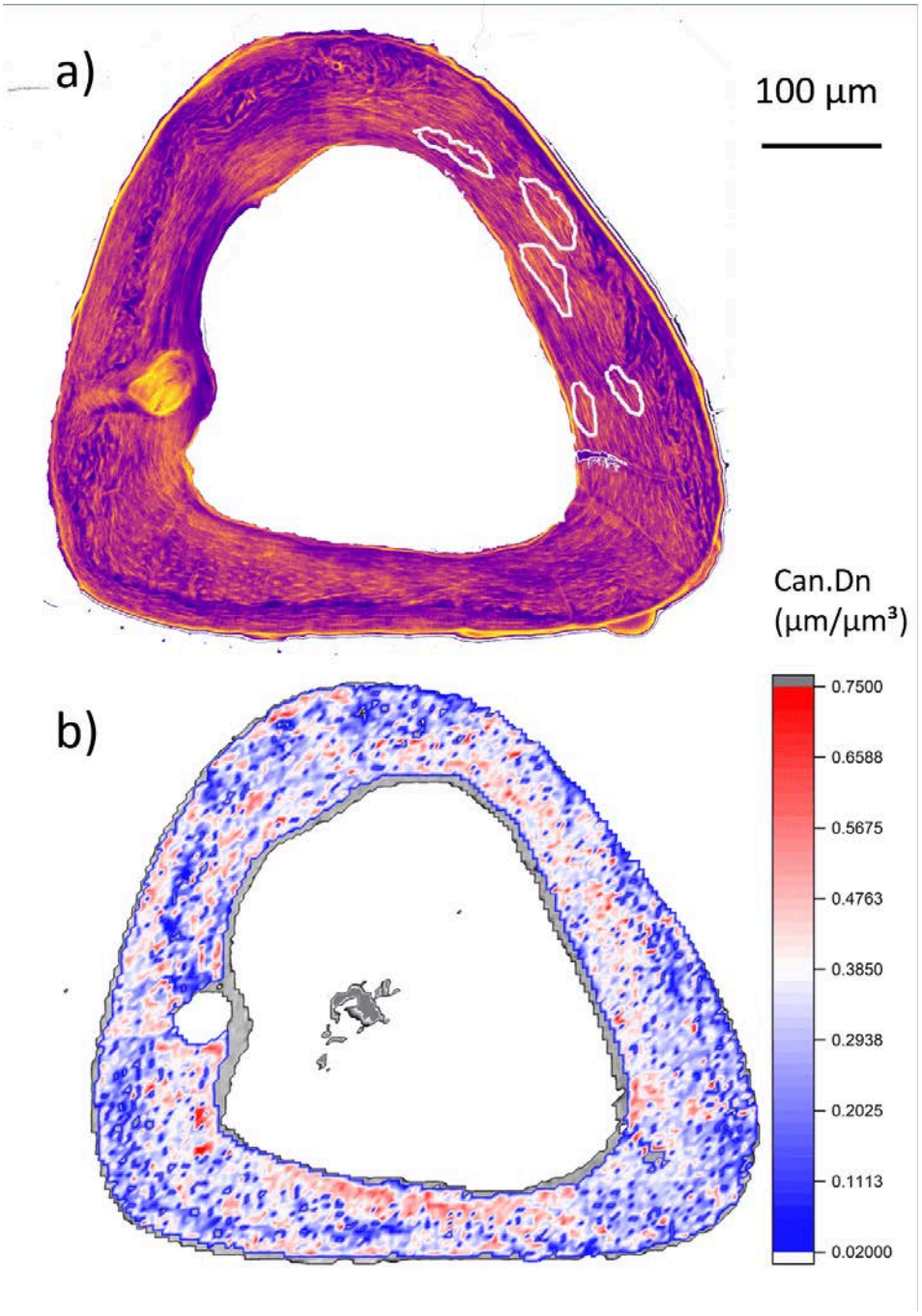

Figure 5.1.: Example of microcracks in the lacuno-canalicular network of a murine cortex. Figure (a) is the sum of the z-projections of the lacunoc-canalicular network imaged with CLSM. The brighter the color in a point, the more images in the stack showed a fluorescence signal. Marked with white contours are some example microcracks, observable as longer yellow lines – meaning, that they are observable throughout several layers. These microcracks are seen in some of the samples and may be caused by dehydration during the preparation process. Perpendicular to these big lines a lot of small cracks are observable leading to high values in the Can.Dn (b).

severe bone damage after the in-vivo experiments. The reason could not be clarified yet.

Three of the non-loaded tibiae show plane like structures in the 3D CLSM images, which are referred to as microcracks (see for example Figure 5.1a). They are characterized by long lines quite parallel to the cross section, which are observable over several z projections, with many small connections between these lines. These patterns are mainly seen at endosteal surfaces of non-loaded / right bones. Similar effects can be seen in [Kerschnitzki et al., 2011b] and [Kerschnitzki, 2012] but are not explained in these studies. Due to the high amount of small lines radial to the long lines, the areas of microcracks show high canalicular densities after calculations with the TINA software (see for example Figure 5.1 b). They might be caused by dehydration during the preparation process, for example during the cutting with the diamond saw, which takes several minutes without any solution. In future experiments, all steps outside of the solution before embedding have been shortened up to decrease the possibility of microcracks.Since these patterns do not seem to mirror natural behavior, but originate from sample preparation, the samples 1R, 2R and 6R are taken out from this part of the evaluation. Due to this, it is only possible to compare right and left cortices of two samples - mouse 4 and 5. Thus, further studies are needed to evaluate this behavior.

The sample 2L is taken out because its images seem to be deformed during repeated confocal laser scanning microscopy (CLSM) measurement. Due to the difficulties in cutting ultra-thin cross sections of bones and limited measurement time at synchrotrons for high-resolution SAXS and WAXS, it is also not possible to scan the whole cross section of all samples completely with this methods. Rather, only parts of some samples are measured. Exemplary, only one sample for the left, loaded bone will be shown as well as one representing the right, non-loaded bones. Additional maps can be found in the appendix (B).

The bone regions are distinguished only by organisational features of the lacuno-canalicular network (LCN). According to the description of Kerschnitzki et al. the cortices of the murine long bones are divided into ordered and less organized regions (see Figure 5.2 for brief description of method) [Kerschnitzki et al., 2011a]. In the ordered region the osteocytic network is highly aligned; the long axes of the elongated, ellipsoid-shaped lacunae run mainly parallel to the bone cross section, while the canaliculi run mainly perpendicular to the short axes of the lacunae and therefore also to the bone cross section. The less organized or disordered bone shows neither osteocyte lacunae nor canaliculi of a predominant direction with respect to bone geometry. All regions of uncertainty are excluded. This manual method is quite subjective, but serves as a base for more objective criteria for future studies. For example the classification can be done by the difference of the main orientation of neighbouring lacunae.

The comparison of left and right bone as well as the comparison of the different bone regions are done with paired t-test. All statistical analyses are performed with Origin 2021b on a personal computer. Differences were considered statistically significant when $p < 0.05$.

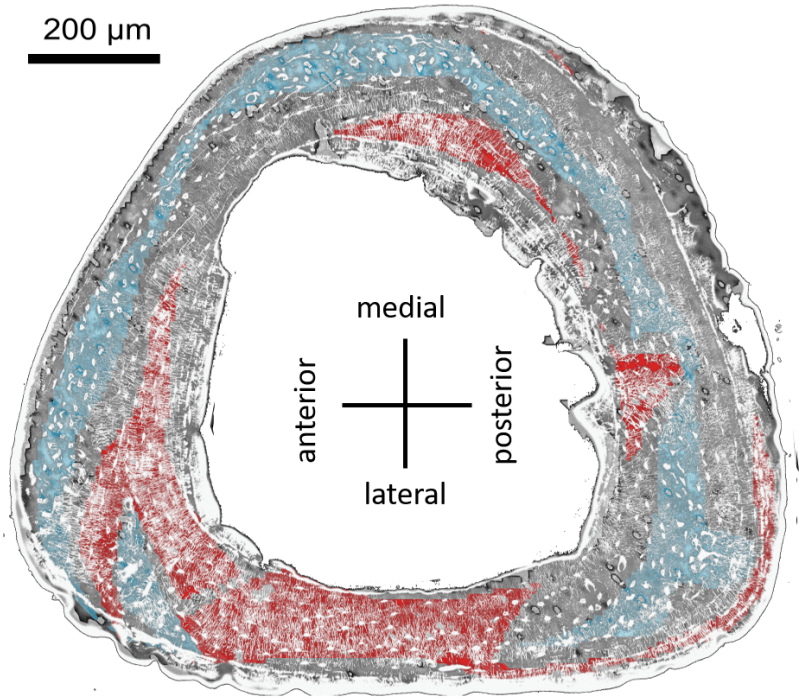

Figure 5.2.: Selection of ordered (red) and unordered (blue) regions. Comparing the properties of the LCN in the cortex of the murine tibia, two different regions can be observed. A band with no preferred orientation of lacunae and canaliculi, surrounded by more ordered regions. For an intensive investigation, the regions were classified manually on a CLSM area that is closest to the SAXS and WAXS measurements. This was also used for image registration in the following. For this purpose, each area was enlarged to the maximum and thus showed more details than can be shown here. If the lacunae have a clear alignment and the canaliculi are aligned perpendicular to their longitudinal axes, the sub-region is counted as an ordered region (red). If the canaliculi and lacunae do not show a dominant orientation, this is an unordered region (blue). All regions that are not clearly ordered or unordered are removed from the classification and shown here in gray.

5.3. The effect of mechanical stimulation on bone geometry

To better assess the changes of bone geometry caused by the mechanical stimulation, the status quo of the mouse bones must first be ascertained. Therefore, first in-vivo μCT measurements are done before the in-vivo loading experiments. The results are shown in Table 5.1 and partially illustrated in Figure 5.3. The evaluated bone parameters show values which are in a similar range in comparison to previous observations [Willie et al., 2013]. While the right tibiae of mice 4, 5 and 6 show higher values in cortical area (Figure 5.3a), cortical thickness (Figure 5.3b) and volume fraction (Figure 5.3c), the difference are very small. From this it can be concluded that there is no influence on these bone parameters due to handedness. In contrast, mouse 1 shows higher values in the left bone with bigger differences to the right bone than its littermates, for example 7% difference in the bone volume fraction (see Figure 5.3c). This may be a hint, that mouse 1 has prefered limb.

The time lapse image registration of the in-vivo μCT measurements provided information about where on the inner endosteal and outer periosteal surface has been formed or resorbed during the two weeks of mechanical stimulation as well as the partial amount. In contrast to former observations on adult mice [Birkhold et al., 2016], Figure 5.4 shows that less bone is formed endosteal than periosteal. Most bone formation occurs posterior and anterior. Little amount of new bone is formed along the medial and lateral axes, but more bone is resorbed.

Table 5.1.: Static morphometric parameters at the endosteal cortical bone surface at day 0 of the loading experiment after [Bouxsein et al., 2010].bone volume (BV), total volume (TV), cortical thickness (Ct.Th), total area (Tt.Ar), cortical area (Ct.Ar , Marrow area (marrow area (Ma.Ar)), periosteal perimeter (Ps.Pm), endosteal perimeter (Ec.Pm) are calculated with CTan (see also chapter 4.1.4).

bone	units	1L	1R	2L	2R	4L	4R	5L	5R	6L	6R
BV	mm^3	1.00	0.97	0.83	0.82	0.68	0.57	0.44	0.46	0.88	0.62
TV	mm^3	1.46	1.54	1.23	1.18	1.09	0.88	0.69	0.69	1.34	0.91
BV/TV		0.68	0.63	0.67	0.69	0.62	0.64	0.65	0.67	0.65	0.68
Ct.Th	mm	0.25	0.24	0.25	0.26	0.23	0.24	0.23	0.24	0.25	0.25
Tt.Ar	mm^2	0.93	0.96	0.99	0.96	0.95	0.99	0.92	0.92	1.00	1.01
Ct.Ar	mm^2	0.63	0.61	0.67	0.66	0.59	0.63	0.59	0.61	0.65	0.69
Ma.Ar	mm^2	0.20	0.24	0.23	0.20	0.26	0.27	0.24	0.22	0.23	0.23
Ps.Pm	µm	10.24	10.30	9.53	9.32	9.04	8.41	7.72	7.72	9.75	8.52
Ec.Pm	µm	6.56	6.46	5.73	5.63	5.21	4.79	3.74	3.72	5.76	4.76

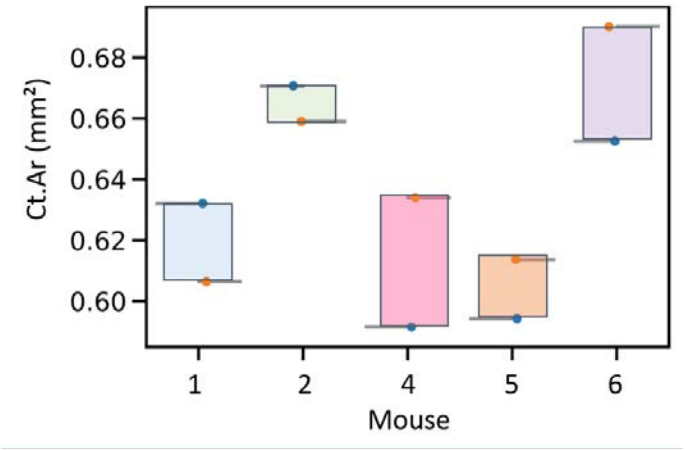

(a)

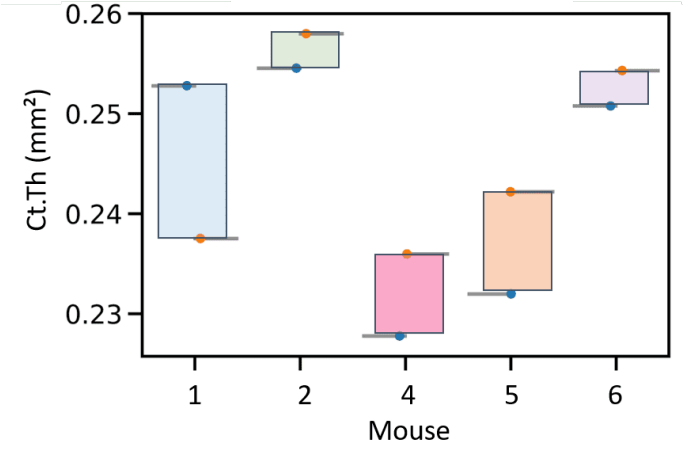

(b)

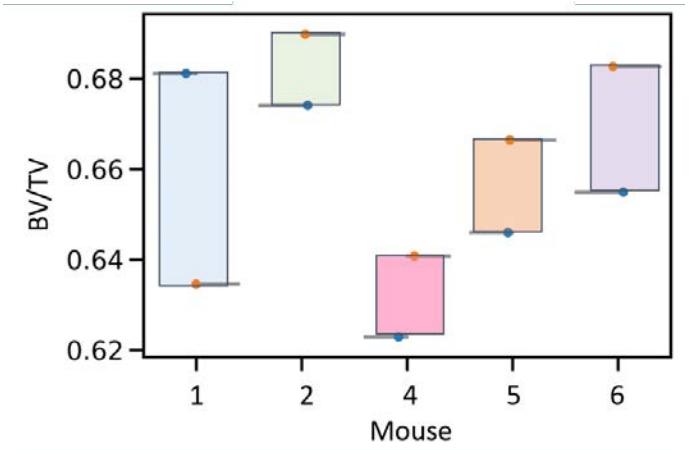

(c)

Figure 5.3.: Visualization of the static bone morphometry parameters. Cortical area, cortical thickness and volume fraction are shown for all six mice of this study. Each mouse is shown not only by its own box defined by the values for left (blue) and right (orange) tibia, but also by its own color.

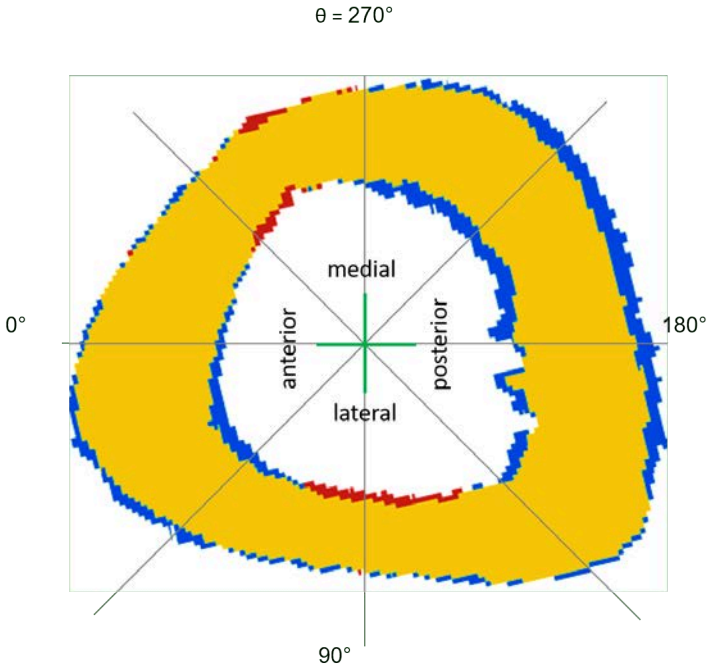

Figure 5.4.: Result of the time lapse image registration showing where bone was formed or resorbed in response to mechanical loading. Newly formed bone is colored blue, resorbed bone red and quiescent bone yellow. The figure is adapted from [Van Tol et al., 2020] with permission from PNAS.

5.4. The lacuno-canalicular-network in healthy and mechanically stimulated bones

In this section, the structural properties of the LCN in the different bone regions will be presented and discussed.

Images of the stained LCN using CLSM are shown in Figure 5.5. All cortices exhibit the same pattern like described before [Kerschnitzki et al., 2011b, Kerschnitzki, 2012]. In the unordered region, the lacunae are more roundish with lower number of connecting canaliculi, which do not show any preferred orientation. In contrast the ordered region shows a network which is aligned parallel to the short axis of the elliptical lacunae and radially with respect to the bone cross section.

The LCN of the newly formed bone can not be characterized due to over-staining of the low mineralized region. The non-loaded (right) cross sections (Figure 5.5b, d, f, h and j) are surrounded only by a thin layer of a red line and have relative even edges. In contrast, the loaded (left) bones (see Figure 5.5 a, c, e, g and i) show broad seams with outstanding intense and diffuse fluorescence signals (red areas) (see Figure 5.6a). These seams correspond to newly formed bone after mechanical stimulation (see also Figure 5.4) which are non-mineralized or not very mineralized yet (see Figure 5.6b). Here, the mineral content (and thus the matrix density) is too low to prevent the ethanol/Rhodamine mixture from penetrating the interfibrillar matrix, resulting in the described blurred diffuse signal. This is in line with other observations in human samples where broad Rhodamine staining patches are found at mineralization defective sites [Roschger, 2015]. That means, there is a threshold value of mineralization (larger than zero) below which the tissue is completely stained and above which Rhodamine can not enter.

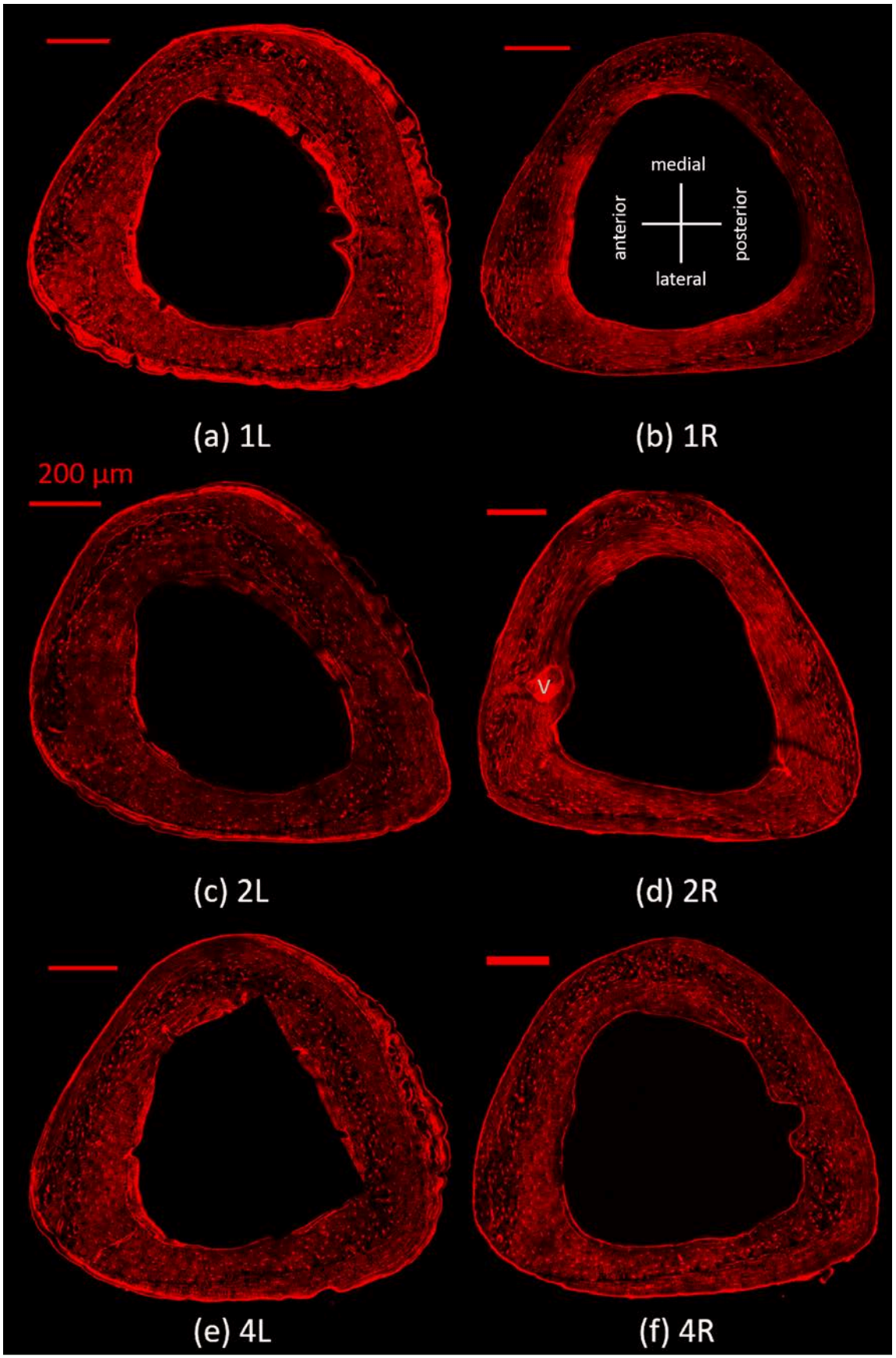
medial
anterior
posterior
lateral
(a) 1L
(b) 1R
200 µm
v
(c) 2L
(d) 2R
(e) 4L
(f) 4R

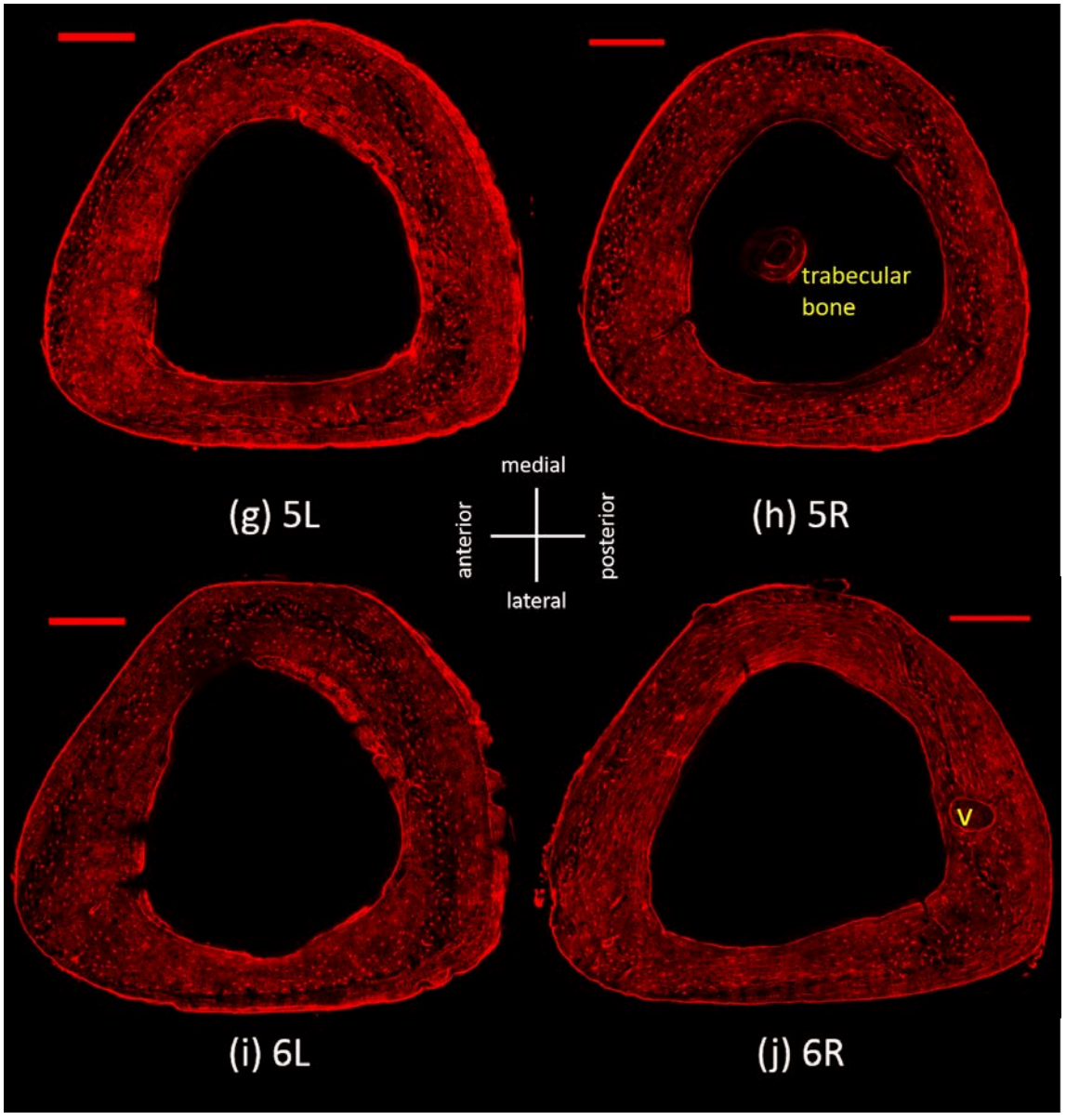

Figure 5.5.: Visualization of the lacuno-canalicular network in cortices of loaded tibiae (a, c, e, g, i) and the non-loaded bones (b, d, f, h, j) of the same mice. The LCN is colored red to mirror its staining with Rhodamine. Osteocyte lacunae and vascular channels appear red or are surrounded by a red line depending on their size. (d) and (j) exhibit a big vascular channel (V). All shown cross sections originate from approximately the same height of the tibia midshaft. The scale bars are equal to 200 μm While the non-loaded bones show a quite even and thin edge line, the loaded bones exhibit a broad red seam at the outer edges, which represents the newly formed bone.

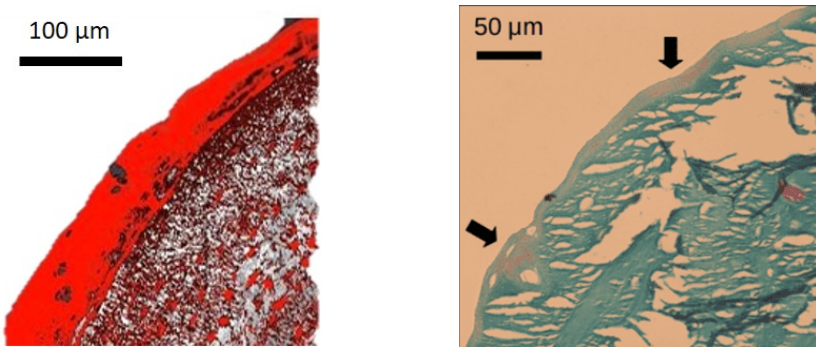

(a) (b)

Figure 5.6.: Rhodamine staining of lowly mineralized bone. (a) Rhodamine 6G stains soft tissue and the lacuno-canalicular network and is shown here in red. The newly formed bone shows a uniformly colored area, where no canaliculi can be identified. (b) Goldner staining shows in the same part of the sample early stages of mineralization as reddish spots inside the greenish matrix as well as a reddish seam at the edge.

The canalicular density (Can.Dn) is determined from the CLSM images to quantitatively describe the LCN in different regions. Figure 5.7 shows the maps of Can.Dn for the whole cross sections of all measured tibiae. The values are distributed between 0.02 and 0.7 $\mu m/\mu m^3$. The highest values can be observed posterior periosteal and anterior endosteal. Comparing these maps with FEM models as shown in Figure 5.8, they are positioned at areas of higher tension or compression. Since the in-vivo loading experiments mimic the normal locomotor strain measured in-vivo [De Souza et al., 2005], these areas have also high load in normal behavior.

The Can.Dn is lower in the right/non-loaded bone $Can.Dn_{right} = 0.34 \pm 0.04\ \mu m/\mu m^3$ compared to the left/loaded bone $Can.Dn_{left} = 0.29 \pm 0.04\ \mu m/\mu m^3$ (see Table 5.2 and Figure 5.9). The higher Can.Dn in the loaded bone could be observed in the ordered bone, but hardly in the unordered regions (see Figure 5.10). Furthermore the unordered regions show significantly lower values of Can.Dn than the ordered regions ($Can.Dn_{ordered} = 0.31 \pm 0.04\ \mu m/\mu m^3 > Can.Dn_{unordered} = 0.19 \pm 0.05$). There, the unordered region is readily identifiable by less canaliculi. Several areas do not even show stained canaliculi at all. The unordered region is known to be rapidly formed while the ordered region uses the very bone as a scaffold for slower but highly organized growth (see chapter 2.2.1 and [Kerschnitzki et al., 2011a]). The surface of the unordered bone may guides the cells in bone formation. This organization then in turn also serves as a template for the osteocyte network. Hence, the newer bone has a denser and better organized network.

Table 5.2.: Quantitative comparison of canalicular density of different bone regions.

bone region	$Can.Dn_{mean}$ $(\mu m/\mu m^3)$	$Can.Dn_{median}$ $(\mu m/\mu m^3)$	$Can.Dn_{FHMW}$ $(\mu m/\mu m^3)$
ordered bone	0.29 ± 0.02	0.31 ± 0.04	0.25 ± 0.04
unordered bone	0.20 ± 0.03	0.19 ± 0.05	0.26 ± 0.05
whole bone	0.25 ± 0.02	0.25 ± 0.02	0.28 ± 0.03
left bone	0.27 ± 0.01	0.29 ± 0.04	
right bone	0.24 ± 0.01	0.34 ± 0.04	

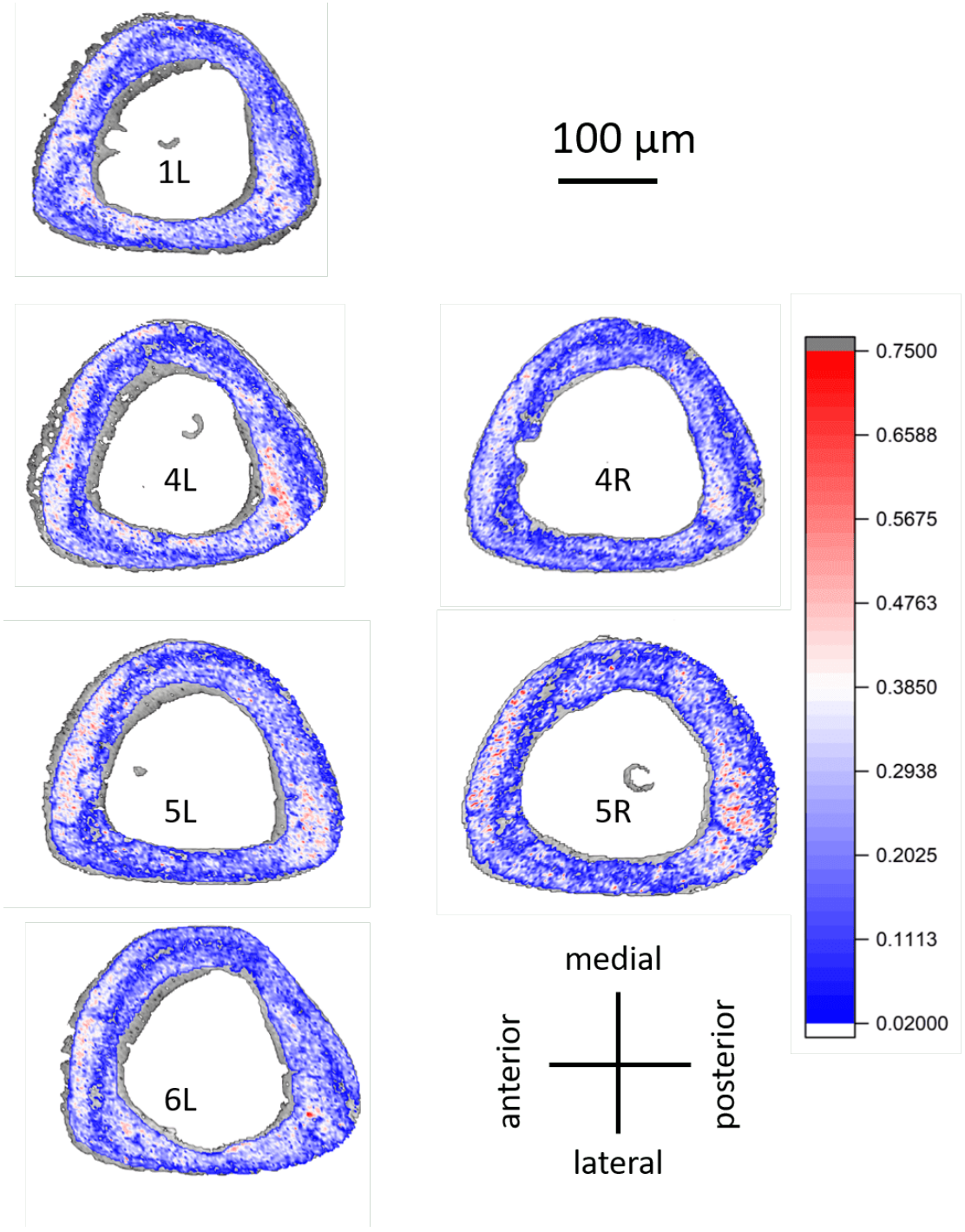

Figure 5.7.: Visualization of the canalicular density (Can.Dn) of the lacuno-canalicular network in cortices of loaded tibiae (left) and the non-loaded bones (right) of the same mice. Can.Dn is calculated by the software tool for interactive network analysis (TINA). The scale is chosen to seperate lower and higher densities splitted by a Can.Dn = $0.38\,{}^{\mu m}/_{\mu m^3}$. The calculation of 2L is not shown because of the strong deformation of the CLSM image and therefore missleading data. The CLSM image of 1R, 2R and 6R show a lot of microcracks. Because of that, their Can.Dn are not shown. Mostly, the higher Can.Dn can be observed posterior close to the periosteal and anterior close to the endosteal surface. The bones of mouse 3 show larger defects after transport and have broken apart. Hence, these bones are not part of this study.

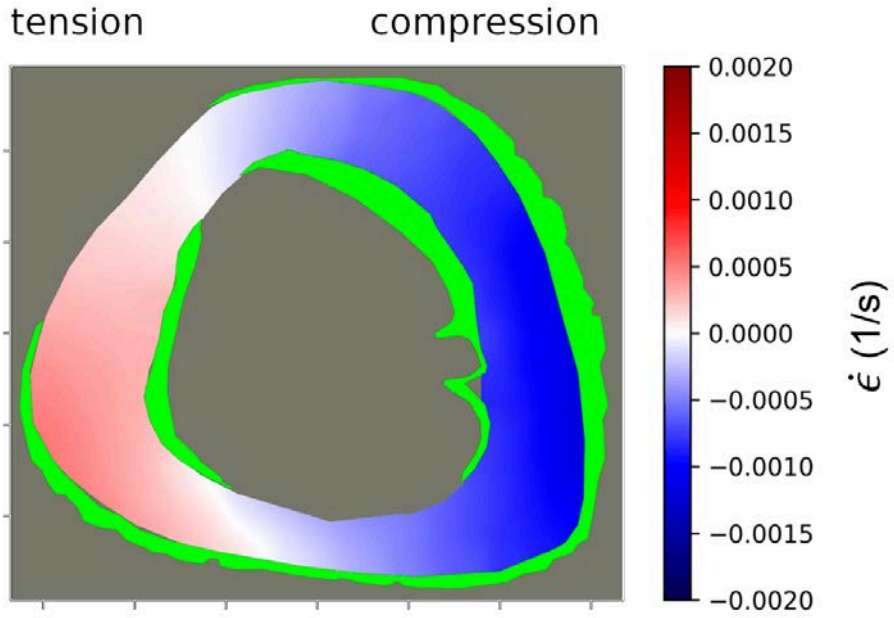

Figure 5.8.: Spatial distribution of the strain induced by the in-vivo loading experiment calculated using FE modeling. The spatial tensile (red) and compressive (blue) strain magnitude and distribution within the bones are calculated by finite element modeling (FEM) [Razi et al., 2015] with Data from day 0. The green area shows the new formed bone after two weeks of mechanical loading.

The differences in the Can.Dn between left and right bones (see Figure 5.9) could be an effect of different loading because of (i) handedness or (ii) the additional in-vivo loading. The denser network in the left bones could be caused by

1. increasing canaliculi because of osteocytic osteolysis in diameter, leading to stained canaliculi, which would have been hardly accessible to Rhodamine before,
2. secondary network structures in the bone, that can be activated if necessary,
3. really newly formed canaliculi because of the mechanical stimulation or
4. more canaliculi because of higher loads of the more used limb.

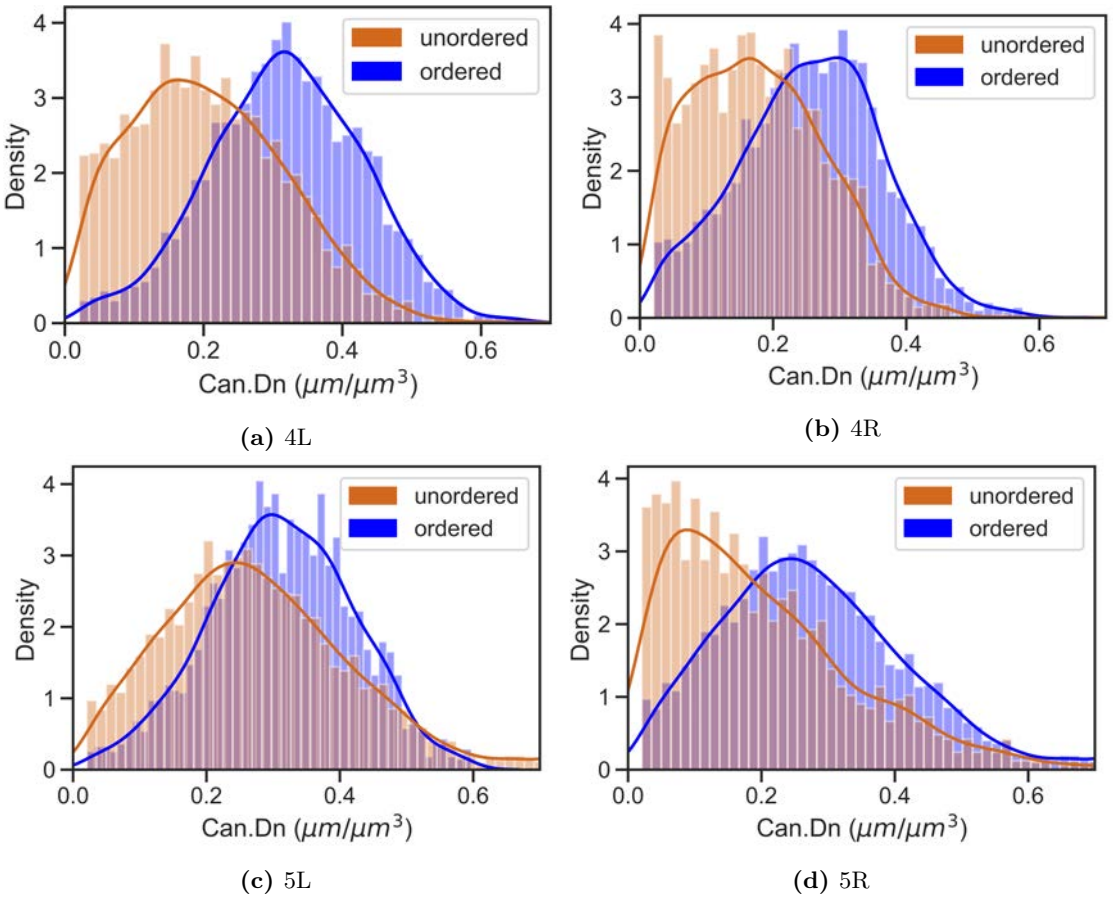

(a) 4L **(b)** 4R

(c) 5L **(d)** 5R

Figure 5.9.: Exemplary histograms of the Can.Dn in tibia cross sections. For a more quantitative comparison than in Figure 5.7 the frequency of all Can.Dn is counted and plotted as histograms for the bones of mouse 4 (a and b) and mouse 5 (c and d). In all cross sections, the unordered region (orange bars) shows lower Can.Dn than the ordered region (blue).

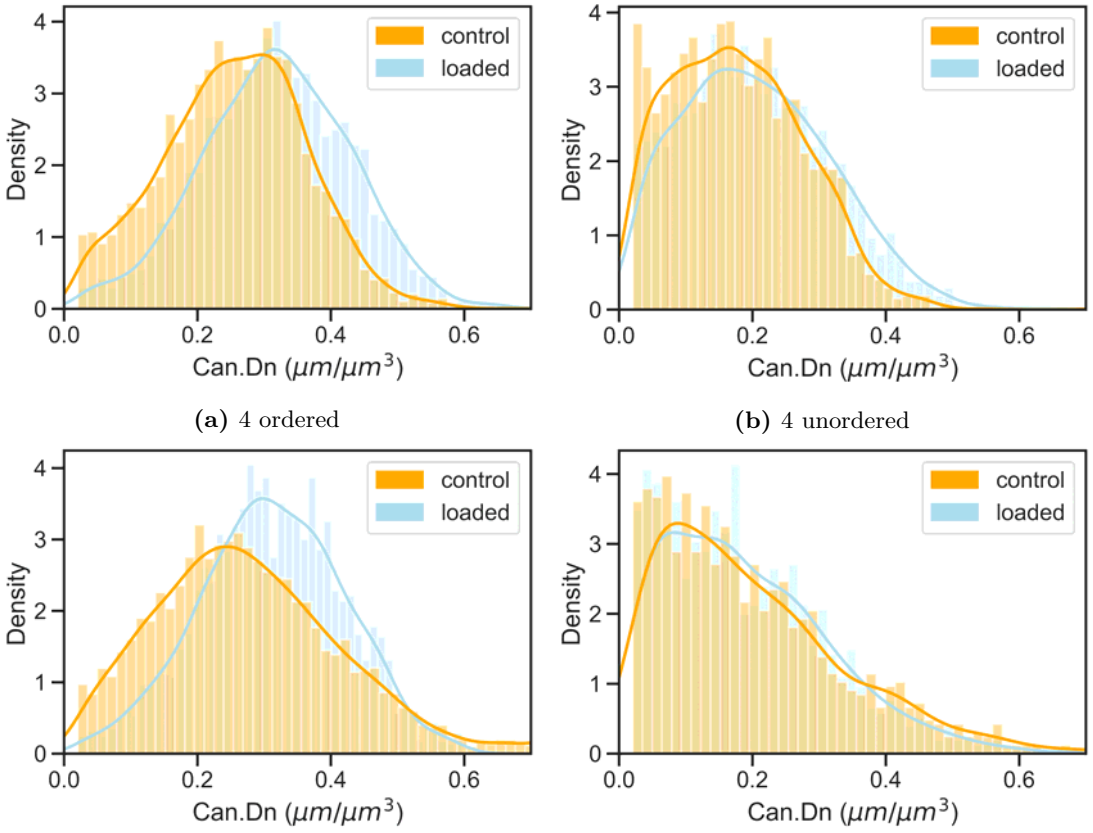

(a) 4 ordered

(b) 4 unordered

(c) 5 ordered

(d) 5 unordered

Figure 5.10.: Comparison of the Can.Dn of left and right bones in the different regions. The Can.Dn shows a similar behavior in both mice (4 and 5). The left/loaded bone (blue) shows higher Can.Dn in the ordered region than the right/non-loaded bone (a and c). The unordered regions show hardly any differences (b and d). In conclusion, the Can.Dn is slightly higher in the left/loaded bone than in the right/non-loaded bone (comparison of the whole bone).

5.5. Mineral and matrix properties in healthy and mechanically stimulated bones

The Calcium content in healthy and mechanically stimulated bones

The different regions of murine cortical bone can be identified in quantitative backscattered electron imaging (qBEI) images. Figure 5.11b shows a cross-section of the right tibia and and Figure 5.11a from the left tibia, which has experienced two weeks of loading. The grey value distribution in the right bone seems quite even. There is a darker band surrounded by lighter bands endosteal and periosteal. This observation fits to what other studies have observed [Shipov et al., 2013, Bach-Gansmo et al., 2013]. Furthermore, the inner band shows some very bright spots, which might be cartilage islands with high calcium content like they are observed by Bach-Gansmo et al. [Bach-Gansmo et al., 2013]. The right bone shows also a quite even surface, endosteal as well as periosteal, while the periosteal surface of the left bone seems more jagged - especially in medial and posterior direction. Here, a seam of low Calcium content can be observed. It is the newly formed bone. That this area of young bone has a low calcium content goes together with the observation of increasing calcium content with age [Roschger et al., 2001, Grabner et al., 2001].

There are no significant differences in the bone mineralization density distribution (BMDD) of right and left bones (see Figure 5.11c), when the newly formed bone is taken into account. The newly formed bone is young bone leading to a Gauss distribution of lower calcium content. Together with the distribution of the old left bone (blue line), this results in the broader, green curve for the whole bone.

Comparing the BMDD of ordered and unordered bone, there is also no statistical difference observable (Figure 5.12a). The difference between the observation in the maps and the quantitave analyzation could be explained by the stronger contrast of the black background, respectively the bright seam, to the ordered region than in the inner region. Another explanation might be, highly mineralized cartilage islands in the woven band [Bach-Gansmo et al., 2013] with a surrounding blending in to the rest of the band. Nonetheless, it remains to be said that the BMDD is very stable as long as bone of the same tissue age is compared.

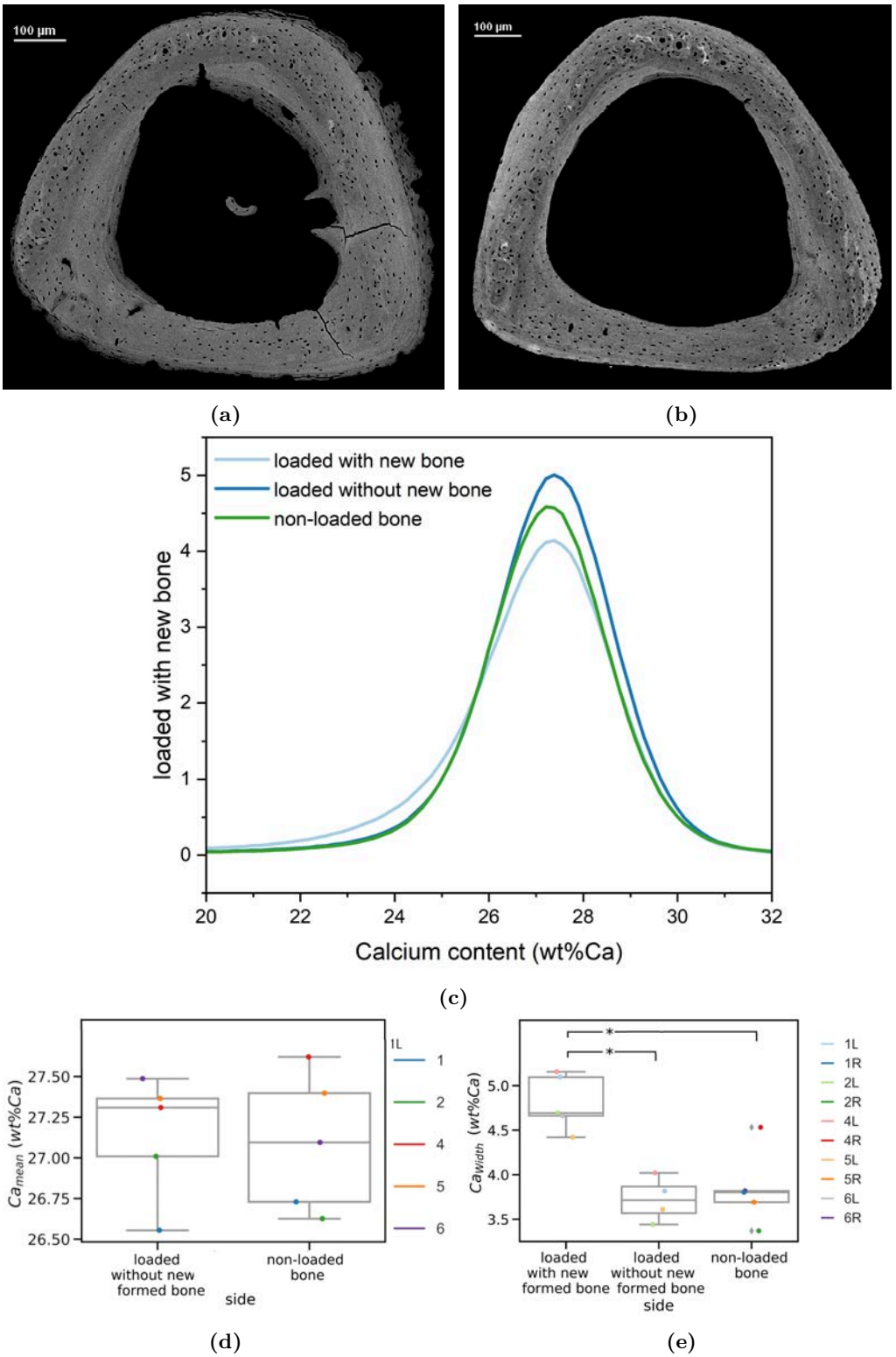

Figure 5.11.: Quantitative backscattered electron imaging (qBEI) of loaded and non-loaded bone. (a) Representative cross section of a cortex in the mid-shaft of a loaded sample imaged with SEM in BE-mode (single images were merged to one image). Each grey level represents a corresponding mineral content. The newly formed bone shows a lower grey value, which goes along with lower calcium content. (b) Representative cross section of a cortex in the mid-shaft of a loaded sample imaged with SEM in BE-mode (single images were merged to one image). Additional maps can be found in the appendix in Figure B.4. (c) The lines show the average of the bone mineralization density distributions (BMDD) of the cortical left bones with newly formed bone (light blue), without newly formed bone (blue) and the right bones (green). Asterisks indicate a significant difference between the linked groups ($p < 0.05$).

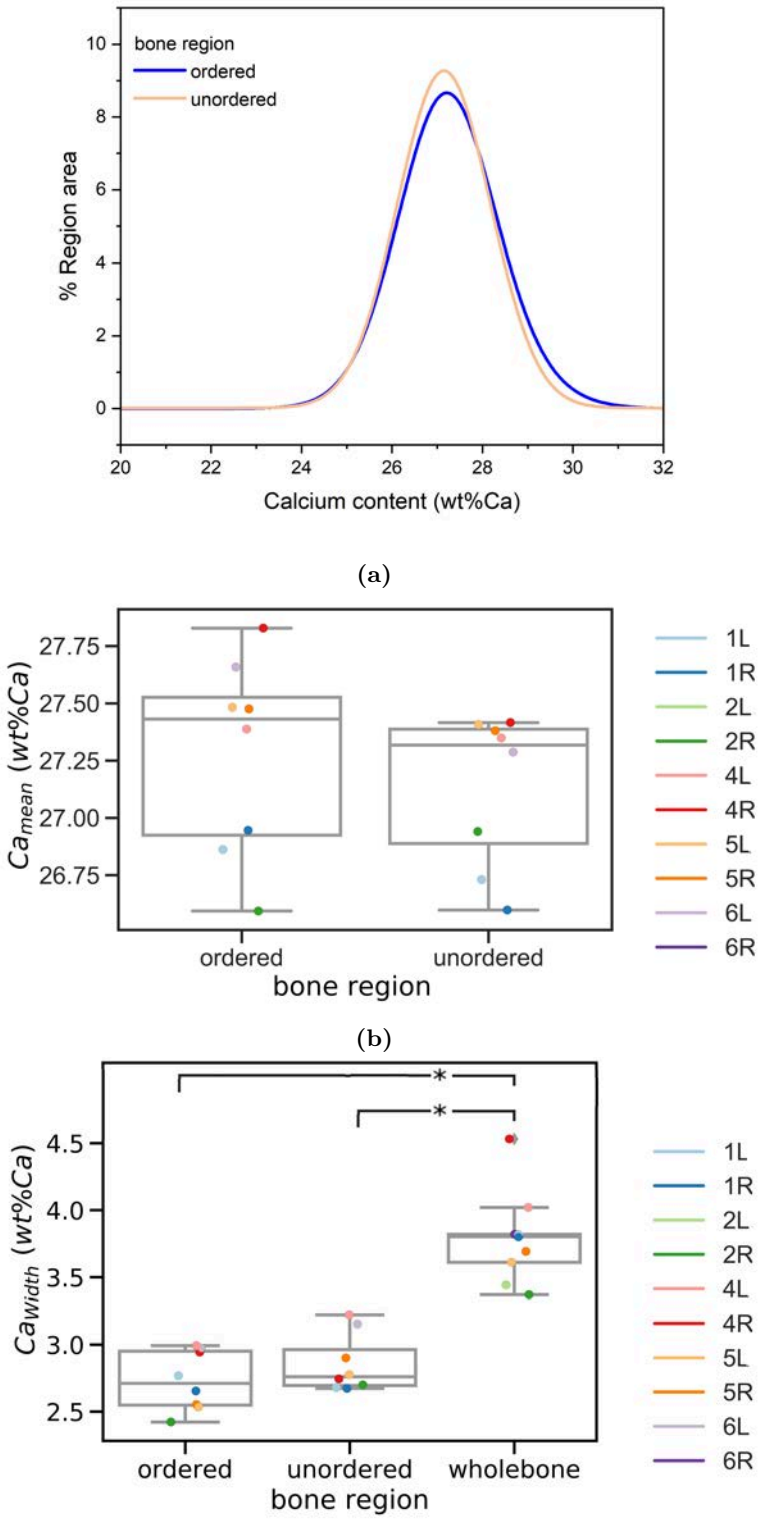

Figure 5.12.: Quantitative backscattered electron imaging (qBEI) of ordered and unordered bone regions. (a) The lines show the average of the bone mineralization density distributions (BMDD) of the ordered bone region (blue) and the unordered region (orange). Asterisks indicate a significant difference between the linked groups ($p < 0.05$).

Table 5.3.: Quantitative comparison of mineral parameters in loaded and non-loaded cortices. Both, L parameter and T parameter values of the ordered and unordered bone regions show significant differences.

bone region	T_{mean} (nm)	T_{median} (nm)	T_{FHMW} (nm)	L_{mean} (nm)	L_{median} (nm)	L_{FHMW} (nm)
ordered bone	2.68 ± 0.60	2.70 ± 0.08	0.8 ± 0.1	20.0 ± 1.0	21.0 ± 1.0	5.0 ± 1.0
unordered bone	2.40 ± 0.10	2.40 ± 0.10	1.0 ± 0.2	19.0 ± 1.0	20.0 ± 1.0	5.7 ± 0.8
whole bone	2.63 ± 0.06	2.63 ± 0.08	1.0 ± 0.1	20.2 ± 0.8	20.0 ± 1.0	6.2 ± 0.8

Mineral parameter properties in healthy and mechanically stimulated bones

High resolution scanning synchrotron SAXS and WAXS are used to determine the nanostructural patterns of mineral particle properties in the murine cortices. Figure 5.13 a and b show exemplary maps of the T parameter distribution in the tibia cross sections. Due to the difficult sample preparation and limited beam time, not all of the cross sections could be measured with SAXS and WAXS. In fact, only two almost full cross sections are measured, for the rest of samples only parts could be used, i.e. 1L and 2R stand exemplary for left and right bones, respectively (all maps are shown in B.5, B.6, B.7 and B.8). Both cross sections show a (blue) band of low T parameter which coincides more or less with the area of the unordered bone. The quantitative evaluations in Figure 5.13c and d, Figure 5.14a and b as well as Table 5.3 mirror this observation and show that the median of the T parameter is significantly lower in the unordered region ($T_{\text{median, unordered}} = (2.4 \pm 0.1)\,\text{nm}$) compared to the ordered region ($T_{\text{median, ordered}} = (2.70 \pm 0.08)\,\text{nm}$). The values of the L parameter show a similar behavior ($L_{\text{median, unordered}} = (19 \pm 1)\,\text{nm} < L_{\text{median, ordered}} = (20 \pm 1)\,\text{nm}$), but with a lower difference.

Lower T and L parameter in the central, unordered bone compared to the outer, ordered bone regions have also been observed in rat bones by [Turunen et al., 2016]. With increasing age of the bones during bone development, both thickness and length of the mineral particles are increasing. As bone ages during bone development and remodeling, both the thickness and length of the mineral particles increase [Lange et al., 2011]. In the current study, the plate like mineral particles reach T parameter values up to 3.5 nm and L parameter values close to 25 nm in mature bone. In general, length and thickness are correlated, i.e. the longer minerals are, the thicker they are. That means, the mineral particles are thin and short in the unordered bone region, which is a remnant bone from rapid enchondral ossification. As a result of the slower and more ordered bone growth and maturation, the minerals in the periosteal and endosteal areas are thicker and longer.

The edges of (old) bone show lines of lower T parameter in comparison to the inner region. This leads to a clear border between old and new bone in the left, loaded bones. The lines may be comparable to cement lines in human osteons seperating them from interstitial bone. The reason for the characteristic difference to the surrounding bone can not be answered with the used methods. It probably plays a role, however, that this layer of bone was built up last and that it is the boundary layer to the outside. Lining cells, osteopontin or interactions with the environment of the bone could be named as the cause of the thin mineral particles. In contrast, in the resorption areas the edge appears blurred (see the dotted ellipses in Figure 5.13a).

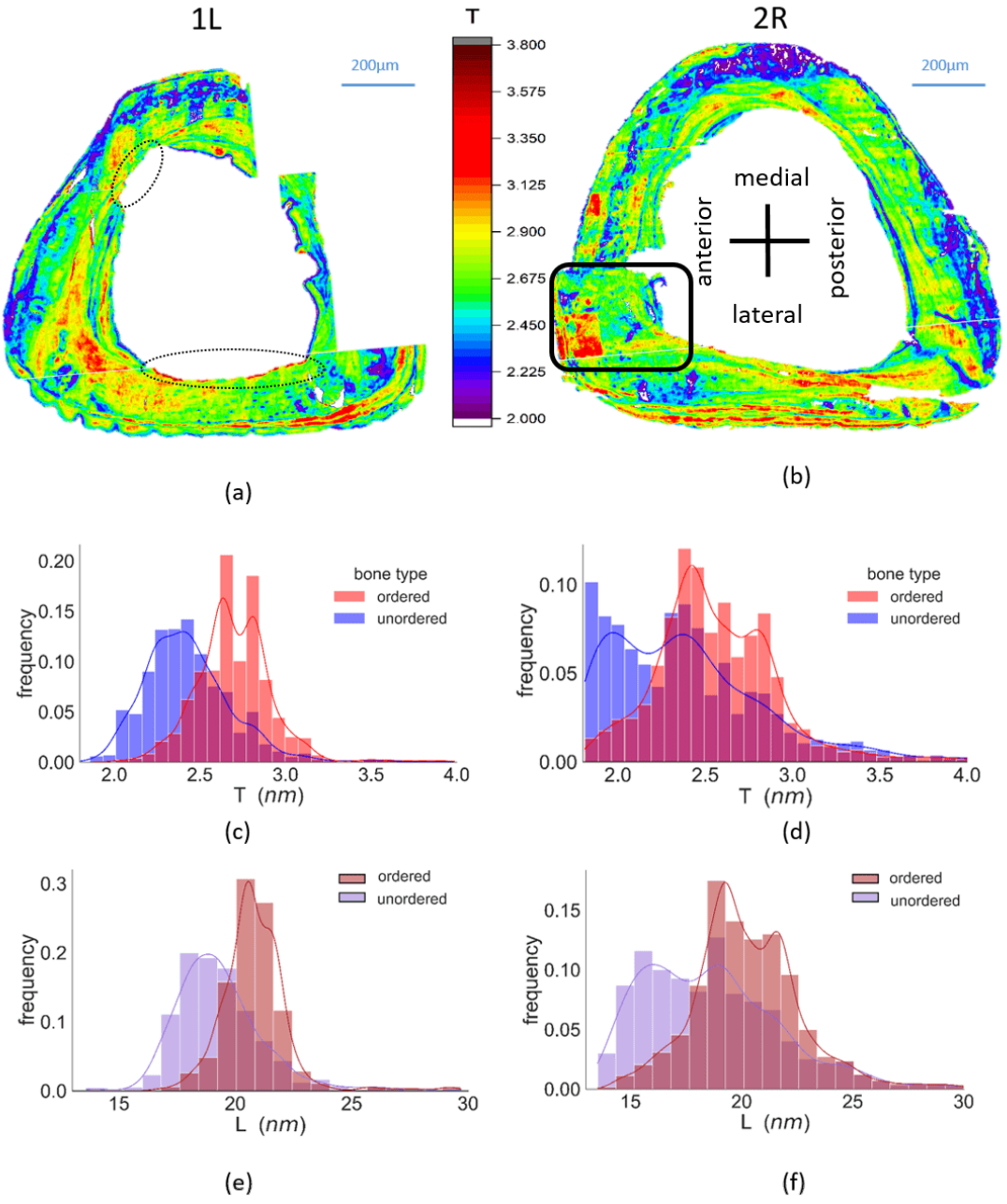

Figure 5.13.: Comparison of mineral parameter properties of a loaded and non-loaded bone. (a) and (b) show maps of the T parameter in the respective cross sections. The dotted ellipses indicate regions of bone resorption. The black rectangle shows a region with a fold in the sample. Below the T (c, d) and L parameter (e, f) of the ordered (pinkish) and unordered (blueish) region are compared quantitatively. The lines smooth the observed data with a Gaussian kernel and produce a continuous density estimate, instead of using discrete bins. Both, T and L parameter show lower values for the unordered region than for the ordered region.

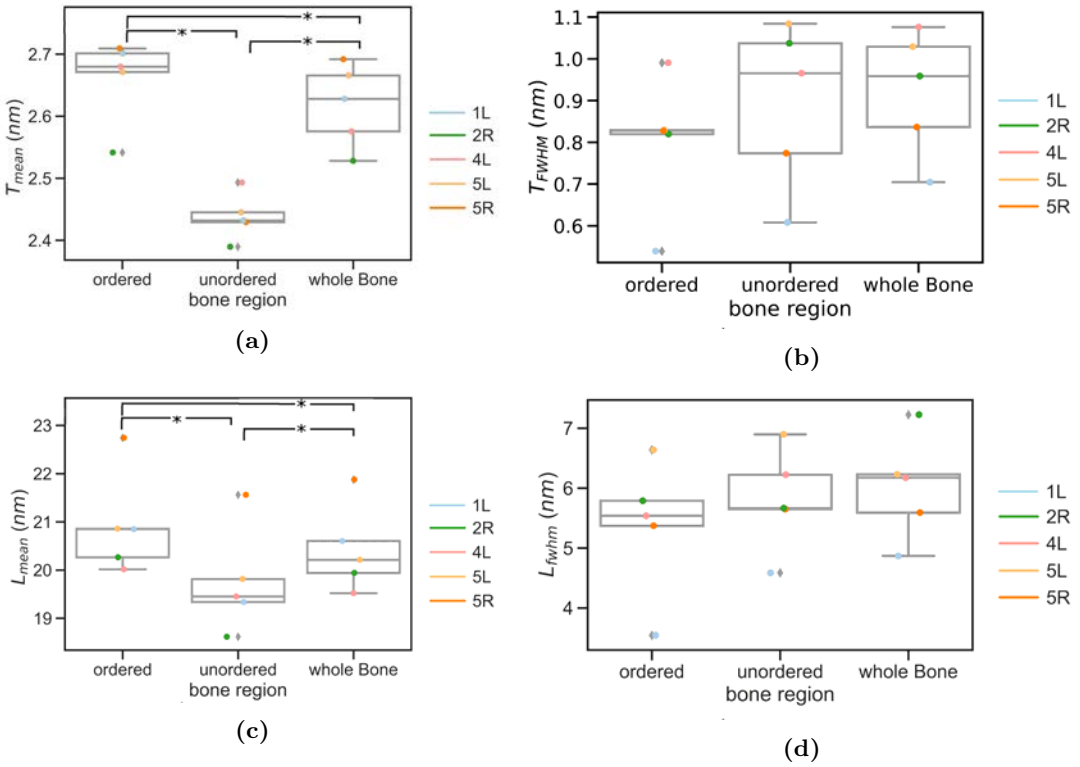

Figure 5.14.: Quantitative comparison of L and T parameter in ordered and unordered bone region. Both, L and T parameter show lower values (a, c) but broader distribution (b, d) in the unordered region than in the ordered one. Both, T and L parameter show significant differences (indicate with asterisks). Note: Differences between unordered and ordered regions were assessed using a paired T-test, p value less than 0.05 was considered significant.

All samples show also double (red) lines of high T parameters at the lateral side (at the edge of old bone) as it can be seen in Figure 5.15b. These special features could be caused by the special mechanical needs on this side [Statnik et al., 2020]. Comparing to Figure 5.8 as well as [Razi et al., 2015, Main et al., 2020] the bending pattern is changing from compression on one side and tension on the other side due to bone curvature. Former studies have also observed bigger particle sizes in the cranial cortex of horses and explained this by lower remodeling of the bone in this area and therefore higher maturity of the minerals [Fratzl et al., 1996a].

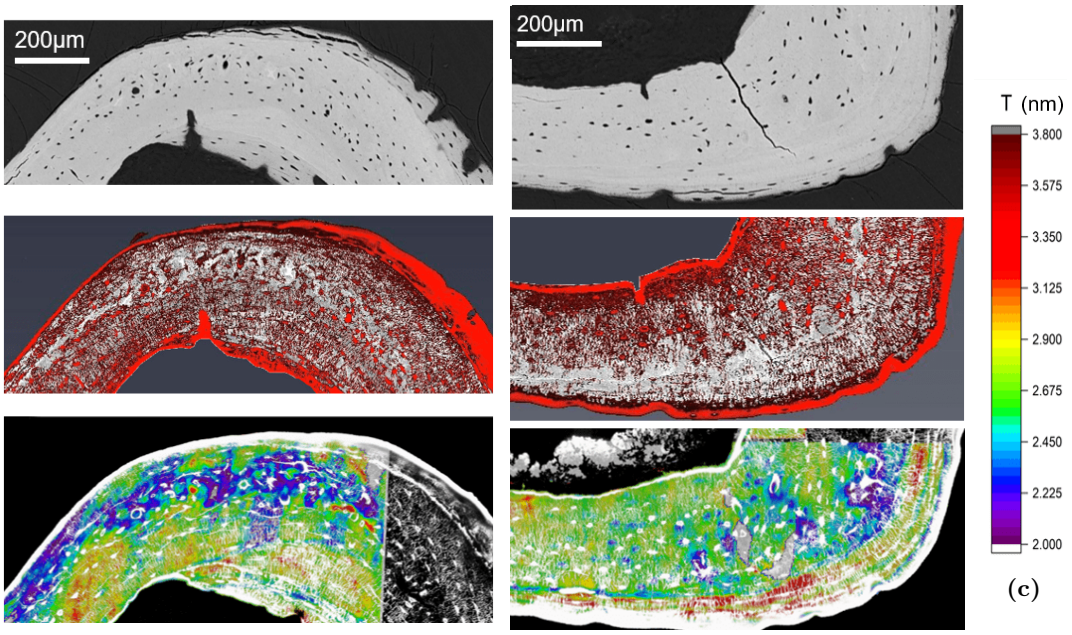

Figure 5.15.: Comparison of calcium content (top image), LCN (middle image), and T parameter (lowest image) of (a) medial and (b) lateral bone region. The medial side (a) shows several features, including ordered and unordered bone region, newly formed bone (endosteal and periosteal) and also a region of resorption on the left endosteal corner. The lateral side (b) exhibits red double lines in the T parameter (lowest image), which are also mirrored in the other maps.

5.6. Relationship between mineral properties and topology of the lacuno-canalicular network

Most of the properties described in the last chapters are linked to one another. In order to compare the different bone properties with each other, it is important that all parameters use the same coordinations. For this purpose, the resulting maps of all measurements have been superimposed to each other (see chapter 4.6) and are evaluated with a resolution of 8 µm, if not mentioned differently. Regions like the fold in Figure 5.13b are taken out of the evaluation.

The unordered bone region is known as quickly grown bone, where the collagen bundles do not show long range orientation but are rather interwoven [Weiner and Wagner, 1998]. As mentioned before, the region is easy to identify in the CLSM image because of its lack of organization compared to the ordered region with a well aligned network (see for example Figure 5.15a). There is also a reduced number of canaliculi and lower values of the T parameter compared to the environment (blue and violet pixels compared to yellow and red ones in the ordered region). That is, because the unordered region serves as a scaffold for the later bone formation [Kerschnitzki et al., 2011a]. At the same time, the distribution of the cell processes is based on the topographical information of the surrounding matrix [Dunn and Heath, 1976] and guides again the orientation of later deposited extracellular matrix fibers [Wang et al., 2003, Lamers et al., 2010]. This consistent feedback between cells and their environment leads to better coordinated structures [Kollmannsberger et al., 2017].

Cartilage islands in the unordered region are shown as areas without stained canaliculi and high grey values in qBEI images. In contrast to the observations of [Turunen et al., 2016] in rats, no general trend of the L and T parameter at the cartilage islands could be identified.

The newly formed bone in the loaded bone has a lower calcium content, but T (and L) parameter values are similar to the average values in the ordered regions. This means, the new bone formation occurs without a phase of woven bone [Checa et al., 2015], probably because of a regulation of the homeostasis by the osteocytes and their network [Krempien et al., 1976, Blaber et al., 2013]. While most of the LCN is over-stained in the newly formed bone after Rhodamine staining, because of low mineralization, there are some canaliculi connecting old and new bone. However, former investigations have observed a dense network [do Aido, 2015]). Therefore, it could be assumed as efficient for transporting ions and other substances, which again could be responsible for the fact that the newly formed tissue has a similar quality to the normally formed tissue, even if it was formed faster.

The red double lines of the T parameter (see Figure 5.13 and 5.15b), can be observed by changing grey values, i.e. changing calcium content at the same area in the qBEI images. The region is characterized by an ordered network. Additionally, the areas exhibit high Can.Dn (see Figure 5.7), increasing high flow velocity [Van Tol et al., 2020] and changing bending pattern from compression to tension (see Figure 5.8 and [Main et al., 2020]). As mentioned in chapter 5.6, load-induced fluid flow has been proposed to provide the mechanism for mechano-sensing [Klein-Nulend et al., 1995]. This may explain the increased remodeling activity and bone adaptations not only the new bone formation in this area but also growth of the mineral crystals [Turunen et al., 2016].

To evaluate the correlation of the calcium content and the canaliculi density, Roschger et al. have introduced the so-called SLOPE, which is equal a parameter equal to the slope of the linear regression of a calcium content vs Can.Dn plot [Roschger et al., 2019] (see also chapter 4.7). Exemplary plots of a left and a right bone of the same mouse can be seen in Figure 5.16 (the other diagrams can be found in Figure B.9 and B.10). In contrast to the former observations in human osteonal bone, the observed values of the SLOPE are rather small and in the unordered region slightly negative, but definitely higher than the theoretical estimation due to the porosity of the LCN and the estimated reduction of the calcium content [Roschger et al., 2019].

In the ordered region the SLOPE changes to higher, positive values. Additionally, mice 4 and 5 show lower SLOPES in the right than in the left limbs($\text{SLOPE}_{\text{ordered, loaded}}$= $0.74\,wt\%Ca/(\mu m/\mu m^3)$, $\text{SLOPE}_{\text{ordered, non-loaded}}$=$0.74\,wt\%Ca/(\mu m/\mu m^3)$). That indicates, that in loaded tibiae more mineral is put into interim storage in the LCN of the ordered region. Here, more bones have to be evaluated to explain the reasons. Positive SLOPEs could be caused by an improved transport due to the denser network and better access to the mineral reservoir [Roschger et al., 2019]. Another possibility is that the porosity of the LCN is compensated by the locally increased calcium content [Roschger et al., 2019]. In summary, the networks are not only structurally different (arranged / disordered) but may also function differently.

Reznikov et al. observed that canaliculi in humans are mainly localized in narrow regions of loose, disordered collagen packs [Reznikov et al., 2014a, Reznikov et al., 2014b]. Such a disordered arrangement of collagen fibrils could explain local hypermineralization. This fits with the hypothesis that regions around canaliculi (zone of influence) may have stored more or less minerals. This finding of a systemic storage of calcium in relation to the LCN thus complements the work of Hesse et al. who used a high-resolution method

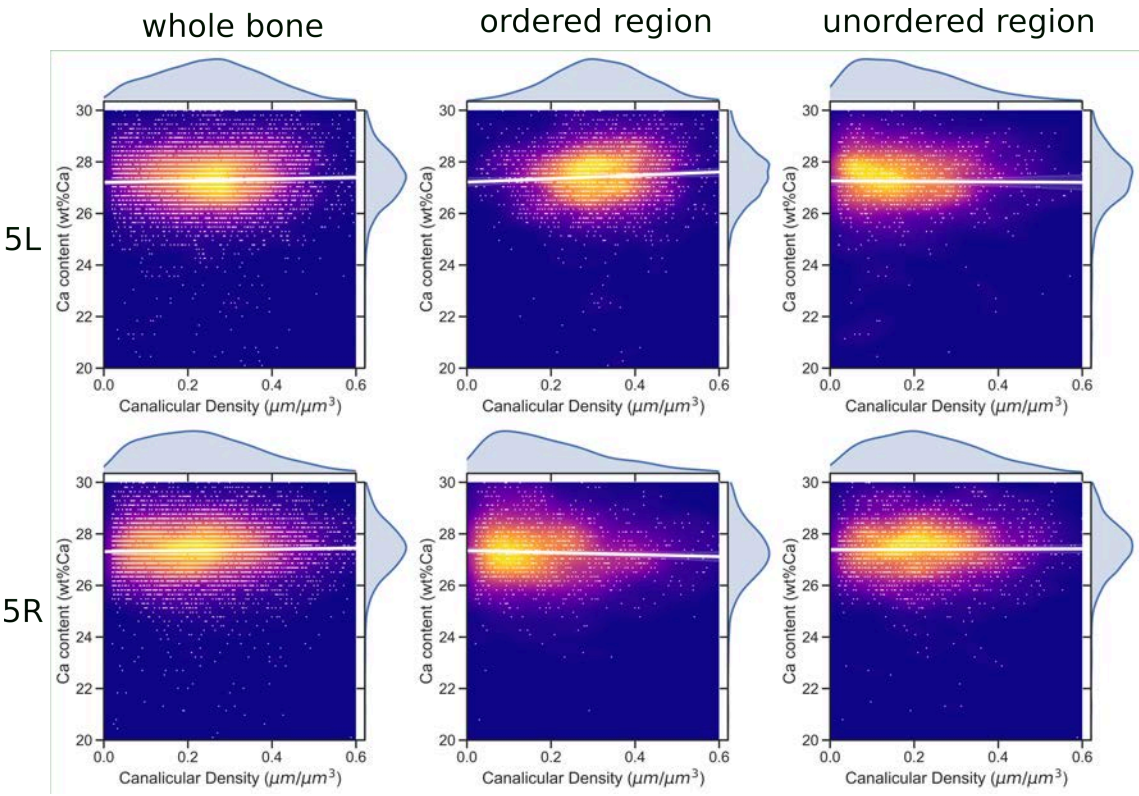

Figure 5.16.: Evaluation of the correlation between canalicular density and calcium content within the cortices of one mouse. Each data point corresponds to a CSLM and qBEI measurement on the same subvolume of edge size 7.37 µm, where the subvolumes cover the whole cross-sectional area of the cortex (left), regions of ordered network (middle) and unordered network (right) (see Fig. 5.2). The white lines display linear regression of the data.

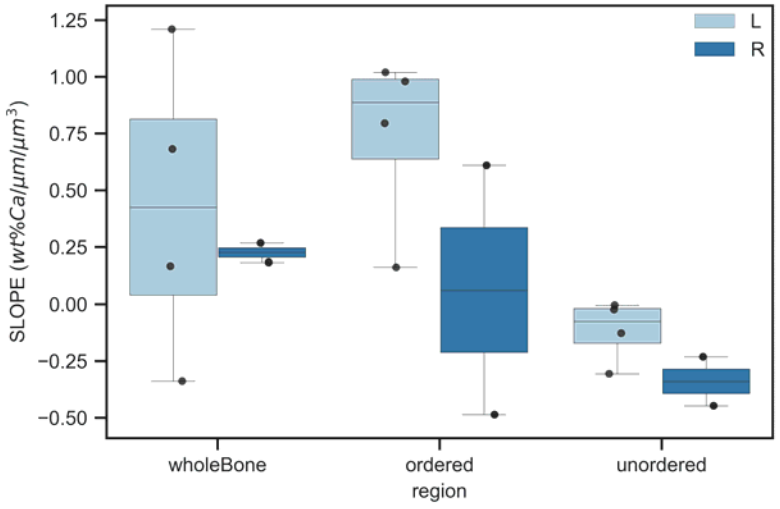

Figure 5.17.: Boxplots of the SLOPES (wt%Ca/µm/µm^3) for the different bone regions. The line corresponds to the median, while the boxes show the range between 25% to 75% percentile and the whiskers the whole data range) of the SLOPES for the different bone regions (whole cortex, regions of ordered network and unordered network). The data are based on the evaluation of four left and two right cortices following the evaluation procedure shown in 5.16.

to image the immediate vicinity of the canaliculi in the osteonal and interstitial bones [Hesse et al., 2015]. They found a spatial dependence of the mineral content on the distance to the canaliculus with the highest mineral content in the vicinity of the canaliculus. By combining these two studies, which characterize mineral heterogeneities in bone on two different length scales, and the measured results of this work, suggest that the proximity of the canaliculi could be used by the osteocytes as an easily accessible mineral source. Osteocytes would then change the pericanalicular matrix by depositing or resorbing mineral, depending on the homeostatic mineral requirement, and the additional calcium loading of the network could be interpreted as the filling amount of a mineral reservoir. The results obtained seem to be characteristic of the individual systemic conditions of the organism.

The comparison of Can.Dn vs. calcium content has shown interesting results. Therefore, one of the objectives of this work was to look for correlations of other parameters. Because of very individual behavior of the different bone properties from mouse to mouse and different amounts of measured samples and points, density plots comparing the measured parameters are difficult to compare directly. Instead, the median values of each measured parameter of the individuals are compared with Pearson´s correlation coefficient (see Figure 5.18). The range of correlation coefficients is -1 to 1. If the absolute value is exactly 1, the linear equation describes the relationship between X and Y perfectly, meaning that all data points are on a single line. The correlation sign is determined by the regression gradient. A value of +1 means that all data points are on the line where Y increases with increasing X, and vice versa for 1. A value of 0 means that there are no linear dependencies between the variables.

Several studies have shown already, that the organization of the osteocyte network reflects the matrix organization and, to some extent, even the mineral properties in the submicron range [Kerschnitzki, 2012, Roschger et al., 2020, Turunen et al., 2016]. Figure 5.18 shows even more, that the bone properties of different hierarchical levels correlate quite strongly. The correlation of Can.Dn and L parameter is particularly noticeable, meaning the higher the median of Can.Dn is, the lower is the expected L parameter. Though hardly any differences in the BMDD of the different bone regions are observable, Ca_{median} is correlated with the morphological bone parameters (Figure 5.18b). Since the periosteal perimeter and the bone volume might have a strong relation to the stiffness of the bone itself, it is not very surprising, that these values also show high interactions to the different parameters. Taken these results into account, it should be possible in the future to predict bone properties based on small numbers of simple measurements.

Although the overarching goal of this work is to better understand the processes in the bone, it is only possible to observe the coincidence of different properties and whether these show a dependency or correlation with one another. A phenomenon that has been observed several times gives reason to assume that there could be a connection between these events. However, the temporal and spatial coincidence of two events does not establish a causal relationship. Whether there is a connection between the two, and if so, which of the two events is the cause and which is the effect, or whether events are jointly the result of a third event, cannot be deduced from this. Finally, correlation alone cannot be used as evidence of a cause-and-effect relationship between a treatment and benefit. To draw more detailed conclusions on specific mechanisms in bone, further studies and analyzes beyond correlations must be performed. Nevertheless, assumptions can be made and existing hypotheses can be confirmed.

	Ca un-ordered	Ca whole-bone	Can. Dn ordered	Can. Dn un-ordered	Can. Dn whole-bone	T ordered	T un-ordered	T whole-bone	L ordered	L un-ordered	L whole-bone
Ca-median-ordered	0.81	0.98	-0.67	-0.72	-0.75	0.82	0.67	0.69	0.61	0.34	0.64
Ca-median-unordered		0.90	-0.23	-0.36	-0.32	0.51	0.51	0.24	0.30	0.31	0.29
Ca-median-whole-bone			-0.52	-0.59	-0.60	0.78	0.63	0.57	0.51	0.30	0.55
Can.Dn-median-ordered				0.66	0.97	-0.28	-0.46	-0.86	-0.98	-0.98	-0.98
Can.Dn-median-unordered					0.83	-0.52	-0.86	0.61	-0.74	-0.65	-0.56
Can.Dn-median-whole-bone						-0.43	0.98	0.51	-0.98	-0.96	-0.91
T-median-ordered							0.54	0.78	0.49	0.01	0.68
T-median-unordered								0.73	0.90	0.82	0.92
T-median-whole-bone									0.87	0.44	0.93
L-median-ordered										0.82	0.95
L-median-unordered											0.67
L-median-whole-bone											

-1 0 1

(a)

	BV	BS/BV	Ct.Th	TV	BV/TV	Tt. Ar	Ct. Ar.	Ma. Ar.	Ps.Pm
Ca-median-ordered	-0.78	0.96	-0.81	-0.73	-0.75	0.20	-0.57	0.84	-0.72
Ca-median-unordered	-0.83	0.88	-0.91	-0.76	-0.87	0.13	-0.73	0.84	-0.75
Ca-median-whole-bone	-0.80	0.97	-0.89	-0.74	-0.84	0.18	-0.67	0.89	-0.72
Can.Dn-median-ordered	0.45	-0.35	-0.12	0.48	-0.12	-0.45	-0.55	-0.16	0.47
Can.Dn-median-unordered	0.82	-0.67	0.13	0.87	-0.06	0.01	-0.06	-0.13	0.87
Can.Dn-median-whole-bone	0.63	-0.50	-0.03	0.67	-0.09	-0.32	-0.40	-0.17	0.66
T-median-ordered	-0.38	0.73	-0.70	-0.32	-0.62	-0.69	-0.84	0.62	-0.31
T-median-unordered	-0.56	0.47	-0.30	-0.56	-0.20	-0.50	-0.38	0.22	-0.56
T-median-whole-bone	-0.44	0.53	-0.27	-0.46	-0.10	-0.94	-0.46	0.12	-0.46
L-median-ordered	-0.58	0.43	-0.11	-0.62	0.06	-0.76	-0.25	-0.02	-0.62
L-median-unordered	-0.57	0.20	0.07	-0.62	0.18	-0.29	0.05	-0.15	-0.62
L-median-whole-bone	-0.44	0.43	-0.20	-0.46	-0.06	-0.76	-0.36	0.08	-0.46

-1 0 1

(b)

Figure 5.18.: Pearson´s correlation coefficient for comparison of bone properties. The range of correlation coefficients is -1 (blue) to 1 (green), whereby the sign indicates the regression gradient. For better visualization a temperature scale has been choosen. Thereby, a darker color goes together with higher value of the coefficient and therefore stronger correlation.

This chapter raised questions regarding the differences between bone regions with different degrees of organization, which can be answered in short by: An unordered LCN goes together with lower T and L parameter, while the ordered bone regions exhibit increased mineral parameters. Across the transition zone of the bone regions, there is continuous transition of mineral length and thickness. Qualitative observations also show a continuous increase in canaliculi density and degree of orientation of the LCN in general.

The LCN of newly formed bone after mechanical stimulation is only connected to the older bone by a few channels. While the calcium content in the newly formed bone is significantly lower than in the older bone, the L and T parameters are very similar in both regions. Although, a line of lower T parameter values separates both regions and precludes a smooth transition.

The approach of correlating several parameters describing various structural characteristics has been applied successfully to identify the following most relevant insights: (i) the calcium content depends more on the age of the tissue and the form of the bone, than on other micro-structural characteristics, (ii) the T parameter relates to the organization of the network, while (iii) the L parameter has a strong correlation to the Can.Dn.

This study calls for the hypothesis that there is a mineral reservoir around the canaliculi that can be actively manipulated by osteocytes in order to make a quickly accessible contribution to mineral homeostasis.

The hypothesis that loading influences bone properties has to be confirmed with more samples. Nevertheless, the regions of high load go together with higher Can.Dn as well as higher L and T parameter. Higher SLOPES and higher Can.Dn indicate a difference between left and right bone or loaded and non-loaded bone.

6. Heterogeneity of bone tissue types in healing bone

The results presented in this chapter are already published in [Schemenz et al., 2020] and figures and parts of the text are taken from there.

6.1. Objectives

During the healing process after a fracture, a large amount of bone is formed via multiple steps including formation of mineralized cartilage and bony callus (see chapter 2.2.4). Hence, there are two special bone-bone interfaces developing. The first interface evolves between the fractured cortex and the newly built callus. The second interface appears within the callus, where the tissue organization changes from a less ordered arrangement to a more ordered one, which may arise from differences in the strains sensed by the osteocytes. To identify mechanisms that guide the formation of different tissue types, mineral particle properties are characterized depending on their proximity to different density or orientation characteristics of the LCN. The objectives of this chapter are investigating (i) the structural characteristics of the main tissue types in healing bone: cortical bone, bony callus, calcified cartilage, (ii) the behavior of these characteristics when passing one of these interfaces, (iii) the spatial correlations between the lacuno-canalicular network (LCN) and the mineral nanostructure of the bone matrix to study the role of osteocytes in the mineralization processes.

6.2. Measurement procedure

Six female, skeletally mature (26 weeks) C57BL/6J mice (Jackson Laboratory, Bar Harbor, Maine, USA) have undergone an osteotomy at the mid-diaphysis of the left femur like it is described in chapter 4.1.1. One littermate without operation served as control. 21 days after the osteotomy, the mice are euthanized, the femora are dissected and the external fixator is removed. Then, the bones are put directly in 70 % ethanol solution. The animal experiments are carried out according to the policies and procedures approved by the local legal research animal welfare representative (Shriners FACC 2016-7821). Afterwards, the femora are dehydrated, stained and embedded in PMMA as described in chapter 4.2. Here, the obtained PMMA blocks are cut in longitudinal direction into two halves. Therefore, it is possible to study cortical bone regions and different states of the callus at once. As shown in Figure 6.1, one half of the blocks are polished, imaged by CLSM to examine the architecture of the LCN. Later, the same blocks are measured with qBEI. Furthermore, this block is imaged with synchrotron-based phase contrast enhanced micro-computed tomography (μCT) at the beamline ID19 at the European Synchrotron Radiation Facility (ESRF). The other halves are cut into slices along their longitudinal axis with a microtome (Leica SM2500S and Leica VMH 400 knife, Nussloch, Germany) and polished (PM5 Logitech, Glasgow, UK). These 5 µm thin slices are used for SAXS and WAXS experiments.

Since not all of the examined bones have formed a callus or even a bridging, the following chapter concentrates on those three samples which did. In the following they will be called mouse femur (MF)1, 2 and 3. The healing process could be influenced by surgery and debris from the Gigli saw, leading to increased inflammation [Wataha et al., 2001]. The heterogeneity of healing may also be influenced due to interfragmentary movement,

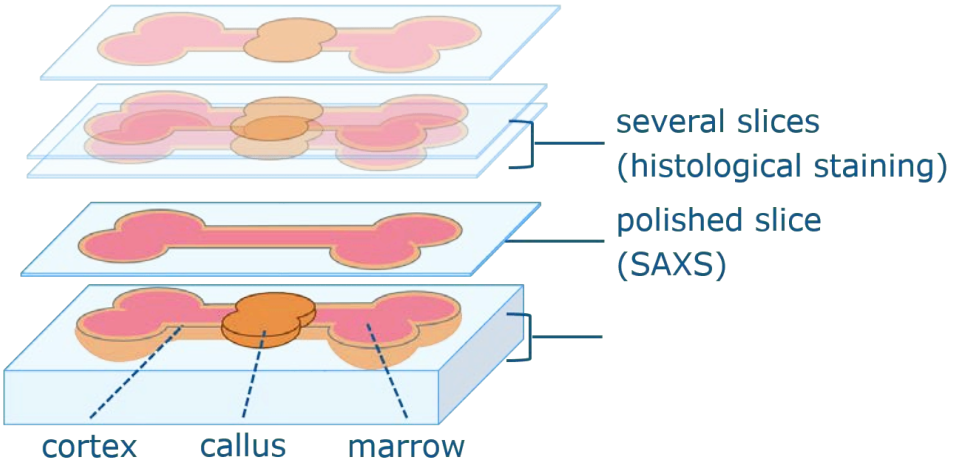

Figure 6.1.: Sketch of preparation of healing bone samples. After embedding in PMMA, the osteotomized samples are cut longitudinal into two halves. One half is polished and used for confocal laser scanning microscopy (CLSM) and quantitative backscattered electron imaging (qBEI) measurements, while the other half is cut into slices. The first slices are measured with small angle X-ray scattering (SAXS) and wide angle X-ray scattering (WAXS). The following slices are stained and analyzed histological. The figure is taken from [Gjardy, 2017, p. 22] with permission from André Gjardy.

which is affected by the stress on the operated limb from gravity, muscular forces and the fixation stiffness. The activity of the mice have not been measured, but within the study all factors should have been similar. Nonetheless, other studies with better healing results, i.e. bridging of the osteotomy, show comparable features to the samples in this study [Hoerth et al., 2018, Kruck et al., 2018, Röntgen et al., 2010]. It is therefore assumed that the structural features discussed are representative of the respective tissue types. Future studies with the same osteotomy model in skeletal mice have been performed with an extended healing time of an additional week, i.e. 28 days instead of 21.

6.3. The heterogeneous lacuno-canalicular network in healing bone

Figure 6.2 shows an overlay of qBEI measurements with results of the CLSM from the LCN for different regions. MF1 [i] shows a large area of the osteotomy gap. A large part of the cartilage area appears completely colored here. This can have various causes: On one hand, rhodamine not only stains soft tissue and bone surfaces, but also weakly mineralized tissue. On the other hand, the strong straining could also be explained by a the cartilage canals in the connective tissue containing blood vessels. Blood vessels transport fibroblasts and chondroclasts and are therefore important for the development, growth and resorption of cartilage [Hall, 2015, Shipov et al., 2013]. However, regions without any staining can also be found in MF1 [i]. By comparing them with qBEI measurements, these regions are identified as cortex fragments (marked with CF in Figure 6.2) that have been separated from the cortex throughout the osteotomy. The lack of a stained network may be caused by a surface sealed with osteopontin secreted by macrophages and osteoclasts to inhibit extracellular bone resorption or phagocytosis [Dodds et al., 2009, McKee et al., 2011]. Similar areas without staining can also be identified in the bony callus, which have a particularly high calcium content (indicated by black asterisks), whereby the surrounding area of these mineralized islands is less stained than the rest of the bone.

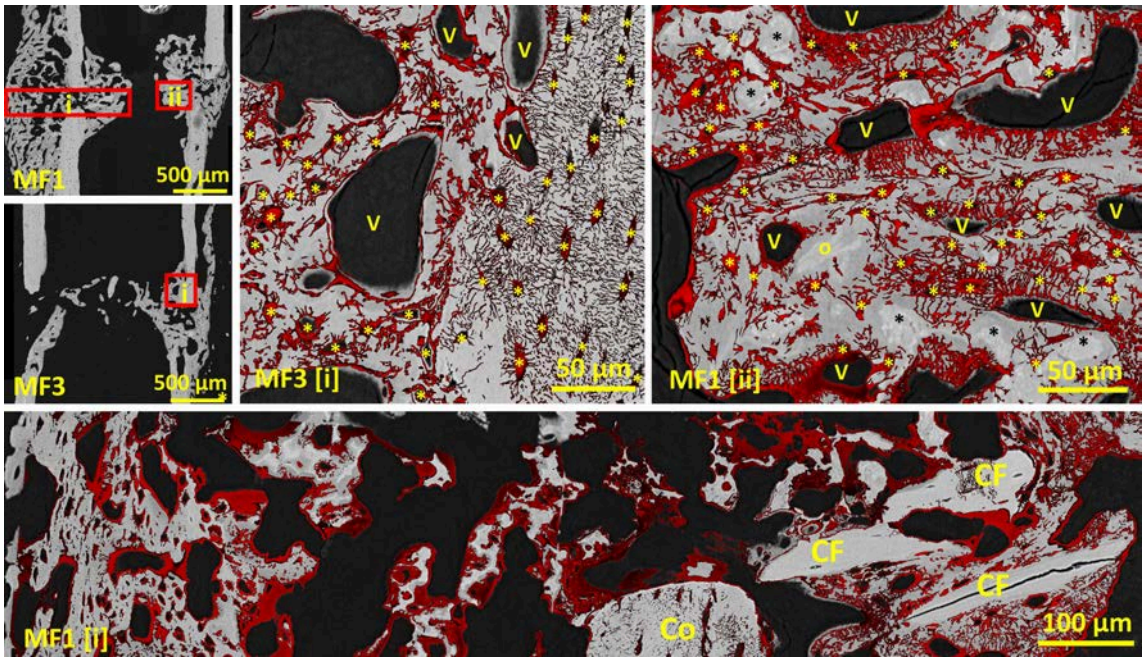

Figure 6.2.: Visualization of the lacuno-canalicular network and the surrounding matrix in healing bone. On the left side, there are two overview images showing qBEI measurements of two osteotomized femora after three weeks of healing. In qBEI the grey level indicates the calcium content (lighter grey means more calcium). The other images show the LCN measured via CLSM in selected regions, which are indicated in the overview pictures. The LCN is stained red to mirror its staining with rhodamine. Osteocyte lacunae (yellow asterisks) and vascular channels (V) appear red or are surrounded by a red line depending on their size. For better interpretation, qBEI and CLSM z-projections are stacked. MF3 I depicts an interface zone between the cortical and endosteal callus regions. While MF1[i] demonstrates several kinds of mineralized tissue, including cortical region (Co), bony callus, calcified cartilage and cortex fragments (CF). MF1 [ii] is showing a callus structure region including mineralized islands (black asterisks). Figure from [Schemenz et al., 2020] with permission from Elsevier.

The architecture of the LCN in the cortical region differs from that in the callus (see Figure 6.2 MF3 [i]). The lacunae of the cortical region appear as elongated ellipsoids, whose longest axis is aligned with the long axis of the femur. The canaliculi are mainly aligned perpendicular to it and appear to be thinner than in the callus. In contrast, the LCN in the callus (Figure 6.2 MF1 [ii] and MF3 [i]) appears to be arranged rather randomly. The callus also seem to have more lacunae than the cortex, but a lower number of connecting canaliculi. Whereby the canaliculi run mainly radially from the vascular canals (marked with V) or from the lacunae (yellow asterisks) connecting other lacunae, without any preferential orientation.

At the interface between the cortical and callus regions there are vascular canals and areas with a high calcium content. Some canaliculi actually connect the cortical region with the callus region (see Figure 6.2 MF3 [i]). They may mediate between the injured bone matrix and the lamellar bone during ossification [Kusuzaki et al., 2000].

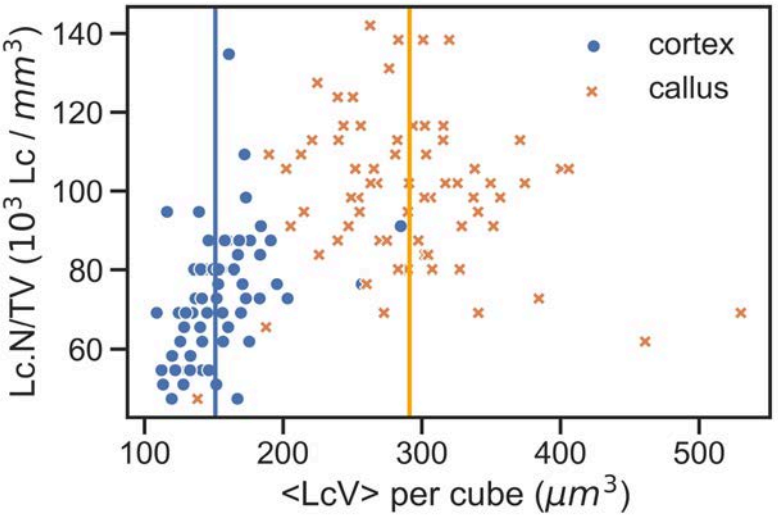

Figure 6.3.: Lacunae number density vs. average lacunar volume from μCT data using the evaluation approach with cubic subvolumes. Analysis of individual subvolumes distributed throughout the imaged bone volume (cortex and callus). The orange crosses correspond to average lacunar properties from cubes in the callus and the blue circles from cubes in the cortex, respectively. The dashed lines indicate the mean value of the respective bone type. Figure and description are taken from [Schemenz et al., 2020] with permission from Elsevier.

6.4. The morphology of lacunae in different tissue types of healing bone

The average lacunar density of the callus ($Lc.N/TV \approx 100\,^{10^3}/_{\mathrm{mm}}$) is 34 % higher than in the cortex ($\approx (73 \pm 15) \cdot 10^3\, mm^{-3}$ (Figure 6.3). The value for the cortex is higher than older reported values for bones in rodents [Mader et al., 2013, Voide et al., 2011]. The lacunar properties in callus tissue have not been further studied, but Hernandez et al. also have found the higher lacunar density in callus tissue areas compared to rat cortical bone with two-dimensional data from CLSM measurements [Hernandez et al., 2004].

The change in lacunar density could be due to increased osteoblast activity in the early stages of the bone healing process compared to the intramembranous growth process of the cortex [Hernandez et al., 2004]. Therefore, high lacunar density, i.e. high osteocyte density, as found in woven callus bone, has the potential to promote tissue removal and replacement with lamellar bone with lower cell density [Vashishth et al., 2002]. The number of osteocytes can be an indicator of the rate of bone turnover [Canè et al., 1982, Qiu et al., 2002] and may explain the transient nature of callus. Moreover, a greater number of osteocytes may be associated with the functional adaptation required by stress stimuli, what is also in line with the hypothetical contribution of osteocytes to bone matrix maintenance [Barros et al., 2009].

The average lacunar volume in the cortex (<Lc.V> =151 µm^3) tends to be lower [Mader et al., 2013, Voide et al., 2011] or in a similar range [Tiede-Lewis et al., 2017] as previously reported values. Several studies show a decrease in the lacunar volume of osteocytes with increasing age, which can be combined with an age-related decrease in lacuna size [Tiede-Lewis and Dallas, 2019]. It has also been reported that the lacunar volume in rat bone [Hemmatian et al., 2018] and in human bone [Milovanovic et al., 2017] decreases with age. Although the mice in this study are older (26 weeks) than the mice in the mentioned studies ($\approx$ 16 weeks), the effects of aging are insufficient to explain the systematic difference in lacuna size.

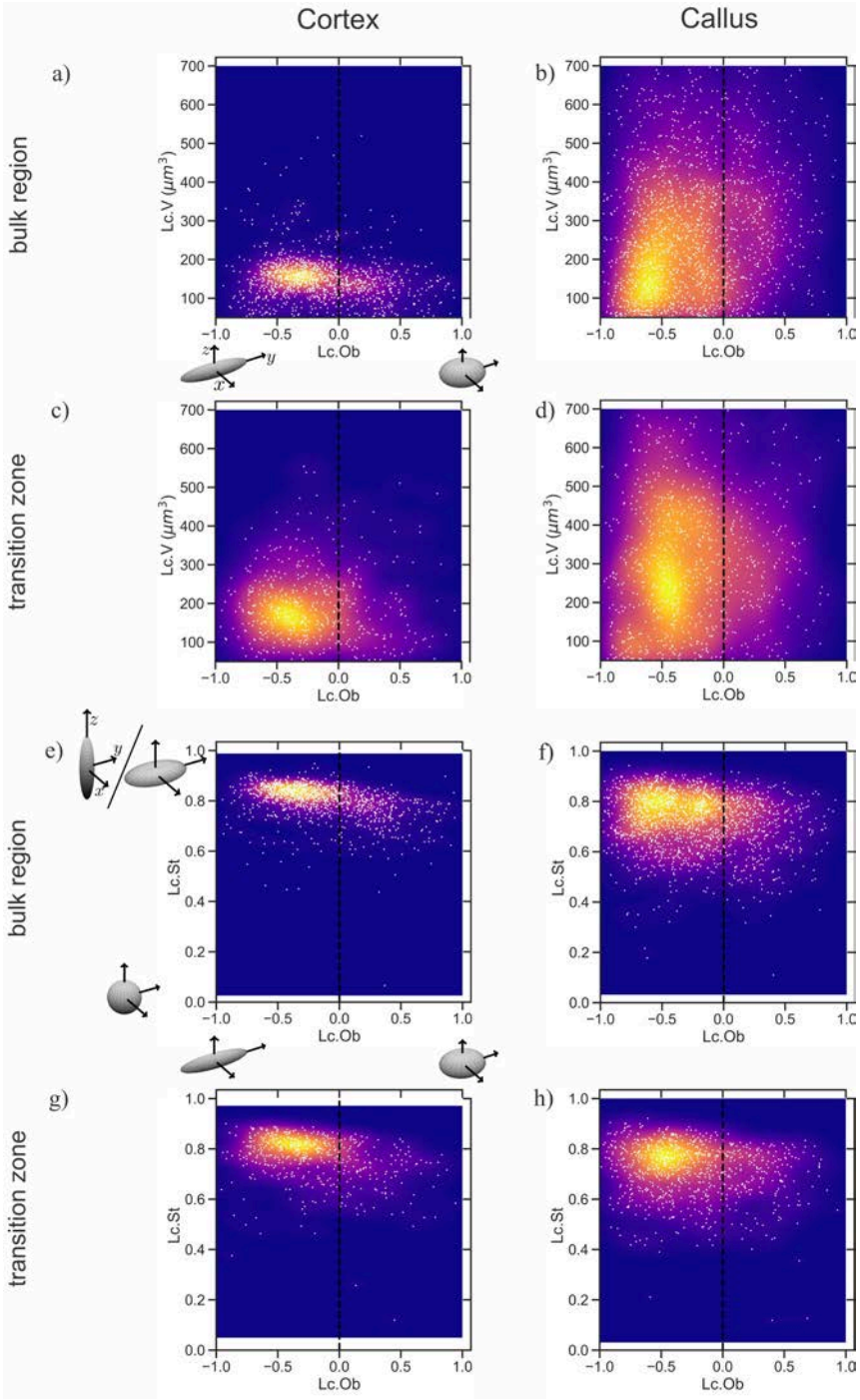

Figure 6.4.: Visualization of the lacuna parameters after the measurement by synchrotron-based phase contrast μCT. The oblateness of the lacunae (Lc.Ob) in relation to the lacunar volume (Lc.V) in the cortical area (a) and for the callus (b). Lacunar stretch (Lc.St) plotted against oblateness in the cortical region (e) and for the callus (f). The corresponding plots for the transition zone between cortical and callus regions are shown in (c), (d) and (g), (h), respectively. These results are compared with the lacunar properties for the cortical (c,g) and callus regions (d, h) near the interface between the two tissue types (see Figure 4.4). The dashed line denotes Lc.Ob equal to zero. Each white dot in the diagrams corresponds to one lacuna. For better understanding, the scatterplots are underlaid with a density diagram, where lighter colors mean a higher density of the measured points. The resulting surfaces highlight possible dependencies of the various parameters. Additionally, the drawn ellipsoids illustrate the stretched or roundish shape of lacunae (a, e). The The figure is taken from [Schemenz et al., 2020] with the permission from Elsevier.

Table 6.1.: Lacunar properties in cortex and callus. Mean value and standard deviations of the lacunar volume (Lc.V), the lacunar stretch (Lc.St), lacunar oblateness (Lc.Ob) and lacunar density (Lc.N/TV) are reported. Entries marked with a, b, c and d are significantly different . Hereby, (a) means the values are significantly different between cortex and callus within the tissue, (b) between cortex and callus at the interface, (c) between the cortex within the tissue and at the interface, (d) between the callus within the tissue and at the interface. The significant difference is tested by Welch's-tests for all. Here, all comparisons show either p<0.001 or no significance at all. In total, 4007 lacunae have been analyzed.

	Within tissue		At the interface	
	Cortex	Callus	Cortex	Callus
Lc.N(#)	1152	1544	496	815
Lc.V (µm)$_{a,b,c,d}$	151 ± 55	291 ± 177	197 ± 93	327 ± 187
Lc.Ob$_{a,b}$	-0.16 ± 0.37	-0.25 ± 0.40	-0.22 ± 0.39	-0.26 ± 0.41
Lc.St$_{a,b,c}$	0.80±0.06	0.72±0.11	0.76±0.09	0.71±0.11
Lc.N/TV $(^{10^3}/_{\mathrm{mm}})_a$	73±15	100±19		

The lacunae in the callus (<Lc.V$_{callus}$>= 290 µm^3) are 40 % larger than in the cortex (see Figure 6.3 as well as Figure 6.5a and b). Lacunae larger than 400 µm are found almost exclusively in bony callus. In addition, the analysis shows that lacunae of the cortex near the transition zone are larger than the reference values (197 µm^3 (see Table 6.1 and Figure 6.4c in comparison to Figure 6.4a). The same applies to the lacunae volume in the callus near the interface (<Lc.V>=327 µm^3) (see Figure 6.4b and h).

It has been suggested that osteocyte size and associated voids correlate with the size of osteoblasts before they differentiate into osteocytes, see [Boyde, 1980], as well as their deposition rate [Buenzli, 2015]. This would explain the bigger lacunae in the fast deposited callus. Furthermore, it has been reported that callus stiffness is only $60 - 70$ % of cortical stiffness [Hoerth et al., 2018, Manjubala et al., 2009]. At the same time, the present data show a 34% higher lacuna number density and 40% larger lacunae in the cortical region compared to the cortical region. It can therefore be assumed that the density and volume of the lacunae have an influence on the respective mechanical properties, as Yeni et al. [Yeni et al., 2001] showed earlier.

In the cortex the lacunae tend to have a rod-like shape ($<$ Lc.Ob $>_{cortex} = -0.16 \pm 0.37$). Lacunar volume (Lc.V) (Figure 6.4a) and the lacunar stretch (Figure 6.4e) (<Lc.St>$_{cortex}$ = 0.80 ± 0.06) show low variability. In contrast to the observations by Bach-Gansmo et al. in rats, there are no significant differences in the lacunar parameter between the central, unordered bone and the outer lamellar band [Bach-Gansmo et al., 2015]. Lacunae in the callus seem to show more variety in sizes and shapes, i.e. the data spread much more in Figure 6.4b and f compared to a and e. More specific, the lacunae of the callus are more roundish (<Lc.St>$_{callus} = 0.72 \pm 0.11$) (Figure 6.4f compared to the cortex 6.4e) and more prolate (<Lc.Ob>$_{callus} = -0.25 \pm 0.40$) (Figure 6.4f) compared to the cortex. The interface between cortex and callus cannot be identified without the information on the x-axis of the diagram, for the oblateness(Figure 6.5 b).

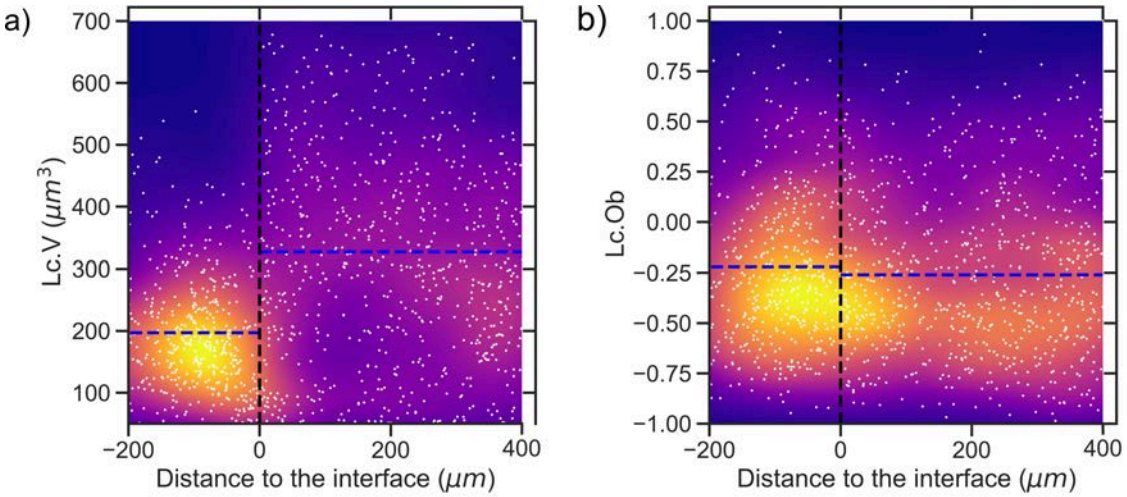

Figure 6.5.: Behaviour of lacunar volume (a) and lacunae oblateness (b) at the cortex-callus interface. The location of the interface is indicated by a black dashed line. To the left of this line (negative distances) is the cortex, to the right (positive distances) is the bony callus. The blue dashed lines mark the respective reference values for Lc.V and Lc.Ob. Each point corresponds to an evaluated lacuna and the scale represents the density of those points. The denser the points, the brighter the region is represented. The comparison of the lacunae parameters, shows that the lacunae in the transition zone between the cortical region and callus (VOI of Figure 4.4b, c) differ from the reference values, which indicates an interaction of the two different tissues.

There is evidence that the lacunar shape reflects the shape of osteocytes [Vatsa et al., 2008] and that more rounded osteocytes could be more mechanosensitive [Bacabac et al., 2008]. Finite element models show that the perilacunar environment is directly related to stress in osteocytes and that reduced lacunar size leads to decreased mechanoreaction [Kola et al., 2020]. These observations fit to the presented results of different shapes in cortex and callus and the differences of their mechanical properties found in other studies [Hoerth et al., 2018, Manjubala et al., 2009].

6.5. Development of mineral particle properties

The nanostructural properties of the mineral particles are characterized using high-resolution synchrotron SAXS and WAXS. With the measurements from the beamline ID13 at the ESRF, color maps can be created that show the thickness and length (T and L parameters) and the degree of their orientation (ρ parameters) and the c-lattice parameters over the different tissue types in the healing bones spatially resolved. Figure 6.6 and Figure 6.7 show the measurement results for sample MF1 as an example, but the following observations apply to all three samples examined. Comparing these maps (see Figure 6.6) with the previous measurements shows that the different tissue types also have different nanostructure properties.

In the cortical tissue, the mineral particles are long ($<L_{Cortex}> = 24.36 \pm 2.93$ nm), thick ($<T_{Cortex}> = 2.86 \pm 0.26$ nm), relatively strongly oriented ($<\rho_{Cortex}> = 0.5$) and have a high lattice parameter ($<c_{cortex}> = 6.822 \pm 0.006$ Å). It should be noted, however, that the crystal length (L-parameter) measured here with WAXS has lower values ($\approx$ 15-25 nm) than with electron microscopic determination [Ascenzi et al., 1965, Boyde and Jones, 1998] .

Compared to the cortical tissue, the mineral particles in the regions of the bony callus mass are thinner ($<T_{callus}> \approx$ 2.50 nm) and shorter. They also show a lower degree of orientation ($<\rho_{callus}> = 0.37$), which is often observed in woven bones

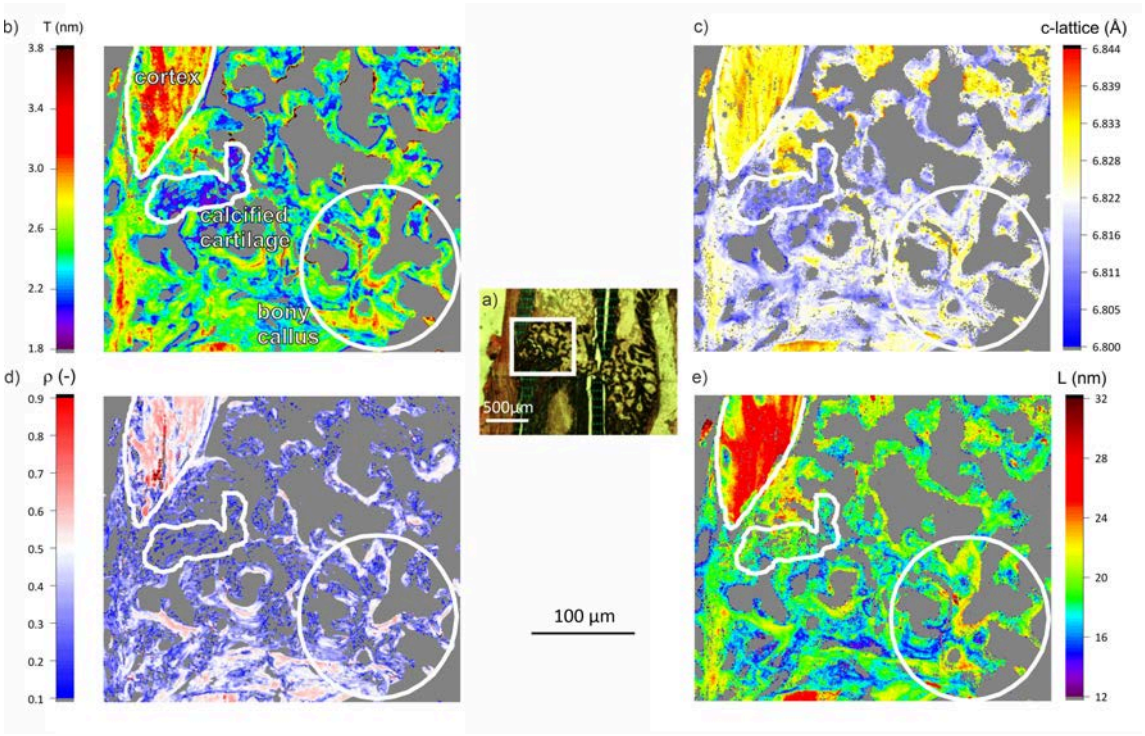

Figure 6.6.: Overview maps of synchrotron small and wide angle X-ray scattering (SAXS/WAXS) measurements in healing bone. All images are from the same sample MF1 shown in the light microscopic image (a). The combined SAXS and WAXS measurements were taken at the marked position between the fracture ends so that all tissue types are imaged. The mean mineral particle thickness (T parameter) (b), degree of orientation (ρ parameter), c-lattice parameter (c) and the length L of the crystals (e) are color-coded for each measuring point. This is shown in (d). The measurement points that do not contain enough mineral to provide a sufficient X-ray scatter signal are shown in grey. The cortex of the original bone is marked in the upper left corner from Each map. Underneath is mineralized cartilage, part of which is marked by the white line. From the callus, the regions in the white circle are considered, as features such as tissue and lamellar bone can be observed here. The figure is taken from [Schemenz et al., 2020] with permission from Elsevier.

[Hoerth et al., 2018, Kerschnitzki et al., 2011a, Kerschnitzki et al., 2011b]. These woven areas form relatively quickly at an early stage of mineralization and presumably serve as a scaffold for the deposition of more ordered, lamellar bone [Kerschnitzki et al., 2011b].

The enveloping lamellar areas in the callus bone show a higher degree of orientation but thinner mineral particles ($T < 2.4\,\text{nm}$), which is consistent with the observations of Hoerth et al. [Hoerth et al., 2018]. The regions around the lacunae, on the other hand, already show thicker minerals (T greater than 2.9 nm) (see also Figure 6.8). This change in shape could contribute to the stiffening of the mineralized tissue as healing progresses [Hoerth et al., 2018, Manjubala et al., 2009].

In the calcified cartilage, the mineral particles are poorly oriented $<\rho_{cartilage}>= 0.22$) and thin ($<T_{cartilage}>\approx 2.17\,\text{nm}$. However, the thickness and mineral length increase in the transition zone to the bony callus 18.70 nm.

In the transition zone from callus (young bone) to older cortical tissue, the mineral particle dimensions increase (Figure 6.7). This fits with previous observations that the length and thickness of the mineral particles in mice increases with the age of the animals

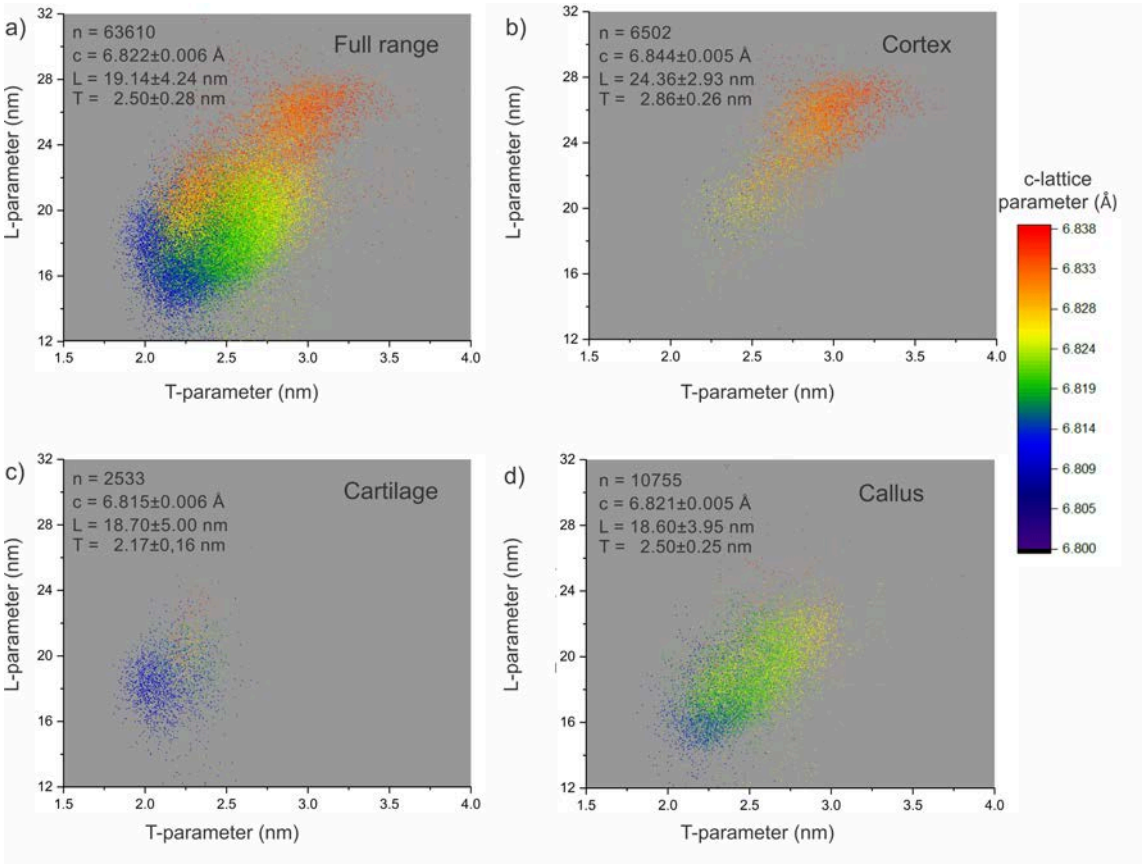

Figure 6.7.: Correlations of mineral particle properties measured with wide and small angle X-ray scattering (WAXS and SAXS) in different bone types. The different types of bone (the entire area (a), cortical tissue (b), calcified cartilage (c), bony callus (d)) in the healing bone can be identified using the crystal properties (L: crystal length; c-lattice parameters: crystal lattice spacing; T: particle thickness) clearly differentiate from each other. The areas correspond to those drawn in figure 6.6 of MF1. The number from Evaluated points (n) and the average values of the crystal properties are displayed in the top left of the respective diagrams. Figure from [Schemenz et al., 2020] with permission from Elsevier

[Lange et al., 2011]. While the T parameter and the c-lattice constant increase from calcified cartilage to bony callus, the length of the mineral crystals remains predominantly in a small range around 19 nm, which corresponds to the crystal size of fetal bone [Lange et al., 2011] corresponds. This may indicate that the mineral particles first become thicker and later longer [Hoerth et al., 2018].

In the transition zone from the callus to the cortex, a continuous increase in the c-lattice constant can be observed. A similar observation is also identified at the mineralization front of osteonal remodeling in human bone. There the lattice constant at the mineralization front is smaller than in the volume tissue [Roschger et al., 2020]. In human teeth, too, the decrease in the c-lattice parameter from the outer (cementum) to the inner (pulp) regions was observed. At the same time, a decrease in the apatite-carbonate content was found, which is interpreted as a function of root maturation [Forien et al., 2015]. Transferred to the present healing fracture specimens in this study, younger callus and cartilage regions have lower carbonate content compared to the older cortical bone regions. In addition, changes in lattice constants can also be caused by inclusions of trace elements and hydration.

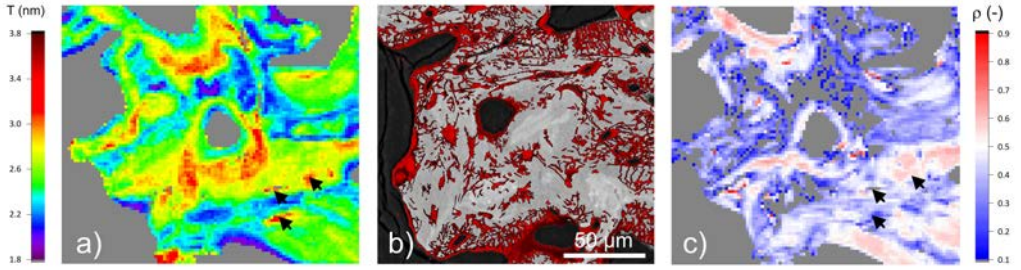

Figure 6.8.: Comparison between T parameter (a), calcium content, superimposed with z-projection of LCN (b) and ρ parameter (c). The color maps (a) and (c) show the same position in the MF1 sample. (b) is from the same sample, but a slightly different sample volume. The black arrows indicate the presumed location of the osteocyte void.

6.6. Correlation of LCN architecture and surrounding bone matrix

The fracture healing model examined here features different tissue types within a relatively small sample volume. This not only allows the characterization of cortex, bony and soft callus, but also their interfaces and transition zones between tissues (as shown in Table 6.2). This makes it possible to discuss mechanisms of how the different tissue types develop and how they are structurally related.

Cortical bone areas show comparable features to earlier studies, namely high mineral particle thickness and degree of orientation together with an organized LCN [Kerschnitzki et al., 2011b, Hoerth et al., 2018]. In the callus, the mean lacunar density ($<$Lc.N/ TV$>$ $\approx 100 \cdot 10^3 \mathrm{mm}^{-3}$ and the mean lacunar volume (Lc.V $\approx 290\,\mu\mathrm{m}^3$) are both significantly higher than in the cortical region, while the mineral particles are smaller and poorly oriented.

The volumes of the lacunae (Lc.V) approach each other within the transition zone from cortex to callus, but there is no clear transition (cortical region near interface: $197 \pm 93\,\mu\mathrm{m}^3$; callus near interface: $327 \pm 187\,\mu\mathrm{m}^3$) (Figure 6.5a). In contrast, the oblateness of the lacunae shows a continuous decrease across the interface (Figure 6.5b). The particle thickness and the calcium content also decrease towards the cortical edges, which Liu et al. also observe [Liu et al., 2010]. One reason for this could be that osteocytes remodel, more specifically dissolve, parts of the cortex around them to provide calcium and phosphate for mineralization of the newly formed callus. A similar effect is observed during lactation in mice [Qing et al., 2012]. In addition, several studies have also found a decrease in stiffness with decreasing distance from the osteotomy [Hoerth et al., 2014] and the callus [Preininger et al., 2011].

The calcified cartilage islands within the bony callus(see Figure 6.2, MF1 [ii]) and exhibit a positive correlation between T and ρ parameter as well as a relatively high calcium content. Lacunae located around these islands connect only to a few canaliculi.

Calcified cartilage plays an important role as an interface between two materials of very different stiffness, bone and unmineralized cartilage. The cartilage serves as the initial stabilization of the fracture. Later, the cartilage transforms into bone through endochondral mechanisms. In the examined tissue, the calcified cartilage shows a very heterogeneous calcium content, and the mineral particles are small and rather randomly arranged compared to the other tissue types. These characteristics indicate that the mechanical competence of this region differs from that of other mineralized regions.

Table 6.2.: The main structural features of the different bone types in healing bone as shown by the corresponding techniques.

Tissue / Method	Cortex	Transition Zone (cortex to callus)	Bony Callus woven-like	Bony Callus lamellar	Mineralized Cartilage
qBEI	high, homogeneous Ca-content	decreasing Ca-content	heterogenous Ca-content, high mineralized islands Ca-content (very low up to highest detected Ca-values)	lower Ca-content than in woven like region	strongly heterogeneous
CLSM	elongated lacunae along bone axis, canaliculi run mainly perpendicular to bone axis	tilted lacunae, few connecting canaliculi	randomly arranged LCN, low number of canaliculi	more (arranged) canaliculi at edges and around vascular channels	red staining across tissue
µCT	very well defined lacunar properties	harmonization of lacunar properties of cortex + callus	broad distribution of lacunar properties		
	lower lacunae density and Lc.V compared to callus	in general: increasing Lc.V, but random value distribution	higher density and Lc.V compared to callus		
	more oblate lacunae	decrease of oblateness	more prolate lacunae		
SAXS / WAXS	high T, ρ, L, d	lower T, ρ, L	relatively high T, low ρ, L similar to cartilage	edges: low T, higher ρ and L compared to woven around lacunae: high T, high ρ	low T, ρ and L

7. The effect of the Marfan syndrome on murine long bones

7.1. Objectives

Mutations in the fibrillin-1 (Fbn1) gene cause several disorders in the connective tissue. Typical skeletal symptoms are long bone overgrowth, arachnodactyly, loose joints and more generally spoken a low bone mass, a low bone mineral density (osteopenia) [Kohlmeier et al., 1995, Carter et al., 2000, Moura et al., 2006] and increased fracture risks [Folkestad et al., 2021]. A recent study also showed that individuals with Marfan syndrome (MFS) also have inferior bone microstructure and lower volumetric BMD compared to healthy control individuals, assessed using high-resolution peripheral quantitative computed tomography [Folkestad et al., 2020] (see chapter 2.3 for more background information).

Together these data suggest that Fbn1 plays a major role in regulating skeletal homeostasis. Especially the osteopenia could be explained by an imbalance in the coordinated interplay of resorbing osteoclasts and bone forming osteoblasts. However, the origin of this imbalance could not be clarified yet. While the roles of osteoclasts [Tiedemann et al., 2013, Nistala et al., 2010b] and osteoblasts [Nistala et al., 2010b, Nistala et al., 2010c] in MFS has been topic of different investigations, the role of osteocytes is not known yet. Therefore, this chapter is characterizing the correlations of the bone material properties and architecture of the LCN in the severly affected $Fbn1^{mgr/mgr}$ mice compared to healthy littermates.

Different symptoms seem to be linked in Marfan syndrome, so there is a positive and significant correlation between body growth in infancy and adolescence and aortic dilation [Vetter et al., 1990]. The tall stature and rapid, early growth as well as long bone growth have also been associated with the etiology of idiopathic scoliosis [Nissinen et al., 1993] [Erkula et al., 2002]. Therefore, this study is also investigating the long bone overgrowth. Does the overgrowth of long bones in mice with Marfan syndrome results from differences in longitudinal growth rates or also temporal differences in growth patterns?

7.2. Measurement procedure

Fibrillin-1 hypomorphic mice ($Fbn1^{mgr/mgr}$) are used to study the effect of Marfan syndrome by comparing the measurements with their wt littermates ($Fbn1^{+/+}$). The mouse model, where the Fbn1 gene is dysfunctional, is referred as mgr/mgr or mice with MFS and wt to simplify terminology throughout the text. They are genetically modified C57BL/6 mice by inserting a neomycin cassette between exons 18 and 19 of the Fbn1 gene [Pereira et al., 1999]. That means, that the wt mice should be comparable to C57BL/6 mice of the same age. The mgr/mgr mice are known to show severe symptoms of MFS, like overgrowth of the limbs and short life expectancy of 3 to 4 month because of aortic aneurysms [Pereira et al., 1999].

To study the bone growth and developement of mice with MFS, the tibiae of a group of mgr/mgr mice (n=4) and their littermates (n=5) are imaged using time-lapsed in-vivo μCT (SkyScan 1276 μCT, Bruker, Kontich, Belgium; 70 kV, 57 µA, 0.3 ms integration time, no frame averaging, 180° rotation). The scanning schedule is shown in Figure 7.1 and

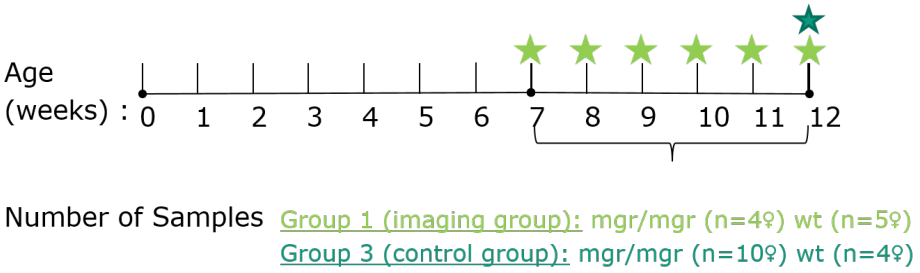

Figure 7.1.: Scheme of μCT schedule for studying bone growth in mice with Marfan syndrome. The tibiae of 5 mgr/mgr mice and 4 wild-type (wt) littermates are imaged every week in micro-computed tomography (μCT) - starting with an age of 7 weeks up to 12 weeks. Additionally, a radiation control group of 10 mgr/mgrand 7 wtmice are imaged with an age of 12 weeks. In the figure, each star represents a scanning session of in-vivo μCT.

contains in-vivo μCT measurements every seven days for 5 weeks starting with week 7 to determine changes in bone length, mass, mineral density and microstructure. The nominal isotropic image resolution of the resulting images is $8\mu m$ (compare with Figure 7.1). To prevent motion artifacts, mice were anesthetized via isofluran and kept in a fixed position using a custom-made mouse bed during the scans (see Figure 4.2). Calcein was injected 12 and 3 days before euthanasia. Additionally, tibiae of 10 mgr/mgr mice and 7 litter mates are imaged with μCT serving as radiation control group. The experiments are carried out according to the policies and procedures approved by the local legal research animal welfare representative (Shriners FACC 2016-7821).

After sacrificing, the left tibiae of these mice are fixed with 70 % ethanol and undergo the described process of ex-vivo sample preparation of chapter 4.2 including second harmonic generation microscopy and bone growth rate assessment by dynamic histomorphometry. QBEI measurements are performed at the Ludwig Boltzmann Institute for Osteology (LBIO) in Vienna using the Zeiss DSM962 (Oberkochen, Germany). Thereby, the samples are cut transversal in the midshaft to assess the cortical cross section and the proximal part is also cut longitudinal for studying the growth plate.

7.3. The effect of Marfan syndrome on murine long bone growth

The body mass of both mice strains, mgr/mgrând wtincreases from an age of 7 weeks to 11 weeks (see Figure 7.2). The body mass is not significantly different between mgr/mgr and wt. Also in Marfan patients, the body mass is comparable to the normal population [Erkula et al., 2002]. This may lead to the tall and slender appearance of the marfanoid habitus.

The longitudinal growth of the tibiae from mgr/mgr and wt mice measured with in-vivo μCT is shown in Figure 7.3. Neither the wt nor the mgr/mgr mice show any significant handedness. Nevertheless, only the right tibiae show significant differences in size from week 8 onward. The left tibiae do not show any significant difference. This might be a false negative, type II error because of the small sample size and it should be checked by measurements of additional mice, whether the tibiae of the mgr/mgr mice are longer than those of their littermates over the whole observation time. It has been shown mainly on C57BL/6J mice, that growth is fastest during the postnatal period and slows down at puberty ($\approx 4-5$ weeks)[Richman et al., 2001]. Growth patterns after puberty are not consistent even within a given mouse genotype [Buie et al., 2008, Glatt et al., 2007]. This is reflected in the calculation of the growth pattern of the measured data as well. Comparing

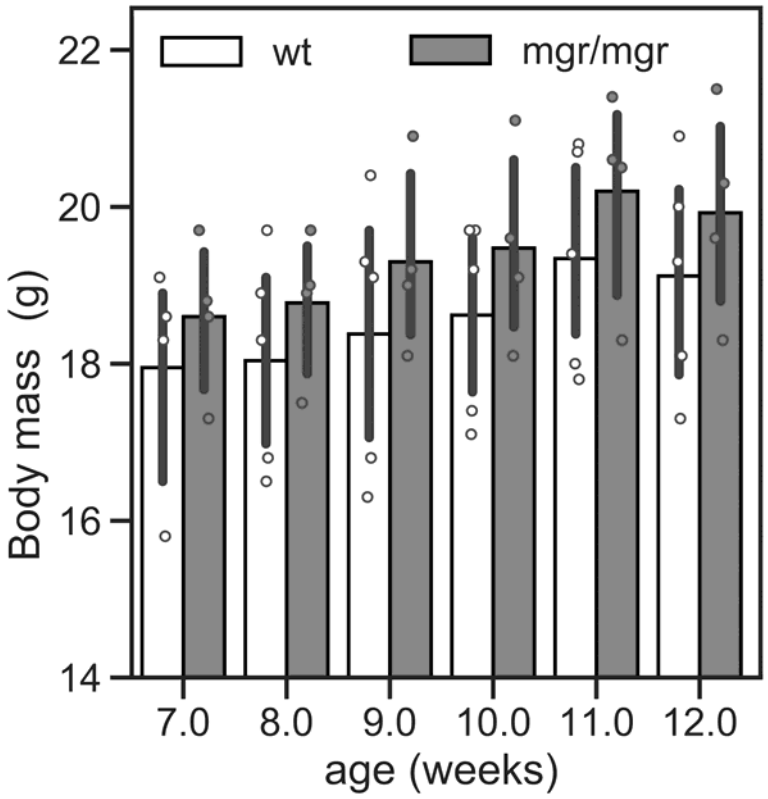

Figure 7.2.: Temporal change in body mass in mgr/mgr and wt mice. The mice are weighed right after the in-vivo μCT. Two way repeated measurement ANOVA does not show significant differences in the body mass for age and genotype.

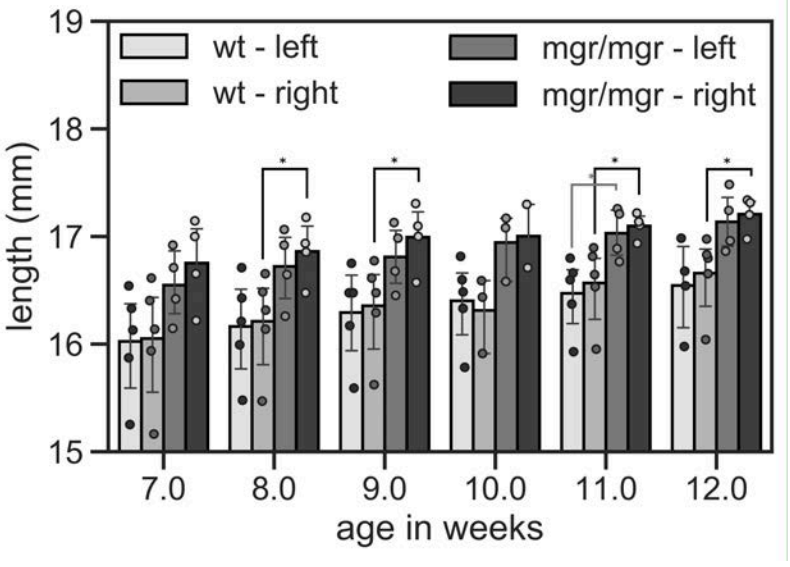

Figure 7.3.: Temporal change of tibiae length in mgr/mgr and wt mice. The lighter bars show the tibia length of the wild-type control mice, while the darker ones represent the tibia length of the mgr/mgr mice, respectively. The particular limb length for each side of both genotypes are plotted. Every point represents one measurement and asterisks indicate a significant difference between the linked groups ($p < 0.05$).

the growth of the limbs from each mouse shows different developments resulting in big standard deviations. However, the growth rates are quite similar to each other between the genotypes and decrease with age. Probably, an increased sample size would lead to a clearer picture here. Nevertheless, further studies including younger animals are needed (and already in progress).

7.4. The effect of Marfan syndrome on murine long bone morphometry

The static bone morphometry is done according to chapter 4.1.4. The volume of interest (VOI) in the diaphyseal region was centered at the midpoint of the tibia and extended 5 % of total tibial length. To test the effects in genotype, age and handedness an oneway ANOVA tests are performed. If a factor is significant, the difference between mouse genotypes at a given age is analyzed using two sample t-test. The comparison of left and right bone is done with paired Welch-test. All statistical analyses were performed with Origin 2021b on a personal computer. Differences were considered statistically significant when $p < 0.05$. The results are shown in Figure 7.4.

The bone content (bone volume over total volume; BV/TV) is lower in mgr/mgr mice compared with the wild-type counterparts (Figure 7.4c), but no significant differences in the indivudal components (bone volume (BV) and total volume (TV)). In contrast, the cortical thickness of mgr/mgr mice is significantly smaller than in wt mice starting from week 7 on (Figure 7.4g). This is mainly caused by a larger endosteal perimeter (Ec.Pm) which goes together with a larger marrow area (Ma.Ar). At the same time the outer radius (periosteal perimeter (Ps.Pm)) hardly shows any changes. Similar observation have been made before [Nistala et al., 2010a, Arteaga-Solis et al., 2011] concluding, that the endocortical should have only minimal effects on bone stiffness. [Arteaga-Solis et al., 2011]

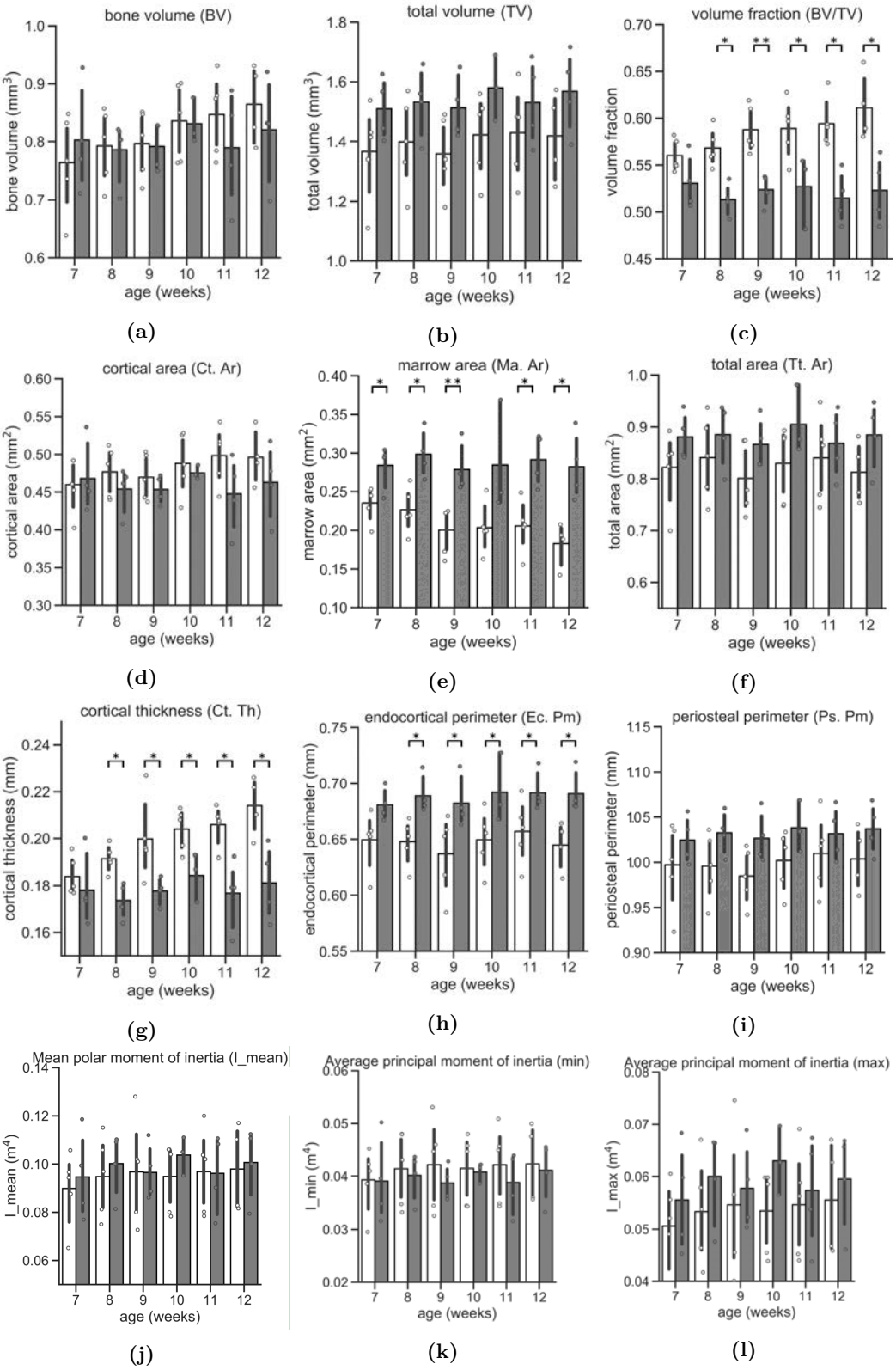

Figure 7.4.: Development of the static morphometric bone parameters for mgr/mgr and wt mice at the cortical bone over 5 weeks. The individual values are plotted for each mouse by points. The grey boxes show the mean values ± standard deviation for mgr/mgr mice and white for their wt littermates. Two-way repeated measures ANOVA shows no significant difference for and significant difference for the genotype in: TV, BV/TV, Tt, Ar, Ma.Ar, Ct.Th, Ec.Pm, I_{max} (Significance for all tests was set at $p \leq 0.05$). If a factor is significant, the difference between mouse genotypes at a given age is analyzed using Welch-test. The results of the Welch-test are indicated with asterisks with : $1.00e-02 < p <= 5.00e-02$, : $1.00e-03 < p <= 1.00e-02$.

7.5. The effect of the Marfan syndrome to the lacuno-canalicular network

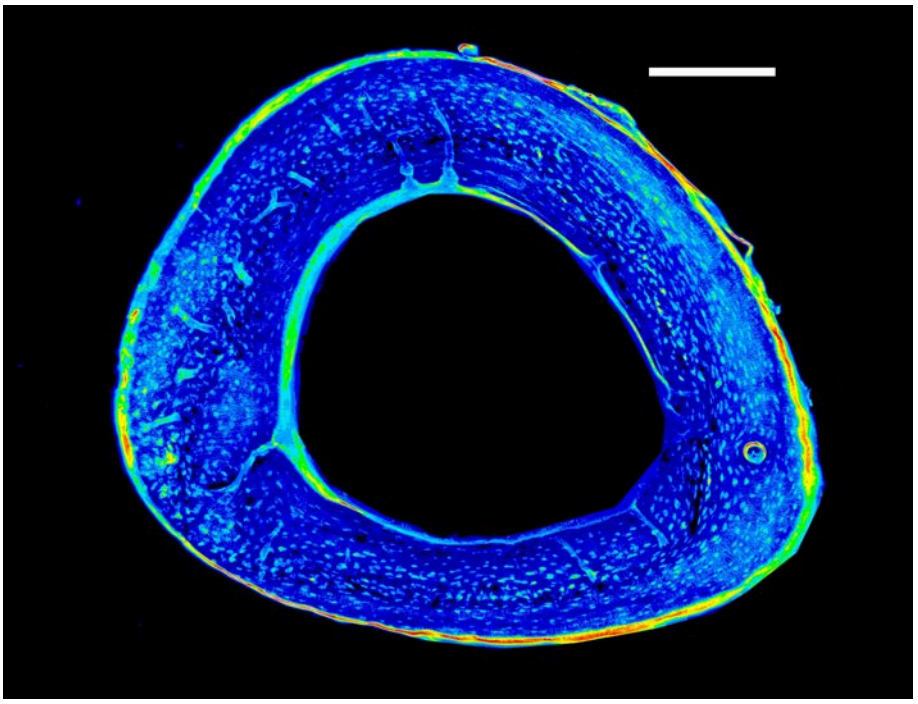

(a)

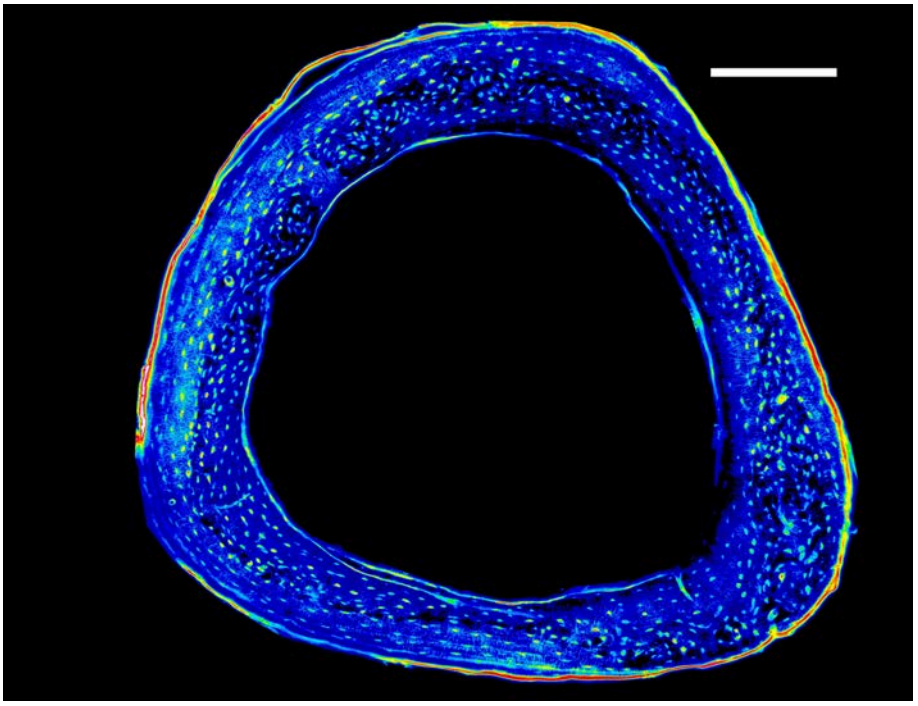

(b)

Figure 7.5.: Representative maps of the lacuno-canalicular network in the cortex of a mice with Marfan syndrome and a wt littermate. The LCN is stained with Rhodamine6G and measured with CLSM. The resulting stacks have a depth of $\approx 60\,\mu m$. The images above are the sum of the z-projections. The brighter the color, the more images in the stack showed a fluorescence signal. The scale bar in both images is equal to $200\,\mu m$ but cannot be used to read distances between objects as the images are z-projections.

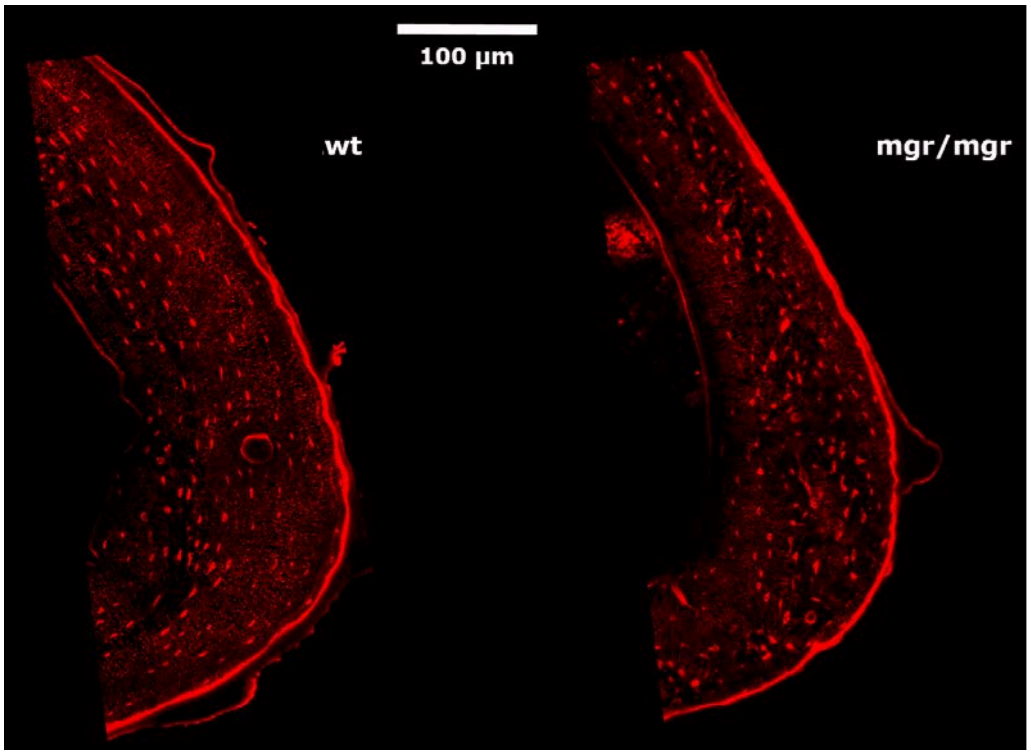

Figure 7.6.: Magnification of the LCN at posterior side from wt (left) and mgr/mgr (right) mice. Qualitative analyzing implies that the LCN of the wt mouse is more ordered and denser than its littermate with Marfan syndrome.

Cortices of murine limbs show remnants of early bone formation in the form of a unordered woven-like band which is surrounded by more ordered bone [Bach-Gansmo et al., 2013] (see also chapter 2.2.1 and 5). This behavior can also be observed in the cross sections of the tibiae from mgr/mgr mice (see Figure 7.5b and Figure 7.6). However, the cross sections of the tibiae from wt mice show only parts of this band. Although quantitative analyzes still need to verify it, qualitative assessment showed a much denser network in these wt mice (see Figure 7.5a and Figure 7.6 right). Additionally, Figure 7.5a reveals more blood vessels. All these observations lead to the assumption, that the remodeling of the mgr/mgr bones is decelerated in contrast to the wt bone.

7.6. The effect of the Marfan syndrome on mineral and matrix properties

Characterization of the collagen orientation in mgr/mgrmice

Several studies in the nineteen eighties hypothesize, that changes in the arrangement of collagen I cause the symptoms of MFS [Nogami et al., 1979, Byers et al., 1981]. Newer studies do not find any differences in the structure of collagen itself [Harley et al., 1990], but differences in the alignment [Nistala et al., 2010a]. qualitative assessment of Figure 7.7 shows more aligned regions of collagen in the control mice than in mgr/mgr mice. This can be seen especially at the endosteal surface, where several lines run parallel to each other and to the cross section. In contrast, the mgr/mgr show more unorganized regions and batches with short collagen fibrils similar to observation of [Cui et al., 2014].

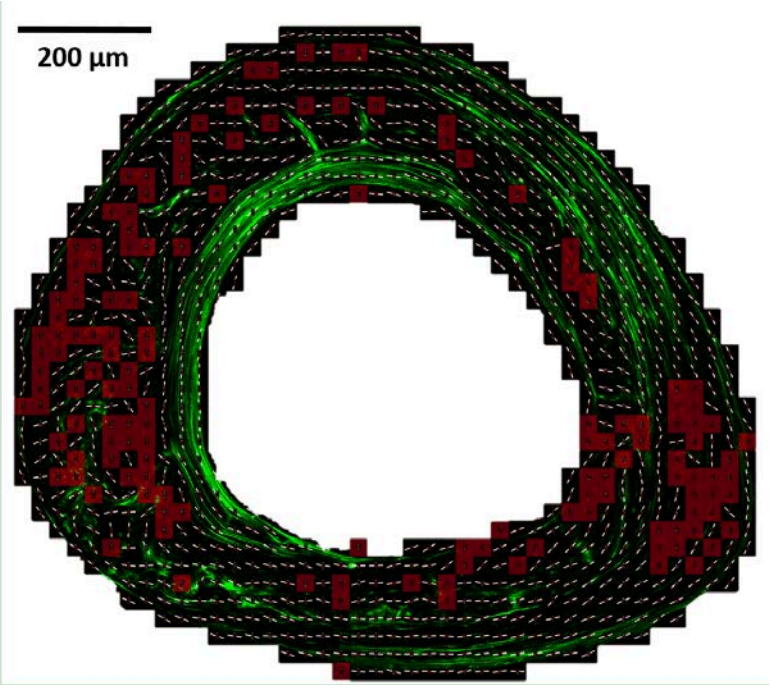

(a)

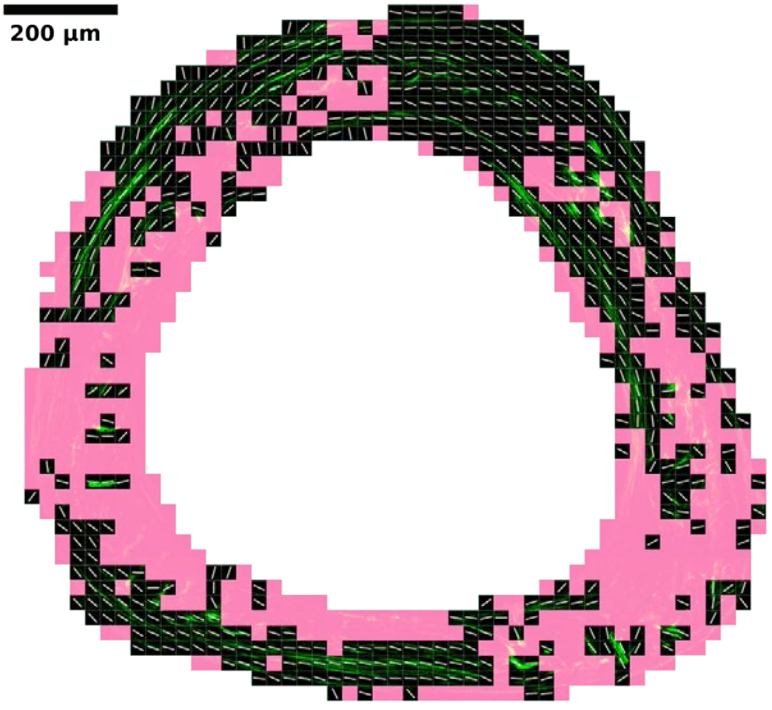

(b)

Figure 7.7.: Collagen orientation in the tibia cross section of a wt (a) and a mgr/mgr mice (b). The the cross-sections were divided into small squares and the major orientation of the collagen orientation shown in green (measured with SHG) determined. This major alignment is indicated by the white lines. No main alignment could be found in the red or pink regions, mostly due to missing signals or low contrast differences. The wt mouse shows more coherent collagen orientation than the mgr/mgr mouse.

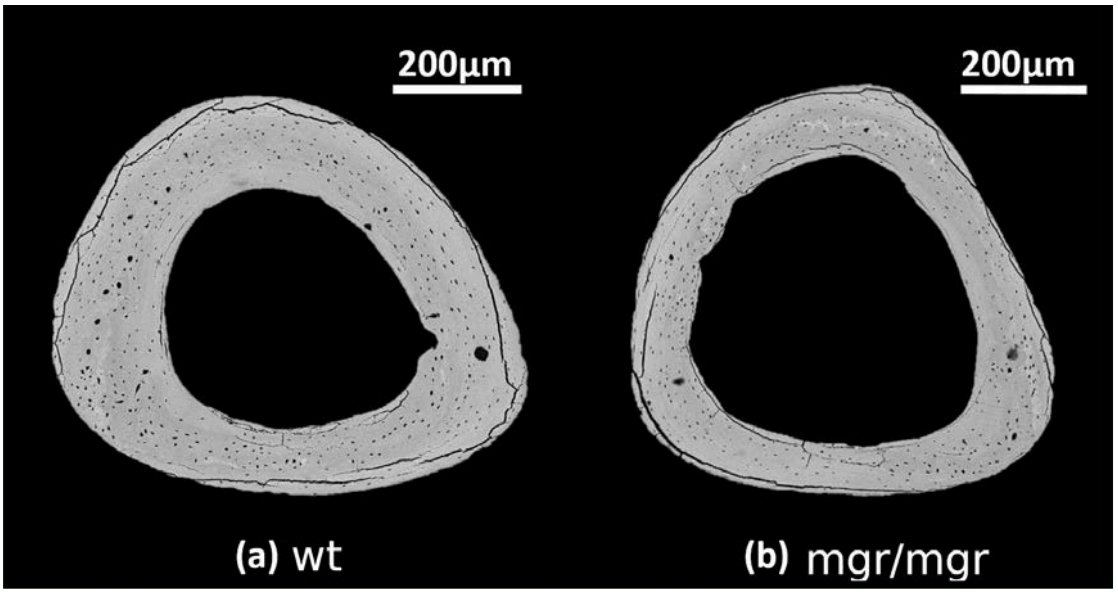

Figure 7.8.: Representative maps of the Calcium content in the cortex of a mice with Marfan syndrome and a wt littermate. The maps are measured with qBEI at LBIO in Vienna. The grey values correspond with certain calcium content, whereby a lighter grey value indicates more calcium.

Characterization of the calcium content properties in mgr/mgr mice

The qBEI measurements (shown in Figure **??** and Figure 7.9 as well as in Table 7.1) hardly show any differences in calcium content and bone mineralization density distribution (BMDD). This is in contrast to studies in human Marfan patients [Whitworth et al., 2006, Folkestad et al., 2020] and former observations of a lower BMD in mgr/mgr mice [Nistala et al., 2010a]. However, the indirect methods to determine the BMD by DEXA or μCT deliver varying results in different studies and stay under discussion [Giampietro et al., 2003]. Quantitative backscattered electron imaging relies on direct interactions with the bone surface and its elements (see chapter 3.3.2), thus assessing the calcium content. As already mentioned, the calcium content does change with age, but it seems to be quite stable under similar circumstances like it is shown in chapter 5).

Table 7.1.: BMDD characterizing parameters of the tibiae of 8 mgr/mgr and 6 wt mice.

genotype	Ca_{Mean}	Ca_{Peak}	Ca_{Width}	Ca_{Low}	Ca_{High}
wt	25.99	26.39	3.32	2.43	5.21
mgr/mgr	25.82	26.25	3.36	2.70	5.66

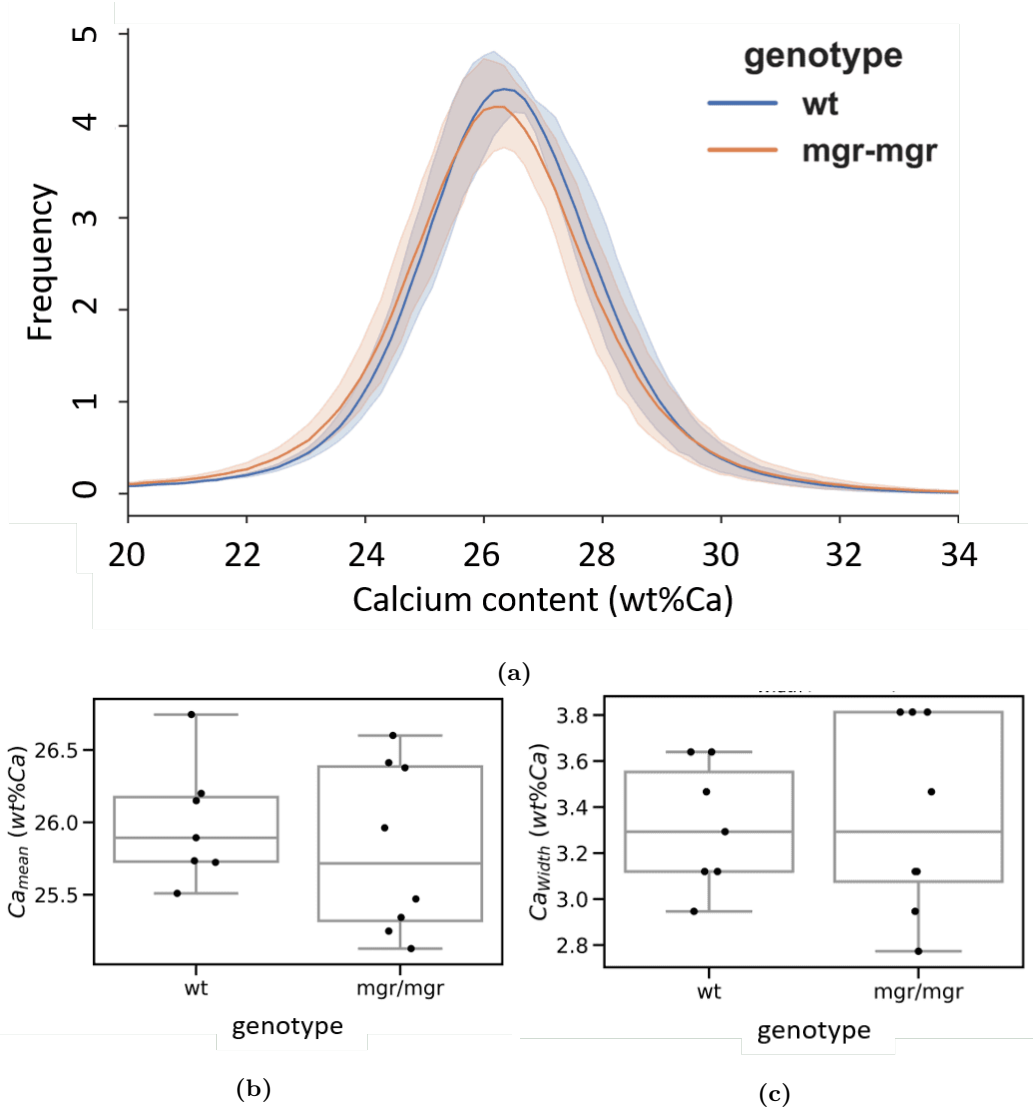

Figure 7.9.: Results of qBEI analyses of tibiae cross section from mice with Marfan syndrome and their wild-type littermates. a) Averaged BMDD of mgr/mgr (blue) and wt (orange) tibiae with 95% confidence interval. b-c) Statistical analysis of the BMDD curves. No significant difference could be observed in the calcium content between genotypes.

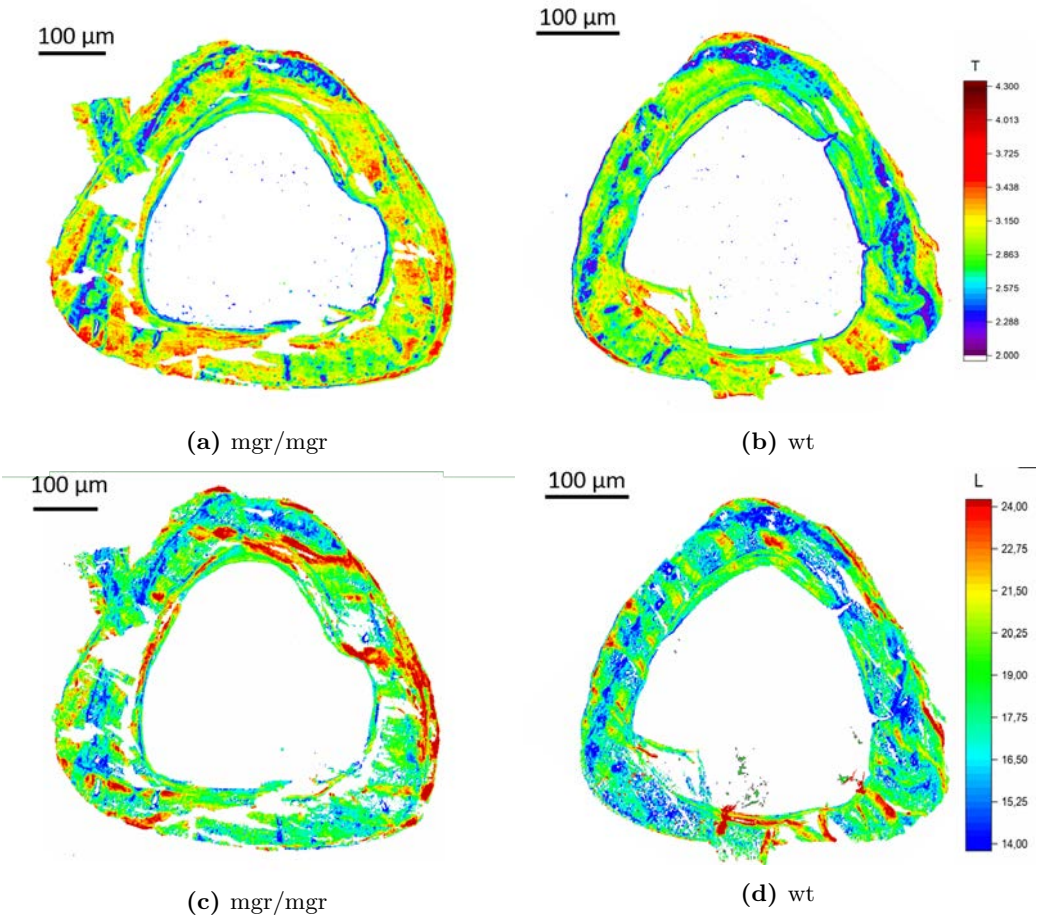

(a) mgr/mgr **(b)** wt

(c) mgr/mgr **(d)** wt

Figure 7.10.: Mineral particle properties in the cortex of a mice with Marfan syndrome and a wt littermate. Color maps of the T parameter in a mgr/mgr mouse and a wt mouse (a,b). Corresponding L parameter (c, d). Both parameters show lower values in the mouse with Marfan syndrome (a, c) than in the healthy littermate (b, d). Furthermore, the woven band is more prevalent in the mgr/mgr mouse (blue band in a).

Characterization of the mineral particle properties in mgr/mgr mice

Assessing the properties of mineral particles using small angle X-ray scattering (SAXS) and wide angle X-ray scattering (WAXS), the mgr/mgr mice show lower values for the T parameter (particle thickness) than their littermates (Figure 7.10b vs. Figure 7.10a). Furthermore, in Figure 7.10b there is a blue band going around almost the whole cortex, while such low values for the T parameter can be seen only partially in Figure 7.10a. In Figure 7.11 there is a trend of lower T parameter in mgr/mgr than in wt mice. This might be a false negative, type II error because of the small sample size and should be checked by measurements of additional cross sections. The L parameter shows a similar behavior, i.e. a clear band and smaller values in the mgr/mgr mice in contrast to the wt mice (see Figure 7.10d and Figure 7.10c). However, the differences are even even smaller. It has been shown, that T and L parameter values are higher with increasing tissue age [Roschger et al., 2001, Lange, 2011, Hoerth et al., 2018, Schemenz et al., 2020] and therefore it could also serve as an indicator of bone remodeling. Future studies focusing on different age groups could elucidate whether the bone mineral particle develop slower or are smaller in general.

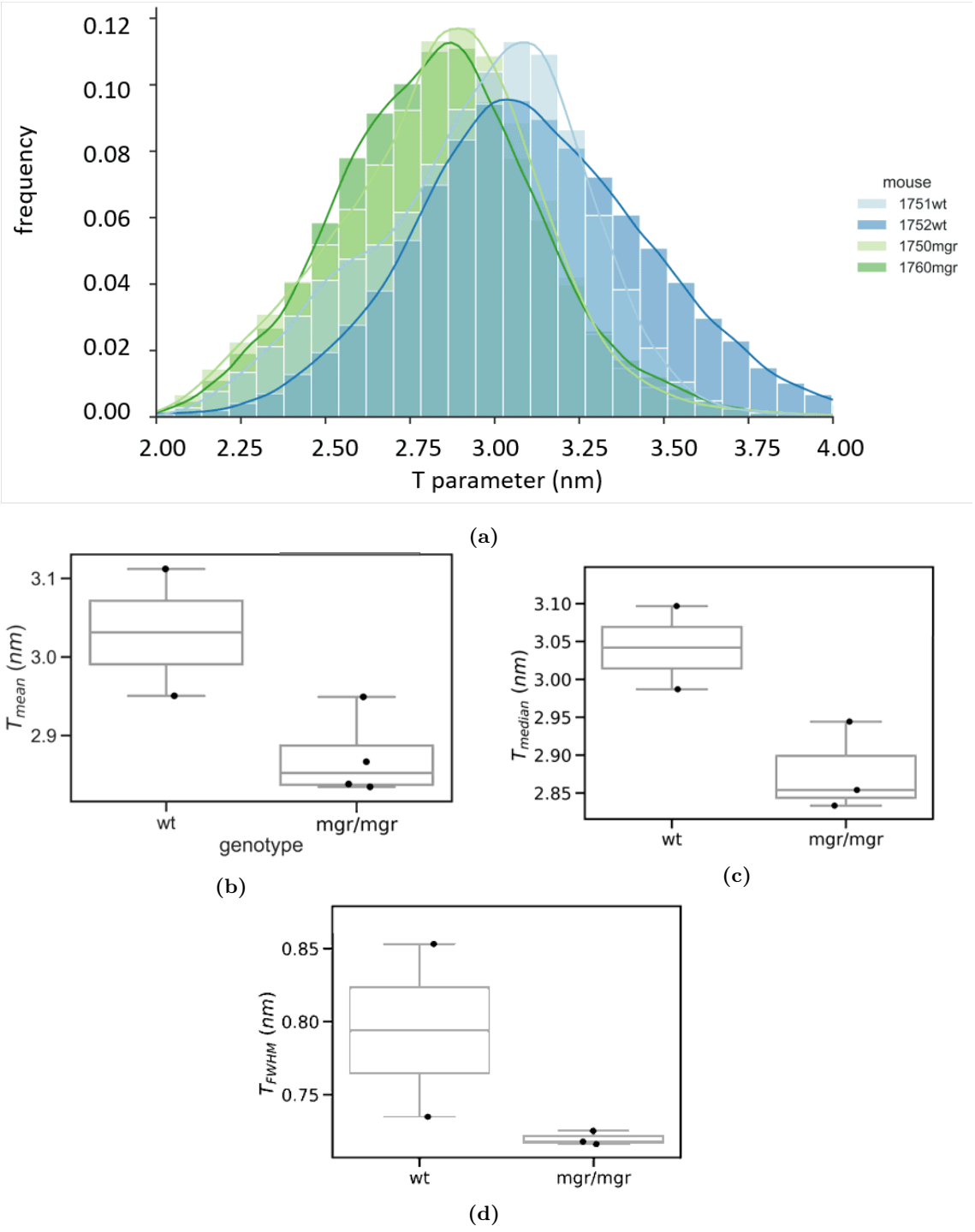

Figure 7.11.: Quantitative comparison of mineral properties in wt and mgr/mgr mice. (a) Histogram of exemplary T parameter distributions in mgr/mgr mice (green) and wildtype littermates (blue). The mean (b), median (c) and full width at half maximum (d) are compared below. T-tests showed that no significant difference of the T parameter between the two strains. This might be a false negative, type II error because of the small sample size and it should be checked by measurements of additional mice. Nevertheless, there is a trend of lower T parameters (T_{mean}, T_{median}) in mgr/mgr mice combined with a lower variation of the values compared to wt mice(d).

7.7. Relationship between the topology of the lacuno-canalicular network and its surrounding bone matrix

The right tibiae of the mgr/mgr mice are longer than those of their littermates from week 8 onwards with similar growth rates. This leads to the question: When does the overgrowth start? Therefore, also the tibiae of younger mice should be compared. This longer observation should also lead to a complete image of the growing pattern, because the growth follows an exponential function and is fastest during postnatal period. Nevertheless, also the sample size should be increased.

Differences in the diaphyseal cortical bone structure are observed in the 12 weeks old mgr/mgr mice and their littermates. The cortical thickness is much smaller in mgr/mgr mice accompanied by a larger endosteal perimeter (Fig. 7.4 c, g). The LCN (Figure 7.5) and collagen orientation (Figure 7.7) show less alignment in the mice with Marfan syndrome than in wt mice as well as a clear band of unordered network and collagen fibers. This band is also visible in the maps of the mineral parameters after SAXS and WAXS measurements (see Figure 5.13). Additionally, mineral particles are thinner and shorter in the mgr/mgr than in their healthy littermates. All these properties could be explained by a retarded bone remodeling in the cortex. To verify this hypothesis, younger bones should be studied as well.

However, the negative impact of the reduced structural properties could be compensated for the overall increase in bone size resulting in similar bone strength, like it is observed in human Marfan patients [Whitworth et al., 2006].

In general, the measured properties fit to those of the healthy bone cortex (see chapter 5); the lower degree of LCN organisation goes together with smaller mineral particles. To get a better idea, whether the interplay of the LCN with the surrounding mineral bone matrix is different in MFS than in healthy bones, the properties of the LCN have to be quantified and put into relation to the mineral properties. This will be done in the near future using the methods, which have been developed in this work (see for example chapter 4.6). Thereby, ordered and unordered region should be evaluated seperately, since it is shown in chapter 5 that the two regions have different properties and probably also functions.

8. Conclusion and Outlook

This work examines and quantifies the structural organization of the cellular component of bone as well as the material component within the same volume of bone samples and then analyzes the spatial correlations between them. This is intended to provide information whether osteocytes and their network can act directly on the surrounding bone material through deposition and resorption of minerals and thus directly control the properties of their environment. Therefore, characterization methods of material science are used to achieve the aim of detecting traces of this interaction between osteocytes and the extracellular matrix. First, healthy murine tibiae are characterized. Their properties are then compared with three different mouse models: 1) mouse tibiae, which underwent mechanical stimulation via in-vivo loading, 2) a healing mouse femur after osteotomy, which recapitulates parts of the developmental process and including substantial formation of new bone, 3) a mouse model, where the Fbn1 gene is dysfunctional causing defects in the formation of the extracellular tissue similar to the Marfan syndrome, which causes long bone overgrowth, loose joints, scoliosis and osteopenia.

The measurement techniques to characterize the topology of the lacuno-canalicular network (LCN), calcium content and mineral properties are applied not only to the same bone sample, but also the same volume of interest. Hence, direct comparisons of different parameters are possible. While only qualitative comparisons of the measurement results have been possible through manual image registration, a script has been developed in the course of this work that also enables quantitative comparisons at the same measurement points. A summary of the main results is shown in Table 8.1.

The healthy murine cortex contains two main regions. A band with unordered LCN is a remnant of early bone formation being described in earlier studies as a scaffold for the formation of more aligned bone with more ordered LCN. The unordered region is enveloped by a more ordered region, which has an average 31% higher canalicular density (Can.Dn), 10% thicker and 5% longer mineral particles. In contrast, the bone mineral density distribution (BMDD) does not show significant differences between these regions. Not the entire cortex can be divided into these two regions, rather there is also a transition zone connecting the different regions via some canaliculi (more than in the unordered, but less than in the ordered region).

The newly formed bone after mechanical stimulation shows similar properties of the mineral particles like the ordered region, but a lower calcium content. Between old and new bone, there is a clear border recognizable (especially in the particle thickness). Nevertheless, some canaliculi go through this border connecting old and new bone. Rhodamine also stains regions with low mineralization and therefore, the LCN could not be characterized due to the overstaining of such areas.

The comparison of mechanically stimulated bones with their controls does not show any differences in the calcium content. Differences become observable by taking the newly formed bone into account, which broadens the BMDD curves due its low mineralization. The evaluations have shown higher Can.Dn in mechanically stimulated bones compared to their controls. Comparing the ratio between calcium content and canalicular density (the so-called SLOPE) the ordered regions show only positive SLOPES with an 8% higher

mean value compared to the control bones. This leads to the suggestion that the LCN may serve as a mineral reservoir. Due to a small sample number, more investigations are needed here to draw conclusions that are more robust.

The healing bone model shows 21 days after osteotomy different tissue types representing the different steps of bone formation; namely calcified cartilage, bony callus and healthy cortex. During this evolution of tissue types, the mineral particles develop from short and thick to on average long and thin. The calcium content increases and becomes more homogeneous. The LCN becomes more and more organized. Furthermore, the bony callus exhibits a 34% higher lacunae number density and 40% larger lacunar volume compared to cortical bone. The bony callus plays a special role, because different phases of bone tissue can be observed here at the same time. While the majority of the callus is more woven-like, the edges reveal lower calcium content and thinner mineral particles, which is a sign for younger bone and therefore a hint, that another remodeling process takes place. The woven-like callus may serve as a scaffold for more aligned structures. In the transition zone between the cortical region and callus, continuous convergence of the calcium content, the mineral parameters and lacunae shape can be observed but discontinuities in the lacunae volume and LCN connectivity (only some canaliculi connect the tissue types).

The mice with Fbn1 mutation, to investigate the Marfan syndrome, show longer tibiae than their healthy littermates from an age of 7 weeks already. In contrast, the cortical development seems retarded, which is observable across all measured characteristics. The cortical thickness of the mutated mice is smaller than their littermates from week 8 on. This is mainly caused by a larger endosteal perimeter (Ec.Pm), but similar periosteal perimeter (Ps.Pm). The diseased mice show larger unordered bone regions than the wild-type mice, which is reflected in larger areas of looser and less organized lacuno-canalicular networks–especially at the endosteal side. This study showed also a lower degree of collagen orientation via second harmonic generation (SHG). Additionally, the mineral particles tend to be thinner and also shorter in the tibiae of the mice with the Fbn1 mutation. Only the calcium content is similar in both genotypes.

In summary, several correlations between the osteocyte network organization and the mineral matrix could be shown even down to the submicron mineral properties, which can be displayed in particular via the ratio between calcium content and canalicular density. Regions with dense and ordered network have thicker and longer mineral particles. How the osteocytes can control the mineral properties in their surroundings remains unclear. Most likely, the interaction is not only one-way since the extracellular matrix provides both a changing mechanical environment and contains biochemical signaling molecules that can alter osteocyte behavior. However, it seems that in highly organized bones, the LCN is so dense that its short distances to the mineral particles enable to better control their properties. Therefore, remodeling cannot only be understood as a method to resolve defects, or to adapt to external mechanical stimuli, but also to increase the efficiency of possible osteocyte mineral interactions during bone homeostasis. From a bone tissue engineering perspective, it seems helpful to employ scaffolds that mimic the primary bone architecture to promote bone regeneration and bone quality improvement .

In view of the results of this work, it seems reasonable to include the properties of osteocytes and their network in the treatment of bone diseases that cause changes in bone composition and mechanical properties. It will most likely require the combined effort of materials scientists, cell biologists and molecular biologists to gain a deeper understanding of how bone cells respond to their material environment.

Table 8.1.: Comparison of the main structural features of the different studied bone types. The main techniques analyzing all bones types are quantitative backscattered electron imaging (qBEI) to measure the calcium content, confocal laser scanning microscopy (CLSM) imaging the LCN architecture as well as small and wide angle X-ray scattering (SAXS and WAXS) to measure the mineral properties.

		qBEI	CLSM	Can.Dn	T	L
cortex	ordered region	Gaussian curve	elongated lacunae ∥ to bone axes ∥ canaliculi ⊥ to bone axes	high	high T	high L
	unordered region	no difference to ordered bone	randomly arranged LCN	lower than ordered bone	lower T	lower L
newly formed bone after mechanical stimulation		lower Ca content,			similar to ordered bone	similar to ordered bone
callus	woven	heterogeneous Ca-content	randomly arranged LCN, low number of canaliculi		high T	low L
	lamellar	lower Ca content than woven bone	more (arranged) canaliculi at edges than in woven bone		at edges: low T around lacunae: high T	higher L than in woven bone
cartilage		strongly heterogeneous	red staining across tissue		low T	low L
Marfan		no difference to wt	more unordered LCN than in wt		lower T	slightly lower L than wt

This study left open some questions and lead to possible directions for future research:

In the chapter 6.4 it is shown that an extended quantification of the lacunae could reveal information about the effect and functions of osteocytes. This is possible due to the high resolution of the synchrotron-based micro-computed tomography and should be carried out on a higher number of samples. To investigate the influence of the osteocytes to their surrounding, future studies may not only measure the properties of the LCN, but also of the osteocytes like it is done by Tiede-Lewis et al. [Tiede-Lewis et al., 2017]. Additionally, the load-induced fluid flow that can be sensed by the cells should be examined to judge effects on mechanosensing amongst osteocytes in enlarged lacunae.

One aim was to find out whether in-vivo loading influences the bone characteristics or not. But due to problems in the sample preparation, no reliable results could be achieved. However, further investigations are needed to prove the difference of Can.Dn and SLOPE between loaded and non-loaded bones. It must be noted that mice, like humans, have a certain handedness. Due to this, they could put more weight on one leg than the other. Therefore, it should first be examined whether there are already different bone properties due to handedness and clearly differentiate these from the effects of in-vivo loading experiments.

Extending the study of the mouse model of Marfan syndrome to higher numbers and younger ages in both, the in-vivo micro-computed tomography (μCT) imaging and the bone characteristic, should also give clearer explanations of the bone development in bones with Marfan syndrome and related questions are as follows. Does the overgrowth of the murine long bones starts from birth or even in the fetus state? Is the cortical development only retarded or does fibrilin-1 directly influence the LCN and bone mineral matrix properties?

Acronyms

BESSY	Berliner Elektronenspeicherring-Gesellschaft für Synchrotronstrahlung m. b. H. (English: Berlin Electron Storage Ring Society for Synchrotron Radiation)
BMDD	bone mineralization density distribution
BMP	bone morphogenetic proteins
BSE	backscattered electrons
BV	bone volume
CLSM	confocal laser scanning microscopy
CT	computed tomography
CTAn	CT-Analyser®
Ct.Ar	cortical area
Ct.Th	cortical thickness
DESY	Deutsche Elektronen-Synchrotron
DPDAK	Directly Programmable Data Analysis Kit
Ec.Pm	endosteal perimeter
ECM	extracellular matrix
ESRF	European Synchrotron Radiation Facility
Fbn1	fibrillin-1
FEM	finite element modeling
FESEM	field emission cathode scanning electron microscope
FWHM	full width at half maximum
GAG	glycosaminoglycans
GV	grey value
HAP	hydroxyapatite particles
LBIO	Ludwig Boltzmann Institute for Osteology
LCN	lacuno-canalicular network
Lc.V	Lacunar volume
Ma.Ar	marrow area
MCL	Materials Center Leoben Forschung GmbH
μCT	micro-computed tomography
MF	mouse femur
MFS	Marfan syndrome
MPIKG	Max Planck Institute of Colloids and Interfaces
PG	proteoglycans
PMMA	polymethyl methacrylate
Ps.Pm	periosteal perimeter

qBEI	quantitative backscattered electron imaging
RANKL	receptor activator of nuclear factor $\kappa - B$ ligand
SAXS	small angle X-ray scattering
SE	secondary electrons
SEM	scanning electron microscopy
SHG	second harmonic generation
SR	synchrotron radiation
TGFβ	transforming growth factor beta
TINA	tool for interactive network analysis
Tt.Ar	total area
TV	total volume
VOI	volume of interest
WAXS	wide angle X-ray scattering
wt	wild-type
XRF	X-ray fluorescence

List of Figures

List of Tables

Bibliography

[Abad et al., 2002] Abad, V., Meyers, J. L., Weise, M., Gafni, R. I., Barnes, K. M., Nilsson, O., Bacher, J. D., and Baron, J. (2002). The role of the resting zone in growth plate chondrogenesis. *Endocrinology*, 143(5):1851–1857.

[Aido et al., 2014] Aido, M., Kerschnitzki, M., Hoerth, R., Burghammer, M., Montero, C., Checa, S., Fratzl, P., Duda, G. N., Willie, B. M., and Wagermaier, W. (2014). Relationship between nanoscale mineral properties and calcein labeling in mineralizing bone surfaces. *Connective Tissue Research*, 55(SUPPL. 1):15–17.

[Akkus et al., 2004] Akkus, O., Adar, F., and Schaffler, M. B. (2004). Age-related changes in physicochemical properties of mineral crystals are related to impaired mechanical function of cortical bone. *Bone*, 34(3):443–453.

[Al-Aql et al., 2008] Al-Aql, Z. S., Alagl, A. S., Graves, D. T., Gerstenfeld, L. C., and Einhorn, T. A. (2008). Molecular Mechanisms Controlling Bone Formation during Fracture Healing and Distraction Osteogenesis. *J Dent Res*, 87(2):107–118.

[Arteaga-Solis et al., 2011] Arteaga-Solis, E., Sui-Arteaga, L., Kim, M., Schaffler, M. B., Jepsen, K. J., Pleshko, N., and Ramirez, F. (2011). Material and mechanical properties of bones deficient for fibrillin-1 or fibrillin-2 microfibrils. *Matrix Biology*, 30(3):188–194.

[Ascenzi et al., 1965] Ascenzi, A., Bonucci, E., and Steve Bocciarelli, D. (1965). An electron microscope study of osteon calcification. *Journal of Ultrasructure Research*, 12(3):287–303.

[Bacabac et al., 2008] Bacabac, R. G., Mizuno, D., Schmidt, C. F., Mackintosh, F. C., Loon, J. J. W. A. V., Klein-Nulend, J., and Smit, T. H. (2008). Round versus flat: Bone cell morphology, elasticity, and mechanosensing. *Journal of Biomechanics*, 41:1590–1598.

[Bach-Gansmo et al., 2013] Bach-Gansmo, F. L., Irvine, S. C., Brüel, A., Thomsen, J. S., and Birkedal, H. (2013). Calcified cartilage islands in rat cortical bone. *Calcified Tissue International*, 92(4):330–338.

[Bach-Gansmo et al., 2015] Bach-Gansmo, F. L., Weaver, J. C., Jensen, M. H., Leemreize, H., Mader, K. S., Stampanoni, M., Brüel, A., Thomsen, J. S., and Birkedal, H. (2015). Osteocyte lacunar properties in rat cortical bone: Differences between lamellar and central bone. *Journal of Structural Biology*, 191(1):59–67.

[Balerna and Mobilio, 2015] Balerna, A. and Mobilio, S. (2015). Introduction to Synchrotron Radiation. In Mobilio, S., Meneghini, C., and Boscherini, F., editors, *Synchrotron Radiation - Basics, Methods and Applications*, chapter 1, pages 3–28. Springer Berlin Heidelberg, Berlin.

[Barros et al., 2009] Barros, R. R., Degidi, M., Novaes, A. B., Piattelli, A., Shibli, J. A., and Iezzi, G. (2009). Osteocyte Density in the Peri-Implant Bone of Immediately Loaded and Submerged Dental Implants. *Journal of Periodontology*, 80(3):499–504.

[Bélanger et al., 1967] Bélanger, L. F., Bélanger, C., and Semba, T. (1967). Technical approaches leading to the concept of osteocytic osteolysis. *Clinical Orthopaedics and Related Research*, 54:187–196.

[Benecke et al., 2014] Benecke, G., Wagermaier, W., Li, C., Schwartzkopf, M., Flucke, G., Hoerth, R., Zizak, I., Burghammer, M., Metwalli, E., Müller-Buschbaum, P., Trebbin, M., Förster, S., Paris, O., Roth, S. V., and Fratzl, P. (2014). A customizable software for fast reduction and analysis of large X-ray scattering data sets: Applications of the new DPDAK package to small-angle X-ray scattering and grazing-incidence small-angle X-ray scattering. *Journal of Applied Crystallography*, 47(5):1797–1803.

[Bergström et al., 2017] Bergström, I., Kerns, J. G., Törnqvist, A. E., Perdikouri, C., Mathavan, N., Koskela, A., Henriksson, H. B., Tuukkanen, J., Andersson, G., Isaksson, H., Goodship, A. E., and Windahl, S. H. (2017). Compressive loading of the murine tibia reveals site-specific micro-scale differences in adaptation and maturation rates of bone. *Osteoporosis International*, 28(3):1121–1131.

[Birkhold et al., 2014] Birkhold, A. I., Razi, H., Duda, G. N., Weinkamer, R., Checa, S., and Willie, B. M. (2014). Mineralizing surface is the main target of mechanical stimulation independent of age: 3D dynamic in vivo morphometry. *Bone*, 66:15–25.

[Birkhold et al., 2016] Birkhold, A. I., Razi, H., Duda, G. N., Weinkamer, R., Checa, S., and Willie, B. M. (2016). The Periosteal Bone Surface is Less Mechano-Responsive than the Endocortical. *Scientific Reports*, 6(March):1–11.

[Blaber et al., 2013] Blaber, E. A., Dvorochkin, N., Lee, C., Alwood, J. S., and Yousuf, R. (2013). Microgravity Induces Pelvic Bone Loss through Osteoclastic Activity, Osteocytic Osteolysis, and Osteoblastic Cell Cycle Inhibition by CDKN1a/p21. *PLoS ONE*, 8(4):61372.

[Bonar et al., 1983] Bonar, L. C., Roufosse, A. H., Sabine, W. K., Grynpas, M. D., and Glimcher, M. J. (1983). X-ray diffraction studies of the crystallinity of bone mineral in newly synthesized and density fractionated bone. *Calcified Tissue International*, 35(1):202–209.

[Bonewald, 2011] Bonewald, L. F. (2011). The amazing osteocyte. *Journal of Bone and Mineral Research*, 26(2):229–238.

[Bonewald et al., 2013] Bonewald, L. F., Kneissel, M., and Johnson, M. (2013). Preface: The Osteocyte. *Bone*, 54(2):181.

[Bonucci, 2009] Bonucci, E. (2009). The osteocyte: The underestimated conductor of the bone orchestra. *Rendiconti Lincei*, 20(3):237–254.

[Bortel et al., 2015] Bortel, E. L., Duda, G. N., Mundlos, S., Willie, B. M., Fratzl, P., and Zaslansky, P. (2015). Long bone maturation is driven by pore closing: A quantitative tomography investigation of structural formation in young C57BL/6 mice. *Acta Biomaterialia*, 22:92–102.

[Bouxsein et al., 2010] Bouxsein, M. L., Boyd, S. K., Christiansen, B. A., Guldberg, R. E., Jepsen, K. J., and Müller, R. (2010). Guidelines for assessment of bone microstructure in rodents using micro-computed tomography. *Journal of Bone and Mineral Research*, 25(7):1468–1486.

[Boyde, 1980] Boyde, A. (1980). Evidence against Osteocytic osteolysis. *Metab Bone Dis Rel Res*, 2:239–255.

[Boyde and Jones, 1998] Boyde, A. and Jones, S. B. T. (1998). Aspects of Anatomy and Development of Bone: the nm, μm and mm Hierarchy. In *Molecular and Cellular Biology of Bone - Advances in Organ Biology*, volume 5, pages 3–44. Elsevier.

[Boyde and Jones, 1983] Boyde, A. and Jones, S. J. (1983). Back-scattered electron imaging of skeletal tissues. *Metabolic Bone Disease and Related Research*, 5(3):145–150.

[Brooke et al., 2008] Brooke, B. S., Habashi, M, J., Judge, D. P., Patel, N., Loeys, B., and Dietz, H. C. (2008). Angiotensin II blockade slows aortic root dilation in Marfan's? *The New England Journal of Medicine*, 358:2787–95.

[Buckley et al., 2014] Buckley, K., Kerns, J. G., Birch, H. L., Gikas, P. D., Parker, A. W., Matousek, P., and Goodship, A. E. (2014). Functional adaptation of long bone extremities involves the localized "tuning" of the cortical bone composition; evidence from Raman spectroscopy. *Journal of Biomedical Optics*, 19(11):111602.

[Buenzli, 2015] Buenzli, P. R. (2015). Osteocytes as a record of bone formation dynamics: A mathematical model of osteocyte generation in bone matrix. *Journal of Theoretical Biology*, 364:418–427.

[Buie et al., 2008] Buie, H. R., Moore, C. P., and Boyd, S. K. (2008). Postpubertal architectural developmental patterns differ between the L 3 vertebra and proximal tibia in three inbred strains of mice. *Journal of Bone and Mineral Research*, 23(12):2048–2059.

[Bushberg et al., 2012] Bushberg, J. T., Seibert, J. A., Boone, J. M., and Leidholdt, E. M. (2012). *The Essential Physics of Medical Imaging*. Wolters Kluwer Health/Lippincott Williams & Wilkins, 3 edition.

[Byers et al., 1981] Byers, P. H., Siegel, R. C., Peterson, K. E., Rowe, D. W., Holbrook, K. A., Smith, L. T., Chang, Y. H., and Fu, J. C. (1981). Marfan syndrome: Abnormal α2 chain in type I collagen. *Proceedings of the National Academy of Sciences of the United States of America*, 78(12 II):7745–7749.

[Cadet et al., 2003] Cadet, E. R., Gafni, R. I., McCarthy, E. F., McCray, D. R., Bacher, J. D., Barnes, K. M., and Baron, J. (2003). Mechanisms responsible for longitudinal growth of the cortex: Coalescence of trabecular bone into cortical bone. *Journal of Bone and Joint Surgery - Series A*, 85(9):1739–1748.

[Canè et al., 1982] Canè, V., Marotti, G., Volpi, G., Zaffe, D., Palazzini, S., Remaggi, F., and Muglia, M. A. (1982). Size and density of osteocyte lacunae in different regions of long bones. *Calcified Tissue International*, 34(1):558–563.

[Carter et al., 2000] Carter, N., Duncan, E., and Wordsworth, P. (2000). Bone mineral density in adults with Marfan syndrome. *Rheumatology*, 39(3):307–309.

[Checa et al., 2015] Checa, S., Hesse, B., Roschger, P., Aido, M., Duda, G. N., Raum, K., and Willie, B. M. (2015). Skeletal maturation substantially affects elastic tissue properties in the endosteal and periosteal regions of loaded mice tibiae. *Acta Biomaterialia*, 21:154–164.

[Compton, 1923] Compton, A. H. (1923). A Quantum Theory of the Scattering of X-rays by Light Elements. *Physical Review*, 21(5):483–502.

[Cook and Ramirez, 2014] Cook, J. R. and Ramirez, F. (2014). Clinical, Diagnostic, and Therapeutic Aspects of the Marfan Syndrome. In Halper, J., editor, *Progress in Heritable Soft Connective Tissue Diseases*, volume 802, pages 77–94. Springer Netherlands, Dordrecht.

[Cox et al., 2003] Cox, G., Kable, E., Jones, A., Fraser, I., Manconi, F., and Gorrell, M. D. (2003). 3-Dimensional imaging of collagen using second harmonic generation. *Journal of Structural Biology*, 141(1):53–62.

[Cui et al., 2014] Cui, J. Z., Tehrani, A. Y., Jett, K. A., Bernatchez, P., van Breemen, C., and Esfandiarei, M. (2014). Quantification of aortic and cutaneous elastin and collagen morphology in Marfan syndrome by multiphoton microscopy. *Journal of structural biology*, 187(3):242–253.

[Currey, 2006] Currey, J. D. (2006). *Bones: Structure and Mechanics*. Princeton University Pres, New Jersey.

[Currey and Shahar, 2013] Currey, J. D. and Shahar, R. (2013). Cavities in the compact bone in tetrapods and fish and their effect on mechanical properties. *Journal of Structural Biology*, 183(2):107–122.

[Danielsen et al., 1993] Danielsen, C. C., Mosekilde, L., and Svenstrup, B. (1993). Cortical bone mass, composition, and mechanical properties in female rats in relation to age, long-term ovariectomy, and estrogen substitution. *Calcified Tissue International*, 52(1):26–33.

[Danilchenko et al., 2002] Danilchenko, S. N., Kukharenko, O. G., Moseke, C., Protsenko, I. Y., Sukhodub, L. F., and Sulkio-Cleff, B. (2002). Determination of the bone mineral crystallite size and lattice strain from diffraction line broadening. *Crystal Research and Technology*, 37(11):1234–1240.

[De Souza et al., 2005] De Souza, R. L., Matsuura, M., Eckstein, F., Rawlinson, S. C., Lanyon, L. E., and Pitsillides, A. A. (2005). Non-invasive axial loading of mouse tibiae increases cortical bone formation and modifies trabecular organization: A new model to study cortical and cancellous compartments in a single loaded element. *Bone*, 37(6):810–818.

[Dimitriou et al., 2005] Dimitriou, R., Tsiridis, E., and Giannoudis, P. V. (2005). Current concepts of molecular aspects of bone healing. *Injury*, 36(12):1392–1404.

[do Aido, 2015] do Aido, M. I. F. (2015). *The Influence of Age and Mechanical Loading on Bone Structure and Material Properties/ Einfluss von Alter und mechanischer Belastung auf Struktur und Materialeigenschaften des Knochens*. PhD thesis, Technische Universität Berlin.

[do Aido et al., 2015] do Aido, M. I. F., Kerschnitzki, M., Hoerth, R., Checa, S., Spevak, L., Boskey, A. L., Fratzl, P., Duda, G. N., Wagermaier, W., and Willie, B. M. (2015). Effect of in vivo loading on bone composition varies with animal age. *Experimental Gerontology*, 63:48–58.

[Dodds et al., 1993] Dodds, R. A., Ali, N., Pead, M. J., and Lanyon, L. E. (1993). Early loading-related changes in the activity of glucose 6-phosphate dehydrogenase and alkaline phosphatase in osteocytes and periosteal osteoblasts in rat fibulae in vivo. *Journal of Bone and Mineral Research*, 8(3):261–267.

[Dodds et al., 2009] Dodds, R. A., Connor, J. R., James, I. E., Lee Rykaczewski, E., Appelbaum, E., Dul, E., and Gowen, M. (2009). Human osteoclasts, not osteoblasts, deposit osteopontin onto resorption surfaces: An in vitro and ex vivo study of remodeling bone. *Journal of Bone and Mineral Research*, 10(11):1666–1680.

[Dong et al., 2014] Dong, P., Haupert, S., Hesse, B., Langer, M., Gouttenoire, P.-J., Bousson, V., and Peyrin, F. (2014). 3D osteocyte lacunar morphometric properties

and distributions in human femoral cortical bone using synchrotron radiation micro-CT images. *Bone*, 60:172–185.

[Dooley et al., 2012] Dooley, C., Tisbo, P., Lee, T. C., and Taylor, D. (2012). Rupture of osteocyte processes across microcracks: The effect of crack length and stress. *Biomechanics and Modeling in Mechanobiology*, 11(6):759–766.

[Duncan and Turner, 1995] Duncan, R. L. and Turner, C. H. (1995). Mechanotransduction and the Functional Response of Bone to Mechanical Strain. *Calcified Tissue International*, 57:344–358.

[Dunn and Heath, 1976] Dunn, G. A. and Heath, J. P. (1976). A new hypothesis of contact guidance in tissue cells. *Experimental Cell Research*, 101(1):1–14.

[Einhorn, 1998] Einhorn, T. A. (1998). The Cell and Molecular Biology of Fracture Healing. *Clinical Orthopaedics and Related Research*, 355S(355):S7–S21.

[Elder et al., 1947] Elder, F. R., Gurewitsch, A. M., Langmuir, R. V., and Pollock, H. C. (1947). Radiation from Electrons in a Synchrotron. *Phys. Rev.*, 71(11):829–830.

[Enlow, 1962] Enlow, D. H. (1962). A Study of the Post-Natal Growth and Remodeling of Bone. *Am J Anat*, 110:79–101.

[Erkula et al., 2002] Erkula, G., Jones, K. B., Sponseller, P. D., Dietz, H. C., and Pyeritz, R. E. (2002). Growth and maturation in Marfan syndrome. *American Journal of Medical Genetics*, 109(2):100–115.

[Fazzalari et al., 1997] Fazzalari, N. L., Moore, A. J., Byers, S., and Byard, R. W. (1997). Quantitative analysis of trabecular morphogenesis in the human costochondral junction during the postnatal period in normal subjects. *Anatomical Record*, 248(1):1–12.

[Felsenberg, 2001] Felsenberg, D. (2001). Struktur und Funktion des Knochen. *Pharmazie in unserer Zeit*, 30(6):488–494.

[Feng et al., 2013] Feng, J. Q., Clinkenbeard, E. L., Yuan, B., White, K. E., and Drezner, M. K. (2013). Osteocyte regulation of phosphate homeostasis and bone mineralization underlies the pathophysiology of the heritable disorders of rickets and osteomalacia. *Bone*, 54(2):213–221.

[Ferguson et al., 2003] Ferguson, V. L., Ayers, R. A., Bateman, T. A., and Simske, S. J. (2003). Bone development and age-related bone loss in male C57BL/6J mice. *Bone*, 33(3):387–398.

[Finean and Engström, 1953] Finean, J. B. and Engström, A. (1953). The low-angle scatter of X-rays from bone tissue. *BBA - Biochimica et Biophysica Acta*, 11(C):178–189.

[Folkestad et al., 2020] Folkestad, L., Groth, K. A., Shanbhogue, V., Hove, H., Kyhl, K., Østergaard, J. R., Jørgensen, N. R., Andersen, N. H., and Gravholt, C. H. (2020). Bone Geometry, Density, and Microarchitecture in the Distal Radius and Tibia in Adults With Marfan Syndrome Assessed by HR-pQCT. *Journal of Bone and Mineral Research*, 35(12):2335–2344.

[Folkestad et al., 2021] Folkestad, L., Stochholm, K., Groth, K., Hove, H., Andersen, N. H., and Gravholt, C. H. (2021). Fracture Rates and Fracture Risk in Patients With Marfan Syndrome: A Nationwide Register-Based Cohort Study. *Journal of Bone and Mineral Research*, 36(5):901–909.

[Forien et al., 2015] Forien, J. B., Fleck, C., Cloetens, P., Duda, G., Fratzl, P., Zolotoyabko, E., and Zaslansky, P. (2015). Compressive Residual Strains in Mineral Nanoparticles as a Possible Origin of Enhanced Crack Resistance in Human Tooth Dentin. *Nano Letters*, 15(6):3729–3734.

[Franken et al., 1961] Franken, P. A., Hill, A. E., Peters, C. W., and Weinreich, G. (1961). Generation of optical harmonics. *Physical Review Letters*, 7(4):118–119.

[Franz-Odendaal et al., 2006] Franz-Odendaal, T. A., Hall, B. K., and Witten, P. E. (2006). Buried alive: How osteoblasts become osteocytes. *Developmental Dynamics*, 235(1):176–190.

[Fratzl, 1994] Fratzl, P. (1994). Statistical Model of the Habit and Arrangement of Mineral Crystals in the Collagen of Bone. *Journal of Statistical Physics*, 77(12):125–143.

[Fratzl, 2008] Fratzl, P., editor (2008). *Collagen*. Springer US, Boston, MA.

[Fratzl et al., 1991] Fratzl, P., Fratzl-Zelman, N., Klaushofer, K., Vogl, G., and Koller, K. (1991). Nucleation and Growth of Mineral Crystals in Bone Studied by Small-Angle X-Ray Scattering. *Calcif Tissue Int*, 48:407–413.

[Fratzl et al., 2004] Fratzl, P., Gupta, H. S., Paschalis, E. P., and Roschger, P. (2004). Structure and mechanical quality of the collagen–mineral nano-composite in bone. *J. Mater. Chem.*, 14(14):2115–2123.

[Fratzl et al., 1996a] Fratzl, P., Schreiber, S., and Boyde, A. (1996a). Characterization of bone mineral crystals in horse radius by small-angle X-ray scattering. *Calcified Tissue International*, 58(5):341–346.

[Fratzl et al., 1996b] Fratzl, P., Schreiber, S., and Klaushofer, K. (1996b). Bone Mineralization as Studied by Small-Angle X-Ray Scattering. *Connective Tissue Research*, 34(4):247–2549.

[Fratzl and Weinkamer, 2007] Fratzl, P. and Weinkamer, R. (2007). Nature's hierarchical materials. *Progress in Materials Science*, 52(8):1263–1334.

[Freund et al., 1986] Freund, I., Deutsch, M., and Sprecher, A. (1986). Connective tissue polarity. Optical second-harmonic microscopy, crossed-beam summation, and small-angle scattering in rat-tail tendon. *Biophysical Journal*, 50(4):693–712.

[Frost, 1987] Frost, H. M. (1987). Bone "mass" and the "mechanostat": A proposal. *The Anatomical Record*, 219(1):1–9.

[Gauderon et al., 2001] Gauderon, R., Lukins, P. B., and Sheppard, C. J. (2001). Optimization of second-harmonic generation microscopy. *Micron*, 32(7):691–700.

[Gerber et al., 1999] Gerber, H. P., Vu, T. H., Ryan, A. M., Kowalski, J., Werb, Z., and Ferrara, N. (1999). VEGF couples hypertrophic cartilage remodeling, ossification and angiogenesis during endochondral bone formation. *Nature Medicine*, 5(6):623–628.

[Giampietro et al., 2003] Giampietro, P. F., Peterson, M., Schneider, R., Davis, J. G., Raggio, C., Myers, E., Burke, S. W., Boachie-Adjei, O., and Mueller, C. M. (2003). Assessment of bone mineral density in adults and children with Marfan syndrome. *Osteoporosis International*, 14(7):559–563.

[Giraud-Guille et al., 2008] Giraud-Guille, M. M., Belamie, E., Mosser, G., Helary, C., Gobeaux, F., and Vigier, S. (2008). Liquid crystalline properties of type I collagen: Perspectives in tissue morphogenesis. *Comptes Rendus Chimie*, 11(3):245–252.

[Gjardy, 2017] Gjardy, A. (2017). *Investigation of osteocyte networks and bone material properties in healing bone*. PhD thesis, Humboldt Universität zu Berlin.

[Glatt et al., 2007] Glatt, V., Canalis, E., Stadmeyer, L., and Bouxsein, M. L. (2007). Age-related changes in trabecular architecture differ in female and male C57BL/6J mice. *Journal of Bone and Mineral Research*, 22(8):1197–1207.

[Glatter and Kratky, 1982] Glatter, O. and Kratky, O. (1982). *Small angle x-ray scattering.*, volume 36. London, Academic Press Inc.

[Goldstein et al., 2012] Goldstein, J., Newbury, D. E., Echlin, P., Joy, D. C., Jr., A. D. R., Lyman, C. E., Fiori, C., and Lifshin, E. (2012). Scanning Electron Microscopy and X-Ray Microanalysis: A Text for Biologists, Materials Scientists, and Geologists.

[Goldstein et al., 1981] Goldstein, J. I., Newbury, D. E., Echlin, P., Joy, D. C., Fiori, C., and Lifshin, E. (1981). Electron-Beam-Specimen Interactions. In *Scanning Electron Microscopy and X-Ray Microanalysis - A Text for Biologists*, chapter 3, pages 53–122. Plenum Press, New York, 2 edition.

[Gourrier et al., 2007] Gourrier, A., Wagermaier, W., Burghammer, M., Lammie, D., Gupta, H. S., Fratzl, P., Riekel, C., Wess, T. J., and Paris, O. (2007). Scanning X-ray imaging with small-angle scattering contrast. *Journal of Applied Crystallography*, 40(SUPPL. 1):78–82.

[Grabner et al., 2001] Grabner, B., Landis, W. J., Roschger, P., Rinnerthaler, S., Peterlik, H., Klaushofer, K., and Fratzl, P. (2001). Age- and genotype-dependence of bone material properties in the osteogenesis imperfecta murine model (oim). *Bone*, 29(5):453–457.

[Groth et al., 2015] Groth, K. A., Hove, H., Kyhl, K., Folkestad, L., Gaustadnes, M., Vejlstrup, N., Stochholm, K., Østergaard, J. R., Andersen, N. H., and Gravholt, C. H. (2015). Prevalence, incidence, and age at diagnosis in Marfan Syndrome Rare systemic diseases. *Orphanet Journal of Rare Diseases*, 10(1):1–10.

[Hall, 2015] Hall, B. K. (2015). Vertebrate Cartilages. In *Bones and Cartilage*, chapter 3, pages 43–59. Elsevier, London, 2 edition.

[Handschin and Stern, 1995] Handschin, R. G. and Stern, W. B. (1995). X-ray diffraction studies on the lattice perfection of human bone apatite (Crista Iliaca). *Bone*, 16(4 SUPPL.):355S–363S.

[Harley et al., 1990] Harley, V. R., Chan, D., Rogers, J. G., and Cole, W. G. (1990). Marfan syndrome: Absence of type I or III collagen structural defects in 25 patients. *Journal of Inherited Metabolic Disease*, 13(2):219–226.

[Hart et al., 2017] Hart, N. H., Nimphius, S., Rantalainen, T., Ireland, A., Siafarikas, A., and Newton, R. U. (2017). Mechanical basis of bone strength: Influence of bone material, bone structure and muscle action. *Journal of Musculoskeletal Neuronal Interactions*, 17(3):114–139.

[Hartley et al., 2020] Hartley, C., Folland, J. P., Kerslake, R., and Brooke-Wavell, K. (2020). High-Impact Exercise Increased Femoral Neck Bone Density With No Adverse Effects on Imaging Markers of Knee Osteoarthritis in Postmenopausal Women. *Journal of Bone and Mineral Research*, 35(1):53–63.

[Hartmann et al., 2021] Hartmann, M. A., Blouin, S., Misof, B. M., Fratzl-Zelman, N., Roschger, P., Berzlanovich, A., Gruber, G. M., Brugger, P. C., Zwerina, J., and Fratzl, P. (2021). Quantitative Backscattered Electron Imaging of Bone Using a Thermionic or a Field Emission Electron Source. *Calcified Tissue International*, 109(2):190–202.

[Hauge Bünger et al., 2006] Hauge Bünger, M., Foss, M., Erlacher, K., Bruun Hovgaard, M., Chevallier, J., Langdahl, B., Bünger, C., Birkedal, H., Besenbacher, F., and Skov Pedersen, J. (2006). Nanostructure of the neurocentral growth plate: Insight from scanning small angle X-ray scattering, atomic force microscopy and scanning electron microscopy. *Bone*, 39(3):530–541.

[Hemmatian et al., 2018] Hemmatian, H., Laurent, M. R., Bakker, A. D., Vanderschueren, D., Klein-Nulend, J., and van Lenthe, G. H. (2018). Age-related changes in female mouse cortical bone microporosity. *Bone*, 113:1–8.

[Hernandez et al., 2004] Hernandez, C. J., Majeska, R. J., and Schaffler, M. B. (2004). Osteocyte density in woven bone. *Bone*, 35(5):1095–1099.

[Hesse et al., 2015] Hesse, B., Varga, P., Langer, M., Pacureanu, A., Schrof, S., Männicke, N., Suhonen, H., Maurer, P., Cloetens, P., Peyrin, F., and Raum, K. (2015). Canalicular network morphology is the major determinant of the spatial distribution of mass density in human bone tissue: Evidence by means of synchrotron radiation phase-contrast nano-CT. *Journal of Bone and Mineral Research*, 30(2):346–356.

[Hoerth et al., 2018] Hoerth, R. M., Kerschnitzki, M., do Aido, M. I. F., Schmidt, I., Burghammer, M., Duda, G. N., Fratzl, P., Willie, B. M., and Wagermaier, W. (2018). Correlations between nanostructure and micromechanical properties of healing bone. *Journal of the Mechanical Behavior of Biomedical Materials*, 77:258–266.

[Hoerth et al., 2014] Hoerth, R. M., Seidt, B. M., Shah, M., Schwarz, C., Willie, B. M., Duda, G. N., Fratzl, P., and Wagermaier, W. (2014). Mechanical and structural properties of bone in non-critical and critical healing in rat. *Acta Biomaterialia*, 10(9):4009–4019.

[Hörl et al., 2019] Hörl, D., Rojas Rusak, F., Preusser, F., Tillberg, P., Randel, N., Chhetri, R. K., Cardona, A., Keller, P. J., Harz, H., Leonhardt, H., Treier, M., and Preibisch, S. (2019). BigStitcher: reconstructing high-resolution image datasets of cleared and expanded samples. *Nature Methods*, 16(9):870–874.

[Iagodovskiĭ et al., 1977] Iagodovskiĭ, V. S., Triftanidi, L. A., and Gorokhova, G. P. (1977). O vliianii kosmicheskogo poleta na kosti skeleta krysy (svetoopticheskoe i élektronno-mikroskopicheskoe issledovanie) [Effect of space flight on rat skeletal bones (an optical light and electron microscopic study)]. *Kosmicheskaia biologiia i aviakosmicheskaia meditsina*, 11(1):14–20.

[Isaksson et al., 2009a] Isaksson, H., Tolvanen, V., Finnilä, M. A., Iivarinen, J., Turunen, A., Silvast, T. S., Tuukkanen, J., Seppänen, K., Arokoski, J. P., Brama, P. A., Jurvelin, J. S., and Helminen, H. J. (2009a). Long-term voluntary exercise of male mice induces more beneficial effects on cancellous and cortical bone than on the collagenous matrix. *Experimental Gerontology*, 44(11):708–717.

[Isaksson et al., 2009b] Isaksson, H., Tolvanen, V., Finnilä, M. A., Iivarinen, J., Tuukkanen, J., Seppänen, K., Arokoski, J. P., Brama, P. A., Jurvelin, J. S., and Helminen, H. J. (2009b). Physical exercise improves properties of bone and its collagen network in growing and maturing mice. *Calcified Tissue International*, 85(3):247–256.

[Isojima and Sims, 2021] Isojima, T. and Sims, N. A. (2021). Cortical bone development, maintenance and porosity: genetic alterations in humans and mice influencing chondrocytes, osteoclasts, osteoblasts and osteocytes. *Cellular and Molecular Life Sciences*, 78(15):5755–5773.

[Jilka et al., 2012] Jilka, R. L., Noble, B., and Weinstein, R. S. (2012). Osteocyte apoptosis. *Bone*, 54(2):264–271.

[Judge et al., 2004] Judge, D. P., Biery, N. J., Keene, D. R., Geubtner, J., Myers, L., Huso, D. L., Sakai, L. Y., and Dietz, H. C. (2004). Evidence for a critical contribution of haploinsufficiency in the complex pathogenesis of Marfan syndrome. *Journal of Clinical Investigation*, 114(2):172–181.

[Kerschnitzki, 2012] Kerschnitzki, M. (2012). *Bone Material Characteristics Influenced by Osteocytes*. PhD thesis, Humboldt-Universität zu Berliln.

[Kerschnitzki et al., 2013] Kerschnitzki, M., Kollmannsberger, P., Burghammer, M., Duda, G. N., Weinkamer, R., Wagermaier, W., and Fratzl, P. (2013). Architecture of the osteocyte network correlates with bone material quality. *Journal of Bone and Mineral Research*, 28(8):1837–1845.

[Kerschnitzki et al., 2011a] Kerschnitzki, M., Wagermaier, W., Liu, Y., Roschger, P., Duda, G. N., and Fratzl, P. (2011a). Poorly ordered bone as an endogenous scaffold for the deposition of highly oriented lamellar tissue in rapidly growing ovine bone. *Cells, tissues, organs*, 194(2-4):119–23.

[Kerschnitzki et al., 2011b] Kerschnitzki, M., Wagermaier, W., Roschger, P., Seto, J., Shahar, R., Duda, G. N., Mundlos, S., and Fratzl, P. (2011b). The organization of the osteocyte network mirrors the extracellular matrix orientation in bone. *Journal of Structural Biology*, 173(2):303–311.

[Kesavan et al., 2005] Kesavan, C., Mohan, S., Oberholtzer, S., Wergedal, J. E., and Baylink, D. J. (2005). Mechanical loading-induced gene expression and BMD changes are different in two inbred mouse strains. *Journal of Applied Physiology*, 99(5):1951–1957.

[Kieffer and Wright, 2013] Kieffer, J. and Wright, J. P. (2013). PyFAI: A python library for high performance azimuthal integration on GPU. *Powder Diffraction*, 28(SUPPL.2):339–350.

[Klein-Nulend et al., 2013] Klein-Nulend, J., Bakker, A. D., Bacabac, R. G., Vatsa, A., and Weinbaum, S. (2013). Mechanosensation and transduction in osteocytes. *Bone*, 54(2):182–190.

[Klein-Nulend et al., 1995] Klein-Nulend, J., van der Plas, A., Semeins, C. M., Ajubi, N. E., Frangos, J. A., Nijweide, P., and Burger, E. H. (1995). Sensitivity of osteocytes to biomechanical stress in vitro. *the Fa*, 9:441–445.

[Knothe Tate, 2003] Knothe Tate, M. L. (2003). "Whither flows the fluid in bone?" An osteocyte's perspective. *Journal of Biomechanics*, 36(10):1409–1424.

[Kohlmeier et al., 1995] Kohlmeier, L., Gasner, C., Bachrach, L. K., and Marcus, R. (1995). The bone mineral status of patients with Marfan syndrome. *Journal of Bone and Mineral Research*, 10(10):1550–1555.

[Kohn et al., 2008] Kohn, D. H., Sahar, N. D., Wallace, J. M., Golcuk, K., and Morris, M. D. (2008). Exercise alters mineral and matrix composition in the absence of adding new bone. *Cells Tissues Organs*, 189(1-4):33–37.

[Kola et al., 2020] Kola, S. K., Begonia, M. T., Tiede-Lewis, L. A. M., Laughrey, L. E., Dallas, S. L., Johnson, M. L., and Ganesh, T. (2020). Osteocyte lacunar strain determination using multiscale finite element analysis. *Bone Reports*, 12(October 2019):100277.

[Kollmannsberger et al., 2017] Kollmannsberger, P., Kerschnitzki, M., Repp, F., Wagermaier, W., Weinkamer, R., and Fratzl, P. (2017). The small world of osteocytes: connectomics of the lacuno-canalicular network in bone. *New Journal of Physics*, 19(7):073019.

[Kratky et al., 1951] Kratky, O., Porod, G., and Kahovec, L. (1951). Einige Neuerungen in der Technik und Auswertung von Röntgen-Kleinwinkelmessungen. *Zeitschrift für Elektrochemie und angewandte physikalische Chemie*, 55(1):53–59.

[Krempien et al., 1976] Krempien, B., Manegold, C., Ritz, E., and Bommer, J. (1976). The influence of immobilization on osteocyte morphology - Osteocyte differential count and electron microscopical studies. *Virchows Archiv A Pathological Anatomy and Histology*, 370(1):55–68.

[Kruck et al., 2018] Kruck, B., Zimmermann, E. A., Damerow, S., Figge, C., Julien, C., Wulsten, D., Thiele, T., Martin, M., Hamdy, R., Reumann, M. K., Duda, G. N., Checa, S., and Willie, B. M. (2018). Sclerostin Neutralizing Antibody Treatment Enhances Bone Formation but Does Not Rescue Mechanically Induced Delayed Healing. *Journal of Bone and Mineral Research*, 33(9):1686–1697.

[Kusuzaki et al., 2000] Kusuzaki, K., Kageyama, N., Shinjo, H., Takeshita, H., Murata, H., Hashiguchi, S., Ashihara, T., and Hirasawa, Y. (2000). Development of bone canaliculi during bone repair. *Bone*, 27(5):655–659.

[LaComb et al., 2008] LaComb, R., Nadiarnykh, O., Townsend, S. S., and Campagnola, P. J. (2008). Phase matching considerations in second harmonic generation from tissues: Effects on emission directionality, conversion efficiency and observed morphology. *Optics Communications*, 281(7):1823–1832.

[Lafage-Proust et al., 1998] Lafage-Proust, M. H., Collet, P., Dubost, J. M., Laroche, N., Alexandre, C., and Vico, L. (1998). Space-related bone mineral redistribution and lack of bone mass recovery after reambulation in young rats. *American Journal of Physiology - Regulatory Integrative and Comparative Physiology*, 274(2 43-2).

[Lamers et al., 2010] Lamers, E., Frank Walboomers, X., Domanski, M., te Riet, J., van Delft, F. C., Luttge, R., Winnubst, L. A., Gardeniers, H. J., and Jansen, J. A. (2010). The influence of nanoscale grooved substrates on osteoblast behavior and extracellular matrix deposition. *Biomaterials*, 31(12):3307–3316.

[Lange, 2011] Lange, C. (2011). *Dissertation: Mineral deposition and maturation during bone development*. PhD thesis, Freie Univjersität Berlin.

[Lange et al., 2011] Lange, C., Li, C., Manjubala, I., Wagermaier, W., Kühnisch, J., Kolanczyk, M., Mundlos, S., Knaus, P., and Fratzl, P. (2011). Fetal and postnatal mouse bone tissue contains more calcium than is present in hydroxyapatite. *Journal of Structural Biology*, 176(2):159–167.

[Lavoie et al., 2005] Lavoie, P., Robitaille, G., Agharazii, M., Ledbetter, S., Lebel, M., and Larivière, R. (2005). Neutralization of transforming growth factor-β attenuates hypertension and prevents renal injury in uremic rats. *Journal of Hypertension*, 23(10):1895–1903.

[Liu et al., 2010] Liu, Y., Manjubala, I., Schell, H., Epari, D. R., Roschger, P., Duda, G. N., and Fratzl, P. (2010). Size and habit of mineral particles in bone and mineralized callus during bone healing in sheep. *Journal of Bone and Mineral Research*, 25(9):2029–2038.

[Lutz et al., 2012] Lutz, V., Sattler, M., Gallinat, S., Wenck, H., Poertner, R., and Fischer, F. (2012). Impact of collagen crosslinking on the second harmonic generation signal and the fluorescence lifetime of collagen autofluorescence. *Skin Research and Technology*, 18(2):168–179.

[Lynch et al., 2010] Lynch, M. E., Main, R. P., Xu, Q., Walsh, D. J., Schaffler, M. B., Wright, T. M., and Van Der Meulen, M. C. (2010). Cancellous bone adaptation to tibial compression is not sex dependent in growing mice. *Journal of Applied Physiology*, 109(3):685–691.

[Mader et al., 2013] Mader, K. S., Schneider, P., Müller, R., and Stampanoni, M. (2013). A quantitative framework for the 3D characterization of the osteocyte lacunar system. *Bone*, 57(1):142–154.

[Maggiano et al., 2015] Maggiano, I. S., Maggiano, C. M., Tiesler, V. G., Chi-Keb, J. R., and Stout, S. D. (2015). Drifting Diaphyses: Asymmetry in Diametric Growth and Adaptation Along the Humeral and Femoral Length. *Anatomical Record*, 298(10):1689–1699.

[Main et al., 2020] Main, R. P., Shefelbine, S. J., Meakin, L. B., Silva, M. J., van der Meulen, M. C., and Willie, B. M. (2020). Murine Axial Compression Tibial Loading Model to Study Bone Mechanobiology: Implementing the Model and Reporting Results. *Journal of Orthopaedic Research*, 38(2):233–252.

[Manjubala et al., 2009] Manjubala, I., Liu, Y., Epari, D. R., Roschger, P., Schell, H., Fratzl, P., and Duda, G. N. (2009). Spatial and temporal variations of mechanical properties and mineral content of the external callus during bone healing. *Bone*, 45(2):185–192.

[Marenzana et al., 2005] Marenzana, M., Shipley, A. M., Squitiero, P., Kunkel, J. G., and Rubinacci, A. (2005). Bone as an ion exchange organ: Evidence for instantaneous cell-dependent calcium efflux from bone not due to resorption. *Bone*, 37(4):545–554.

[Margaritondo, 2015] Margaritondo, G. (2015). Characteristics and Properties of Synchrotron radiation. In Mobilio, S., Boscherini, F., and Meneghini, C., editors, *Synchrotron Radiation - Basics, Methods and Applications*, chapter 2, pages 29–61. Springer Berlin Heidelberg, Berlin.

[Marotti et al., 1995] Marotti, G., Ferretti, M., Remaggi, F., and Palumbo, C. (1995). Quantitative evaluation on osteocyte canalicular density in human secondary osteons. *Bone*, 16(1):125–128.

[Marsell and Einhorn, 2012] Marsell, R. and Einhorn, T. A. (2012). The biology of fracture healing. *Injury*, 42(6):551–555.

[McKee et al., 2011] McKee, M. D., Pedraza, C. E., and Kaartinen, M. T. (2011). Osteopontin and wound healing in bone. *Cells Tissues Organs*, 194(2-4):313–319.

[Milovanovic et al., 2017] Milovanovic, P., Zimmermann, E. A., vom Scheidt, A., Hoffmann, B., Sarau, G., Yorgan, T., Schweizer, M., Amling, M., Christiansen, S., and Busse, B. (2017). The Formation of Calcified Nanospherites during Micropetrosis Represents a Unique Mineralization Mechanism in Aged Human Bone. *Small*, 13(3):1–10.

[Minsky, 1987] Minsky, M. (1987). Memoir on Inventing the Confocal Scanning Microscope. *Scanning*, 10(1988):128–138.

[Moura et al., 2006] Moura, B., Tubach, F., Sulpice, M., Boileau, C., Jondeau, G., Muti, C., Chevallier, B., Ounnoughene, Y., and Parc, J.-m. L. (2006). Bone mineral density in Marfan syndrome . A large case-control study. *Joint Bone Spine*, 73(6):733–735.

[Neumann and Gest, 2020] Neumann, P. E. and Gest, T. R. (2020). How many bones? Every bone in my body. *Clinical Anatomy*, 33(2):187–191.

[Nissinen et al., 1993] Nissinen, M., Heliövaara, M., Seitsamo, J., and Poussa, M. (1993). Trunk Asymmetry, Posture, Growth, and Risk of Sciolosis. *Spine*, 18(1):8–13.

[Nistala et al., 2010a] Nistala, H., Lee-Arteaga, S., Carta, L., Cook, J. R., Smaldone, S., Siciliano, G., Rifkin, A. N., Dietz, H. C., Rifkin, D. B., and Ramirez, F. (2010a). Differential effects of alendronate and losartan therapy on osteopenia and aortic aneurysm in mice with severe Marfan syndrome. *Human Molecular Genetics*, 19(24):4790–4798.

[Nistala et al., 2010b] Nistala, H., Lee-Arteaga, S., Smaldone, S., Siciliano, G., and Ramirez, F. (2010b). Extracellular microfibrils control osteoblast-supported osteoclastogenesis by restricting TGFβ stimulation of RANKL production. *Journal of Biological Chemistry*, 285(44):34126–34133.

[Nistala et al., 2010c] Nistala, H., Lee-Arteaga Sui, Smaldone, S., Siciliano, G., Carta, L., Ono, R. N., Sengle, G., Arteaga-Solis, E., Levasseur, R., Ducy, P., Sakai, L. Y., Karsenty, G., Ramirez, F., Lee-Arteaga, S., Smaldone, S., Siciliano, G., Carta, L., Ono, R. N., Sengle, G., Arteaga-Solis, E., Levasseur, R., Ducy, P., Sakai, L. Y., Karsenty, G., and Ramirez, F. (2010c). Fibrillin-1 and -2 differentially modulate endogenous TGF-β and BMP bioavailability during bone formation. *Journal of Cell Biology*, 190(6):1107–1121.

[Nogami et al., 1979] Nogami, H., Oohira, A., Ozeki, K., Oki, T., Ogino, T., and Murachi, S. (1979). Ultrastructure of cartilage in heritable disorders of connective tissue. *Clinical Orthopaedics and Related Research*, No. 143:251–259.

[Nuzzo et al., 2002] Nuzzo, S., Lafage-Proust, M. H., Martin-Badosa, E., Boivin, G., Thomas, T., Alexandre, C., and Peyrin, F. (2002). Synchrotron radiation microtomography allows the analysis of three-dimensional microarchitecture and degree of mineralization of human iliac crest biopsy specimens: Effects of etidronate treatment. *Journal of Bone and Mineral Research*, 17(8):1372–1382.

[O'Brien et al., 2013] O'Brien, C. A., Nakashima, T., and Takayanagi, H. (2013). Osteocyte control of osteoclastogenesis. *Bone*, 54(2):258–263.

[Olszta et al., 2007] Olszta, M. J., Cheng, X., Jee, S. S., Kumar, R., Kim, Y. Y., Kaufman, M. J., Douglas, E. P., and Gower, L. B. (2007). Bone structure and formation: A new perspective. *Materials Science and Engineering R: Reports*, 58(3-5):77–116.

[Orgel et al., 2011] Orgel, J. P., San Antonio, J. D., and Antipova, O. (2011). Molecular and structural mapping of collagen fibril interactions. *Connective Tissue Research*, 52(1):2–17.

[Otsu, 1979] Otsu, N. (1979). A Threshold selection method from gray-level histograms. *IEEE TRANSACTIONS ON SYSTREMS, MAN, AND CYBERNETICS,*, SMC-9(1):62–66.

[Owan et al., 1997] Owan, I., Burr, D. B., Turner, C. H., Qiu, J., Tu, Y., Onyia, J. E., and Duncan, R. L. (1997). Mechanotransduction in bone: osteoblasts are more responsive to fluid forces than mechanical strain. *Physiology*, 273(3 Pt 1):C810–C815.

[Pabisch et al., 2013] Pabisch, S., Wagermaier, W., Zander, T., Li, C., and Fratzl, P. (2013). Imaging the Nanostructure of Bone and Dentin Through Small- and Wide-Angle X-Ray Scattering. In De Yoreo, J. J. B. T. M. i. E., editor, *Methods in Enzymology*, volume 532 Resear, chapter 18, pages 391–413. Academic Press, San Diego, 1st edition.

[Pereira et al., 1999] Pereira, L., Lee, S. Y., Gayraud, B., Andrikopoulos, K., Shapiro, S. D., Bunton, T., Biery, N. J., Dietz, H. C., Sakai, L. Y., and Ramirez, F. (1999). Pathogenetic sequence for aneurysm revealed in mice underexpressing fibrillin-1. *Proceedings of the National Academy of Sciences*, 96(7):3819–3823.

[Perkins et al., 1994] Perkins, S. L., Gibbons, R., Kling, S., and Kahn, A. J. (1994). Age-related bone loss in mice is associated with an increased osteoclast progenitor pool. *Bone*, 15(1):65–72.

[Porod, 1951] Porod, G. (1951). Die Röntgenkleinwinkelstreuung von dichtgepackten kolloiden Systemen - I. Teil. *Kolloid-Zeitschrift*, 124(2):83–114.

[Prasad et al., 2010] Prasad, J., Wiater, B. P., Nork, S. E., Bain, S. D., and Gross, T. S. (2010). Characterizing gait induced normal strains in a murine tibia cortical bone defect model. *Journal of Biomechanics*, 43(14):2765–2770.

[Preininger et al., 2011] Preininger, B., Checa, S., Molnar, F. L., Fratzl, P., Duda, G. N., and Raum, K. (2011). Spatial-temporal mapping of bone structural and elastic properties in a sheep model following osteotomy. *Ultrasound in medicine and biology*, 37(3):474–483.

[Price and Jerome, 2018] Price, R. L. and Jerome, W. G. (2018). Introduction and Historical Perspective. In Price, R. L. and Jerome, W. G., editors, *Basic Confocal Microscopy*, chapter 1, pages 1–21. Springer Nature Switzerland AG, Cham, 2 edition.

[Qing et al., 2012] Qing, H., Ardeshirpour, L., Divieti Pajevic, P., Dusevich, V., Jähn, K., Kato, S., Wysolmerski, J., and Bonewald, L. F. (2012). Demonstration of osteocytic perilacunar/canalicular remodeling in mice during lactation. *Journal of Bone and Mineral Research*, 27(5):1018–1029.

[Qing and Bonewald, 2009] Qing, H. and Bonewald, L. F. (2009). Osteocyte remodeling of the perilacunar and pericanalicular matrix. *International journal of oral science*, 1(2):59–65.

[Qiu et al., 2002] Qiu, S., Rao, D., Palnitkar, S., and Parfitt, A. (2002). Relationships between osteocyte density and bone formation rate in human cancellous bone. *Bone*, 31(6):709–711.

[Raggatt and Partridge, 2010] Raggatt, L. J. and Partridge, N. C. (2010). Cellular and molecular mechanisms of bone remodeling. *The Journal of biological chemistry*, 285(33):25103–8.

[Rauch, 2005] Rauch, F. (2005). Bone growth in length and width: The Yin and Yang of bone stability. *Journal of Musculoskeletal Neuronal Interactions*, 5(3):194–201.

[Razi et al., 2015] Razi, H., Birkhold, A. I., Zaslansky, P., Weinkamer, R., Duda, G. N., Willie, B. M., and Checa, S. (2015). Skeletal maturity leads to a reduction in the strain magnitudes induced within the bone: A murine tibia study. *Acta Biomaterialia*, 13:301–310.

[Repp et al., 2017] Repp, F., Kollmannsberger, P., Roschger, A., Kerschnitzki, M., Berzlanovich, A., Gruber, G., Roschger, P., Wagermaier, W., and Weinkamer, R. (2017). Spatial heterogeneity in the canalicular density of the osteocyte network in human osteons. *Bone Reports*, 6:101–108.

[Reznikov et al., 2018] Reznikov, N., Bilton, M., Lari, L., Stevens, M. M., and Kröger, R. (2018). Fractal-like hierarchical organization of bone begins at the nanoscale. *Science*, 360(6388):eaao2189.

[Reznikov et al., 2015] Reznikov, N., Chase, H., Brumfeld, V., Shahar, R., and Weiner, S. (2015). The 3D structure of the collagen fibril network in human trabecular bone: Relation to trabecular organization. *Bone*, 71:189–195.

[Reznikov et al., 2014a] Reznikov, N., Shahar, R., and Weiner, S. (2014a). Bone hierarchical structure in three dimensions. *Acta Biomaterialia*, 10(9):3815–3826.

[Reznikov et al., 2014b] Reznikov, N., Shahar, R., and Weiner, S. (2014b). Three-dimensional structure of human lamellar bone: The presence of two different materials and new insights into the hierarchical organization. *Bone*, 59:93–104.

[Rho et al., 1998] Rho, J. Y., Kuhn-Spearing, L., and Zioupos, P. (1998). Mechanical properties and the hierarchical structure of bone. *Medical Engineering and Physics*, 20(2):92–102.

[Richman et al., 2001] Richman, C., Kutilek, S., Miyakoshi, N., Srivastava, A. K., Beamer, W. G., Donahue, L. R., Rosen, C. J., Wergedal, J. E., Baylink, D. J., and Mohan, S. (2001). Postnatal and pubertal skeletal changes contribute predominantly to the differences in peak bone density between C3H/HeJ and C57BL/6J mice. *Journal of Bone and Mineral Research*, 16(2):386–397.

[Rinnerthaler et al., 1999] Rinnerthaler, S., Roschger, P., Jakob, H. F., Nader, A., Klaushofer, K., and Fratzl, P. (1999). Scanning small angle X-ray scattering analysis of human bone sections. *Calcified Tissue International*, 64(5):422–429.

[Röntgen et al., 2010] Röntgen, V., Blakytny, R., Matthys, R., Landauer, M., Wehner, T., Göckelmann, M., Jermendy, P., Amling, M., Schinke, T., Claes, L., and Ignatius, A. (2010). Fracture healing in mice under controlled rigid and flexible conditions using an adjustable external fixator. *Journal of Orthopaedic Research*, 28(11):1456–1462.

[Roschger, 2015] Roschger, A. (2015). *Quantitative analysis of local mineral content and composition during bone growth and remodeling*. PhD thesis, Humboldt-Universität zu Berlin.

[Roschger et al., 2019] Roschger, A., Roschger, P., Wagermaier, W., Chen, J., van Tol, A. F., Repp, F., Blouin, S., Berzlanovich, A., Gruber, G. M., Klaushofer, K., Fratzl, P., and Weinkamer, R. (2019). The contribution of the pericanalicular matrix to mineral content in human osteonal bone. *Bone*, 123:76–85.

[Roschger et al., 2020] Roschger, A., Wagermaier, W., Gamsjaeger, S., Hassler, N., Schmidt, I., Blouin, S., Berzlanovich, A., Gruber, G. M., Weinkamer, R., Roschger, P., Paschalis, E. P., Klaushofer, K., and Fratzl, P. (2020). Newly formed and remodeled human bone exhibits differences in the mineralization process. *Acta Biomaterialia*, 104:221–230.

[Roschger et al., 1998] Roschger, P., Fratzl, P., Eschberger, J., and Klaushofer, K. (1998). Validation of quantitative backscattered electron imaging for the measurement of mineral density distribution in human bone biopsies. *Bone*, 23(4):319–26.

[Roschger et al., 2001] Roschger, P., Grabner, B. M., Rinnerthaler, S., Tesch, W., Kneissel, M., Berzlanovich, A., Klaushofer, K., and Fratzl, P. (2001). Structural Development of the Mineralized Tissue in the Human L4 Vertebral Body. *Journal of Structural Biology*, 136:126–136.

[Roschger et al., 2008] Roschger, P., Paschalis, E. P., Fratzl, P., and Klaushofer, K. (2008). Bone mineralization density distribution in health and disease. *Bone*, 42(3):456–466.

[Ruffoni et al., 2007] Ruffoni, D., Fratzl, P., Roschger, P., Klaushofer, K., and Weinkamer, R. (2007). The bone mineralization density distribution as a fingerprint of the mineralization process. *Bone*, 40(5):1308–1319.

[Sawae et al., 2003] Sawae, Y., Sahara, T., and Sasaki, T. (2003). Osteoclast differentiation at growth plate cartilage-trabecular bone junction in newborn rat femur. *Journal of Electron Microscopy*, 52(6):493–502.

[Schemenz et al., 2020] Schemenz, V., Gjardy, A., Chamasemani, F. F., Roschger, A., Roschger, P., Zaslansky, P., Helfen, L., Burghammer, M., Fratzl, P., Weinkamer, R., Brunner, R., Willie, B. M., and Wagermaier, W. (2020). Heterogeneity of the osteocyte lacuno-canalicular network architecture and material characteristics across different tissue types in healing bone. *Journal of Structural Biology*, 212(2):2–14.

[Scherrer, 1912] Scherrer, P. (1912). *Bestimmung der inneren Struktur und der Größe von Kolloidteilchen mittels Röntgenstrahlen*, pages 387–409. Springer Berlin Heidelberg, Berlin, Heidelberg.

[Schmidt-Bleek et al., 2014] Schmidt-Bleek, K., Petersen, A., Dienelt, A., Schwarz, C., and Duda, G. N. (2014). Initiation and early control of tissue regeneration – bone healing as a model system for tissue regeneration. *Expert Opinion on Biological Therapy*, 14(2):247–259.

[Schneider et al., 2012] Schneider, C. A., Rasband, W. S., and Eliceiri, K. W. (2012). NIH Image to ImageJ: 25 years of image analysis. *Nature Methods*, 9(7):671–675.

[Schneider et al., 2007] Schneider, P., Stauber, M., Voide, R., Stampanoni, M., Donahue, L. R., and Müller, R. (2007). Ultrastructural properties in cortical bone vary greatly in two inbred strains of mice as assessed by synchrotron light based micro- and nano-CT. *Journal of Bone and Mineral Research*, 22(10):1557–1570.

[Seeman, 2003] Seeman, E. (2003). Periosteal Bone Formation — A Neglected Determinant of Bone Strength. *New England Journal of Medicine*, 349(4):320–323.

[Seiler, 1983] Seiler, H. (1983). Secondary electron emission in the scanning electron microscope. *Journal of Applied Physics*, 54(11).

[Sfeir et al., 2005] Sfeir, C., Ho, L., Doll, B. a., Azari, K., and Holinger, J. O. (2005). Fracture repair. In Lieberman, J. R. and Friedlaender, G. E., editors, *Bone Regeneration and Repair: biology and clinical applications*, chapter 2, pages 21–45. Humana Press, Totowa, New Jersey, 1 edition.

[Shapiro, 2008] Shapiro, F. (2008). Bone development and its relation to fracture repair. The role of mesenchymal osteoblasts and surface osteoblasts. *European Cells and Materials*, 15:53–76.

[Sharir et al., 2013] Sharir, A., Milgram, J., Dubnov-Raz, G., Zelzer, E., and Shahar, R. (2013). A temporary decrease in mineral density in perinatal mouse long bones. *Bone*, 52(1):197–205.

[Shipov et al., 2013] Shipov, A., Zaslansky, P., Riesemeier, H., Segev, G., Atkins, A., and Shahar, R. (2013). Unremodeled endochondral bone is a major architectural component of the cortical bone of the rat (Rattus norvegicus). *Journal of Structural Biology*, 183(2):132–140.

[Shores et al., 1994] Shores, J., Berger, K. R., Murphy, E. A., and Pyeritz, R. E. (1994). Progression of aortic dilatation and the benefit of long-term beta-adrenergic blockade in marfan´s syndrome. *The New England Journal of Medicine*, 330(19):1335–1341.

[Siddiqui and Partridge, 2016] Siddiqui, J. A. and Partridge, N. C. (2016). Physiological bone remodeling: Systemic regulation and growth factor involvement. *Physiology*, 31(3):233–245.

[Silbermann et al., 1987] Silbermann, M., Weiss, A., AZ, R., Eilam, Y., Szydel, N., and Gershon, D. (1987). Age-related trend for osteopenia in femurs of female C57BL/6 mice. *Comprehensive gerontology. Section A, Clinical and Laboratory Sciences*, 1(1):45–51.

[Skedros et al., 1993] Skedros, J. G., Bloebaum, R. D., Bachus, K. N., and Boyce, T. M. (1993). The meaning of graylevels in backscattered electron images of bone. *Journal of Biomedical Materials Research*, 27(1):47–56.

[Skerry et al., 1989] Skerry, T. M., Lanyon, L. E., Bitensky, L., and Chayen, J. (1989). Early strain-related changes in enzyme activity in osteocytes following bone loading in vivo. *Journal of Bone and Mineral Research*, 4(5):783–788.

[Snyder, 1999] Snyder, R. L. (1999). X-Ray Diffraction. In Lifshin, E., editor, *X-ray Characterization of Materials*, chapter 1, pages 4–100. Wiley-VCH, Weinheim.

[Sontag, 1986] Sontag, W. (1986). Quantitative measurements of periosteal and cortical-endosteal bone formation and resorption in the midshaft of female rat femur. *Bone*, 7(1):55–62.

[Stampanoni et al., 2002] Stampanoni, M., Borchert, G., Abela, R., and Rüegsegger, P. (2002). Bragg magnifier: A detector for submicrometer x-ray computer tomography. *Journal of Applied Physics*, 92(12):7630–7635.

[Statnik et al., 2020] Statnik, E. S., Salimon, A. I., Besnard, C., Chen, J., Wang, Z., Moxham, T., Dolbnya, I. P., and Korsunsky, A. M. (2020). Ovine Bone Morphology and Deformation Analysis Using Synchrotron X-ray Imaging and Scattering. *Quantum Beam Science*, 4(3):29.

[Stauber and Müller, 2008] Stauber, M. and Müller, R. (2008). Micro-Computed Tomography: A Method for the Non-Destructive Evaluation of the Three-Dimensional Structure of Biological Specimens. In Westendorf, J. J., editor, *Osteoporosis - Methods and Protocols*, chapter Part V Ima, pages 273–292. Humana Press, Rochester, MN, USA.

[Stein et al., 1998] Stein, M. S., Thomas, C. D., Feik, S. A., Wark, J. D., and Clement, J. G. (1998). Bone size and mechanics at the femoral diaphysis across age and sex. *Journal of Biomechanics*, 31(12):1101–1110.

[Stock et al., 2011] Stock, S. R., Yuan, F., Brinson, L. C., and Almer, J. D. (2011). Internal strain gradients quantified in bone under load using high-energy X-ray scattering. *Journal of Biomechanics*, 44(2):291–296.

[Sugiyama et al., 2012] Sugiyama, T., Meakin, L. B., Browne, W. J., Galea, G. L., Price, J. S., and Lanyon, L. E. (2012). Bones' adaptive response to mechanical loading is essentially linear between the low strains associated with disuse and the high strains associated with the lamellar/woven bone transition. *Journal of Bone and Mineral Research*, 27(8):1784–1793.

[Sugiyama et al., 2010] Sugiyama, T., Price, J. S., and Lanyon, L. E. (2010). Functional adaptation to mechanical loading in both cortical and cancellous bone is controlled locally and is confined to the loaded bones. *Bone*, 46(2):314–321.

[Sugiyama et al., 2008] Sugiyama, T., Saxon, L. K., Zaman, G., Moustafa, A., Sunters, A., Price, J. S., and Lanyon, L. E. (2008). Mechanical loading enhances the anabolic effects of intermittent parathyroid hormone (1-34) on trabecular and cortical bone in mice. *Bone*, 43(2):238–248.

[Tatsumi et al., 2007] Tatsumi, S., Ishii, K., Amizuka, N., Li, M., Kobayashi, T., Kohno, K., Ito, M., Takeshita, S., and Ikeda, K. (2007). Targeted Ablation of Osteocytes Induces Osteoporosis with Defective Mechanotransduction. *Cell Metabolism*, 5(6):464–475.

[Teti and Zallone, 2009] Teti, A. and Zallone, A. (2009). Do osteocytes contribute to bone mineral homeostasis? Osteocytic osteolysis revisited. *Bone*, 44(1):11–16.

[Tidswell et al., 2008] Tidswell, H. K., Innes, J. F., Avery, N. C., Clegg, P. D., Barr, A. R., Vaughan-Thomas, A., Wakley, G., and Tarlton, J. F. (2008). High-intensity exercise induces structural, compositional and metabolic changes in cuboidal bones - findings from an equine athlete model. *Bone*, 43(4):724–733.

[Tiede-Lewis and Dallas, 2019] Tiede-Lewis, L. A. M. and Dallas, S. L. (2019). Changes in the osteocyte lacunocanalicular network with aging. *Bone*, 122(January):101–113.

[Tiede-Lewis et al., 2017] Tiede-Lewis, L. A. M., Xie, Y., Hulbert, M. A., Campos, R., Dallas, M. R., Dusevich, V., Bonewald, L. F., and Dallas, S. L. (2017). Degeneration of the osteocyte network in the C57BL/6 mouse model of aging. *Aging*, 9(10):2187–2205.

[Tiedemann et al., 2013] Tiedemann, K., Boraschi-Diaz, I., Rajakumar, I., Kaur, J., Roughley, P., Reinhardt, D. P., and Komarova, S. V. (2013). Fibrillin-1 directly regulates osteoclast formation and function by a dual mechanism. *Journal of Cell Science*, 126(18):4187–4194.

[Tomboulian and Hartman, 1956] Tomboulian, D. H. and Hartman, P. L. (1956). Spectral and Angular Distribution of Ultraviolet Radiation from the 300-Mev Cornell Synchrotron. *Physical Review*, 102(6):1423–1447.

[Turunen et al., 2016] Turunen, M. J., Kaspersen, J. D., Olsson, U., Guizar-Sicairos, M., Bech, M., Schaff, F., Tägil, M., Jurvelin, J. S., and Isaksson, H. (2016). Bone mineral crystal size and organization vary across mature rat bone cortex. *Journal of Structural Biology*, 195(3):337–344.

[Van der Rest and Garrone, 1991] Van der Rest, M. and Garrone, R. (1991). Collagen family of proteins. *The FASEB Journal*, 5(13):2814–2823.

[Van Tol, 2020] Van Tol, A. F. (2020). *Function of the Osteocyte Lacunocanalicular Network in Bone Mechanoresponsiveness*. PhD thesis, Humboldt Universität zu Berlin.

[Van Tol et al., 2020] Van Tol, A. F., Schemenz, V., Wagermaier, W., Roschger, A., Razi, H., Vitienes, I., Fratzl, P., Willie, B. M., and Weinkamer, R. (2020). The mechanoresponse of bone is closely related to the osteocyte lacunocanalicular network architecture. *Proceedings of the National Academy of Sciences of the United States of America*, 117(51):32251–32259.

[Varga et al., 2014] Varga, P., Hesse, B., Langer, M., Schrof, S., Männicke, N., Suhonen, H., Pacureanu, A., Pahr, D., Peyrin, F., and Raum, K. (2014). Synchrotron X-ray phase nano-tomography-based analysis of the lacunar–canalicular network morphology and its relation to the strains experienced by osteocytes in situ as predicted by case-specific finite element analysis. *Biomechanics and Modeling in Mechanobiology*, 14(2):267–282.

[Vashishth et al., 2002] Vashishth, D., Gibson, G., Kimura, J., Schaffler, M. B., and Fyhrie, D. P. (2002). Determination of bone volume by osteocyte population. *Anatomical Record*, 267(4):292–295.

[Vatsa et al., 2008] Vatsa, A., Breuls, R. G., Semeins, C. M., Salmon, P. L., Smit, T. H., and Klein-Nulend, J. (2008). Osteocyte morphology in fibula and calvaria — Is there a role for mechanosensing? *Bone*, 43(3):452–458.

[Verborgt et al., 2000] Verborgt, O., Gibson, G. J., and Schaffler, M. B. (2000). Loss of Osteocyte Integrity in Association with Microdamage and Bone Remodeling After Fatigue In Vivo. *Journal of Bone and Mineral Research*, 15(1):60–67.

[Verbruggen et al., 2014] Verbruggen, S. W., Vaughan, T. J., and McNamara, L. M. (2014). Fluid flow in the osteocyte mechanical environment: A fluid-structure interaction approach. *Biomechanics and Modeling in Mechanobiology*, 13(1):85–97.

[Vetter et al., 1990] Vetter, U., Mayerhofer, R., Lang, D., v. Bernuth, G., Ranke, M. B., and Schmaltz, A. A. (1990). The Marfan syndrome -analysis of growth and cardiovascular manifestation. *European Journal of Pediatrics*, 149(7):452–456.

[Villemure and Stokes, 2009] Villemure, I. and Stokes, I. A. F. (2009). Growth plate mechanics and mechanobiology. A survey of present understanding.

[Voide et al., 2011] Voide, R., Schneider, P., Stauber, M., van Lenthe, G. H., Stampanoni, M., and Müller, R. (2011). The importance of murine cortical bone microstructure for microcrack initiation and propagation. *Bone*, 49(6):1186–1193.

[Walji et al., 2016] Walji, T. A., Turecamo, S. E., DeMarsilis, A. J., Sakai, L. Y., Mecham, R. P., and Craft, C. S. (2016). Characterization of metabolic health in mouse models of fibrillin-1 perturbation. *Matrix Biology*, 55:63–76.

[Wang et al., 2003] Wang, J. H., Jia, F., Gilbert, T. W., and Woo, S. L. (2003). Cell orientation determines the alignment of cell-produced collagenous matrix. *Journal of Biomechanics*, 36(1):97–102.

[Wang et al., 2007] Wang, Y., McNamara, L. M., Schaffler, M. B., and Weinbaum, S. (2007). A model for the role of integrins in flow induced mechanotransduction in osteyocytes. *Bioengineering, Proceedings of the Northeast Conference*, 104(40):39–40.

[Wataha et al., 2001] Wataha, J. C., O'Dell, N. L., Singh, B. B., Ghazi, M., Whitford, G. M., and Lockwood, P. E. (2001). Relating nickel-induced tissue inflammation to nickel releasein vivo. *Journal of Biomedical Materials Research*, 58(5):537–544.

[Webster et al., 2012] Webster, D., Wirth, A., Van Lenthe, G. H., and Müller, R. (2012). Experimental and finite element analysis of the mouse caudal vertebrae loading model: prediction of cortical and trabecular bone adaptation. *Biomech Model Mechanobiol*, 11:221–230.

[Weinbaum et al., 1994] Weinbaum, S., Cowin, S., and Zeng, Y. (1994). A model for the excitation of osteocytes by mechanical loading-induced bone fluid shear stresses. *Journal of Biomechanics*, 27(3):339–360.

[Weiner and Wagner, 1998] Weiner, S. and Wagner, H. D. (1998). THE MATERIAL BONE: Structure-Mechanical Function Relations. *Annual Review of Materials Science*, 28(1):271–298.

[Weinkamer and Fratzl, 2011] Weinkamer, R. and Fratzl, P. (2011). Mechanical adaptation of biological materials — The examples of bone and wood. *Materials Science and Engineering: C*, 31(6):1164–1173.

[Wenk and Heidelbach, 1999] Wenk, H. R. and Heidelbach, F. (1999). Crystal alignment of carbonated apatite in bone and calcified tendon: Results from quantitative texture analysis. *Bone*, 24(4):361–369.

[Whalen et al., 1988] Whalen, R. T., Carter, D. R., and Steele, C. R. (1988). Influence of physical activity on the regulation of bone density. *Journal of Biomechanics*, 21(10):825–837.

[Whitworth et al., 2006] Whitworth, A. L., Mann, N. H., and Larkum, A. W. D. (2006). Bone Geometry, Density, and Microarchitecture in the Distal Radius and Tibia in Adults With Marfan Syndrome Assessed HR-pQCT. *Ultrasound Obstet Gynecol.*, 50(6):776–780.

[Willie et al., 2013] Willie, B. M., Birkhold, A. I., Razi, H., Thiele, T., Aido, M., Kruck, B., Schill, A., Checa, S., Main, R. P., and Duda, G. N. (2013). Diminished response to in vivo mechanical loading in trabecular and not cortical bone in adulthood of female C57Bl/6 mice coincides with a reduction in deformation to load. *Bone*, 55(2):335–346.

[Willie et al., 2020] Willie, B. M., Zimmermann, E. A., Vitienes, I., Main, R. P., and Komarova, S. V. (2020). Bone adaptation: Safety factors and load predictability in shaping skeletal form. *Bone*, 131(July 2019):115114.

[Winick, 1998] Winick, H. (1998). Synchrotron radiation sources - Present capabilities and future directions. *Journal of Synchrotron Radiation*, 5(3):168–175.

[Winkler et al., 2003] Winkler, D. G., Sutherland, M. K., Geoghegan, J. C., Yu, C., Hayes, T., Skonier, J. E., Shpektor, D., Jonas, M., Kovacevich, B. R., Staehling-Hampton, K., Appleby, M., Brunkow, M. E., and Latham, J. A. (2003). Osteocyte control of bone formation via sclerostin, a novel BMP antagonist. *EMBO Journal*, 22(23):6267–6276.

[Wolff, 1867] Wolff, J. (1867). Ueber die innere Architectur der linochen und ihre Bedeutung fiir die Frage vom Knochenwachsthum . *Archiv für pathologische Anatomie und Physiologie und für klinische Medicin*, 50:389–450.

[Yang et al., 2011] Yang, P. F., Brüggemann, G.-P., and Rittweger, J. (2011). What do we currently know from in vivo bone strain measurements in humans? *Journal of Musculoskeletal and Neuronal Interactions*, 11(1):8–20.

[Yeni et al., 2001] Yeni, Y. N., Vashishth, D., and Fyhrie, D. P. (2001). Estimation of bone matrix apparent stiffness variation caused by osteocyte lacunar size and density. *Journal of Biomechanical Engineering*, 123(1):10–17.

[You et al., 2001] You, L., Cowin, S. C., Schaffler, M. B., and Weinbaum, S. (2001). A model for strain amplification in the actin cytoskeleton of osteocytes due to fluid drag on pericellular matrix. *Journal of Biomechanics*, 34(11):1375–1386.

Appendix

A. Python script for image registration

```python
#!/usr/bin/env python3
"""
Created on Fri 12.02.2021

@author: schemenz
"""

import cv2
import numpy as np
import argparse
import os
import csv
from PIL import Image

CSV_ENDING = ".csv"

def table_to_img(table, inv_res, dtype=np.float64):
    table[:, 0:2] *= inv_res
    table[:, 0:2] -= np.amin(table, axis=0)[0:2]
    idxs = table[:, 0:2].astype(int).tolist()
    print(table[:, 0:2].astype(int))
    rows, cols = zip(*idxs)
    vals = table[:, 2].tolist()
    sz = (np.unique(table[:, 0]).size, np.unique(table[:,1]).size)
    print("Size: {}x{}".format(sz[0], sz[1]))
    res = np.empty(sz, dtype)
    res[:] = np.NaN
    res[rows, cols] = vals
    return res

def read_data(dir, offsets):
    files = [f for f in os.listdir(dir) if os.path.isfile(os.path.join(dir,
    f))]
    imgs = []
    for f in files:
        splits = os.path.splitext(f)[0].split("_")
        if len(splits) < 2:
            raise ValueError("File name " + f + "  needs to have the
    resolution behind the last _ ")
        resolution = float(splits[-1])
        offset = offsets[os.path.splitext(f)[0]]
        if os.path.splitext(f)[1] == CSV_ENDING:
            arr = np.genfromtxt(os.path.join(dir, f), delimiter=',')
            arr = table_to_img(arr, 1000 / resolution) # Annahme: Angaben
    in micro meter
            # vermutlich musst du das noch flippen, siehe https://numpy.org
    /doc/stable/reference/generated/numpy.flip.html
        else:
            img_path = os.path.join(dir, f)
            if Image.open(img_path).mode == "F":
                color = cv2.imread(img_path, cv2.IMREAD_ANYDEPTH)
            else:
                color = cv2.imread(img_path)
            arr = cv2.cvtColor(color, cv2.COLOR_BGR2GRAY)
        #perform rotation
```

```
52          rows, cols = arr.shape
53          # cols-1 and rows-1 are the coordinate limits.
54          M = cv2.getRotationMatrix2D(((cols - 1) / 2.0, (rows - 1) / 2.0),
    offset[2], 1)
55          arr = cv2.warpAffine(arr, M, (cols, rows), borderMode=cv2.
    BORDER_CONSTANT, borderValue=np.NaN)
56          imgs.append((arr, resolution, offset))
57      return imgs
58
59
60  def join_data(imgs):
61      by_type = list(zip(*imgs))
62      scales = np.array(by_type[1])
63      scales /= np.amax(scales)
64      scaled_offsets = [s * np.array(offset) for s, offset in zip(scales,
    by_type[2])]
65      ymin = [int(so[0]) for so in scaled_offsets]
66      ymax = [int(img.shape[0] * s + so[0]) for img, so, s in zip(by_type[0],
     scaled_offsets, scales)]
67      xmin = [int(so[1]) for so, s in zip(scaled_offsets, scales)]
68      xmax = [int(img.shape[1] * s + so[1]) for img, so, s in zip(by_type[0],
     scaled_offsets, scales)]
69      w, h = max(xmax) - min(xmin), max(ymax) - min(ymin)
70      canvas = np.zeros((h, w, len(imgs)), dtype=np.float64)
71      as_np = np.stack(scaled_offsets, axis=0)
72      offset_shift = -np.amin(as_np, axis=0).astype(int)
73      for i, img in enumerate(imgs):
74          scaled_img = cv2.resize(img[0], (xmax[i] - xmin[i], ymax[i] - ymin[
    i]))
75          canvas[ymin[i] + offset_shift[0]:ymax[i] + offset_shift[0], xmin[i]
     + offset_shift[0]:xmax[i] + offset_shift[1],
76          i] = scaled_img
77      return canvas
78
79
80  def viz(canvas):
81      weight = 1. / canvas.shape[2]
82      blended = np.zeros_like(canvas[:, :, 0])
83      for i in range(canvas.shape[2]):
84          blended += (weight * canvas[:, :, i]).astype(np.float64).astype(np.
    uint8)
85      cv2.namedWindow('overlay', cv2.WINDOW_NORMAL)
86      cv2.resizeWindow('overlay', 600, 600)
87      cv2.imshow("overlay", blended)
88      cv2.waitKey(0)
89      cv2.destroyAllWindows()
90
91
92  def write_table(canvas, outfile, center_axes=False):
93      dy = -int(canvas.shape[0] / 2) if center_axes else 0
94      dx = -int(canvas.shape[1] / 2) if center_axes else 0
95      with open(outfile, 'w', newline='') as csvfile:
96          fieldnames = ['x', 'y'] + ["z_m" + str(i + 1) for i in range(canvas
    .shape[2])]
97          writer = csv.DictWriter(csvfile, fieldnames=fieldnames)
98          writer.writeheader()
99          for y in range(canvas.shape[0]):
100             for x in range(canvas.shape[1]):
101                 mydict = {**{"x": x + dx, "y": y + dy},**dict(
102                     zip(["z_m" + str(i + 1) for i in range(canvas.shape[2])
    ], canvas[y, x, :].tolist()))}
103                 writer.writerow(mydict)
104
105
```

```
106 if __name__ == "__main__":
107     offsets = { "B4L_network_density_40um_0.62": (450,900, 0), "A4LqBEI_1.4
    ": (0,0, 0), "cells_0.62":(450,900,0), "CLSM_1114L-fluor_0.62":
    (450,900,0),
108                 "Danterior-T_3.2":(60,350,33), "lateral-T_3.0":(0,200,25),"
    medial-T_2.95":(65,260,20), "posterior-T_3.2":(72,103,22)}
109     # offsets = { "B5L_network_density_8.0": (0,0,0), "AVM8tot_0.8841":
    (0,0, 0) }# in px of unscaled image and degree (third value). Change if
     given in metric units!"1LT_2.15": (250, 280, -34), )
110     parser = argparse.ArgumentParser("Align")
111     parser.add_argument("img_dir", type=str, help="Folder with images or
    CSV tables")
112     parser.add_argument("-d", "--show-debug", action="store_true")
113     parser.add_argument("-n", "--no-center", action="store_false", help="
    don't center axes")
114     parser.add_argument("-o", "--out", type=str)
115
116     args = parser.parse_args()
117     data = read_data(args.img_dir, offsets)
118     joined = join_data(data)
119     if args.out:
120         write_table(joined, args.out, args.no_center)
121     if (args.show_debug):
122         viz(joined)
```

Figure A.1.: Python script for image registration.

B. Appendix loading

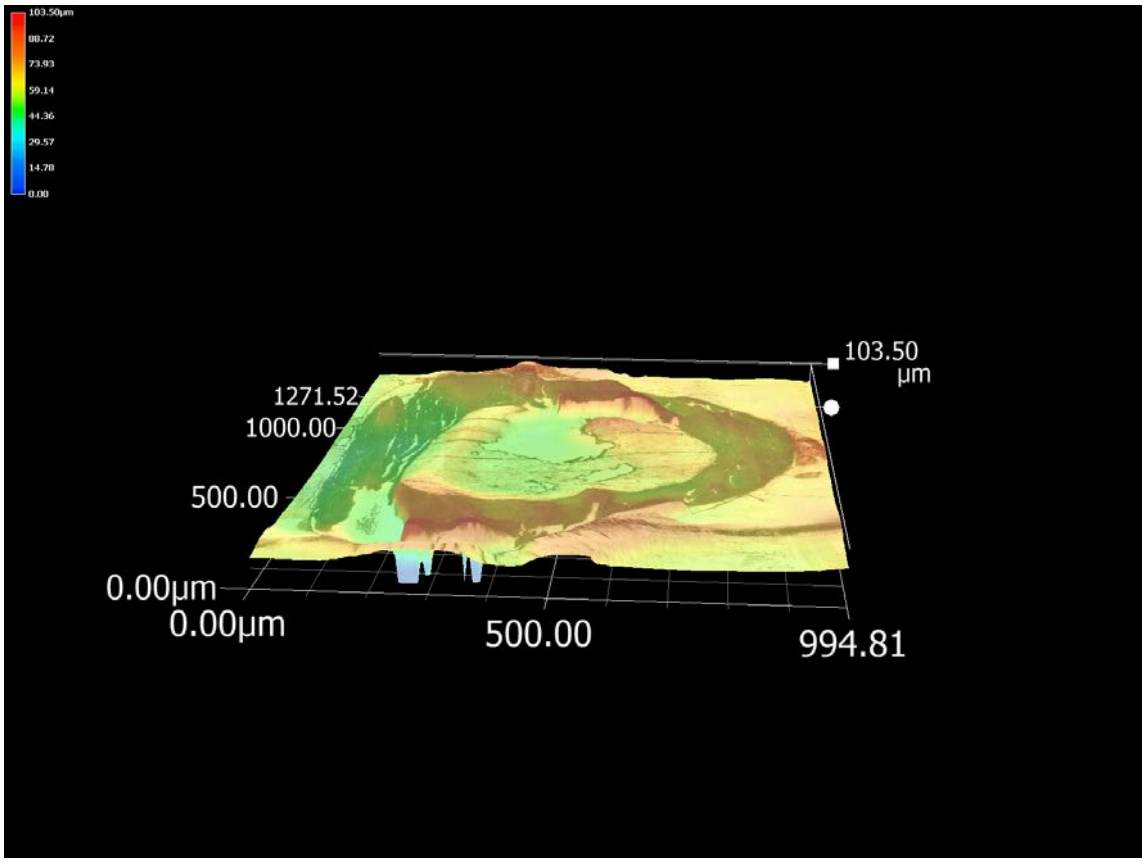

Figure B.1.: Result of surface roughness measurement with Keyence digital microscope VHX-50E map. Slice plane of a $5\mu m$ thick slice from a cortex of a murine tibia.

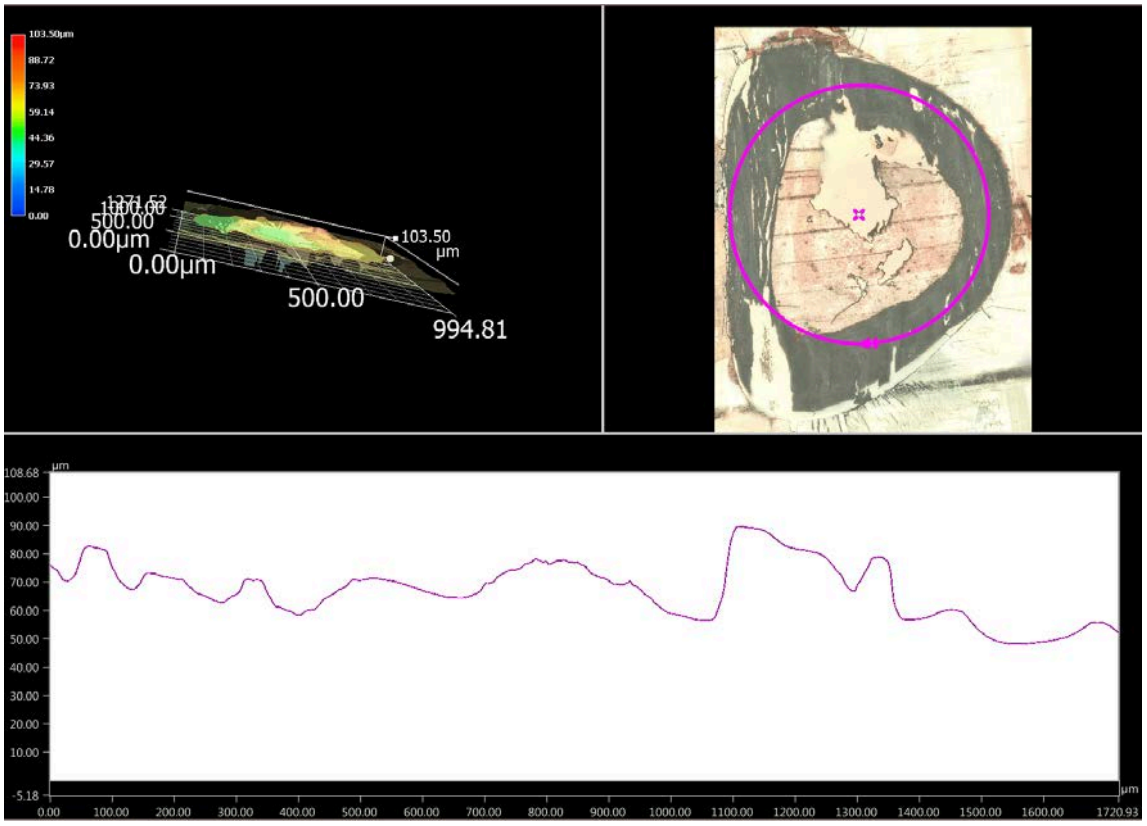

Figure B.2.: Result of surface roughness measurement with Keyence digital microscope VHX-50E map over a whole cortical cross section. A $5\mu m$ thick slice from a cortex of a murine tibia shows a wavy surface which is evaluated here by a line across the cross section. The top picture shows the microscopic image of the cortical cross section where the relative height is indicated by different scale and the line whose topogrophical course is shown in the lower image.

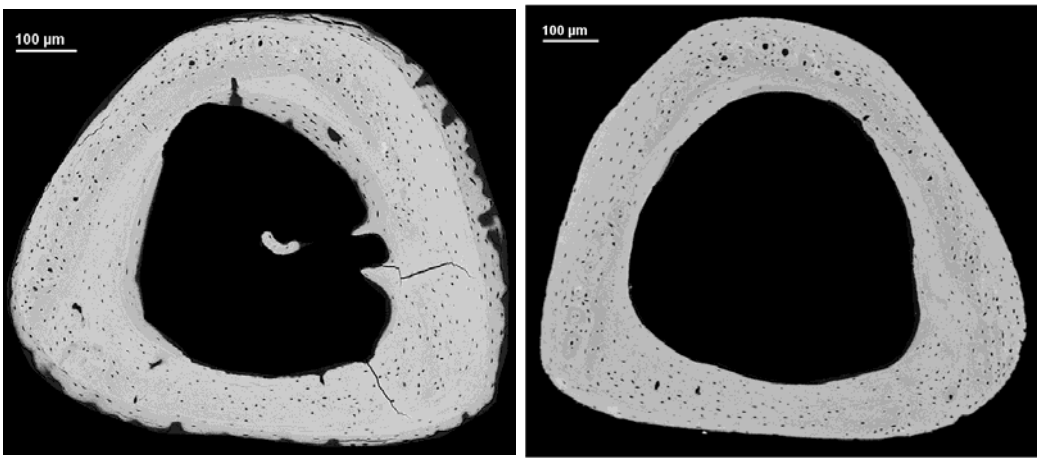

1L 1R

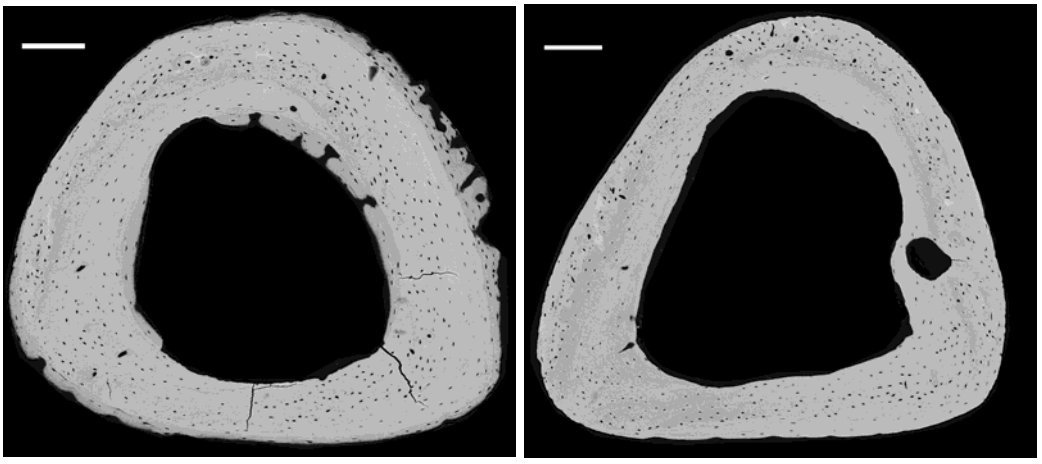

2L 2R

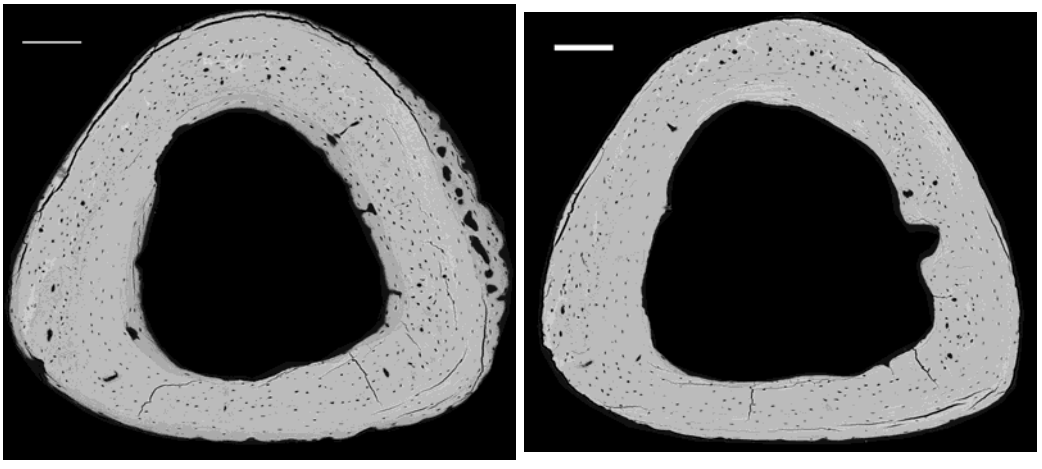

4L 4R

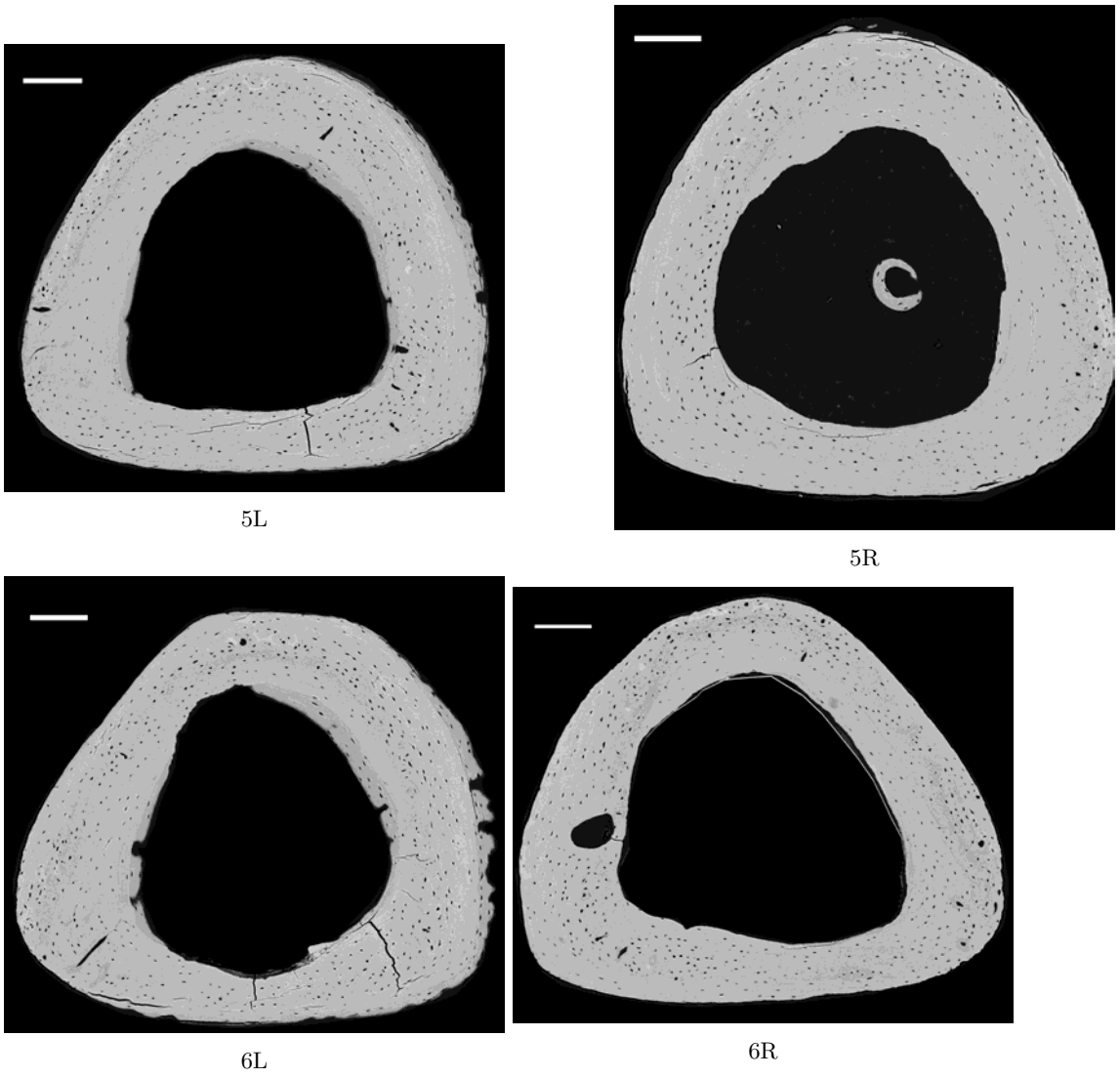

Figure B.4.: Quantitative backscattered electron image of murine bones. Each grey value corresponds with a descent amount of calcium content. Here, the cortices of 5 mice are shown. The left bones were loaded, while the right bone serves as a control. The scale bars are equal to 100 µm

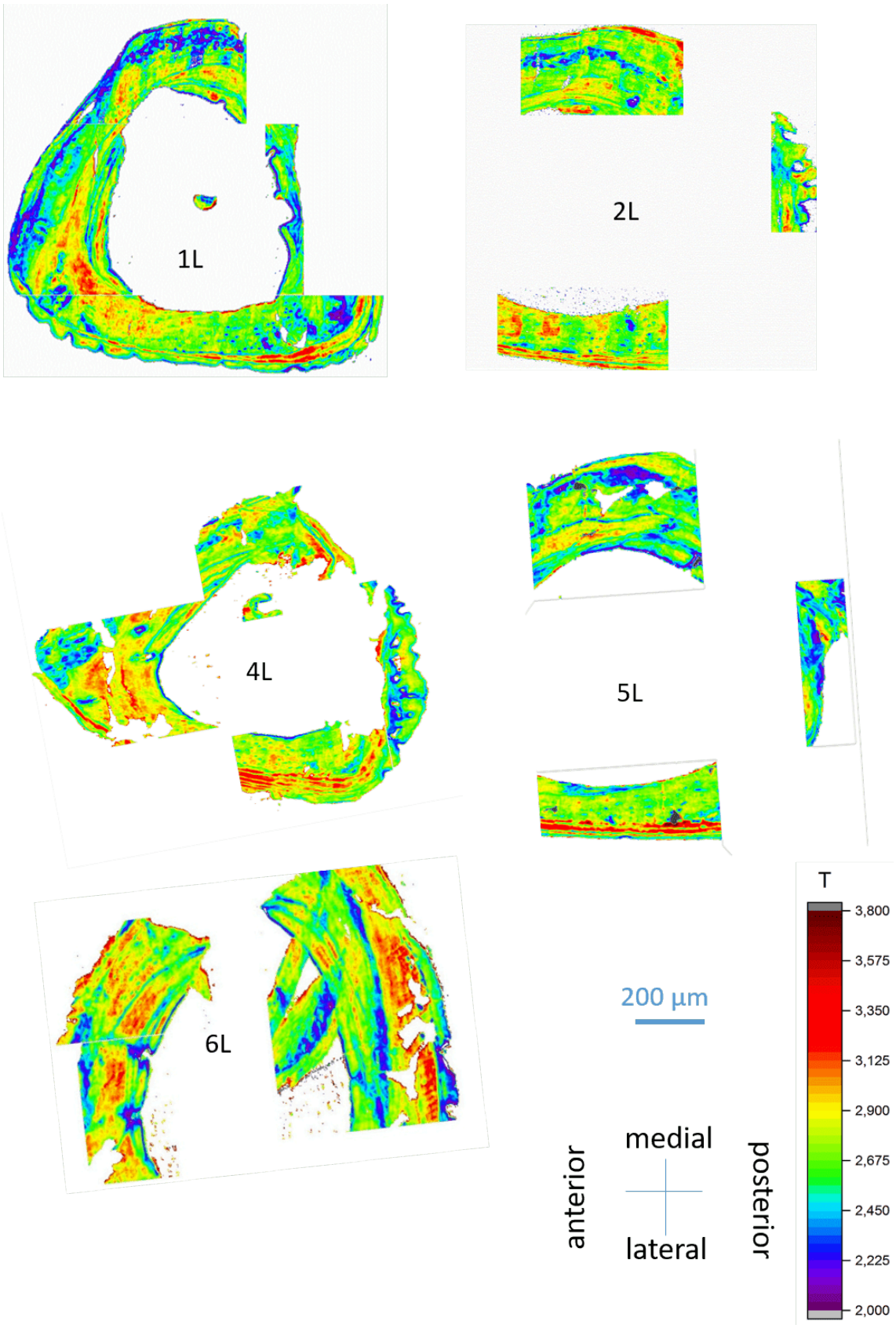

Figure B.5.: T parameter maps of loaded murine tibiae.

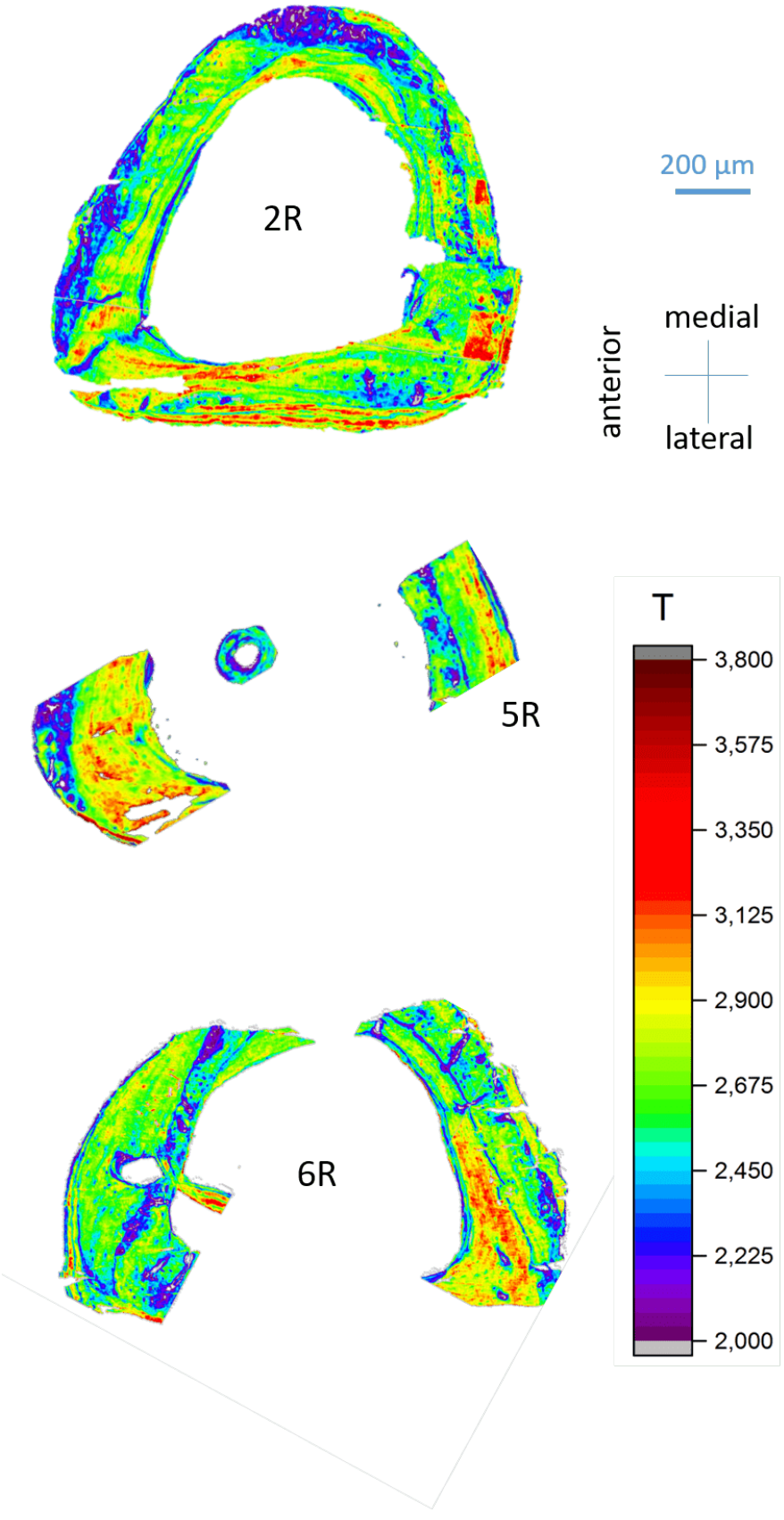

Figure B.6.: T parameter maps of non-loaded murine tibiae.

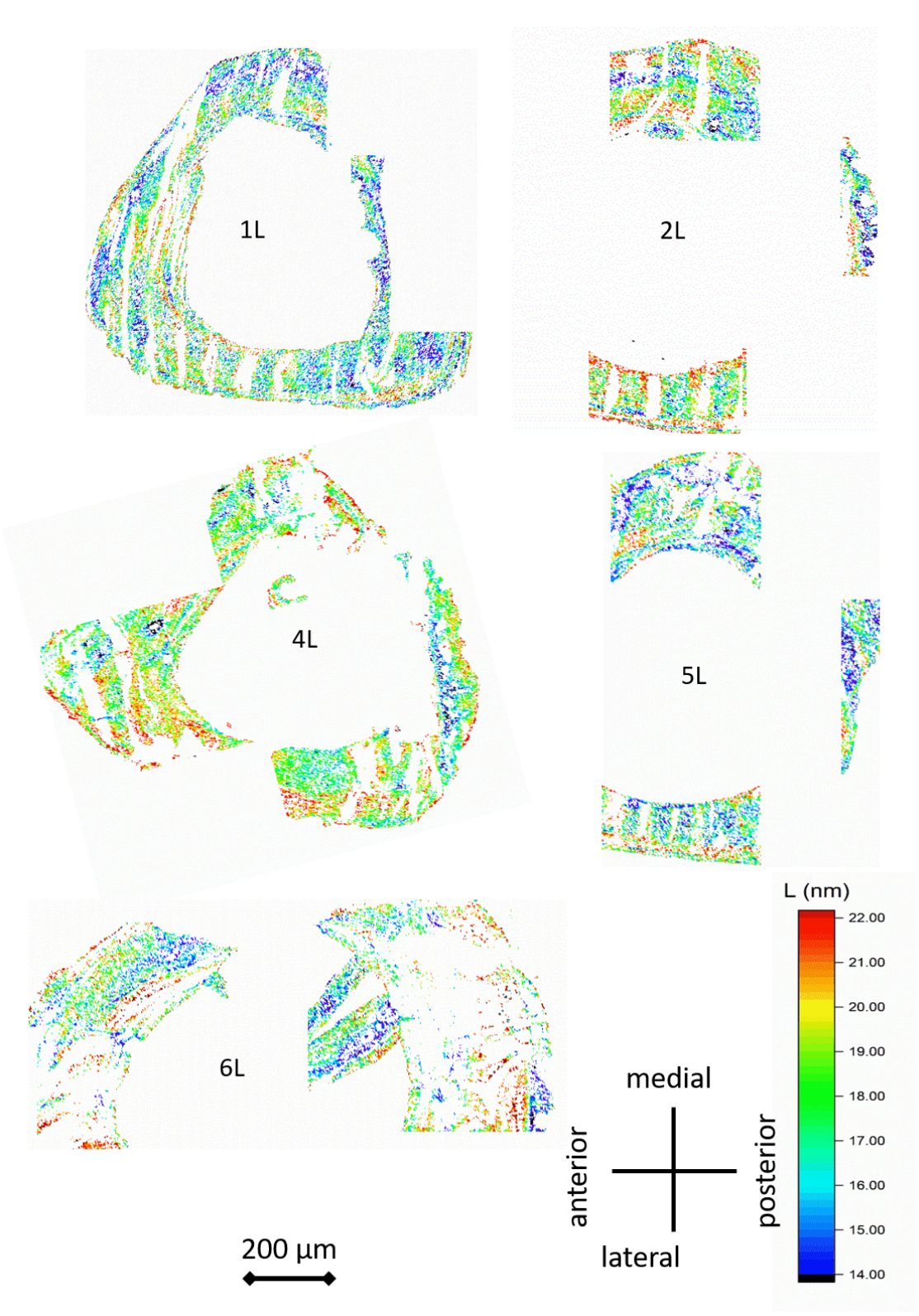

Figure B.7.: L parameter maps of loaded murine tibiae.

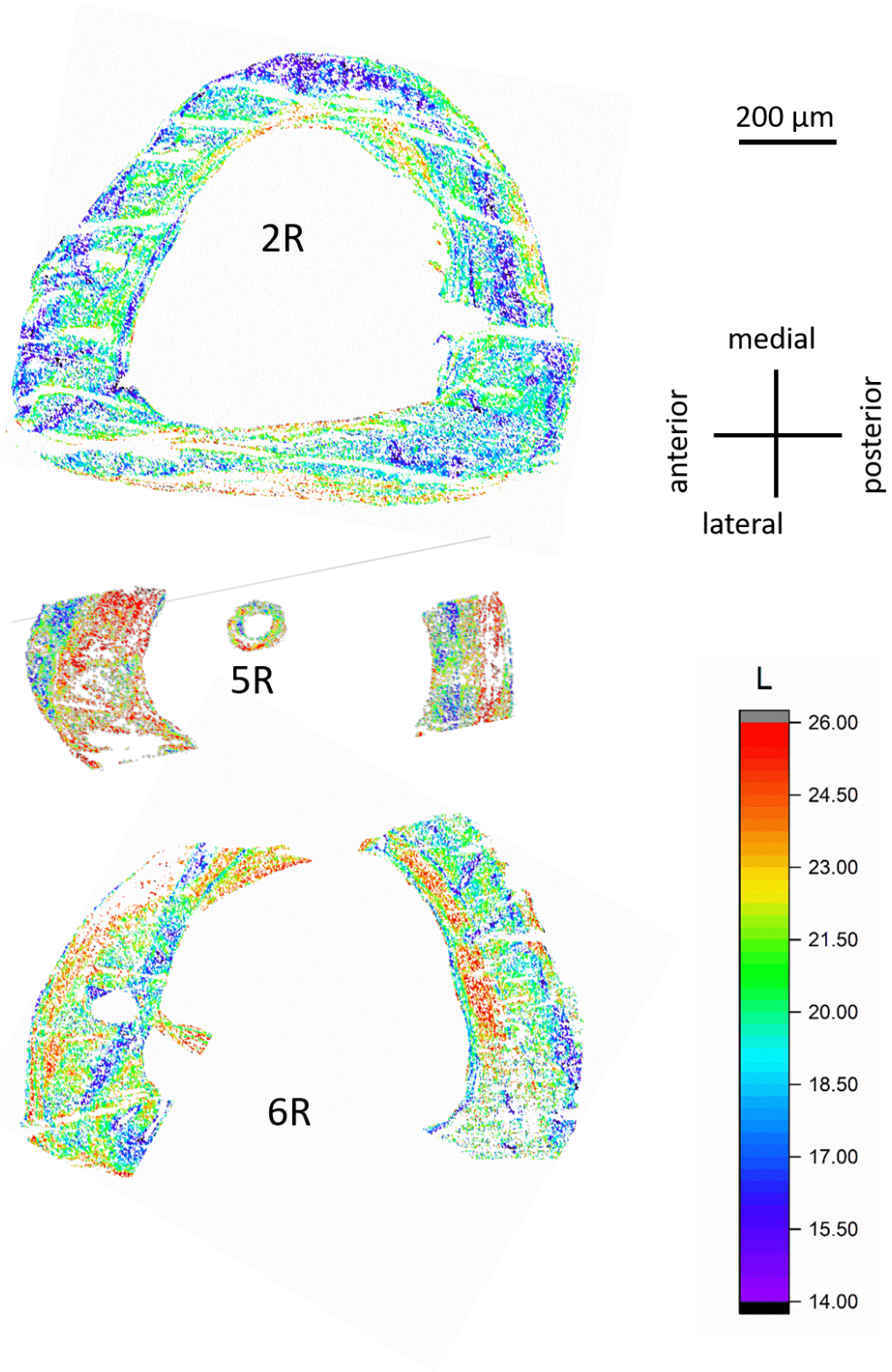

Figure B.8.: L parameter maps of non-loaded murine tibiae.

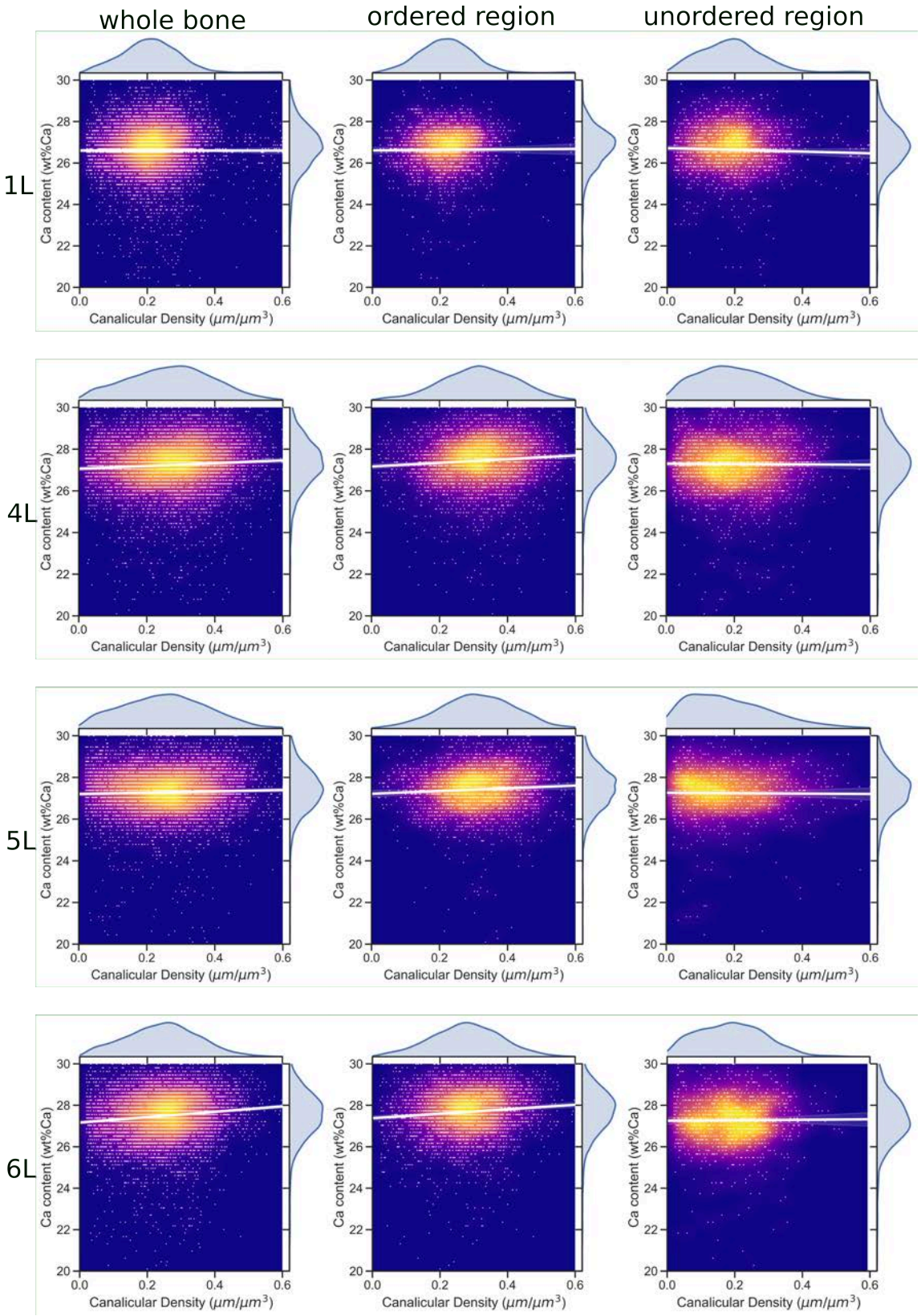

Figure B.9.: Evaluation of the correlation between canalicular density and Ca content in right murine tibia cortices. Each data point corresponds to CSLM and qBEI measurements on the same point after image registration with an resolution of $8\mu m$. The colors indicate the frequency of points in this area. The brighter the color, the more points are in this area. The white line is the linear regression of the data. The resulting SLOPEs are written down in table

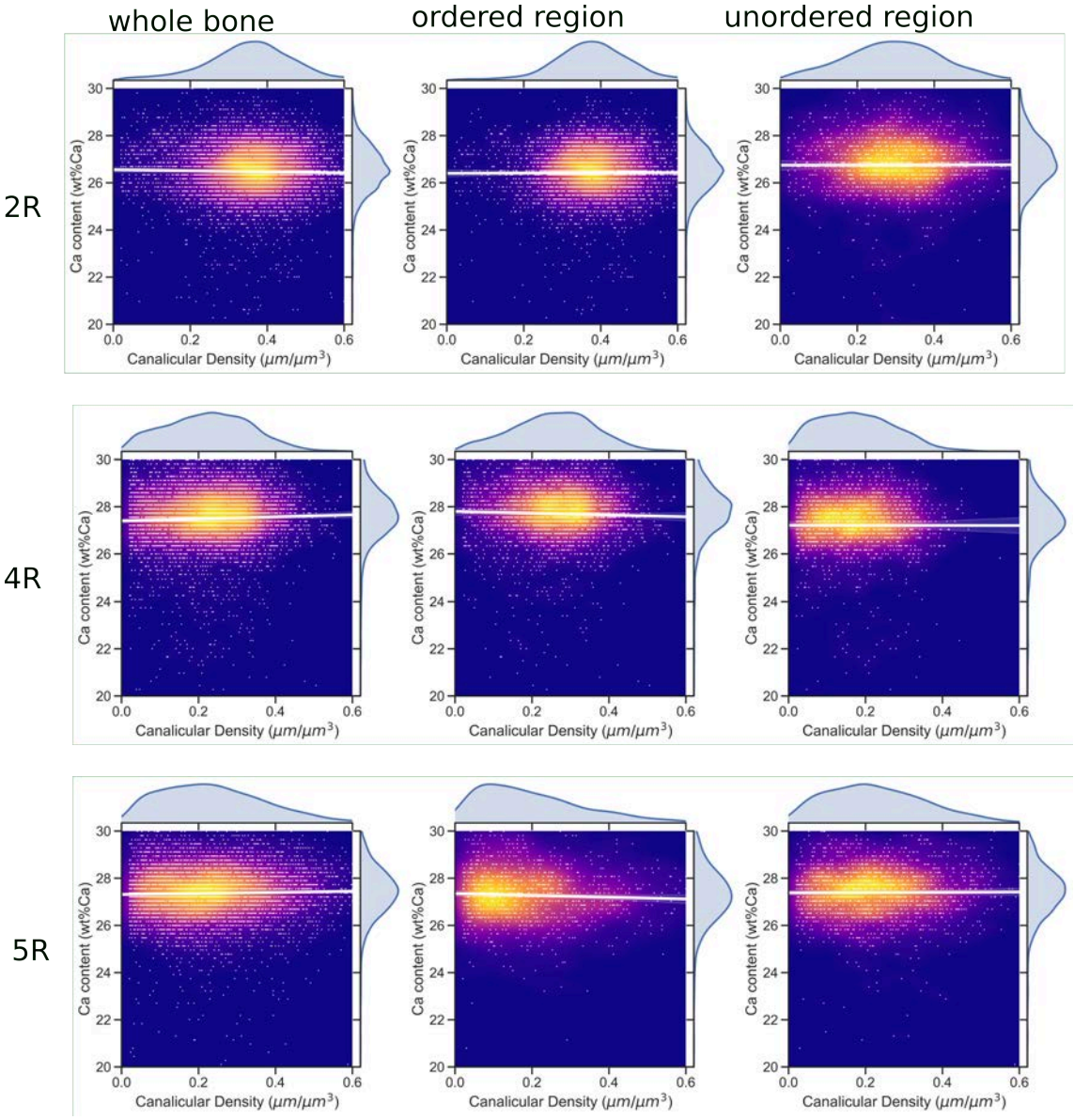

Figure B.10.: Evaluation of the correlation between canalicular density and Ca content in right murine tibia cortices. Each data point corresponds to CSLM and qBEI measurements on the same point after image registration with an resolution of $8\mu m$. The colors indicate the frequency of points in this area. The brighter the color, the more points are in this area. The white line is the linear regression of the data. The resulting SLOPEs are written down in table

C. Appendix healing

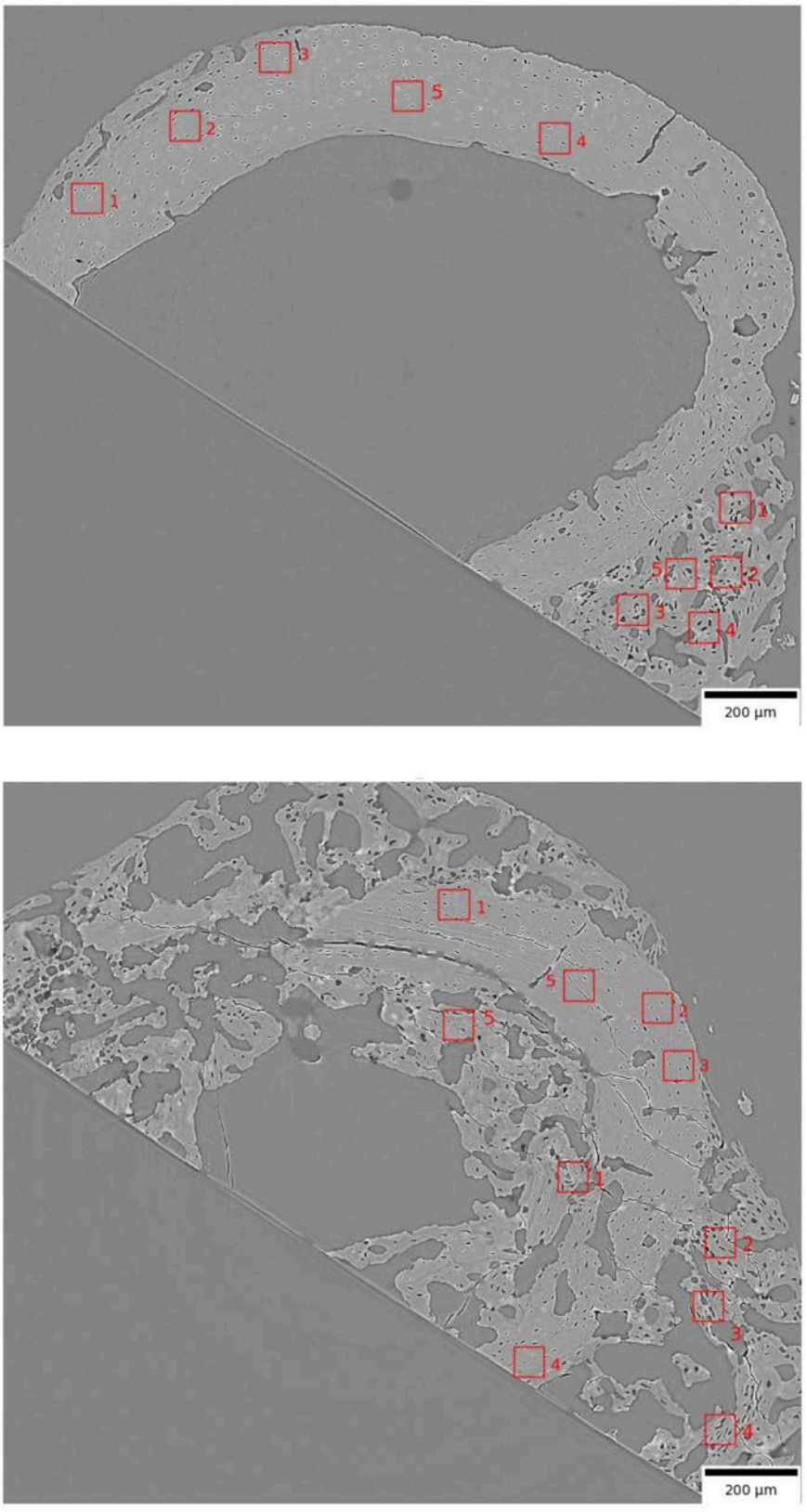

Figure C.1.: Selected cubes in cortex and callus in two slices and representative VOI with 1723 x 1560 x 1300 m^3.